

REPUBLIQUE DU CAMEROUN

Paix-Travail-Patrie

UNIVERSITE DE YAOUNDE I

CENTRE DE RECHERCHE
ET DE FORMATION DOCTORALE EN SCIENCES
TECHNOLOGIES ET GEOSCIENCES

DEPARTEMENT DE CHIMIE
INORGANIQUE



REPUBLIC OF CAMEROON

Peace-Work-Fatherland

UNIVERSITY OF YAOUNDE I

POSTGRADUATE SCHOOL
OF SCIENCE, TECHNOLOGY AND
GEOSCIENCES

DEPARTMENT OF INORGANIC
CHEMISTRY

LABORATORY OF APPLIED ANALYTICAL AND PHYSICAL CHEMISTRY

LABORATOIRE DE CHIMIE ANALYTIQUE ET PHYSIQUE APPLIQUEE

SYNTHESIS AND CHARACTERISATION OF CYCLODEXTRIN
FUNCTIONALISED NANOSPONGES FOR THE REMOVAL OF ORGANIC,
INORGANIC AND MICROBIAL CONTAMINANTS FROM AQUEOUS SOLUTIONS

THESIS

Submitted in partial fulfilment of the requirements for the award of the Degree of
Doctor of Philosophy (PhD/Doctorate) in Inorganic Chemistry

Speciality: Inorganic Chemistry
Option: Physical Chemistry

by

CHE RANDY NANGAH
Registration Number: 15U5989
MSc in Chemistry



Under the Supervision of

Josepha TENDO NGENEFEME FOBA, PhD
Professor
University of Buea

KETCHA Joseph MBADCAM, PhD
Professor
University of Yaounde I

2022

REPUBLIQUE DU CAMEROUN
Paix-Travail-Patrie

UNIVERSITE DE YAOUNDE I

FACULTE DES SCIENCES

DEPARTEMENT DE CHIMIE
INORGANIQUE



REPUBLIC OF CAMEROON
Peace-Work-Fatherland

UNIVERSITY OF YAOUNDE I

FACULTY OF SCIENCE

DEPARTMENT OF INORGANIC
CHEMISTRY

DEPARTMENT OF INORGANIC CHEMISTRY
DEPARTMENT OF INORGANIC CHEMISTRY


ATTESTATION OF CORRECTION OF PhD/DOCTORATE THESIS

We, the undersigned, members of the jury for the defense of Doctorate/Ph.D thesis of Mme CHE Randy NANGAH, matriculation number 15U5989, authorized by correspondence N° 221289/UYI/VREPDTIC/DQQC/SPD/SSPE/CB/nsr of May 16, 2022, attest that, this PhD thesis defended on June 01, 2022, at the Pedagogic Block; Multimedia Hall, of the Faculty of Science, University of Yaoundé I on the topic: **“Synthesis and characterization of cyclodextrin functionalised nanosponges for the removal of organic, inorganic and microbial contaminants from aqueous solutions”** for the award of a PhD/Doctorate degree in Inorganic Chemistry, has been corrected in conformity with the recommendations of the jury.


In testimony whereof, this attestation is issued with the privileges thereunto pertaining. /-

Yaounde, the ... **28 JUL 2022**

Examiner


NDI Julius NSAMI
Professor

President


AGWARA Moïse ONDOH
Professor

DEDICATION

To my father CHE Sylvester FORKOB and younger brother NCHE Jireh CHE.

In memory of my mother AKOH Anna EWET

ACKNOWLEDGEMENTS

I would like to use this occasion to express my sincere thanks to my supervisors, Professor Ketcha Joseph Mbadcam and Professor Josepha Foba Tendo, for their valuable guidance, support and encouragement throughout the research program.

Many thanks to the Pan African Materials Institute (PAMI) for providing a three-month Research Scholarship under the PAMI Scholar Travel Fellowship Program at Worcester Polytechnic Institute (WPI), Massachusetts, USA.

My profound gratitude to Professor Winston Oluwole Soboyejo and Nima Rahbar, Associate Professor of WPI for your endorsement, guidance and for providing the research resources necessary to take this project through in its entirety. To John Obayemi, Associate Professor and Dr Ali Salifu for your guidance and support throughout my stay at WPI.

I am grateful to Professor Simon. J. L. Billinge. and Songsheng Tao for PDF analysis by the NSF MRSEC program through Columbia in the Center for Precision Assembly of Superstratic and Superatomic Solids (DMR-1420634).

I would also like to give my deepest appreciation to all the staff members in the Department of Inorganic Chemical, University of Yaounde I. To Ndi Julius Nsami Associate Professor, my mates in the lab, especially Dr. Lekene Ngouateu René Blaise and Dr Abega Aime Victoire who have given me great help in my research work.

I thank the all the members of my family for their immense financial and moral support towards the realization of this project.

To all my friends, your moral support and encouragement have been a great blessing, through it all.

ABSTRACT

This thesis presents comprehensive experimental studies of goethite and/or hydroxyapatite functionalisation of cyclodextrin nanosponges and the ability of these nanosponges to remove organic, inorganic and microbial pollutants from water. Cyclodextrin nanosponge (CDN), cyclodextrin goethite-based nanosponge (CDG), hydroxyapatite functionalised cyclodextrin nanosponge (CDHA) and goethite/hydroxyapatite functionalised cyclodextrin nanosponge (CDGHA) were synthesized through ultrasound-assisted polycondensation polymerisation using citric acid as a crosslinker. The polymerisation is a two-stage process involving the formation of a dry gel (pre-polymer) and condensation to high molecular weight polymers in the presence of disodium phosphate as catalyst. The structural, morphological, physicochemical and thermal properties of the as-prepared nanosponges were characterized using BET, XRD, FTIR, PDF, SEM and TEM analysis. Goethite and/or hydroxyapatite grafting interactions occurs as an additional crosslinking reaction between the –COOH group of the tertiary carbon of citric acid and –OH of goethite and/or hydroxyapatite to form a hypothetical ester bond. Functionalization of CDN with goethite and/or hydroxyapatite nanopowder yielded more porous (nanopores), highly swellable semi-crystalline materials with additional surface functional groups. CDG for example swells 558.4 % times its weight in water in contrast to CDN (379.8 %). Results from adsorption tests showed that 99.98% (1.93 mg/g), 100% (2.01 mg/g), 93.64% (1.95 mg/g), and 104.73% (2.06 mg/g) of methylene blue dye (0.2 g of adsorbent and 20 ppm of MB solution) was removed for CDN, CDG, CDHA and CDGHA respectively. Additionally, a heavy metal like nickel(II) ion with concentration of 50 ppm, was adsorbed at 98.89 % (4.95 mg/g) for CDN, 97.41 % 4.87 mg/g) for CDG, 97.91% (4.50 mg/g) for CDHA and 100 % (5.00 mg/g) for CDGHA nanosponges. Similarly, inorganic fluoride adsorption (using 0.2 g of adsorbent and 20 ml of 50 ppm fluoride solution) show a maximum equilibrium removal 69.58% (3.48 mg/g), and 71.33% (3.57 mg/g) was observed for CDHA and CDGHA respectively. Studies on E Coli removal showed a removal of 83.75 % using the CDG nanosponge. The mechanism in which these hybrid nanosponges remove the different pollutants were elucidated. Our results clearly demonstrated the affinity of the synthesized nanosponges to bind and remove effectively different classes of pollutants from water. The implications of the results are then discussed for the potential used of these synthesized hybrid nanosponges in different water purification systems.

RESUME

Cette thèse présente des études expérimentales approfondies sur les nanosponges de cyclodextrine fonctionnalisées par goethite et/ou hydroxyapatite et leur capacité à éliminer différentes classes de polluants. Des Nanosponges hybrides à savoir : nanosponge de cyclodextrine (CDN), nanosponge à base de cyclodextrine goethite (CDG), nanosponge de cyclodextrine fonctionnalisée par hydroxyapatite (CDHA) et nanosponge de cyclodextrine fonctionnalisée par goethite/hydroxyapatite (CDGHA) ont été synthétisées par polymérisation assistée par ultrasons en utilisant l'acide citrique comme agent de réticulation. Cette polymérisation se déroule en deux étapes impliquant la formation d'un gel sec (pré-polymère) et la condensation polymères en présence de phosphate disodique comme catalyseur. Les interactions de greffage de la goethite et/ou de l'hydroxyapatite se produisent comme une réaction de réticulation supplémentaire entre le groupe -COOH de l'acide citrique et le groupe -OH de la goethite et/ou de l'hydroxyapatite pour former une hypothétique liaison ester. Leurs propriétés structurales, morphologiques, physico-chimiques et thermiques ont été caractérisées en utilisant la DRX, la MET, MEB, IR à transformée de Fourier et l'analyse thermogravimétrique. La fonctionnalisation du CDN avec de la goethite et/ou de l'hydroxyapatite a donné des matériaux semi-cristallins plus poreux et hautement gonflables avec des groupes fonctionnels de surface supplémentaires. Les résultats des tests d'adsorption ont montré que 99,98% (1,93 mg / g), 100% (2,01 mg / g), 93,64% (1,95 mg / g) et 104,73% (2,06 mg / g) de colorant bleu de méthylène (0,2 g d'adsorbant et 20 ppm de solution de MB) a été éliminé pour CDN, CDG, CDHA et CDGHA respectivement. Dans un autre cas, les résultats de notre expérience ont montré que les métaux lourds comme l'ion nickel (II) avec une concentration de 50 ppm, étaient adsorbés à 98,89% (4,95 mg / g) pour CDN, 97,41% 4,87 mg / g) pour CDG, 97,91% (4,50 mg / g) pour l'ACHD et 100,01% (5,00 mg / g) pour les nanosponges CDGHA. De même, l'adsorption des ions fluorure (en utilisant 0,2 g d'adsorbant et 20 ml de solution de fluorure à 50 ppm) montre une élimination maximale à l'équilibre de 99,98% (19,30 mg / g), 100% (20,13 mg / g), 93,64% (19,55 mg / g) g) et 104,73% (20,95 mg / g) pour l'ACHD et le CDGHA respectivement. Par la suite, des études sur l'élimination d'*E Coli* ont montré une élimination de 83,75% en utilisant le nanosponge CDG. Le mécanisme par lequel ces nanosponges hybrides éliminent les différents polluants a été élucidé. Ces résultats ont clairement démontré l'affinité des nanosponges synthétisés à éliminer efficacement différentes classes de polluants de l'eau.

TABLE OF CONTENTS

DEDICATION	i
ACKNOWLEDGEMENTS	ii
ABSTRACT	iii
RESUME	iv
TABLE OF CONTENTS	v
LIST OF FIGURES	ix
LIST OF TABLES	xiv
LIST OF ABBREVIATIONS	xv
INTRODUCTION	1
Statement of the problem	1
Strategies to Improve the Quality of Water/Shortcomings	3
Proposed Solution	4
Research Objectives	5
General Objective	5
Specific Objectives.....	5
Research Hypotheses.....	6
Research question.....	7
Research Interest and Prospects	7
Scope and Organisation of Thesis	7
Chapter I - LITERATURE REVIEW	9
I.1 Cyclodextrins	11
1.1.1 Reactivity.....	13
1.1.2 Inclusion complex formation.....	14
1.1.3 Polymerisation of Cyclodextrin (Formation of Nanosponges)	15

1.1.4 Cyclodextrin based composite materials	17
1.1.5 Applications.....	17
1.2 Goethite	20
1.2.1. Structure and Properties	20
1.3 Hydroxyapatite	22
1.4 Pollutants, Sources and effects	23
1.4.1 Inorganic pollutants	23
1.4.2 Organic pollutants	25
1.4.3 Microbial contaminants	27
1.4.4 Water treatment technologies	27
1.5 Adsorption.....	28
1.5.1 Factors affecting adsorption	30
1.5.2 Adsorption Isotherms	31
1.5.3 Adsorption Kinetics.....	34
1.5.4 Analysis of Error	36
1.5.5 Fixed bed adsorption	37
1.6 Characterisation Techniques	38
1.6.1 Pore Structure Analysis	38
1.6.2 X-Ray Powder Diffraction	39
1.6.3 Infrared Spectroscopy.....	40
1.6.4 Scanning Electron Microscopy (SEM).....	41
1.6.5 Transmission Electron Microscopy	42
1.6.6 The Pair Distribution Function (PDF) method.....	43
1.6.7 Thermogravimetric analysis	44
Chapter II - MATERIALS AND METHODS.....	46

2.1 Materials.....	46
2.2 Methodology	46
2.2.1 Synthesis.....	47
2.2.2 Characterization.....	49
2.3 Adsorption Studies	55
2.3.1 Batch Adsorption Studies	55
2.3.2 Column Adsorption Studies	55
2.3.3 Analysis of Solution	56
2.4 Bacterial Removal	58
Chapter III - RESULTS AND DISCUSSION	59
3.1 Formation of CD and CD Functionalised Nanosponges	59
3.2 Characterisation.....	62
3.2.1 Swelling test	62
3.2.2 Surface area analysis	62
3.2.3 FTIR	63
3.2.4 XRD.....	68
3.2.5 Pair Distribution Function Analysis	71
3.2.5 Thermal analysis.....	79
3.2.6 Scanning Electron Microscopy (SEM).....	82
3.2.7 TEM.....	85
3.3 Batch Adsorption Studies.....	87
3.3.1 Nickel Ion Removal.....	88
3.3.2 MB Removal	96
3.3.4 Fluoride Removal	99
3.4 Preliminary Column Adsorption Studies	101

3.4.3 <i>E. Coli</i> Removal	102
CONCLUSIONS AND FUTURE WORK	106
Conclusions	106
Suggestions for future work	108
REFERENCES	109
Appendix A - PREPARATION OF SOLUTIONS.....	125
A-1 Preparation of stock solutions of Ni (NO ₃) ₂ .6H ₂ O.....	125
Appendix B - DATA	126
B-1 Data for Batch and Column Adsorption Studies, Ni(II) ion.....	126
B-2 Data for Isotherm Models and Kinetic Models, Ni(II) ion.....	131
B-3 Data for Batch Adsorption Studies, MB	134
B-4 Data for Removal Rate, Methylene Blue Adsorption	135
B-5 Data for Kinetic Models, MB Adsorption.....	136
B-5 Data for Removal Rate, Fluoride adsorption.....	137

LIST OF FIGURES

Figure 1: a) Tap water collected in Yaounde b) Children drinking coloured tap water (Soa, Yaounde)	2
Figure 2: Classification of Nanomaterials [74]	10
Figure 3: Synthesis of nanomaterials via ‘top-down’ or ‘bottom-up’ approach [77]	11
Figure 4: Structure of cyclodextrin	12
Figure 5: Respective dimensions of α -, β -, and γ -cyclodextrins	13
Figure 6: Reactivity of the different positions.....	14
Figure 7: Some areas of applications of cyclodextrin nanosponges	18
Figure 8: Repeating unit, double chain $\text{FeO}_3(\text{OH})_3$ octahedra and crystal structure of goethite	21
Figure 9: Crystal Structure of hydroxyapatite [118]	22
Figure 10: Chemical structure of methylene blue dye	27
Figure 11: Different components in a solid-liquid adsorption system	29
Figure 12: Illustration of Bragg’s Law	39
Figure 13: Illustration of Attenuated Total Reflectance.....	40
Figure 14: Schematic drawing of (a) the typical Scanning Electron Microscope (SEM) column and (b) sample-beam interactions within a SEM.	41
Figure 15: Illustration of how an electron beam passes through the electron microscope in TEM mode (imaging and diffraction) [164]	42
Figure 16: Outline of research methodology	47
Figure 17: Vacuum oven used in the synthesis of the CD nanosponges.....	48
Figure 18: Netzsch 209 F1 Libra instrument.....	51
Figure 19: Bruker Vertex 70 FTIR Instrument	51
Figure 20: JEOL JSM-7000F Field Emission Scanning Electron Microscope.....	53
Figure 21: Philips CM10 transmission electron microscope.....	54

Figure 22: Setup for column adsorption.....	56
Figure 23: DIONEX 2100 Ion Chromatography System.....	57
Figure 24: Perkin Elmer NexION 350X Inductively Coupled Plasma Mass Spectrometer (ICP-MS).....	57
Figure 25: Polymer formation: adding of bicarbonate, goethite and/or hydroxyapatite to the dry gel	60
Figure 26: Proposed mechanism for crosslinking of cyclodextrin with citric acid using disodium phosphate as catalyst	60
Figure 27: Proposed mechanism for the grafting of goethite onto crosslinked cyclodextrin (CDG).....	61
Figure 28: N ₂ -adsorption-desorption Isotherm plot for goethite nanopowder	62
Figure 29: Functionalising CDN with goethite	64
Figure 30: FTIR stacked plot for cyclodextrin, CDN, CDG and goethite	65
Figure 31: FTIR stacked plot for CDN, CDG, CDN and CDGHA.....	66
Figure 32: Overlaid spectra of CDG and CDHA	67
Figure 33: XRD Spectra of Goethite Nanopowder	68
Figure 34: Whole pattern fitted PXRD spectra of goethite nanopowder	69
Figure 35: a) Stacked X-ray powder pattern of goethite, CDN, CDG, CDHA, CDGHA; b) overlaid spectra of CDG-CDHA and c) overlaid spectra of CDG-CDGHA.....	70
Figure 36: PDFs obtained from synchrotron x-ray powder diffraction: (a) PDFs in low- <i>r</i> region; (b) PDFs in high- <i>r</i> region, they are multiplied by the same scale for better visual inspection. All data is normalized for comparison.	72
Figure 37: (top) Measured PDF of CDG and simulated PDFs of crystalline (middle) goethite and (bottom) cyclodextrin. The simulation is based on real space calculation of PDF and the parameters used are $U_{iso} = 0.008 \text{ \AA}^2$, $Q_{max} = 16.0 \text{ \AA}^{-1}$. PDFs are normalized for comparison	73

Figure 38: PDF of CDGHA fitted by a linear combination of PDFs of CDG and CDHA. The yellow dots are the PDF data of CDGHA, blue line is the calculated PDF in best fit and yellow line is the residual.	73
Figure 39: Comparison between PDFs: (a) PDFs in low- <i>r</i> region; (b) PDFs in high- <i>r</i> region, they are multiplied by the same scale for better visual inspection. All data is normalized for comparison.	74
Figure 40: PDF of CD fitted by a linear combination of PDFs from isolated molecule and base line from density modulation. The blue dots are PDF data of CD and the red line is calculated PDF from the best fit to the data. The green line, sky blue line and yellow line show the contribution to the calculated PDF from cyclodextrin, citric acid and base line respectively.	75
Figure 41: PDFs fitted by the structure model. The dots are data from measurement, the overlapping lines are the calculation of PDF from the best fit and the lines with same colour as the data dots are the residuals. The “Rw” is a metric for the goodness of fit.	76
Figure 42: Comparison between measured PDF of CD (blue), calculated PDF of crystal cyclodextrin (red) with $U_{\text{iso}} = 1 \text{ \AA}^2$, and calculated PDF of single cyclodextrin molecule (green) with $U_{\text{iso}} = 1 \text{ \AA}^2$. The calculated PDF of crystal cyclodextrin is attenuated by a Gaussian envelope to simulate the decaying of correlation in polymer network.	78
Figure 43: TGA curves of CD, CDG, CDHA and CDGHA showing mass loss as a function of temperature	79
Figure 44: TGA/DTG curves of CDN and CDG showing mass loss as a function of temperature, and the variation in mass loss (insert figure).....	80
Figure 45: SEM Micrograph of as-synthesized goethite nanoparticles at magnifications: (a) x19000 and (b) x95000; and (c) particle size distribution.....	82
Figure 46: 3D Surface morphology of CDN and CDG at different magnifications using SEM	83
Figure 47: 3D Surface morphology of CDHA and CDGHA at different magnifications using SEM.....	84
Figure 48: Pore size distribution and descriptive statistics	85

Figure 49: TEM micrograph of CDN (a-b) and CDG (c-f) nanosponge showing different structural domains	86
Figure 50: TEM micrograph showing different structural domains of CDHA (a) and CDGHA (b-d) nanosponge	87
Figure 51: Variation of Contact Time for Ni(II) Ion Adsorption.....	88
Figure 52 : Variation of Concentration for Ni(II) Ion Adsorption	89
Figure 53: Langmuir, Freundlich, Redlich Peterson, Sips equilibrium isotherm models for Ni(II) ion adsorption on CDN (at constant time, mass and temperature).....	90
Figure 54: Langmuir, Freundlich, Redlich Peterson, Sips equilibrium isotherm models for Ni(II) ion adsorption on CDG (at constant time, mass and temperature).....	90
Figure 55: Langmuir, Freundlich, Redlich Peterson, Sips equilibrium isotherm models for Ni(II) ion adsorption on CDHA (at constant time, mass and temperature).....	91
Figure 56: Langmuir, Freundlich, Redlich Peterson, Sips equilibrium isotherm models for Ni(II) ion adsorption on CDGHA (at constant time, mass and temperature).....	91
Figure 57: Pseudo-first order, Pseudo-second order and Elovich kinetic models for Ni(II) ion adsorption on CDN (at constant concentration, mass and temperature)	94
Figure 58: Pseudo-first order, Pseudo-second order and Elovich kinetic models for Ni(II) ion adsorption on CDG (at constant concentration, mass and temperature)	95
Figure 59: Pseudo-first order, Pseudo-second order and Elovich kinetic models for Ni(II) ion adsorption on CDHA (at constant concentration, mass and temperature)	95
Fig. 60. Pseudo-first order, Pseudo-second order and Elovich kinetic models for Ni(II) ion adsorption on CDGHA (at constant concentration, mass and temperature)	95
Figure 61: Before and after stacked FTIR plot of Ni(II) ion adsorption on CDN	96
Figure 62: Pseudo-first order, Pseudo-second order and Elovich kinetic models for MB adsorption on CDN (at constant concentration, mass and temperature)	97
Figure 63: Pseudo-first order, Pseudo-second order and Elovich kinetic models for MB adsorption on CDG (at constant concentration, mass and temperature)	98

Figure 64: Pseudo-first order, Pseudo-second order and Elovich kinetic models for MB adsorption on CDHA (at constant concentration, mass and temperature)	98
Figure 65: Pseudo-first order, Pseudo-second order and Elovich kinetic models for MB adsorption on CDN, CDG, CDHA and CDGHA (at constant concentration, mass and temperature).....	99
Figure 66: Pseudo-first order, Pseudo-second order and Elovich kinetic models for Fluoride adsorption on CDHA (at constant concentration, mass and temperature)	100
Figure 67: Pseudo-first order, Pseudo-second order and Elovich kinetic models for Fluoride adsorption on CDGHA (at constant concentration, mass and temperature)	101
Figure 68: Breakthrough curve of relative effluent concentration (C_t/C_o) against time (at constant concentration, mass and temperature).....	102
Figure 69: Determination of maximum wavelength of absorption for MB	134
Figure 70: Calibration curve	134
Figure 71: Variation of Contact Time for MB Adsorption	135

LIST OF TABLES

Table I: Crosslinked CD polymers [73]	16
Table II: Cyclodextrin nanosponges/composite polymers	19
Table III: Heavy metals and their human health effects [131].....	24
Table IV: Human Health Effects of Nickel [135]	25
Table V: Classification dyes [138].....	26
Table VI: Advantages and disadvantages of current techniques for heavy metals removal, adapted from Ihsanullah et al., 2016 [141].....	28
Table VII: Differences between Physisorption and Chemisorption, Atkins 2006 [145].	30
Table VIII: Phase Composition and Lattice Parameters	68
Table IX: Fitting result	77
Table X: DTG mass loss steps for CDN and CDG at the temperature of maximum decomposition.....	81
Table XI: Nonlinear parameter estimates for equilibrium and kinetic adsorption models for Ni(II) ion adsorption.....	92
Table XII: Nonlinear parameter estimates for kinetic adsorption models for MB adsorption on CDN, CDG, CDHA and CDGHA.....	97
Table XIII: Nonlinear parameter estimates for kinetic adsorption models for fluoride ion adsorption on CDHA and CDGHA.....	100
Table XIV: Removal efficiency of <i>E. coli</i> on CDN, CDG, CDHA and CDGHA	103
Table XV: comparison of some of the results obtained by other authors on citric acid crosslinked cyclodextrin or cyclodextrin functionalised polymers and some nanosorbents with that obtained in this work.	104

LIST OF ABBREVIATIONS

S.I. (Système International d'Unités) abbreviations for units and standard notations for chemical elements, formulae and chemical abbreviations are used in this work. Other abbreviations are listed below.

BET	Brunauer-Emmett-Teller
CD	Cyclodextrin
CDG	Goethite Functionalised Cyclodextrin Nanosponge
CDGHA	Goethite/Hydroxyapatite Functionalised Cyclodextrin Nanosponge
CDHA	Hydroxyapatite Functionalised Cyclodextrin Nanosponge
CDN	Cyclodextrin nanosponge
CT	Citric acid
DTG	Differential thermogravimetry
<i>E. coli</i>	<i>Escherichia coli</i>
MB	Methylene Blue
MDG	Millennium Development Goals
PDF	Pair Distribution Function
SEM	Scanning Electron Microscopy
TEM	Transmission Electron Microscopy
TGA	Thermogravimetric Analysis
TNTC	Too Numerous To Count
XRD	X-Ray Powder Diffraction
β -CD	Beta Cyclodextrin
POU	Point-of-Use
POE	Point-of-Entry
HA	Hydroxyapatite
NS	Nanosponge
ICSD PDF	Inorganic Crystal Structure Database Powder Diffraction File
UV	Ultra-Violet
SEI	Secondary Electron in=lens
EGC	Effluent Generator Column
LRV	Log Reduction Values
BJH	Barrett-Joyner-Halenda

EPI	Epihalohydrin
CA	Citric Acid
ADP	Atomic Displacement Parameter
GRG	Generalised Reduced Gradient
FTIR	Fourier Transform Infrared
ICP-MS	Inductively Coupled Plasma Mass Spectrometer

INTRODUCTION

INTRODUCTION

In 2010, the UN General Assembly explicitly recognised the human right to sufficient, continuous, safe, acceptable, physically accessible and affordable water for personal and domestic use [1]. While important gains were made to increase access to improved water supplies during the MDG era, 2020 World Health Organization and United Nations Children's Fund (WHO/UNICEF) Joint Monitoring Programme for Water Supply, Sanitation and Hygiene (JMP) statistics on drinking water indicated that 2 billion people lack access to safe water at home: of these, 282 million people spend more than 30 minutes roundtrip collecting water; 367 million people do not have basic drinking water services and 122 million people drink water directly from surface sources such as streams or lakes [2].

Globally, more people are reported to die as a result of polluted water than are killed by all forms of violence including war [3, 4], and 80 percent of all sickness and disease results directly or indirectly from poor water supply. In 2000, death due to diarrhoeal diseases was reported to be the third leading cause of death worldwide (2.2 million); though this figure has reduced by about half between 2000 and 2016 (2.2- 1.4 million), diarrhoea diseases is still the sixth leading cause of death worldwide[5].

Countries in Sub-Sahara Africa (SSA) are still far from meeting the MDG target with just 24% of the population in this sub-region having access to safely managed water and an additional 34% with access to basic drinking water services [6, 7]. Moreover, these estimates do not take into consideration the water quality [8], hence, several authors have argued that the proportion of those with access to safe drinking water have been grossly overestimated [9-12]. Therefore, the access to adequate portable water is highly imperative to promote public social welfare and development.

Statement of the problem

The quality of water consumed is critical in controlling infectious diseases and other health problems. Contaminated water and poor sanitation are linked to transmission of diseases such as cholera, diarrhoea, dysentery, hepatitis A, typhoid and polio. Almost 240 million people are affected by schistosomiasis – an acute and chronic disease caused by parasitic worms contracted through exposure to infested water. In Cameroon, 49% of the population in 1990

and 76% in 2015 (no data available for Cameroon for 2017 to 2022 WHO reports) [13, 14] is reported to have access to improved drinking water sources. However, many urban municipalities face water crisis characterized by severe irregular and unreliable drinking water supply. These water shortages have prompted people to revert to other sources of water such as shallow dug wells and springs, which have a high risk of infection[15]. Most people use water directly available without any treatment and are therefore exposed to water related diseases. Several reported cases of cholera such as the cholera outbreaks in 2010 and 2011 which resulted to 657 deaths in 8 of the 10 regions in the country, typhoid, and diarrhoea illustrate some the human health effect of consuming poor quality water [16]. Piped water is subject to recontamination during distribution. Brown, and black tint; cloudiness; or heavy sediment can be found in some water because of inadequate treatment or due to corrosive effects on distribution pipes. **Figure 1** shows the near typical colour of tap water collected in Yaounde and primary school children drinking of the same. Heavy metals can be present in some source water, causing a metallic taste and staining of fixtures and laundry, and treatment is necessary to prevent their presence in delivered drinking water [17].



Figure 1: a) Tap water collected in Yaounde b) Children drinking coloured tap water (Soa, Yaounde)

Pollutants in water can be broadly classified into pathogenic microorganisms (bacteria, viruses, protozoa), toxic organic (dyes, herbicides, pharmaceuticals), inorganic (heavy metals and polyatomic compounds) and radiological compounds [18, 19]. Contaminated water often contain a mixture of these classes of pollutants introduced either through natural or man-made

sources (industrial by-products, improper disposal of household chemicals, human and animal wastes) [20].

Microbial contamination of drinking water consumed in the country (Cameroon) has been reported. Total coliform, faecal coliform, *E. coli* and faecal streptococcus are indicator bacterial used to determine water quality. Nguendo-Yongsi [21] carried out a study on 508 drinking water samples (302 from households connected to piped water, 154 from wells and 27 from community standpipes) from different neighbourhoods in Yaounde to evaluate microbial contamination of drinking water. Of the 302 households sampled, 292 (96.7%) households were consuming water with high prevalence of total and faecal coliform, thus unfit for human consumption. *E. Coli* was found in 28 household, 29 wells and 7 spring water samples. He also found no significant difference in the level of microbial contamination between drinking water, improved and non-improved springs and attributed these results to failure of raw water disinfection at the treatment plants, infiltration of contaminated water, leakage points and back siphonage.

Strategies to Improve the Quality of Water/Shortcomings

The removal of contaminants from drinking water is a huge challenge and technologies such as filtration, disinfection, distillation, precipitation/coagulation, and adsorption are constantly being developed to resolve this issue. Filtration systems include: reverse osmosis; ultrafiltration; pleated, melt blown and ceramic filters [17]. Ceramic water filters for example have shown high potential as point-of-use filtration systems [22]. Lately, Nigay et al. [23, 24] have prepared porous ceramic water filters with organic (activated carbon) and inorganic (hydroxyapatite, alumina) additives; these filter could remove a wide range of contaminants (nitrates, lead, fluoride, *E. coli*, and MS2) from water through a combination of trapping, adsorption, and substitution mechanisms.

Adsorption has received wide attention as a separation and purification technique due to its efficiency, fast kinetics and ease of use [25]. In this light, several authors have demonstrated the effectiveness of adsorbents such as activated carbon to remove organic [26, 27] and inorganic pollutants [28]; activated alumina for the removal of inorganic ions (As^{3+} , PO_4^{3-} , Cl^- , F^-); zeolites for NH_4^+ , organic, inorganic ions and microorganisms; graphene for organic and inorganic pollutants [29, 30]. These efforts however focus more on designing systems that

effectively remove single pollutants or a group of pollutants from the same class. A variety of substances (pathogenic microorganism, toxic organic and inorganic compounds) co-exist as pollutants in water and effective water remediation calls for a move from pollutant-specific adsorbents to the design of multifunctional adsorbents to meet various requirements [31-33].

Proposed Solution

Cyclodextrin polymers fall among innovative materials that are being developed for water purification. Cyclodextrins (CDs) are cyclic oligosaccharides produced from the enzymatic degradation of starch. The D-glucopyranose units of cyclodextrins adopt a conformation in the shape of a truncated cone (torus-shaped) with a hydrophobic internal cavity and a hydrophilic exterior, which can form inclusion complexes with apolar molecules. Cyclodextrin nanosponges (CDNS) are a class of insoluble polymeric materials with distinctive nanometre-wide cavities which accounts for their superior adsorption/complexation properties [34]. Through inclusion or host-guest complex formation, they can encapsulate a wide variety of organic compounds, mask odours, remove undesirable taste, enhance solubility and modulate drug release and delivery [35]. The sponges are easily regenerated by washing with an eco-friendly solvent such as ethanol, changing the solution pH, modifying the ionic strength or by mild warming [36].

Cyclodextrin nanosponges were first developed by DeQuan Lee and Min Ma by crosslinking beta cyclodextrin with hexamethylene diisocyanate and toluene-2,4-diisocyanate and have been shown to remove compounds such as phenol to concentrations as low as 1-50 ppb, where activated carbon has essentially no capability [37, 38]. They are synthesized by crosslinking the parent CD or CD derivative with a suitable polyfunctional cross linker. Cyclodextrin nanosponges have been grouped into urethane, carbonate, ester and ether nanosponges based on the types of cross linker used [34, 39]. Epichlorohydrin (EPI) crosslinked nanosponges for example have been employed to remove a wide variety of organic compounds including dyes, aromatics, chlorophenols, pesticides, detergents and odour causing compounds[40]. The one major disadvantage in using EPI is that it is a hazardous environmental pollutant and a potential carcinogen[41]. Polycarboxylic acids are eco-friendly crosslinking agents and the condensation polymerisation is carried out without the use of harmful organic solvents or additives. M.J. Garcia Fernandez carried out acute toxicity tests on both soluble and insoluble citric acid crosslinked β -CD polymer and showed no sign of toxicity [42].

Recent work on CDNS for water treatment applications has focused on functionalising /immobilising CD or CD derivatives with other polymers [43, 44], carbon nanotubes [45, 46], activated carbon [47, 48], graphene oxide [49-52], magnetic iron oxide nanoparticles [53-62], metal ion/oxide, cellulose nanofibers [63], beetroot fibres [64], sawdust [65], chitosan [66, 67], inorganic and nanomaterials to form composites with variable adsorption capacities and functionalities. However, no work has been carried out on the functionalisation of cyclodextrin nanosponges with goethite and hydroxyapatite, specifically through covalent binding through citrate crosslinkers. In this work, we present a robust nanocomposite material, which possesses the ability to remove effectively different classes of pollutants from water. The rapid rate of pollutant removal makes them ideal for use in household tap water faucets to purify instantly drinking water.

In this thesis, we report the synthesis of novel citric acid-cross-linked cyclodextrin (CD) nanosponges through ultrasound-assisted polycondensation polymerisation, functionalised with goethite and/or hydroxyapatite nanopowders and investigate their ability to remove organic, inorganic and microbial contaminants from water. The performance of the nanosponges was tested using methylene blue as a representative organic compound, nickel for heavy metal ions, fluoride as an inorganic ion and *E. coli* as a model microbial contaminant.

Research Objectives

General Objective

The main objective of this thesis was to synthesise novel cyclodextrin functionalised nanosponges and investigate the potential of these materials to remove organic, inorganic and microbial contaminants from aqueous solutions.

Specific Objectives

The specific objectives are:

- To synthesise four different kinds of cyclodextrin functionalised nanosponges (1) citric acid crosslinked nanosponge (CDN), (2) goethite functionalised citric acid crosslinked nanosponge, (3) hydroxyapatite functionalised citric acid crosslinked nanosponge

(CDHA), (4) goethite/hydroxyapatite functionalised citric acid crosslinked nanosponge (CDGHA) through ultrasound assisted polycondensation polymerisation;

- Carry out a detailed structural and surface analysis - Brunauer, Emmett and Teller (BET) analysis (pore structure), Fourier Transform Infrared (FTIR) analysis was used for the identification of functional groups, monitor changes on the resultant material and also to determine the best synthetic route, Pair Distribution Function (PDF) and Powder X-ray Diffraction (PXRD) analysis (phase analysis, atomic structure), Scanning Electron Microscopy (SEM) for atomic resolution imaging of internal material structure at the nanoscale, Transmission Electron Microscopy (TEM) for 3D Imaging, Thermogravimetric Analysis (TGA) to analyse reactions and phase transitions) of the nanosponges to provide an understanding of the dynamics controlling the structure/property relationship and performance of the nanosponges;
- Carry out batch adsorption studies to determine the effects of variation of contact time and initial concentration of adsorbate, on the adsorption of contaminants (methylene blue, nickel and fluoride from aqueous solution);
- Correlate the adsorption data with nonlinear Langmuir, Freundlich and Redlich Peterson and Sips isotherm models and determine the kinetics of contaminant adsorption on our adsorbent through Pseudo-First Order, Pseudo-Second Order and Elovich models.

Research Hypotheses

This work is based on the hypothesis that grafting of goethite nanopowder on β -CD nanosponge can result to a multifunctional hybrid nanosorbent. Grafting of CD nanosponge on nanopowder promises a multifunctional hybrid nanosorbent. Each component of this nanosponge should retain a distinct aspect in the functionality of the as-prepared nanosponges; the CD cavities entrap organic pollutants through inclusion complex formation, the carboxylate groups of the citric acid crosslinks trap cations through electrostatic interactions. The amphoteric nature of nanostructured goethite renders it a good adsorbent for anionic and cationic pollutants [68], and heavy metals [69]; goethite removes ionic species through electrostatic interactions, ligand exchange and hydrogen bonding. Hydroxyapatite, also an amphoteric adsorbent, that through anion exchange on P-sites, cation exchange on C-sites and substitution of OH⁻ with halogens.

Research question

How does functionalisation of citric acid crosslinked nanosponge with goethite and/or hydroxyapatite affect its structure, physico-chemical properties and capacity to remove different classes of pollutants from aqueous solutions?

Research Interest and Prospects

Improved sanitation and drinking water quality are central to poverty reduction and improved human health. Meeting the drinking water challenge is not a luxury but a prudent, practical and transformative act, able to boost public health, secure the sustainability of natural resources and trigger employment. According to a recent report from the Green Economy Initiative, every dollar invested in safe water and sanitation has a pay back of US\$3 to US\$34 [3]. Immediate, targeted and sustained investments should be designed to treat polluted water using appropriate technologies and techniques and provide a platform for the development of new and innovative technologies and management practices. If investments such as these are scaled up appropriately, they will generate social, economic and environmental dividends far exceeding original investments for years to come.

For household or communities without access to tap water, these sponges will be embedded in clay ceramic water filters for point source filtration. Given the major health, environmental and economic challenges posed by polluted water, investing in clean water will pay multiple dividends, and play an active role in the achievement of the governments' sustainable water goals. The impact of utilising this technology can be measured by the number of communities that will have access to clean water, the percentage reduction in the number deaths from water related diseases, the number of jobs created, and the overall improvement in the quality of life.

Scope and Organisation of Thesis

This study covers the synthesis of cyclodextrin nanosponges by ultrasound-assisted polycondensation polymerisation using citric acid as a cross linking agent and disodium phosphate as catalyst. The nanosponges were functionalised with goethite nanopowder and hydroxyapatite nanopowder. These nanosponges were characterised using a combination of BET, XRD, FTIR, PDF, SEM and TEM analytical techniques. Their potential to remove organic, inorganic and microbial contaminants from aqueous solution was tested using

methylene blue as a representative organic compound, nickel for heavy metal ions, fluoride as an inorganic ion and *E. coli* as a model microbial contaminant.

This thesis is organized into three chapters. The thesis begins with an introductory section which situates the research in its context; it further outlines the problem statement, the objectives of the thesis, the research hypothesis, the scope and a structural organization of the whole thesis. Chapter 1 presents a review of related literature on nanoscience, cyclodextrin nanosponges, goethite, hydroxyapatite, pollutants and their sources, adsorption and characterisation techniques employed in this work. Chapter 2 presents the research methodology, including the synthetic methods of the various adsorbents, the equipment used in characterization, batch and column adsorption studies and bacterial removal. Chapter 3 presents the results: this include the synthesis and characterization of the goethite nanopowder and the four different nanosponges. The experimental results on adsorption for the batch and column studies, where the adsorptive removal and interactions of organic pollutant (methylene blue) and inorganic pollutants (nickel, fluoride and nitrates) with the nanosponges are described. The removal of *E. Coli* was also described. The chapter ends with overall conclusions of the work and propositions for future work.

CHAPTER I
LITERATURE REVIEW

CHAPTER I - LITERATURE REVIEW

Nanotechnology, the engineering and art of manipulating matter at the nanoscale (1-100 nm), offers the potential to develop robust materials (nanomaterials). Nanoscience and nanotechnology have been at the interface of research in chemistry, biology, materials science, physics and engineering, leading to remarkable advancement in areas like electronics, mechanics, optics, drug delivery, paint, sensors, photonics, robotics, artificial intelligence, cosmetics, textiles and food packaging. At the annual American Physical Society meeting at Caltech on December 29, 1959, Richard Feynman's lecture on "There's Plenty of Room at the Bottom", set the stage for nanotechnology as a frontier science of the century by considering the possibility of manipulating and controlling matter at the nanoscale (1-100 nm) [70]. Inspired by Richard Feynman, the term 'nanotechnology' was first used by Norio Toniguchi in his talk on 'semiconductor processes in thin film deposition and ion beam milling exhibiting characteristic control on the nanoscale', at the International Conference on Production Engineering in 1974. He defined nanotechnology as the processing, separation, consolidation, and deformation of materials by one atom or one molecule, i.e., the ability to manipulate a single nanoscale object [71-73]. Nanoscience is the study of matter at the nanoscale and focuses on the size-dependent properties of solid-state materials.

Nanomaterials are defined as materials having at least one dimension (width, length or height) between 1-100 nm; they have very reduced sizes and larger surface-to-volume ratio than bulk materials. Due to surface effects and quantum effects, size reduction drastically enhances/alters the mechanical, optical, magnetic and electrical properties of nanomaterials. Gold for example has a characteristic brilliant yellow colour whereas nanosized gold is red in colour. Nanomaterials can be nanoscale in all three dimensions (nano-particles), in two dimensions (thin films and sheet like nanomaterial), in one dimension (nano wires or nanofibers) and all three dimensions in macroscale (combination of other nanomaterials, like bundle of nanofibers, bundle of nanosheets, etc). This classification is illustrated in **Figure 2**.

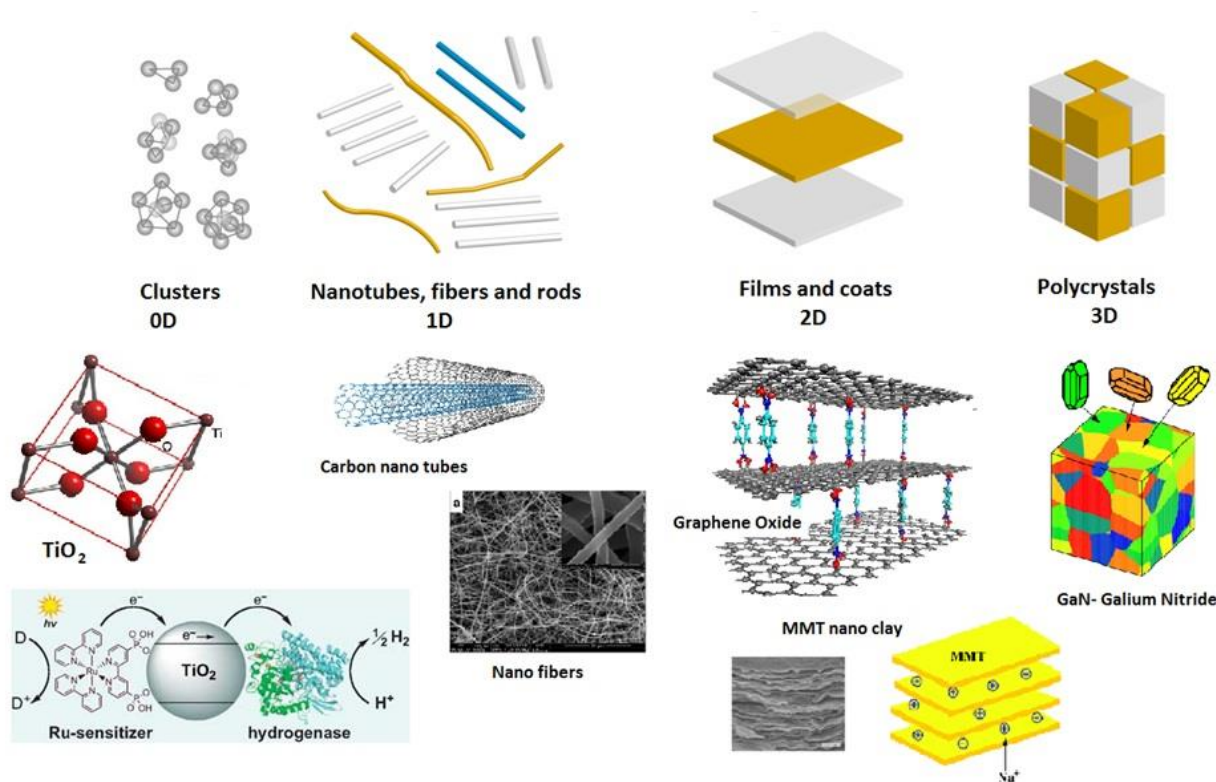


Figure 2: Classification of Nanomaterials [74]

Nanomaterials are manufactured either by the ‘top-down’ or ‘bottom-up’ (synthesis) approach (Figure 3). The top-down approach to nanomaterials involves the breakdown (chemical, mechanical, thermal or laser abrasion) of a bulk material into smaller and smaller particles. This technique is well applicable to metallic and ceramic nanomaterials. Often, a cryogenic liquid is used to facilitate the milling process and to increase the brittleness. Nanoparticles obtained invariably show relevant polydispersity and poor uniformity in particle shape. The “bottom-up” or self-assembly route is based on the assembling of atoms or molecules to get the desired nanomaterial. This method allows the production of nanoparticles with fewer defects, homogenous chemical composition, less contamination, and particles with a narrow size distribution and shape. Some examples are sol–gel process, gas-phase synthesis, flame-assisted ultrasonic spray pyrolysis, gas condensation processing, chemical vapor condensation, sputtered plasma processing, microwave plasma processing. [73, 75].

In this work, we utilise the bottom-up approach to synthesize CD polymers through Solid State Polycondensation (SSP). The polycondensation reaction is a step-growth polymerization process in which a polymeric macromolecule is formed by consecutive condensation reactions, liberating a small molecule (the condensate) in the process. Generally, this involves reactions

of multifunctional monomers that initially form dimers and trimers, followed by short oligomers and finally high molecular weight polycondensates. SSP is carried out below the melting point of a semi-crystalline polymer or crystalline monomer. During a SSP process the reactor is continuously flushed with an inert gas or kept under reduced pressure to remove the formed condensate and protect the material against oxidative degradation. [76]

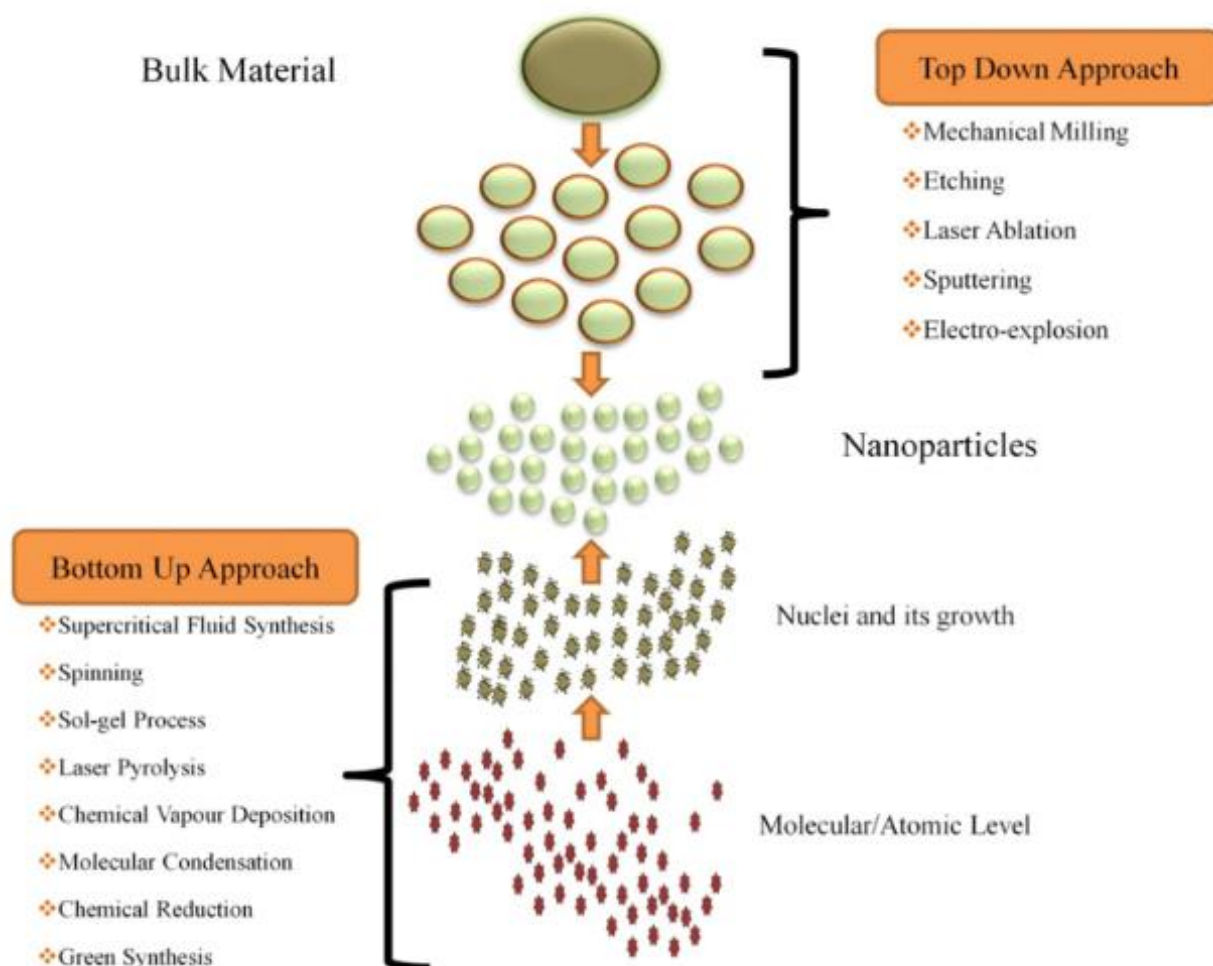


Figure 3: Synthesis of nanomaterials via ‘top-down’ or ‘bottom-up’ approach [77]

I.1 Cyclodextrins

Cyclodextrins are a class of natural cyclic oligosaccharides composed of D-glucopyranose units in the 4C_1 conformation, linked in an α -1,4 manner [78, 79]. They were isolated by Villiers in 1891, but their structure was elucidated only in 1942. They are obtained by enzymatic degradation of starch, using cyclodextrin glucosyltransferase, as a mixture of α -cyclodextrin, β -cyclodextrin, and γ -cyclodextrin, possessing six, seven, or eight glucosides, respectively.

Industrially, they are separated by selective precipitation in yields ranging from 40 to 60%. The annual worldwide production of CDs exceeds 10,000 tons, ~30 % of which is used in pharmaceuticals, ~20 % is used in the food industry, and the rest is used in a variety of consumer products [80].

α -, β -, and γ -cyclodextrins adopt a conformation in the shape of a truncated cone with C_n symmetry, n being the number of glucose units (**Figure 4**). The height of all cyclodextrins is the same (0.79 nm), dictated by the size of the glucose units. The diameter of their cavity increases with the number of glucose units contained in the structure: 0.49 nm for α -cyclodextrin, 0.62 nm for β -cyclodextrin, and 0.79 nm for γ -cyclodextrin. The cone possesses a hydrophobic internal cavity and an external hydrophilic surface. The hydroxyl groups of the glucose unit are oriented to the exterior of the cone: the primary hydroxyls are located on the narrow rim while the secondary hydroxyls are located on the wider rim. These hydroxyls render the outer surface of the cone hydrophilic. The inner cavity is lined by skeletal C-H groups and ethereal oxygen which makes it hydrophobic [35, 61]. As a consequence, cyclodextrins are moderately soluble in polar solvents; the hydrophobic cavities have a remarkable ability to form noncovalent host guest inclusion complexes with a variety of molecules (apolar guests) [81, 82].

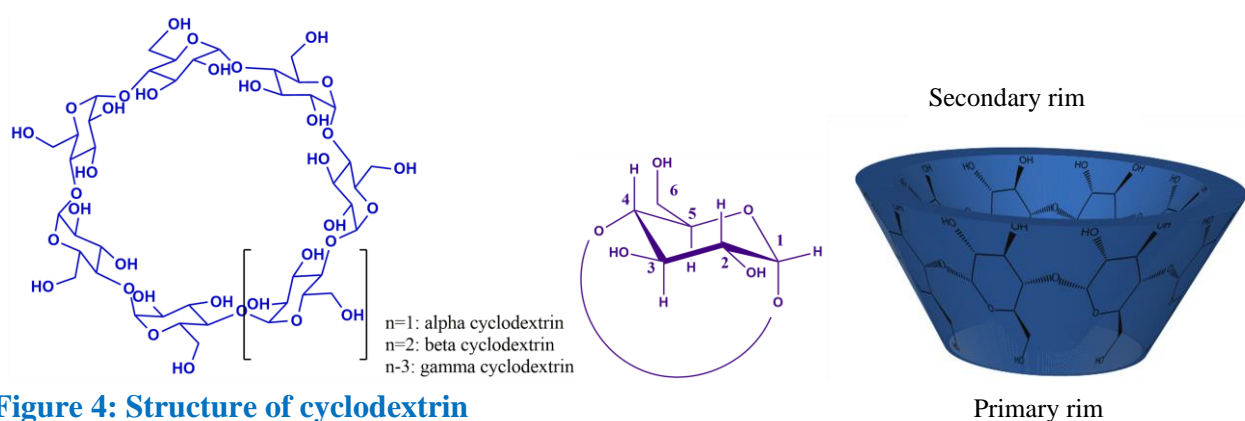


Figure 4: Structure of cyclodextrin

In native cyclodextrins, hydroxyls in position 2 point inward, and hydroxyls in position 3 point outward. The distance between the hydroxyls in positions 2 and 3 of two consecutive glucose units varies from 2.82 (α -cyclodextrin) to 2.98 Å (γ -cyclodextrin), see **Figure 5**. Hydrogen bonds can easily form through these distances and restrain molecular motion. Native cyclodextrins have a relatively rigid structure.

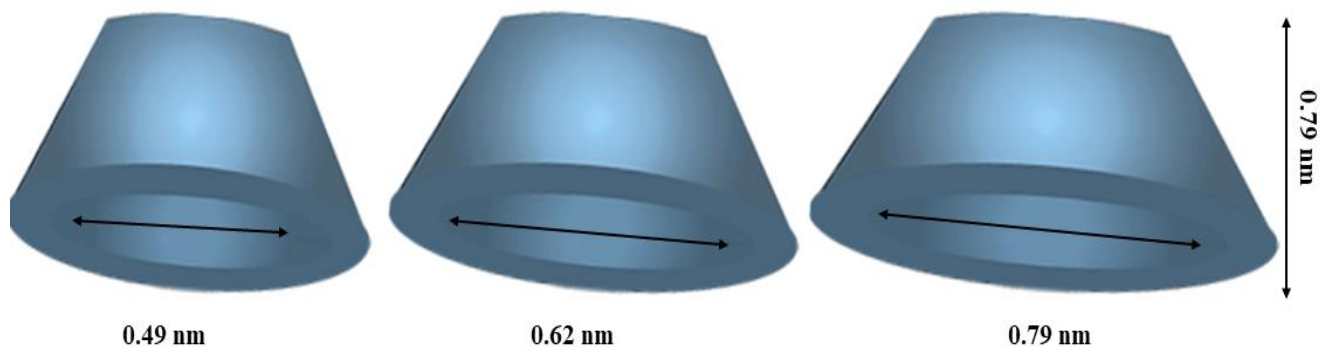


Figure 5: Respective dimensions of α -, β -, and γ -cyclodextrins

These intramolecular hydrogen bonds modulate the solubility of cyclodextrins in water (145 g for α -cyclodextrin, 18.5 g for β -cyclodextrin, and 232 g for γ -cyclodextrin). The structure of β -cyclodextrin is particularly favourable to the intramolecular hydrogen bonds, which explains its particularly poor solubility in water. α -Cyclodextrin is partially distorted, and can only form four hydrogen bonds.

1.1.1 Reactivity

As shown in [Figure 6](#), cyclodextrins possess three different hydroxyl groups (i.e., OH-2, OH-3, and OH-6) exhibiting different reactivities. The hydroxyls can be selectively modified with various functional moieties to impart tailored functionalities [83]. Primary hydroxyls, which compose the primary rim, are less hindered, more basic, and more nucleophilic than the others. They can react with electrophiles, even if they are sterically hindered, using only a weak base. The hydrogen bond between OH-2 and OH-3 of two following glucose units reinforces the acidity of the hydroxyls OH-2, also exalted by the proximity with the electron-withdrawing anomeric acetal function, and they hence become more acidic than the others ($pK_a=12.2$). They can be selectively deprotonated in anhydrous basic conditions. Hydroxyls OH-3 are less reactive, and can only be modified after protection of the other positions. Nevertheless, selectivity between the positions cannot be achieved if the conditions used are too basic or if the electrophile is too strong. This difference of reactivity has been used to direct the per-functionalization of each position, or the mono-functionalization if a default of reagent is employed. But this cannot direct the multi-functionalization toward a particular pattern. The 6-OH group of the primary rim are the most basic and more accessible to a reagent. The 2-OH group are the most basic. The 3-OH groups are the least accessible. Use of a base lead to

modification mainly of position 2 (deprotonated). Less reactive agents will react selectively at position 6.

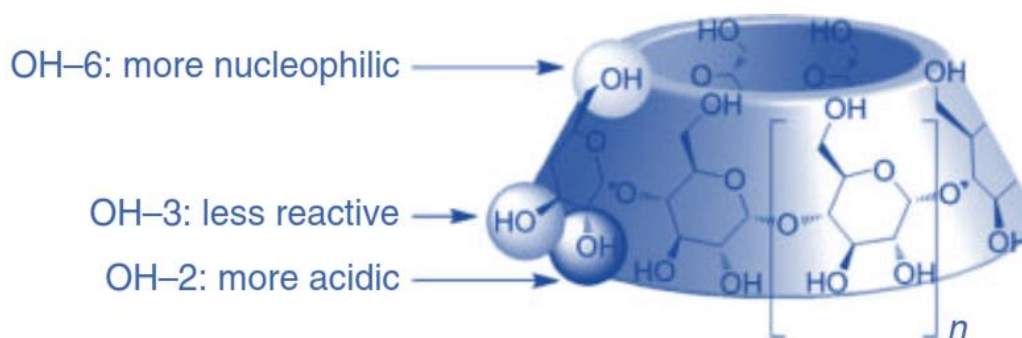


Figure 6: Reactivity of the different positions

The small-sized cavity of α -CD can only contain guest molecules of a smaller size, which limit their scope of application. γ -CD molecules are the most flexible of the three, having a relatively large open space, which causes them to include larger volume molecules. The producer Wacker Chemie has realized the industrial production of γ -CD, but its production costs more than α -CD and β -CD [80]. β -CD is more reactive, has a suitable cavity size and is produced in higher yields from starch than the other two cyclodextrins [84]. It is lowest-priced, having a great capability to improve stabilization and solubilization of lipophilic drugs and has a favourable toxicological profile. Their polymers have been extensively researched in the fields of drug delivery system, separating and absorption of material, environmental protection devices and functional catalysts [56]. Further discussions in this work will be limited to β -cyclodextrin.

1.1.2 Inclusion complex formation

The hydrophobic cavity of cyclodextrins imparts a unique ability to form inclusion complexes with organic molecules of suitable size and polarity [85]. Complexation is controlled by noncovalent host-guest interactions including hydrogen bonding, hydrophobicity, electrostatic forces, van der Waals forces, dispersive forces and dipole-dipole forces [81]. The inclusion process is driven by enthalpy and entropy increase as well as the release of water molecules from the cavity into the bulk phase, which in turn, solubilizes hydrophobic compounds in water. Inclusion complex formation depends on the size of the CD to the size of the guest molecule or some main functional groups within the guest moiety, thermodynamic interactions between the various components of the system (CD, guest, solvent), structure of added substituent to the CD derivative, location of substituent within the CD molecule and number of substituent

per CD molecule [86] . CD also form non-inclusion complexes with lipophilic substances through hydrogen bonds with the hydroxyl group present on the outer surface.

1.1.3 Polymerisation of Cyclodextrin (Formation of Nanosponges)

Native cyclodextrins can encapsulate hydrophobic substances in solution, however, due to their solubility in water, they cannot be directly used as adsorbents. Hence, CDs are either polymerised or functionalised to form porous insoluble materials [87]. These polymers can be prepared through crosslinking, grafting or immobilisation and they can be linear branched or hyperbranched depending on the ratio of monomers used [88]. Polymerisation is carried out by crosslinking the parent CD or CD derivative with a suitable polyfunctional cross linker. The exterior OH groups on CD enable it to act as a polyfunctional monomer, which can react through crosslinking with bi- or polyfunctional compounds (crosslinking agent) such as diisocyanates, epoxides, carboxylic acids to form polymers [34]. These polymers are usually insoluble, linked by a three-dimensional covalent network and referred to as nanosponges.

Nanosponges (NS) are defined as porous materials having all of the three external dimensions in the micro- or macro- range and the internal cavities, pores, or voids in the nanometre range. That is, while nanoparticles (for example) have particle sizes in nanometres, NS have pores in nanometre and their overall size can extend to micro- or macro- range [85]. Nanosponges can be swellable depending on the type and amount of crosslinker. Cyclodextrin nanosponges are hyper cross-linked sponge-like, polymeric structures, derived from β -cyclodextrins [89]. The term ‘nanosponge’ was first coined by Dequan Li and Min Ma because these polymers have nanometre-size pores (0.7-1.2 nm) and exhibit superior ability to absorb organic molecules in water [90]. They synthesised nanosponges by reacting cyclodextrin with diisocyanate compounds such as hexamethylene diisocyanate (HDI) and toluene 2,6-diisocyanate (TDI), with a 1:8 molar ratio in dried DMF solution and heated to 70 °C for 16-24 h to obtain a white nanoporous solid. These polymers have very low surface areas but very high loading capacities for organic molecules and could remove organic molecules like p-nitrophenol to ppb levels (10^{-7} - 10^{-9} M). Through circular dichroism, they found that these nanosponges remove organic pollutants through inclusion complex formation, thus the molecules are not just adsorbed on the surface of the sponge but transferred into the bulk of the polymer (absorption) [38, 91].

Nanosponges are amphiphilic in nature, thus they can simultaneously carry both a hydrophobic molecule in the hydrophobic cyclodextrin cavity and hydrophilic molecules in the interstitial

pores present between the crosslinker units and the external walls of single cyclodextrin moieties [92]. Another attractive feature is their tunability, i.e., the possibility of controlling their structure, nature and size of aperture by varying the proportion of crosslinker to polymer and hence degree of crosslinking.

Nanosponges are classified into four generations: the 1st generation comprises urethane, carbonate, ether and ester nanosponges synthesized by reacting CDs with a crosslinking agent. This generation is sub-divided into four groups based on the nature of the crosslinker [34]. Typically, suitable crosslinkers have two or more reactive groups capable of covalently attaching chemically to specific groups present in CDs to produce crosslinking. CD nanosponges can be synthesised through melt, solvent, ultrasound-assisted and microwave assisted polymerisation. Some examples are given in **Table I**.

Table I: Crosslinked CD polymers [73]

Class	Crosslinker	Properties	Pollutant
CD-based urethane (carbamate) NS	CD with hexamethylene diisocyanate and toluene-2,4-diisocyanate	Rigid structure, resistance to chemical degradation, negligible swelling in aqueous and organic media. Low SA	p-nitrophenol ppb, VOC, DOC, TOC 90, 84 %, Aromatic aa, Bilirubin 92.6 %
CD-based Carbonate NS	Carbonyls: 1,1'-carbonyldiimidazole triphosgene, diphenylcarbonate	Short cross-linking bridges, reduced swelling ability, good stability to acidic and slightly alkaline solutions. Low SA, excellent absorption capabilities for small molecules	Chlorinated persistent organic compounds, hexachlorobenzene 99.5%
CD-based Ester NS	Dianhydrides, di/polycarboxylic acids: pyromellitic dianhydride, EDTA, butanetetracarboxylic dianhydride, citric acid	Absorb remarkable amounts of water (up to 25 times their own weight) and form hydrogels. Hydrolyse in aqueous media more easily than carbonate and urethane NS	Polycyclic aromatic hydrocarbons, alkylphenols
Ether	EPI, bisphenol A, diglycidyl ether, ethylene glycoldiglycidyl ether	High chemical resistance, tuneable swelling capability EPI toxic	Bisphenol A

In the 2nd generation, there are polymers with specific properties, e.g., fluorescence or charged side chains. The 3rd generation contains stimuli-responsive NS modifying their behaviour

according to changes in the environment, such as pH, temperature gradients or oxidative/reducing conditions. The 4th generation includes molecularly imprinted NS with high selectivity towards specific guest molecules.

1.1.4 Cyclodextrin based composite materials

The excellent chemical reactivity of cyclodextrins make them compatible with facile synthetic methods for diverse innovative materials for environmental applications. Co-polymerisation, chemical modification, grafting or functionalisation of cyclodextrin nanosponges has been carried out to enhance their properties and usefulness. The interest in these materials stem from the fact that these modifications may provide a synergistic binding behaviour because such composite materials possess CD inclusion sites (intrinsic micropores) and non-inclusion micropore domains (interstitial micropores) [48]. The modification of CDs on functionalized supports has also attracted attention because of its potential to achieve highly efficient heavy metal remediation. For example, Tamas et al [93] utilized cyclodextrin polymers to stabilize nanosized titanium dioxide (nanoTiO_2) dispersion and found that carboxymethyl β -cyclodextrin polymer enhanced the colloidal stability of the nanoTiO_2 . The polymer also showed synergistic effects in catalysing the photodecomposition process of methylene blue but protected ibuprofen from photocatalytic degradation through inclusion complex formation. Badruddoza et al. [94] developed a novel nano-sorbent with carboxymethyl- β -CD($\text{CM}\beta$ -CD)-modified Fe_3O_4 nanoparticles for the removal of copper ions from aqueous solution. A facile synthesis method was followed in which $\text{CM}\beta$ -CD was grafted onto the magnetite surface via carbodiimide chemistry, and the resulting sorbent showed an enhanced capacity to adsorb metal ions due to the presence of the multiple hydroxyl and carboxyl groups in $\text{CM}\beta$ -CD. **Table II** presents applications of some selected CD composite polymers in pollutant removal.

1.1.5 Applications

Cyclodextrins and their derivatives have attracted substantial attention and have enabled wide applications in the practical fields of science and technology, including pharmaceuticals, biomedicine, the food industry, analytical chemistry, agriculture and environmental protection. They are used as host molecules for molecular recognition, as solubilizing agents for lipophilic drugs, excipients in formulation development, as delivery systems and complexing agents in the food and drug industries, or for masking of undesired odour and taste [95]. Research on cyclodextrins is also very active in fields such as the formulation of detergents, glues and

adhesives, the sector of plastics (packaging) and the industry of fibres and paper. **Figure 7** shows some of these areas of application.

Pharmaceutical applications

Many drugs are hydrophobic and this presents a challenge for in vivo drug delivery. Cyclodextrins improve the permeability, dissolution of poorly soluble drugs by forming inclusion complexes and enhances drug stability through entrapment. CDs have been used in nanosystems such as polymeric nanoparticles, nanosponges, lipid-based nanoparticles, metallic nanoparticles, quantum dots, nanofibers and dendrimers to improve the solubility drugs and consequently increase stability, degradation and encapsulation efficiency [96]. They have been incorporated in a wide range of commercially available drugs. For example, cyclodextrin has been used to induce rapid absorption, rapid onset of analgesia and reduced gastrointestinal irritation in piroxicam tablets (Brexin tablets) over tablets containing un-modified piroxicam [97].

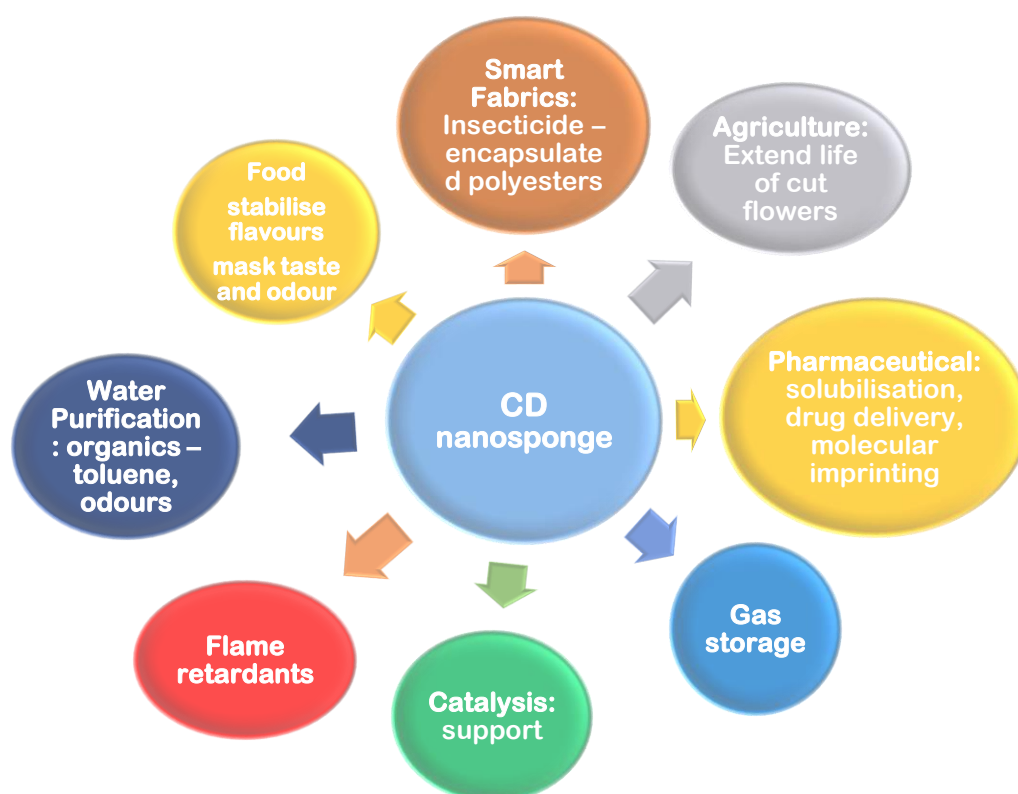


Figure 7: Some areas of applications of cyclodextrin nanosponges

Table II: Cyclodextrin nanosponges/composite polymers

N°	Adsorbent	Method of synthesis	Crosslinker	Pollutant class	Example	Adsorption conditions	Efficiency % Removal	Qty Ads (mg/g)	Ref
1	N-CNTs- β -CD Fe/N-CNTs- β -CD	Microwave assisted synthesis	Toluene 2,4-diisocyanate	Organic	Aspirin and Paracetamol	50 mL, 100 ppm, 0.05 g, 30 min		71.9 and 41.0 respt. for N-CNTs- β -CD 101.0 and 75.2 respt. for Fe/N-CNTs- β -CD	[46]
2	Poly (butylene succinate-co-terephthalate) functionalised CD polymer (PBST/CDP)	In situ polymerization	Critic acid	Organic	Methylene blue	40 mL, 10 ppm, 50 mg	98.8 %	90.9	[98]
3	CD Cellulose nanofiber composites	Physical mixing and chemical grafting	Critic acid	Organic	Toluene	10 mL, 100 ppm toluene, 30 mg,	y-CDs/RCNFs 82 % after 180 min		[99]
4	β -CD functionalized biochar		EPI	Inorganic	Lead	50 ml, 1 g, 3000 mg		130.60	[87]
5	Cyclodextrin-Immobilized Iron Oxide Magnetic Nanoparticle	Immobilisation	[3-(2,3-epoxypropoxy)propyl]trimethoxysilane	Organic	Direct Blue 15, Evans Blue, and Chicago Sky Blue	25 mg, 20 ppm	98, 99, and 99 % at pH 3.0, respectively		[53]
6	B-cyclodextrin grafted poly (isophthalamide)/magnetic nanoparticles (CDPA-MNPs) nanocomposite	Phosphorylation polyamidation	5-hydroxyisophthalic acid.	Bacteria	<i>Bacillus cereus</i> <i>E. coli</i>	3 g, 10 ⁵ CFU/L	97% 98%		[61]

Water treatment

The unique ability of CDs to form inclusion complexes forms the primary mechanism for treating effluent containing highly toxic substances. The applications of native and modified cyclodextrins for water pollution remediation have been iterated in a review article by Sikder and co-workers [88]. They showed that modified CDs can attain elevated sorption in wastewater treatment toward a wide range of pollutants including aromatic compounds, metals, and complex mixtures of pollutants.

CDs have been used in food technology to mask odours and reduce unwanted flavours by complexation, inhibit light and/or heat induced transformations of foods, extend product shelf life through molecular encapsulation with different substances such as flavours, colourants and unsaturated fats [100].

1.2 Goethite

Goethite (α -FeOOH) is the most common iron oxyhydroxide in soils [101, 102], sediments and ore deposits, as well as a common weathering product in rocks of all types [103]. It is also common in various aquatic environments with both acidic and alkaline pH [104]. Given its affinity to adsorb various contaminants: anions, organic acids, and cations including heavy metal ions [105], goethite represents an important component of environmental mediation process [106]. Synthetic goethites are often used as model systems in laboratory studies of adsorption. It can be synthesized in the form of needle-like (acicular) particles of sub-micrometre size, and thus of high specific surface area [107].

1.2.1. Structure and Properties

Goethite is isostructural with diaspore, AlO(OH), and groutite, MnO(OH) [103] and has an orthorhombic unit cell. The structure consists of an hcp array of anions (O^{2-} and OH^-) stacked along the [010] direction with Fe^{3+} ions occupying half the interstices. Each Fe ion is surrounded by three O^{2-} and three OH^- , resulting in facial $FeO_3(OH)_3$ octahedral. The structure of goethite showing the repeating unit, double chain $FeO_3(OH)_3$ octahedra and crystal structure is given in **Figure 8**. The arrangement of anions governs the crystal structure and the ease of topological inter-conversion between different iron oxides. The surface hydroxyl groups present in goethite arise from the adsorption of water or structural OH.

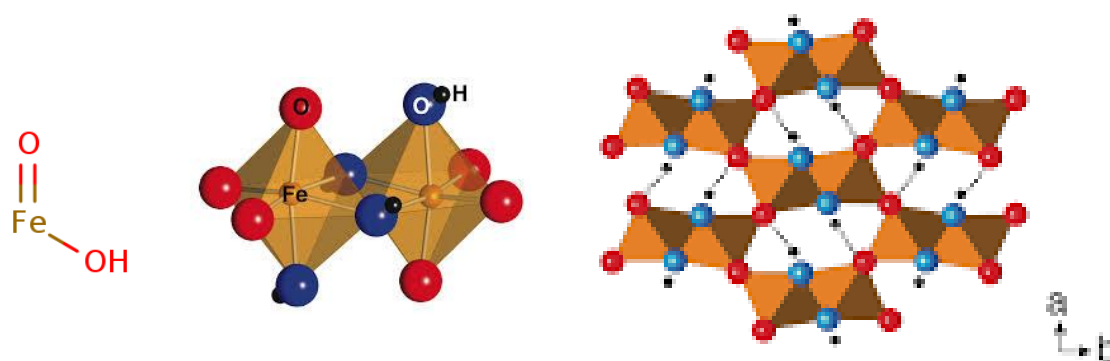


Figure 8: Repeating unit, double chain $\text{FeO}_3(\text{OH})_3$ octahedra and crystal structure of goethite

They possess double pairs of electrons together with H-atom, which enable them to react with acids and bases, hence the amphoteric nature of goethite. Reactivity of model surfaces is critically controlled by the precise nature of the surface functional groups and the structure or distribution of water and electrolyte at the solid-solution interface.

Hydrated iron oxide nanoparticles are nontoxic, inexpensive, readily available and chemically stable over a wide pH range [108]. They can be synthesized by all known wet chemical methods, e.g. chemical precipitation, micro-emulsion precipitation, sol gel [109]. Goethite ($\alpha\text{-FeOOH}$) is the most common iron oxyhydroxide in soils [101], sediments and ore deposits, as well as a common weathering product in rocks of all types. Given its affinity to adsorb various contaminants: anions, organic acids, and cations including heavy metal ions, goethite represents an important component of environmental remediation process [106]. This is highlighted in a review on the role of goethite in the environment by Liu et al., [110] which illustrates the extensive research on goethites, for their capacity to remove anions (over a 100 papers), organic/organic acids (over 50 papers) and cations (over 80 papers) from aqueous solutions.

A number of studies have been carried on the use of nanostructured goethite for heavy metal removal. Hala and Hiba compared the removal of five metal cations (Cr^{3+} , Co^{2+} , Cu^{2+} , Ni^{2+} , Zn^{2+} ions) on nano/micro structured goethite and hematite [111]. Yen-Hua and Fu-An studied the removal of Cu^{2+} ions using goethite and hematite nano-photocatalysts [112], and Vinh et al., investigated the removal of Cr^{3+} by goethite nanoparticles [113]. One study by Mohapatra et al., compared Pb^{2+} , Cd^{2+} , Cu^{2+} , Co^{2+} adsorption from single and binary aqueous solutions on additive assisted nano-structured goethite [114].

1.3 Hydroxyapatite

Apatite is the name given to a group of crystals of the general chemical formula $M_{10}(XO_4)_6Z_2$, where $M = Ca^{2+}, Sr^{2+}, Ba^{2+}, Na^+, Pb^{2+}, La^{3+}$ and many rare earth elements; $XO_4 = PO_4^{3-}, VO_4^3, SiO_4^{2-}, AsO_4^{3-}, CO_3^{2-}$; $Z = OH^-, Cl^-, F^-, CO_3^{2-}$ [115]. Hydroxyapatite or calcium hydroxyapatite (HA) belongs to the apatite family, where M is calcium (Ca^{2+}), X is phosphorus (P^{5+}) and Z is the hydroxy radical (OH^-). HA crystallizes in a hexagonal system, space group $P6_3/m$. The structure (Figure 9) is formed through a tetrahedral arrangement of phosphate (skeleton of the unit cell), where two of the oxygens align with the c axis and the other two are in a horizontal plane. The positively charged pairs of calcium ions are regarded as the C-sites (Ca^{2+}) and clusters of six negatively charged oxygen atoms associated with triplets of phosphates are regarded as the P-site (PO_4^{6-}) [116]. Through coordination, anion exchange on P-sites (for anions such as CrO_4^{3-}, SO_4^{2-}), cation exchange on C-sites (for metal ions such as $Pb^{2+}, Cu^{2+}, Ni^{2+}$) and substitution of OH^- with halogens (F^-, C^-) HA acts as an amphoteric adsorbent [117].

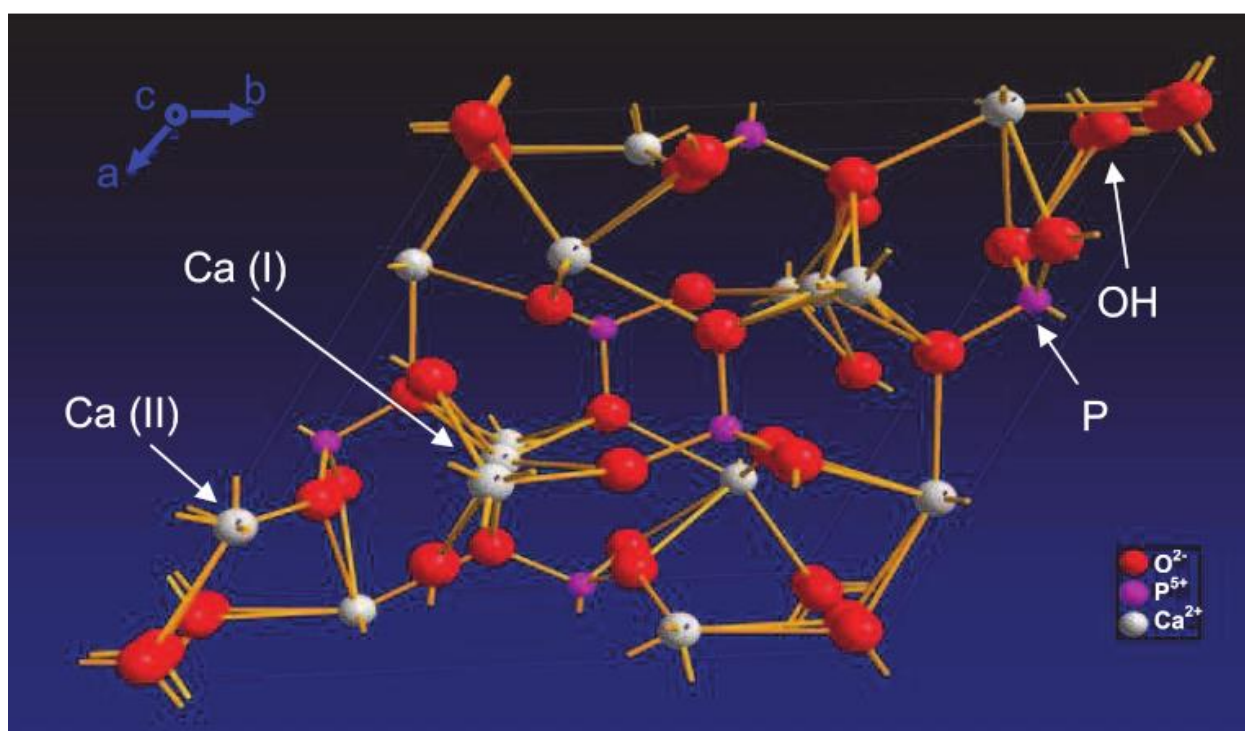


Figure 9: Crystal Structure of hydroxyapatite [118]

HA is a natural mineral component in bones and teeth; it has a unique crystal and porous structure, is nontoxic, biocompatible, biodegradable and has low water solubility [119-121]. HA has been extensively applied either as scaffolds or fillers in bone tissue engineering [122].

Because of its suitable microstructure, HA has a high affinity towards a wide variety of adsorbates. To improve its adsorption performance, HA with variable morphologies and efficiencies for pollutant removal have been synthesised from different natural sources as well as in combination with other materials (fibres, polymeric, metal/non-metals). For example, Mohamed *et al.*, prepared a highly porous and crystalline superparamagnetic hydroxyapatite composite (CaHAP/NF), which could effectively remove europium and terbium rare elements [123]. Oulguidoum *et al.*, developed sulfonate-functionalized hydroxyapatite nanoparticles for the removal of cadmium; they proposed a complexation and dissolution precipitation adsorption mechanism involving interactions between $-SO_3$ and Cd on the hydroxyapatite surface [124].

Composites involving hydroxyapatite and cyclodextrin have also been synthesized. In these studies, the cyclodextrin is used either as template or as a medium for inclusion complex formation. Wen-Jun *et al.* grafted cyclodextrin/citrate on the surface of HA to improve its cell adhesion and osteoinductivity for bone tissue applications [125]. Jegatheeswaran and co-workers synthesised a silver doped fluor-hydroxyapatite/ β -cyclodextrin composite, which exhibited very good antibacterial activities against *Escherichia coli*, *Salmonella typhi*, *Klebsiella pneumonia* and *Serratia liquefaciens* pathogens [126].

1.4 Pollutants, Sources and effects

Pollutants in water can be broadly classified into pathogenic microorganisms (bacteria, viruses, protozoa), toxic organic (dyes, herbicides, pharmaceuticals), inorganic (heavy metals and polyatomic compounds) and radiological compounds [18]. Contaminated water often contain a mixture of these classes of pollutants introduced either through natural or man-made sources (industrial by-products, improper disposal of household chemicals, human and animal wastes) [20].

1.4.1 Inorganic pollutants

Heavy metals have been defined as mutagenic and carcinogenic agents, and may be toxic to aquatic life [127]. Hardness in water can be either carbonated or non-carbonated. Inorganic ions such as fluoride, arsenic, lead, copper, chromium, mercury, antimony, cyanide can get into drinking water from natural sources, industrial processes, as well as from plumbing systems. **Table III** give some selected heavy metals and their human health effects.

Nickel

Nickel is a heavy metal. Heavy metals are components of the earth's crust and are ubiquitous in the environment, they cannot be degraded or destroyed i.e. they are non-bio-degradable [128]. These metals tend to bio-accumulate and are usually carcinogenic at low concentrations [129]. Heavy metals are among the most widespread pollutants and have received extensive attention due to their toxicity and persistence in the environment [130]. Some of the ways in which man introduces heavy metals into the environment are through mining operations, industrial effluents, urban and domestic waste. Nickel is used in various metal alloys, including stainless steels, and in stainless steel welding, electroplating, batteries, pigments, catalysts, and ceramics. Major properties of nickel alloys include strength, corrosion resistance, and good thermal and electrical conductivity.

Table III: Heavy metals and their human health effects [131]

Heavy metal	Human health effect	Permissible limit (drinking water)
Arsenic	Gastrointestinal symptoms, death, melanosis, hepatomegaly	
Lead	Lead poisoning, affects the nervous, cardiovascular, hematopoietic, kidney, digestive and endocrine systems	1.5 x 10 ⁻³ mg/L
Cadmium	Renal failure, birth defects, anaemia	0.005 mg/L
Copper	Liver and kidney disease, cancer, stomach irritation	1.30 mg/L
Nickel	Nickel poisoning, dermatitis, respiratory disorders and respiratory tract cancer	
Manganese	Neurotoxic, sleep dysfunction	
Chromium	Dermatitis, eczema, bronchitis and rhinitis, causing allergic reactions and carcinogenic effects.	
Zinc	Zinc poisoning, vomiting, diarrhoea and other gastrointestinal symptoms, chronic zinc poisoning may have anaemia	
Mercury	Kidney disease, death, muscle movement impairment, gum inflation	

Nickel is an essential trace element and small amounts are needed by the human body to produce red blood cells [132]. However, nickel is a toxic environmental pollutant. Ni(II) ions exist frequently encountered in industrial wastewaters, e.g. from mine drainage, plating plants, paint and ink formulation. Occupational exposure to nickel occurs by inhalation of nickel-containing aerosols, dusts, or fumes, as well as dermal contact in workers engaged in nickel

production (mining, milling, refinery, etc.) and nickel-using operations (melting, electroplating, welding, nickel–cadmium batteries, etc.) [133]. The general population is exposed to low levels of nickel in air pollution, cigarette smoke, water, and food. Epidemiological data supports the carcinogenic potential of certain nickel compounds (Ni₃S and NiO), and nickel toxicity has been reported to cause pulmonary fibrosis and inhibit many enzymatic functions [134]. **Table IV** summarizes some of the health effects of nickel.

Table IV: Human Health Effects of Nickel [135]

Toxicity	Health effect
Genotoxicity	DNA damage caused by reactive oxygen species produced from Ni ²⁺ ions, inhibition of certain steps involved in DNA repair processes
Carcinogenicity	Nickel compounds are collectively considered as human carcinogens and nickel metal is considered as possibly carcinogenic to humans
Lung injury and disease	Acute lung injury, chronic bronchitis, non-small cell lung cancer, nasal cancer
Contact dermatitis	Resulting from an inflammatory reaction mediated by type IV delayed hypersensitivity

Fluoride

Fluorine of the halogen group is the most electronegative element. Fluorine exists in the environment as negatively charged fluoride ion, F⁻. Fluoride has an ionic radius similar to the hydroxide ion, OH⁻, and readily substitutes the hydroxy ion. Fluoride in water may come from geological (weathering of fluoride-bearing minerals such as fluorite, fluorspar, cryolite, fluorapatite) or anthropogenic (medicines, tooth pastes, preservatives, super phosphate fertilizer, insecticides, disinfectants) sources. Low fluoride concentration in drinking water is considered beneficial for the reduction of dental caries, by reducing the ability of plaque bacteria to produce acid that damages teeth [136]. Higher concentrations have been reported to cause dental (1.5 mg/F/L) and skeletal (3 to 6 mg/F/L) fluorosis in children and adolescents [137]. Dental fluorosis results in permanent discoloration of the teeth, erosion of enamel and pitting; skeletal fluorosis results to an increased risk of bone fractures, increased bone density, calcification of the ligaments and tendons, and bone deformity (crippling skeletal fluorosis). Fluoride is also associated with Alzheimer’s disease and other forms of dementia.

1.4.2 Organic pollutants

Organic contaminants can be broadly classified into dyes, drugs, pesticides, aromatic compounds and oily substances. Synthetic dyes are widely used as colourants in the textile,

paint, cosmetic and pigment manufacturing industries. Due to the complexity of their chemical structure, synthetic dyes are classified based on their application and ionic charge into anionic dyes (direct, acid and reactive dyes), cationic dyes (alkaline dyes) and non-ionic dyes. This classification is summarised in [Table V](#).

Table V: Classification dyes [138].

Class	Type of dye	Chemical groups	Property	Example
Anionic	Acid	Azo, anthraquinone, xanthene, nitro and triphenylmethane	Water soluble and anionic	Acid blue 114, acid red 183, indigo carmine, acid fuschin, acid yellow 17 and acid black 2
	Direct	Azo, oxazine, phthalocyanine and stilbene	Water soluble and anionic	Congo red, direct red 23
	Reactive	Azo, oxazine, formazan, anthraquinone and phthalocyanine.	Covalent binding of reactive sites with functional groups of substrates under the effect of heat and pH	Reactive black 5, reactive green 19, reactive blue 4 and reactive red 120
Cationic	Basic	Azo, hemicyanine, cyanine, azine diphenylmethane, xanthene, acridine and oxazine	Water soluble, release of coloured cations in solution and slow biological activity for certain dyes	Crystal violet, methylene blue, basic fuschin, malachite green, rhodamine 6G and Orange 2
Non-ionic	Disperse	Azo, benzodifuranone, anthraquinone, nitro and styryl	Non-ionic, insoluble in water	Disperse red 1, disperse orange 37 and disperse yellow 1
	Vat	Indigoids and anthraquinone	Insoluble in water, soluble in sodium hydrogen sulphite, then spent on reoxidised and fibre	Vat black 8, vat green 9, vat blue 4 and vat yellow 20

Methylene blue

Methylene blue (MB) is a monovalent cationic thiazine dye with a molecular formula of $C_{16}H_{18}N_3ClS$ (Mo. Wt. 319.85 g/mol). It is widely used as a chemical indicator, dye and biological stain. The chemical structure of MB is shown in [Figure 10](#). The width of a methylene blue molecule is approximately 9.5 Å and the length could be 13.82 Å or 14.47 Å depending on the position of the chloride ion, i.e. on whether it connects to the intermediate sulphur located in the centre of the molecule or one of the two nitrogen atoms located at sides [139].



Figure 10: Chemical structure of methylene blue dye

1.4.3 Microbial contaminants

Microbial pollutants found in water includes bacteria, viruses, parasites, protozoa and algae. These are frequently introduced into water supplies through faecal contamination and soil pollution. Infectious diseases caused by pathogenic bacteria, viruses and parasites (e.g., protozoa and helminths) are the most common and widespread health risk associated with drinking-water. The public health burden is determined by the severity and incidence of the illnesses associated with pathogens, their infectivity and the population exposed.

Escherichia coli

Escherichia coli (*E. coli*) is present in large numbers in the normal intestinal flora of humans and animals, where it generally causes no harm. However, in other parts of the body, *E. coli* can cause serious disease, such as urinary tract infections, bacteraemia and meningitis. A large amount of *E. coli* from animal manures and municipal disposal can enter into natural water after a heavy rainfall. *E. coli* is commonly used as an indicator of faecal contamination and to verify water quality [140]. The WHO guidelines for verification of microbial quality of water stipulates that *E. coli* must not be detected in any 100 ml sample for all water directly intended for drinking [131].

1.4.4 Water treatment technologies

Water treatment technologies include both point-of-use (POU) and point-of-entry (POE) applications. Point-of-entry applications are primarily deployed to disinfect water that does not come from a municipal supply, whereas point-of-use applications are typically used for water that may have already been chemically treated. Disinfection technologies that find use in point-of-entry applications include chemical-based disinfection agents (chlorine, chlorine dioxide,

potassium permanganate, hydrogen peroxide, ozone) and Ultraviolet (UV) radiation. Ultraviolet radiation is also used in POU applications along with filtration. All conventional methods that have been applied for heavy metal removal have their capabilities and limitations. **Table VI** summarizes the advantages and disadvantages of different techniques for heavy metals removal.

Table VI: Advantages and disadvantages of current techniques for heavy metals removal, adapted from Ihsanullah et al., 2016 [141]

Method	Advantages	Disadvantages
Ion exchange	<ul style="list-style-type: none"> • High treatment capacity • High removal efficiency • Fast kinetics 	<ul style="list-style-type: none"> • High cost due to synthetic resin • Regeneration of the resins cause serious secondary pollution
Adsorption	<ul style="list-style-type: none"> • Easy operating conditions • High metal binding capacities • Having wide pH range • Low-cost 	<ul style="list-style-type: none"> • Production of waste products • Low selectivity
Chemical precipitation	<ul style="list-style-type: none"> • simple operation • Low capital cost 	<ul style="list-style-type: none"> • Sludge generation • Extra operational cost for sludge disposal • Ineffective for treatment of water with low concentration of heavy metals
Membrane filtration	<ul style="list-style-type: none"> • High separation selectivity • Small space requirement • Low pressure requirement 	<ul style="list-style-type: none"> • High operational cost due to membrane fouling • Process complexity • Low permeate flux
Electrodialysis	<ul style="list-style-type: none"> • High separation selectivity 	<ul style="list-style-type: none"> • High operational cost due to energy Consumption and membrane fouling
Photocatalysis	<ul style="list-style-type: none"> • Removal of metals and organic pollutant simultaneously • Less harmful by-products 	<ul style="list-style-type: none"> • Limited applications • Long duration time
Coagulation and flocculation	<ul style="list-style-type: none"> • Remove the turbidity in addition to heavy metal removal • Produced sludge with good sludge settling and dewatering characteristics 	<ul style="list-style-type: none"> • Increased sludge volume generation • Coagulation flocculation can't treat the heavy metal wastewater and must be followed by other treatment techniques
Flotation	<ul style="list-style-type: none"> • High metal selectivity • High removal efficiency • High overflow rates • Low detention periods • Low operating cost • Production of more concentrated sludge 	<ul style="list-style-type: none"> • High initial capital cost • High maintenance and operation costs

1.5 Adsorption

The term “adsorption” was coined by Kayser in 1881 to describe the increase in concentration of gas molecules in neighbouring solid surfaces, a phenomenon previously noted by Fontana and Scheele in 1777 [142]. Generally, the unpolluted surface of any solid is characterised by

the fact that not all bonds of the atoms which compose the surface are saturated, leading to the existence of an adsorption field over this surface. This adsorption field causes the accumulation of molecules near the solid surface. Adsorption is thus defined as a process in which a species from a liquid or a gas phase is extracted from this phase and concentrated on the surface of a solid phase. The molecule that is transferred is called the adsorbate, while the solid phase it adheres to is called the adsorbent. By changing the properties of the liquid phase (e.g., concentration, temperature, pH) adsorbed species can be released from the surface and transferred back into the liquid phase. This reverse process is referred to as desorption. The different components in a solid-liquid adsorption system are illustrated in **Figure 11**.

The adsorption process has copious advantages when compared to other unit operations, these include simplicity in design and operation; can handle micro level pollutants; vigorous batch and continuous processes; efficient toxicity removal; low energetic investment cost; can be selective; environmentally benign; and probability of adsorbent reuse and regeneration [143].

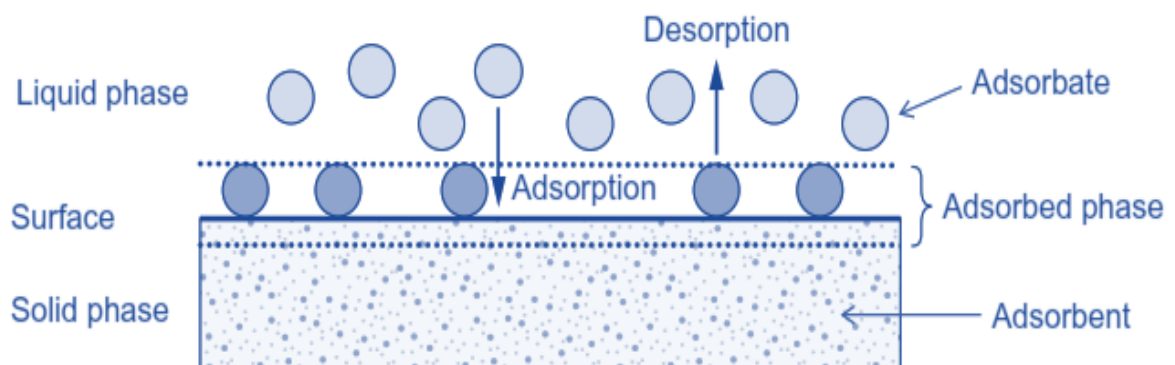


Figure 11: Different components in a solid-liquid adsorption system

Activated carbon (AC), the adsorbent most commonly used in adsorption processes for water treatment applications usually incur a drawback due to high cost. In some cases, a secondary problem can occur with the disposal of the generated sludge. To develop an adequate adsorption system, the adsorbent choice is the first and fundamental aspect.

The term adsorption is used also to describe two kinds of forces of interaction: physisorption and chemisorption. **Table VII** lists the main differences between chemisorption and physisorption. Adsorption occurs in four distinct steps; transport of the adsorbate to the film surrounding the adsorbent particle surface, external diffusion, intra-particle diffusion and physical or chemical surface reactions [144].

Table VII: Differences between Physisorption and Chemisorption, Atkins 2006 [145].

Chemisorption	Physisorption
The molecules (or atoms) stick to the surface by a covalent bond, and tend to find sites that maximize their coordination number with the substrate	There is a van der Waals interaction between the adsorbate and the substrate
Monolayer adsorption	Multilayer adsorption
Desorption is not possible	Desorption is possible
Exothermic or endothermic, chemical bond forms (energy involved can reach several hundreds of kJ/mole)	Always exothermic (energy involved is $< \sim 40$ kJ/mole)

1.5.1 Factors affecting adsorption

Choice of adsorbent

The choice of adsorbent is fundamental. A good adsorbent should have the following characteristics: low cost; availability; efficiency; high surface area and pore volume; mechanical, chemical, and thermal stability; ease of desorption and reuse; and able to provide a fast kinetics and present a high adsorption capacity.

The adsorption of contaminants on a solid surface is mainly determined by the physical structure and chemical properties of the adsorbent (specific surface area, pore structure, and surface functional groups) [146]. Adsorbents are normally porous. The pore width is defined as the diameter, in the case of cylindrical pores, and as the distance between opposite walls, in the case of slit-shape pores. The pore widths of porous adsorbents are classified by the International Union of Pure and Applied Chemistry (IUPAC) as micropores (pore diameters between 0.3 and 2 nm), mesopores (pore diameters between 2 and 50 nm), and macropores (pore diameters greater than 50 nm). The parameters which characterize a porous adsorbent are: the specific surface area measured in $[m^2/g]$; the micropore volume measured in $[cm^3/g]$; the pore volume, which is the sum of the micropore and mesopore volumes of the adsorbent, measured in $[cm^3/g]$; and the pore size distribution (PSD). The surface area is the outer surface, the area out of the micropores. If the adsorbent does not present micropores, the surface area and the outer surface area coincide. The surface area of the adsorbent is very important and usually serves as a limiting factor for adsorption in an ideal situation where all other conditions are optimal for contaminant removal. An increase in surface area will result in an increase in the adsorption of the target contaminant.

Operating conditions

The time of contact between the adsorbate and adsorbent determines the extent of adsorption and hence the adsorption kinetics of an adsorbate at a given initial concentration of the adsorbate. The degree of ionization of a species is affected by pH; this in turn affects adsorption. The pH factor plays an important role on the adsorption capacity, affecting both the degree of ionization of the adsorbate as well as the surface binding sites of the adsorbent [147]. Other factors, which affect the extent of adsorption, include particle size of adsorbent, adsorbate solubility, temperature and degree of ionization of the adsorbate molecule. The pH of the solution affects both the surface charge of the adsorbent and the protonation/deprotonation of pollutants.

To control the design, operation and optimization of water purification technologies through adsorption, adsorption processes are modelled through several nonlinear multivariate mathematical models which can be either theoretical, semiempirical or empirical. These models are used to describe both the adsorption equilibrium and kinetics.

1.5.2 Adsorption Isotherms

The relationship between the amount adsorbed by the adsorbent and the activity (pressure or concentration) of the adsorbate in the fluid phase, in equilibrium and at constant temperature is defined as the adsorption isotherm. The adsorption isotherm is employed to establish the maximum capacity of adsorption of adsorbate [148]. Several models of adsorption isotherms have been proposed to study the adsorption behaviour.

1.5.2.1 Freundlich Isotherm

The Freundlich isotherm is a two-parameter isotherm that relates the amount of material adsorbed to the concentration of the material in solution. It is empirical, describes heterogeneity of the surface binding sites, the exponential distribution of active sites and their energies [149]. The model assumes that adsorption could occur via multiple layers instead of a single layer. It is often expressed as:

$$Q_e = K_f C_e^{1/n} \quad 1$$

Where: Q_e is the quantity of solute adsorbed at equilibrium (adsorption density: mg of adsorbate per g of adsorbent). C_e is the concentration of the adsorbate at equilibrium (mg/L) n is the heterogeneity factor representing the deviation from linearity of adsorption, K_f indicates the adsorption capacity of adsorbent related to the binding energy. The linear form after taking the logarithm of both sides is given as:

$$\ln Q_e = \ln K_f + \frac{1}{n} \ln C_e \quad 2$$

A plot of $\ln Q_e$ against $\ln C_e$ that yields a straight line indicates the confirmation of the Freundlich isotherm for adsorption. The constants can be determined from the slope and intercept. A good fit of Freundlich isotherm to an adsorption system implies there is adsorption on heterogeneous surfaces (i.e. heterogeneity in the surface binding sites). $1/n$ is a constant associated with the surface heterogeneity of the adsorbent; the value of $1/n$ (ranges between 0 and 1) is known as the heterogeneity factor [150]. The closer the value of $1/n$ is to 1, the more heterogeneous the surface of the adsorbent.

1.5.2.2 Langmuir Isotherm

The Langmuir adsorption isotherm is a two-parameter isotherm that calculates the amount of molecules adsorbed onto a solid surface and it is based on the assumptions that adsorption cannot proceed beyond monolayer coverage on a homogeneous surface (all surface sites are equivalent and can accommodate at most one adsorbed atom), and the ability of a molecule to adsorb at a given site is independent of the occupation of neighbouring sites. It is perhaps the best known of all isotherms describing chemisorption and is often expressed as:

$$Q_e = \frac{Q_m K C_e}{1 + K C_e} \quad 3$$

Where, Q_e is the adsorption density at equilibrium (mg of adsorbate per g of adsorbent), C_e is the equilibrium concentration of adsorbate in solution (mg/L) after adsorption. Q_m is the maximum adsorption capacity corresponding to complete monolayer coverage, K is the Langmuir constant related to energy of the adsorption (L of adsorbate per mg of adsorbent). Equation 3 can be rearranged to the following linear form:

$$\frac{1}{Q_e} = \frac{1}{Q_m K C_e} + \frac{1}{Q_m} \quad 4$$

This linear form can be used for linearization of experimental data by plotting $\frac{1}{Q_e}$ against $\frac{1}{C_e}$. The Langmuir constants Q_m and K can be evaluated from the slope and intercept.

1.5.2.3 Redlich–Peterson (R-P) Model

The Redlich-Peterson isotherm is an empirical three-parameter model used to represent the adsorption equilibrium over a wide concentration range and can be applied in either homogeneous or heterogeneous systems [25]. The R-P model combines elements of Langmuir and Freundlich models, thereby improving on the inaccuracies in these two-parameter models [151]. The equation is expressed as follows:

$$Q_e = \frac{K_R C_e}{1 + a_R C_e^\beta} \quad 5$$

Where K_R and a_R are the Redlich-Peterson with respective units of $(Lg^{-1} \text{ and } mgL^{-1})^{-\beta}$ and β is the Redlich-Peterson exponent (dimensionless). The Redlich-Peterson isotherm reduces to the Langmuir isotherm when the parameter β is equal to 1. When the term C_e^β is much higher than 1, the behaviour of the Redlich-Peterson isotherm is similar to the Freundlich isotherm.

1.5.2.4 The Sips (Langmuir-Freundlich) Model

The Sips model, is another three-parameter isotherm model which combines the Langmuir-Freundlich isotherm, it predicts the heterogeneity of an adsorption system and also circumvents the limitations associated with increased concentration in the Freundlich model [25]. The Sips equation takes the following form:

$$Q_e = \frac{k_s C_e^{\beta_s}}{1 + a_s C_e^{\beta_s}} \quad 6$$

Where k_s and a are the Sips isotherm model constant (Lg^{-1}), β is the Sips isotherm exponent. The equation effectively reduces to a Freundlich isotherm at low adsorbate concentrations, while it predicts a monolayer adsorption capacity of the Langmuir isotherm at high adsorbate concentrations [152].

1.5.3 Adsorption Kinetics

Adsorption kinetics describes the rate of adsorbate removal from the fluid phase to the adsorbent and describes the resistance of solute transfer from solution to the boundary layer at the solid-liquid interface through the internal pores to the surface site. This transfer consists of a number of stages which depend on hydrodynamic characteristics of the system (type of apparatus, rate), physical constants of the adsorbent (especially the diffusion coefficient) and the chemical nature of the adsorbent. Kinetic models are used to evaluate the reaction pathways, potential rate-controlling steps and the mechanism of adsorption reactions.

The mathematical models used describe adsorption operations are classified as diffusional and adsorption reaction models. Adsorption and diffusion models are constructed based on three successive steps: external mass transfer, intraparticle diffusion, and adsorption on active sites. Adsorption reaction models originate from chemical reaction kinetics and are based on the whole process of adsorption. In batch systems, the commonly applied models are the pseudo first-order, pseudo-second-order, and Elovich equation.

1.5.3.1 Lagergren's Pseudo-First Order Kinetic Model

This is the earliest known model used to describe the adsorption rate based on solid's adsorption capacity and is expressed as:

$$\frac{dQ}{dt} = k_1(Q_e - Q_t) \quad 7$$

where Q_e and Q_t are the adsorption capacity at equilibrium and at time t respectively (mg/g), k_1 is the rate constant of pseudo-first order adsorption (min^{-1}). Integrating this equation with initial conditions, $Q_t=0$ at $t=0$, and $Q_t=t$ at $t=t$ leads to

$$\ln(Q_e - Q_t) = \ln Q_e - k_1 t \quad 8$$

This is the linear form of the pseudo-first order kinetic adsorption model and the equation is verified if the plot of $\ln(Q_e - Q_t)$ as a function of time gives a straight line. k_1 is deduced from the slope of the line and Q_t gives the vertical intercept.

A nonlinear rearrangement of this equation gives

$$Q_t = Q_e[1 - \exp(-k_1 t)] \quad 9$$

1.5.3.2 Pseudo-Second Order Kinetic Model

This model is based on the assumption that the rate of adsorption is determined by the square of the number of vacancies. The pseudo-second order chemisorption kinetic rate equation is given by:

$$\frac{dQ_t}{dt} = k_2(Q_e - Q_t)^2 \quad 10$$

Where K_2 is the rate constant of pseudo second order adsorption ($\text{mg}^{-1} \text{min}^{-1}$). The linear form of the kinetic rate equation as expressed by Ho is

$$\frac{t}{Q_t} = \frac{1}{h_0} + \frac{t}{Q_e} \quad 11$$

Given that $h_0 = k_2 Q_e^2$ is the initial adsorption rate h_0 ($\text{mg} \cdot \text{g}^{-1} \text{min}^{-1}$). Thus, from Equation 7 a plot of (t/Q_t) versus t gives values of Q_e and k_2 from the slopes and intercepts respectively. The nonlinear form of this model is expressed as

$$Q_t = \frac{k_2 Q_e^2 t}{1 + Q_e k_2 t} \quad 12$$

1.5.3.3 Elovich Model

The Elovich equation assumes that the actual solid surfaces are energetically heterogeneous and that neither desorption nor interactions between the adsorbed species could substantially affect the kinetics of adsorption at low surface coverage. The model is empirical, generally applied to chemisorption kinetics and is often valid for heterogeneous systems with slow adsorption rates [153]. The simplified linearized Elovich equation is generally expressed as:

$$Q_t = \frac{1}{\beta} \ln(\alpha\beta) + \frac{1}{\beta} \ln t \quad 13$$

where: α is the initial sorption rate ($\text{mg g}^{-1}\text{min}$) and β is the rate constant for desorption (g mg^{-1}) during any one experiment. Thus, a plot of Q_t versus $\ln(t)$ should yield a linear relationship with a slope of $(1/\beta)$ and an intercept of $(1/\beta)\ln(\alpha\beta)$ if the sorption process fits the Elovich equation.

1.5.4 Analysis of Error

The goodness of fit is a parameter that estimates (generally through the least square method) how well a curve (prediction) pronounces the experimental data. Adsorption models are nonlinear equations with respect to the respective model parameters. To avoid parameter estimation, a common practice involves the linearization of these equations allowing for the use of linear regression analysis to determine the best fitting model. Linearization can modify the statistical interpretation of the experimental error distributions [86, 87]. In contrast, nonlinear regression quantifies the distribution of adsorbates, analyses the adsorption system, and verifies the consistency of theoretical assumptions of adsorption isotherm model. Thus, unlike linearized adsorption models, nonlinear regression minimizes the error distribution between the experimental data and the predicted model based on its convergence criteria [154]. The value of the error function is either minimised or maximised depending on the definition of the selected error function [155]. The coefficient of determination, residual root mean square error and the chi-square test are used to test the goodness of fit of the equilibrium models; the coefficient of determination, normalized standard deviation and average relative error are used to test the goodness of fit the kinetic models [156].

1.5.4.1 The coefficient of determination (R^2)

The coefficient of determination gives the proportion of the variance of one variable that is predictable from the other variable. The coefficient of determination represents the percent of the experimental data that is the closest to the line of best fit/prediction or how closely a curve fits a given data (in the case of non-linear regression) [157]. The model's fitness is signified by the coefficient of determination expressed as

$$R^2 = \frac{\sum_{n=1}^n (Q_{e.exp.n} - Q_{e.model.n})^2}{\sum_{n=1}^n (Q_{e.exp.n} - Q_{e.exp.n})^2} \quad 14$$

where, $Q_{e.exp}$ is the experimental equilibrium sorption capacity, $Q_{e.model}$ is the prediction from the isotherm model for corresponding C_e and n is the number of observations.

1.5.4.2 Residual root mean square error (RMSE) and Chi-square test (χ^2)

Non-linear error functions such as the residual root mean square error (RMSE) and the chi-square test (χ^2) are used to judge the equilibrium models. The standard equations are as follows:

$$RMSE = \sqrt{\frac{1}{n-1} \sum_{n=1}^n (Q_{e.exp.n} - Q_{e.model.n})^2} \quad 15$$

$$\chi^2 = \sum_{n=1}^n \frac{(Q_{e.exp.n} - Q_{e.model.n})^2}{Q_{e.exp.n}} \quad 16$$

Where, $Q_{e.exp}$ is the equilibrium adsorption, capacity found from the batch experiment, $Q_{e.model}$ is the prediction from the isotherm model corresponding to 'Ce' and 'n' is the number of observations. The Chi-square test is used to determine whether there is a statistically significant difference between the expected frequencies and the observed frequencies in one or more categories of a contingency table.

1.5.4.3 The normalized standard deviation (NSD)

The kinetic models are tested by two non-linear error functions: the normalized standard deviation (NSD) and average relative error (ARE).

$$NSD = 100 \times \sqrt{\frac{1}{N-1} \sum \left[\frac{Q_{t.exp.N} - Q_{t.model.N}}{Q_{t.exp.N}} \right]^2} \quad 17$$

where, $Q_{t.exp}$ is the experimental equilibrium sorption capacity, $Q_{t.model}$ is the prediction from the at time t and N is the number of observations.

1.5.4.4 Average relative error (ARE)

Developed by Kapoor and Yang, this error function attempts to minimize the fractional error distribution across the entire concentration or time range. The model indicates a tendency to under or overestimate the experimental data, attempts to minimize the fractional error distribution across the entire studied concentration [154] It is expressed as:

$$ARE = \frac{100}{N} \sum_{i=1}^N \frac{Q_{t.exp.N} - Q_{t.model.N}}{Q_{t.exp.N}} \quad 18$$

1.5.5 Fixed bed adsorption

In fixed bed adsorption systems, a solution (influent) is pumped through a column with which is packed with a certain amount of adsorbent. During the operation, the adsorbate is transferred from the solution to the adsorbate surface, clarifying the solution. The data here is analysed to estimate breakthrough time, exhaustion time, length of mass transfer zone, effluent volume, maximum capacity of the column, and removal percentage. The breakthrough time is

considered when the outlet adsorbate concentration attains low levels (in general less than 5%) in relation to the initial concentration, and the exhaustion time is considered when the outlet concentration attains 95% of the initial concentration. The length of the mass transfer zone reflects the shortest possible adsorbent bed length needed to obtain the breakthrough time. The breakthrough curve of an adsorbate in a continuous system is the plot of the outlet-to-inlet concentration (C/C_0) ratio against time (t) or throughput volume [158]. The operation and dynamic response of an adsorption column (performance) can be evaluated based on the shape of the breakthrough curve obtained from the plot of C_i/C_0 versus time where C_i and C_0 are the effluent and inlet concentrations in mg/L, respectively [159].

1.6 Characterisation Techniques

1.6.1 Pore Structure Analysis

Adsorbents are normally porous and this property (porosity) is characterised by the pore structure and the nature of the adsorbing surface. The porosity is usually analysed by measuring and quantifying the pore structure through the physical gas (usually nitrogen) adsorption technique. The technique determines the pore properties by measuring the quantity of gas adsorbed to form a monolayer over the surface of the solid. The Brunauer, Emmett and Teller (BET) method, Dubinin and Radushkevich (DR) and the t-plot analysis, which uses nitrogen gas as the adsorbate, are the most common methods used to evaluate the surface area and micropore volume of porous materials [160]. In 1938, S. Brunauer, P. H. Emmet, and E. Teller proposed a theoretical model for gas adsorption (BET model) that allows for multilayer adsorption, as an extension of the Langmuir isotherm. The BET model is based on the following assumptions:

- The surface where the adsorption takes place is homogeneous.
- The heat of adsorption does not depend on the degree of surface coverage.
- Multilayer adsorption is governed by van der Waals interactions between individual layers.
- There is no interaction between adsorbed gas molecules of the same layer.
- Adsorption of an infinite number of layers is possible.

The BET model leads to a two-parameter adsorption isotherm (amount of gas adsorbed) as a function of pressure, P , in equilibrium with the gas phase at constant temperature) of the form

$$\frac{P}{\sigma[P_0 - P]} = \frac{c-1}{\sigma_0 c} \times \left(\frac{P}{P_0}\right) + \frac{1}{\sigma_0 c}$$

19

where σ is the surface coverage (adsorbed molecules per unit area or per cm) and σ_0 is the monolayer adsorbed gas quantity (molecules per unit area or per cm). p_0 is the saturation pressure of the adsorbate gas at which an infinite number of layers can be built up on the surface.

A plot of $\frac{P}{\sigma[P_0 - P]}$ versus $\frac{P}{P_0}$ yields a straight line with slope $\frac{c-1}{\sigma_0 c}$. Using this, the specific amount of monolayer adsorbed gas σ_0 can be determined from the adsorption isotherm [161].

1.6.2 X-Ray Powder Diffraction

X-Ray Diffraction (XRD) is a very powerful technique for studying crystalline materials and XRD methods are the most effective methods for determining the crystal structure of materials. They can be used to determine the phase composition of a sample [162], unit cell lattice parameters (and Bravais lattice symmetry), residual strain (macrostrain), crystal structure, crystallite size and microstrain. Diffraction occurs when light is scattered by a periodic array with long-range order, producing constructive interference at specific angles. The scattering of x-rays from atoms produces a diffraction pattern, which is a product of the unique crystal structure of a material. The position and intensity of peaks in a diffraction pattern are determined by the crystal structure: the distance between parallel planes of atoms. Bragg's law calculates the angle where constructive interference from x-rays scattered by parallel planes of atoms will produce a diffraction peak and provides a simplistic model to understand what conditions are required for diffraction (Figure 12). Ideally, in a powdered sample every possible crystalline orientation is represented equally.

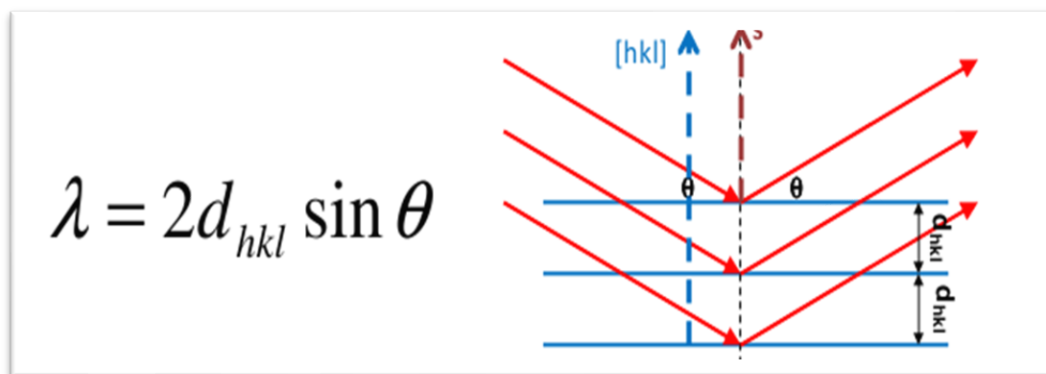


Figure 12: Illustration of Bragg's Law

The XRD pattern of a powdered sample is a plot of the observed diffracted intensity of the x-rays against the Bragg angle. The experimental data are usually obtained in the form of a diffractogram, of intensity versus diffraction angle 2θ . The physically relevant information lies in the position, the power and the half-width of the peaks [163].

1.6.3 Infrared Spectroscopy

Infrared (IR) spectroscopy measures the absorption of IR radiation by materials as the atoms vibrate about their bonds and gives information about which functional groups are present in a sample. The selection rule for a change in vibrational state brought about by absorption or emission of radiation is that the electric dipole moment of the molecule must change when the atoms are displaced relative to one another. The larger this change, the more intense will be the absorption band in the infrared spectra.

In FTIR (Fourier Transform Infrared Spectroscopy), the Fourier Transform method is used to obtain an infrared spectrum in a complete range of wave numbers simultaneously. It provides increased resolution by averaging a large number of spectra to give an improved signal to noise ratio and hence increased sensitivity compared with conventional IR spectroscopy. FTIR also permits more rapid collection of data. A variation of this method is reflectance spectroscopy: this may be external (Diffuse Reflectance-DR FTIR) or internal (Attenuated Total Reflectance-ATR FTIR) reflectance. An ATR-FTIR operates by measuring the changes that occur in a totally internally reflected infrared beam when it encounters a sample as illustrated in **Figure 13**. An infrared beam is directed onto an optically dense crystal with a high refractive index at a certain angle. This internal reflectance creates an evanescent wave that extends beyond the surface of the crystal into the sample held in contact with the crystal.

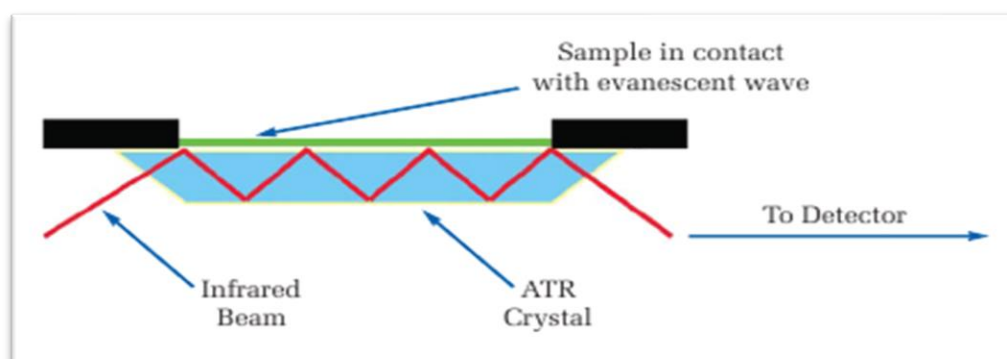


Figure 13: Illustration of Attenuated Total Reflectance

In regions of the infrared spectrum where the sample absorbs energy, the evanescent wave will be attenuated or altered. The attenuated energy from each evanescent wave is passed back to the IR beam, which then exits on the opposite end of the crystal and is passed to the detector in the IR spectrometer. The system then generates an infrared spectrum.

1.6.4 Scanning Electron Microscopy (SEM)

A scanning electron microscope produces images of a sample by scanning it with a focused beam of electrons. SEM is one of the most frequently used instruments in material research today because of the combination of high magnification, large depth of focus, greater resolution and ease of sample observation. The basic operation in SEM entails the interaction of an accelerated highly monoenergetic electron beam, originating from a cathode filament, with the atoms at the sample surface. The electron beam is focused into a fine probe, which is rastered over the sample. The scattered electrons are collected by a detector; modulated and amplified to produce an exact reconstruction of the sample surface and particle profile to perform elemental analysis. The schematic drawing of a typical Scanning Electron Microscope (SEM) column and sample-beam interactions within a SEM is shown in [Figure 14](#).

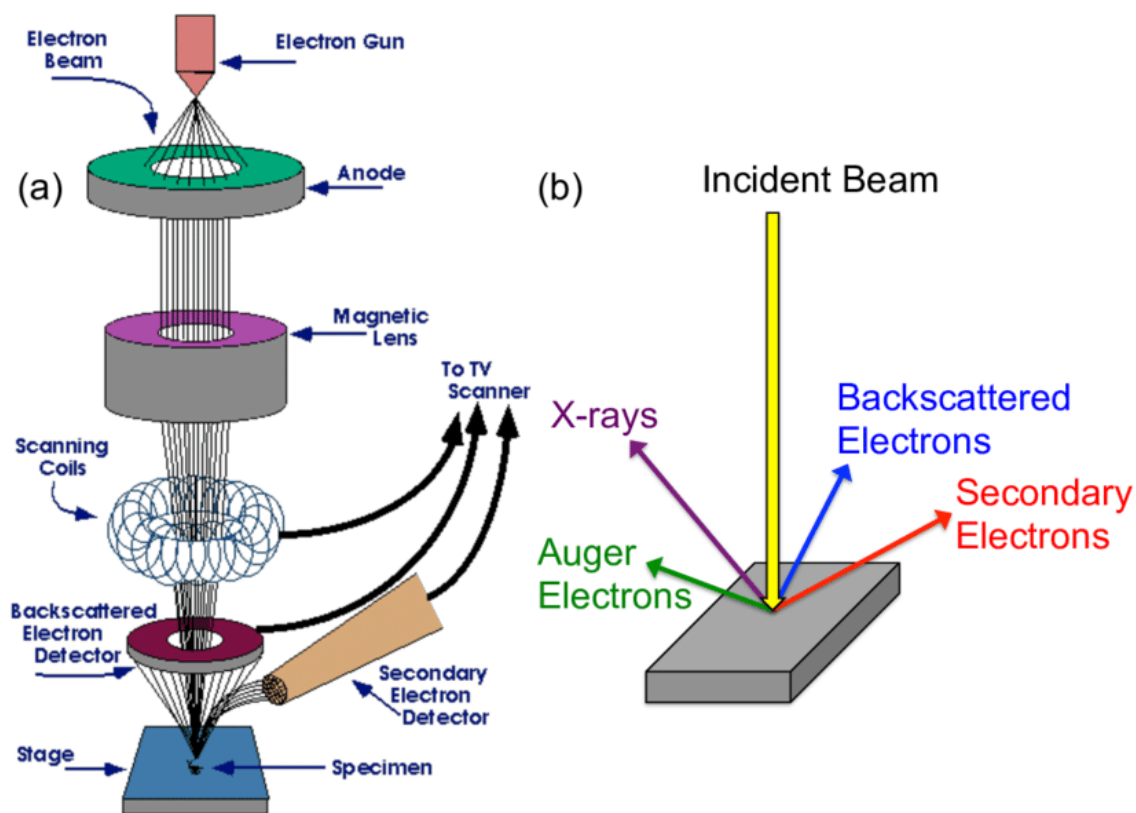


Figure 14: Schematic drawing of (a) the typical Scanning Electron Microscope (SEM) column and (b) sample-beam interactions within a SEM.

1.6.5 Transmission Electron Microscopy

Transmission electron microscopy (TEM) is a versatile technique used to analyse the size, distribution, aggregation, crystallographic structure, dispersion and shape of nanomaterials. The transmission electron microscope was built by James Hillier and Albert Prebus at the University of Toronto in 1938. **Figure 15** illustrates the passage of an electron beam through an electron microscope under the influence of the lens and aperture settings.

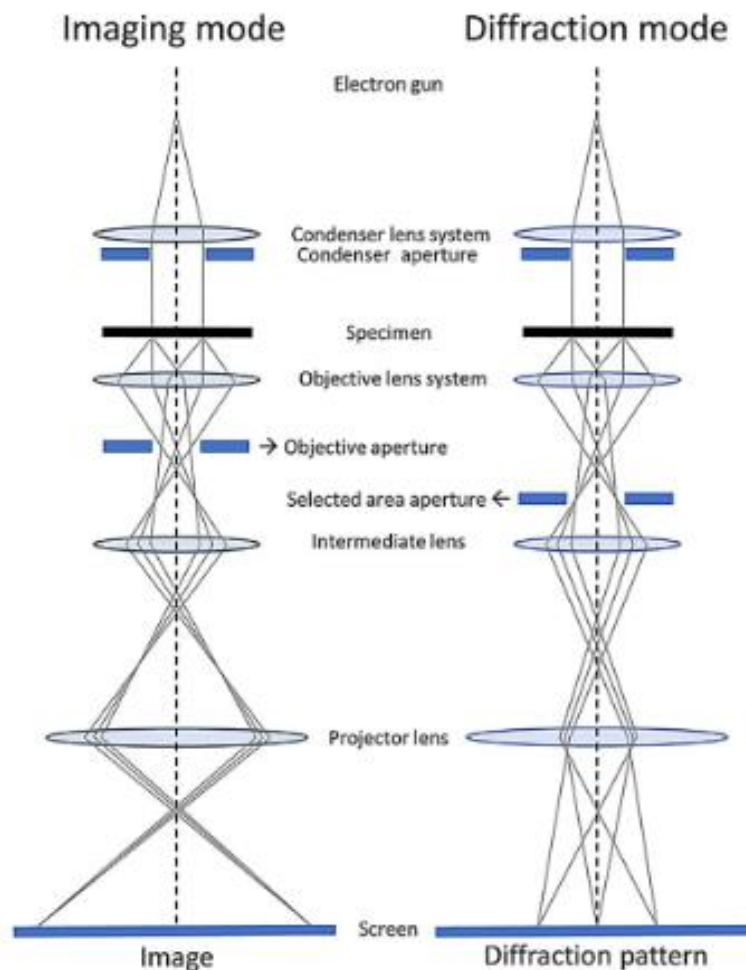


Figure 15: Illustration of how an electron beam passes through the electron microscope in TEM mode (imaging and diffraction) [164]

The equipment operates at high voltages ranging from 50–1000 kV and provides a resolution up to 0.1 nm. It uses a beam of electrons, which is accelerated by an electric potential and projected onto a thin specimen through a set of lenses and apertures. Part of the electron beam passes through the specimen without interacting while the other electrons will be scattered by the atoms in the specimen [165]. Then the unscattered electrons that are transmitted through

the sample hit a fluorescent screen at the bottom of the microscope producing the image. Generally, the images produced by TEM are grey scale and can be interpreted as follows: the lighter areas represent the higher number of electrons transmitted and the darker areas represent lower number and dense areas on the sample. To use with TEM, samples need to be sliced thin enough for electrons to transmit. A dark-field image is formed when the aperture selects only diffracted electrons. At low magnifications, TEM image contrast originates from the absorption and scattering of electrons in the specimen, due to the thickness and composition of the material (i.e., mass–thickness contrast), and from the crystal orientation (i.e., diffraction contrast).

1.6.6 The Pair Distribution Function (PDF) method

The PDF method is a total scattering technique for determining local order in nanostructured materials [166]. This method is rapidly gaining currency due to its ability to provide short-to-medium range order (local structure) in amorphous and nanocrystalline materials, which are typically inaccessible by conventional diffraction methods [167]. The PDF is a histogram of interatomic separations in a material and represents the weighted probability of finding a pair of atoms separated by a given distance [168]. The technique does not require periodicity, so it is well suited for studying nanoscale features in a variety of materials [169, 170]. The experimental PDF, denoted $G(r)$, is the truncated (reverse) Fourier transform of the total scattering structure function, $F(Q) = Q(S(Q) - 1)$ [171]

$$G(r) = \frac{2}{\pi} \int_{Q_{min}}^{Q_{max}} F(Q) \sin(Qr) dQ \quad 20$$

where Q is the magnitude of the scattering momentum. The structure function, $S(Q)$, is extracted from the Bragg and diffuse components of x-ray, neutron or electron powder diffraction intensity. For elastic scattering, $Q = 4\pi \sin(\theta)/\lambda$, where λ is the scattering wavelength and 2θ is the scattering angle. In practice, values of Q_{min} and Q_{max} are determined by the experimental setup and Q_{max} is often reduced below the experimental maximum to eliminate noisy data from the PDF since the signal to noise ratio becomes unfavourable in the high- Q region.

Once the experimental PDFs are determined they can be analysed directly or through modelling. A powerful approach is simply to compare experimentally determined PDFs from samples under study and from known control samples [172]. A great deal can be learned simply from visual inspections and by taking differences to look for residual signals. Numerical tools

that compare the likeness, or degree of correlation, between two curves also give insight [172, 173]. The Pearson correlation coefficient is one such tool [173].

The PDF gives the scaled probability of finding two atoms in a material a distance r apart and is related to the density of atom pairs in the material [166]. For a macroscopic scatterer, $G(r)$ can be calculated from a known structure model according to

$$G(r) = 4\pi r [\rho(r) - \rho_0] \quad 21$$

$$\rho(r) = \frac{1}{4\pi r^2 N} \sum_i \sum_{j \neq i} \frac{b_i b_j}{\langle b \rangle^2 \delta(r - r_{ij})} \quad 22$$

Here, ρ_0 is the atomic number density of the material and $\rho(r)$ is the atomic pair density, which is the mean weighted density of neighbour atoms at distance r from an atom at the origin. The sums in $\rho(r)$ run over all atoms in the sample, b_i is the scattering factor of atom i , $\langle b \rangle$ is the average scattering factor and r_{ij} is the distance between atoms i and j . In practice, we use **Equation 22** to fit the PDF generated from a structure model to a PDF determined from experiment. For this purpose, the delta functions in **Equation 22** are Gaussian-broadened and the equation is modified to account for experimental effects. PDF modelling, where it is carried out, is performed by adjusting the parameters of the structure model, such as the lattice constants, atom positions and anisotropic atomic displacement parameters, to maximize the agreement between the theoretical and an experimental PDF. This procedure is implemented, for example, in PDF_{GUI} [174] and Diffpy-CMI [175].

1.6.7 Thermogravimetric analysis

Thermogravimetric Analysis (TGA) is a quantitative technique that measures weight/mass change (loss or gain) as a function of temperature, time and atmosphere to determine the composition of materials and predict their thermal stability. It can provide information about phase transitions (vaporization, sublimation, absorption/desorption) and also on chemical phenomena which involves mass change (dehydration, decomposition or oxidation).

The technique characterises materials that exhibit weight loss or gain due to sorption/desorption of volatiles, decomposition, oxidation and reduction. The sample is loaded on a high-precision thermobalance within the furnace and weighed continuously during the course of the heating program [176]. The result of TGA measurements is a thermogravimetric curve that can be presented in either integral (TG curve) or differential (DTG curve) form. In a DTG curve, downward and upward peaks respectively represent mass loss and mass gain steps.

Three main regions are considered for thermal analysis of cyclodextrins and their complexes: the first interval corresponds to water and/or solvent dissociation and vaporization up to ~130 °C; the last interval appears after ~270 °C and is attributed to the decomposition of cyclodextrins and possible the guest molecules; dissociation of the guest molecules generally appears in the range between these two temperatures. [177]

CHAPTER II
MATERIALS AND METHODS

CHAPTER II - MATERIALS AND METHODS

This chapter presents the research methodology, including the synthetic methods of the various adsorbents, the equipment used in characterization, batch and column adsorption studies and bacterial removal.

2.1 Materials

All reagents were used as purchased without further purification. β -cyclodextrin monohydrate, anhydrous citric acid, sodium phosphate dibasic and sodium hydrogen carbonate were purchased from EM Science, Hatfield, PA, USA; sodium hydroxide and ferric nitrate nonahydrate, hydroxyapatite nanopowder (200 nm particle size (BET), $\geq 97\%$, synthetic) were purchased from Sigma Aldrich St. Louis, MO, USA. The pollutant model compounds sodium fluoride, nickel nitrate hexahydrate and methylene blue were procured from Fisher Scientific (Waltham, MA, USA). 18 M Ω double de-ionised water was used in synthesis and preparation of solutions. Ferric nitrate 99% PROLABO, Sodium hydroxide was purchased from Fluka and sodium hydrogen carbonate from Analytical.

2.2 Methodology

The commercial production of β -CD from starch by enzymatic degradation of starch by environmentally friendly technologies is a well-documented process [178, 179]. Goethite nanopowder was synthesized through chemical precipitation. The β -CD nanosponge was synthesized by ultrasound assisted polycondensation. The nanosponge was functionalised with goethite and/or hydroxyapatite. Techniques such as BET, TEM, SEM-EDX, NMR, XRD, FTIR, TGA, was used to characterize the as-synthesised nanosponges. Batch and column adsorption studies were carried to study the mechanistic aspects (kinetics and equilibrium) of the adsorption process. The research methodology employed in this thesis is outlined in the chart below given in **Figure 16**.

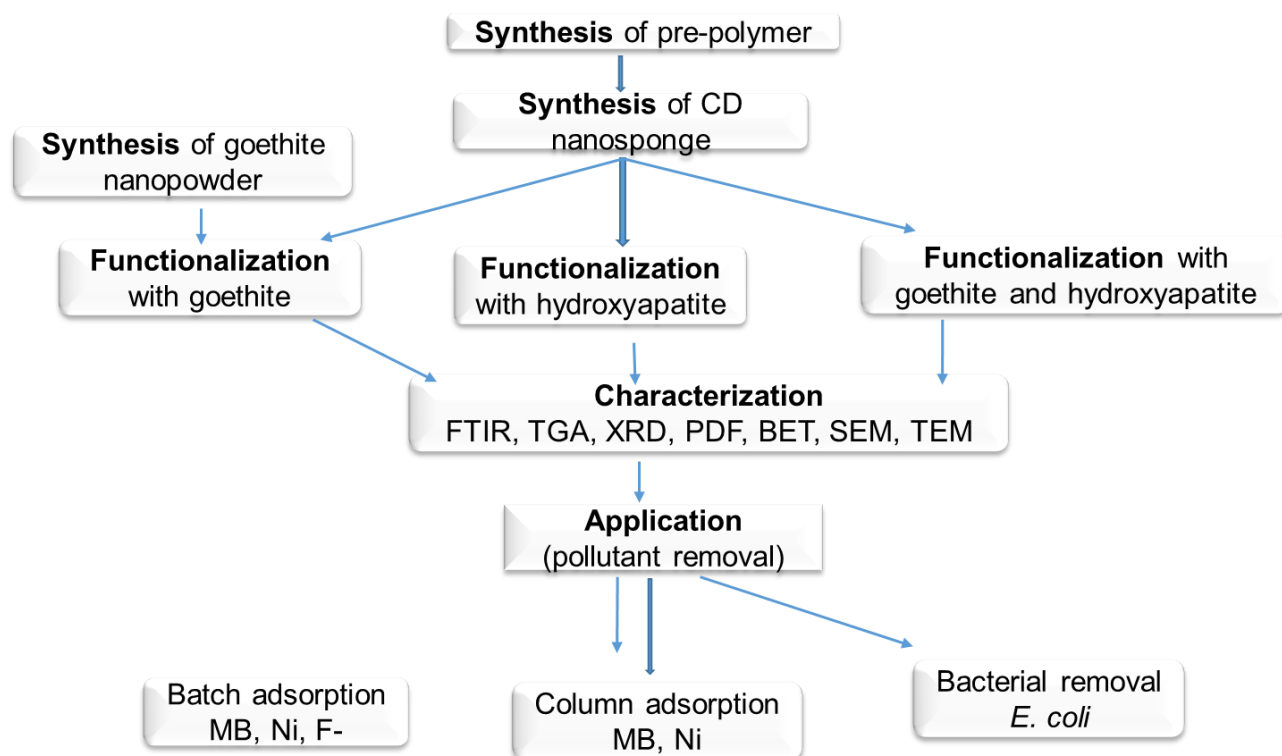


Figure 16: Outline of research methodology

2.2.1 Synthesis

2.2.1.1 Synthesis of goethite nanopowder

Goethite nanopowder was synthesized by fast hydrolysis of ferrihydrite according to a method described by Lee et al.[180], with slight modifications on the temperature and ageing time and the use of NaHCO_3 as dispersant. Thus, 60.71 g of hydrated ferric nitrate was dissolved in 300 mL distilled water in a 1000 mL beaker and agitated for 1 hour. To this solution (pH 2.0), 250 mL of 1 M NaHCO_3 solution was added while stirring to disperse the particles. This solution was then titrated with 1 M NaOH to a pH of 12.06 to precipitate ferrihydrite (red brown suspension). The suspension was stirred continuously for 24 hours, and aged in an electric furnace at 90 °C for 4 hours then at 57 °C for 20 hours to convert the unstable ferrihydrite to goethite. The resulting brown precipitate was washed twice with distilled water to remove associated impurities (NO_3^- , CO_3^{2-} , OH^- , Na^+) and dried at 57 °C for 16 hours. The dried powder sample was then activated by heating at 110 °C for 20 hours, ground, sieved and stored for characterisation and use.

2.2.1.2 Synthesis of cyclodextrin nanosponge

The cyclodextrin nanosponge (CDN) was synthesized by ultrasound-assisted polycondensation polymerisation. Beta cyclodextrin (6 g), citric acid (8 g) and disodium phosphate (3 g) were dispersed in 10 mL of double deionised water. This solution was homogenised under magnetic stirring for 1 hour, sonicated for 3 hours and dried at 110 °C. After drying, 1 g of NaHCO₃ was added to the gel-like solid (pre-polymer) and transferred into a petri dish. The mixture was heated in an electric oven under vacuum (**Figure 17**) at 140 °C and for 45 min. The cream white solid obtained was soaked in double deionised water, washed several times, suction filtered and air-dried.



Figure 17: Vacuum oven used in the synthesis of the CD nanosponges

2.2.1.3 Synthesis of cyclodextrin functionalised nanosponges

The CD nanosponges were functionalised with goethite and hydroxyapatite. Functionalization of CDN with goethite was carried out at varying conditions of synthesis and reaction parameters and FTIR analysis was used to monitor changes on the resultant material and also to determine the best synthetic route.

CDG was synthesised using 1.5 g CD, 1.5 g CT and 0.6 g dibasic. The goethite nanopowder (0.3 g) was added to the mixture before pre-polymerisation, and polymerisation was carried

out at 170 °C under vacuum. Neither sonication nor bicarbonate was used. CDG2 was synthesised with the same ratio of CD to CT to dibasic. The solution was sonicated for 5 min, and dried under vacuum for 5hr at 60 °C. 0.2 g goethite nanopowder was added and the gel was polymerised at 140 °C under vacuum. CDG stirred was synthesised with the same CD to CT to dibasic ratio. This mixture was stirred for 5 hrs and dried in an oven at 110 °C. 0.35 g of goethite nanopowder and 0.5 g NaHCO₃ was added and the prepolymer was further polymerised at 140 °C under vacuum.

CDG suspension (goethite was added as a suspension), CDG freeze dried (sample was freeze dried after synthesis) and CDG air dried (samples were dried at room temperature) were synthesised by preparing a suspension was made by dissolving 0.2 g of goethite nanopowder in 6 ml of double deionised water and sonicated for 4 hours. To this suspension and 1 g NaHCO₃ was added to the gel-like solid cyclodextrin mixture (pre-polymer), heated under vacuum at 140 °C for 45 min. The yellow brown solid obtained was soaked in double deionised water, washed several times, suction filtered and air-dried (room temperature ±22 °C).

The hydroxyapatite functionalised cyclodextrin nanosponge (CDHA) was synthesised by adding 0.2 g hydroxyapatite nanopowder and 1 g NaHCO₃ to the pre-polymer heated under vacuum at 140 °C for 45 min. The white solid obtained was soaked in double deionised water, washed several times, suction filtered and air-dried (room temperature ±22 °C).

The goethite/hydroxyapatite functionalised cyclodextrin nanosponge (CDGHA) was synthesised by adding the goethite suspension, 0.2 g hydroxyapatite nanopowder and 1 g NaHCO₃ to the pre-polymer heated under vacuum at 140 °C for 45 min. The yellowish solid obtained was soaked in double deionised water, washed several times, suction filtered and air-dried (room temperature ±22 °C).

2.2.2 Characterization

2.2.2.1 Swelling capacity

The swelling capacity of the as-synthesised sponges over a period of 72 hours was determined by weighing 0.5 g (wi) of the sponge and soaking in 100 ml distilled water at room temperature. The soaked sponges were filtered using Whatman filter paper, blotted using additional Whatman filter paper to remove the extra water and weighed. This mass was recorded as wf.

The swelling capacity (SC) or absorbency was calculated as a percentage based on Equation 23.

$$SC = \frac{w_f - w_i}{w_i} \times 100 \quad 23$$

2.2.2.2 BET surface area analysis

Nitrogen adsorption–desorption experiments were performed on the goethite nanopowder using a Micromeritics TriStar 3000 V6.05A BET surface area analyser at -196.15 °C. The specific surface area was estimated by applying the Brunauer-Emmet-Teller (BET) equation in the $0.010 \leq P/P_o \leq 0.299$ interval of relative pressure, using 0.1620 nm² for the cross-sectional area of molecular nitrogen and a sample mass of 0.2110 g. Prior to analyses, the sample was degassed in vacuum at 105 °C for 12 h. For CD, CDG, CDHA and CDGHA, nitrogen adsorption–desorption isotherms experiments were performed using Quantachrome® ASiQwin™ Automated Gas Sorption instrument version 5.2 at -196.15 °C. The specific surface area was estimated by applying the Brunauer-Emmet-Teller (BET) equation in the $0.010 \leq P/P_o \leq 0.299$ interval of relative pressure, using 0.1620 nm² for the cross-sectional area of molecular nitrogen and a sample mass of 0.0291 , 0.03167 , 0.0334 and 0.0335 g for CD, CDG, CDHA and CDGHA respectively.

2.2.2.3 Thermogravimetric Analysis

TGA can be applied to measure quantities of component in a material of known qualitative component as long as they differ significantly in thermal stability. A TGA run will normally exhibit weight loss steps corresponding to various stages in the degradation of the original substance plus weight loss corresponding to secondary reactions of the initial degradation products. Thermo-Gravimetric Analysis (TGA) was performed over a temperature range of 20 - 600 °C, under nitrogen, using a NETZSCH 209 F1 Libra instrument as given in Figure 18 under nitrogen environment. Al_2O_3 85 uL crucibles were used. A nitrogen gas flowrate of 20 mL/min was applied for both PURGE 2 FC and Protective MFC, outlet, at a start temperature of 30 °C and 10 °C/min heating rate. The data was analysed using a NETZSCH-Proteus-70 software.

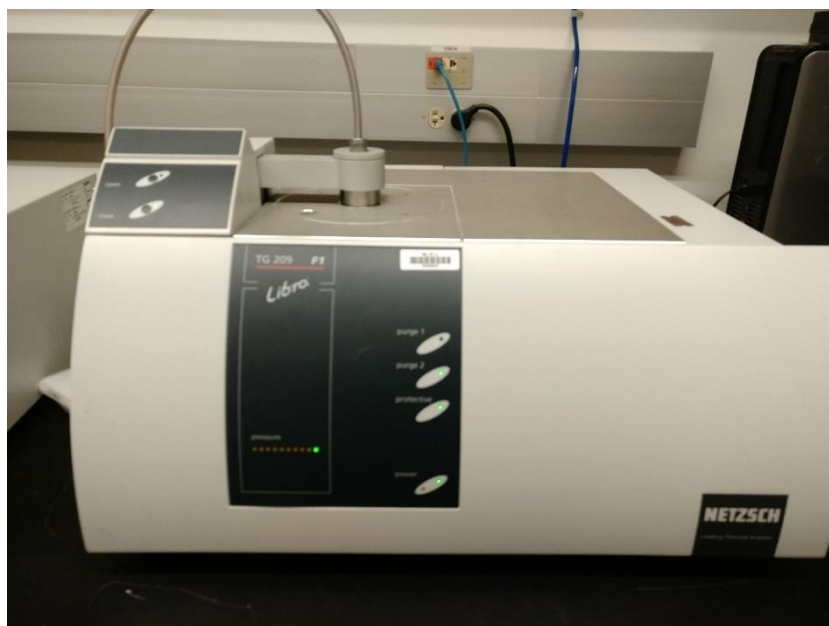


Figure 18: Netzsch 209 F1 Libra instrument

2.2.2.4 Fourier Transform infrared

Fourier Transform Infrared (FTIR) technique was used for the identification of functional groups and interaction between the adsorbed molecule and nanosponge. Fourier Transform Infrared Spectroscopy (FTIR) was performed using a Bruker Vertex 70 instrument with a Specac Golden Gate ATR accessory as shown in **Figure 19**.

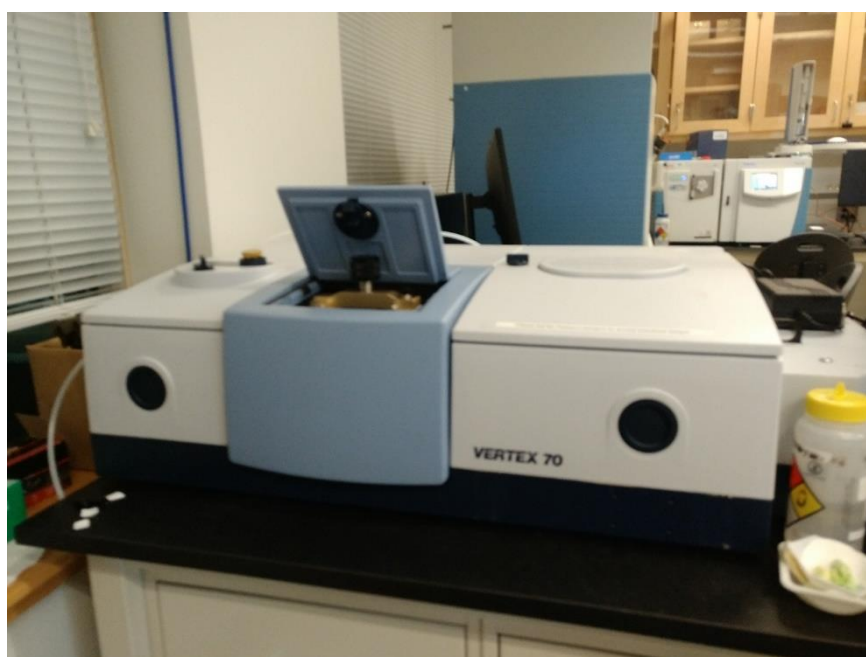


Figure 19: Bruker Vertex 70 FTIR Instrument

The analysis was carried out at a Nitrogen gas pressure of ~25 psi and flow of ~2scfh under transmission mode, signal amplitude 1500-1600 for approximately 15 mins (1024 scans). The data was collected using OPUS software.

2.2.2.5 X-ray diffraction

To determine the phases and the microstructure of the goethite nanoparticles, X-ray powder diffraction (XRD) patterns were collected on a Bruker D2 Phaser diffractometer with theta/theta geometry, operating a Cu K α radiation tube ($\lambda = 1.5418 \text{ \AA}$) at 30 kV and 10 mA. The XRD pattern of all the randomly oriented powder specimen were recorded in the 10° - 70° 2θ range with a step size of 0.026° and a counting time of 18 s per step. The diffraction pattern was matched against the Powder Diffraction File (PDF) of the Inorganic Crystal Structure Data (ICSD) database and qualitative phase analysis conducted using the DIFFRAC Plus EVA software (Bruker AXS GmbH).

Powder diffraction analysis of the as-prepared nanosponges was carried out using a Bruker D8-Advance powder x-ray diffractometer. The spectra were recorded from 10 to 70° , with CuK α radiation, no spin, wavelength $\lambda=1.5418 \text{ \AA}$, and a scan rate of 0.026° every 0.6 seconds.

2.2.2.6 Atomic Pair Distribution Function Analysis

Pair Distribution Function (PDF) experiments were carried out at the PDF at National Synchrotron Light Source II (NSLS-II) at Brookhaven National Laboratory using the rapid acquisition PDF method (RAPDF) [181] during beam time on May 12th, 2019. A 2D Perkin Elmer amorphous silicon detector was placed 227 mm behind the samples, which were loaded in 1 mm ID kapton capillaries. The incident wavelength of the x-rays was 0.1668 \AA . Calibration of the experimental setup was done using nickel as a calibrant.

Datasets were collected at room temperature. The detector exposure time was 20.0 minutes. Raw data were summed and corrected for polarization effects before being integrated along arcs of constant angle to produce 1D powder diffraction patterns using the program pyFAI [182]. Corrections were then made to the data and normalizations are carried out to obtain the total scattering structure function, $F(Q)$, which was Fourier transformed to obtain the PDF using PDFgetX3 [183] within PDFsuite [184]. The maximum range of data used in the Fourier transform was $Q_{\text{max}} = 16.0 \text{ \AA}^{-1}$. The modelling is carried out using Diffpy-CMI [175]. The

PDF is calculated by Fourier transformation of the reduced structure factor generated from discrete structure model according to Debye scattering equation.

2.2.2.6 Scanning Electron Microscopy

High-resolution SEM (Scanning Electron Microscope) images were taken using a JEOL JSM-7000F Field Emission Scanning Electron Microscope, see **Figure 20**. A small quantity of the samples was lightly sprinkled evenly on a SEM sample stub with a double-sided sticky tape. A hand blower was used to blow away loose particles. An ion sputter EMS sputter coater (HL047) was used to perform Pt ion coating under high vacuum.



Figure 20: JEOL JSM-7000F Field Emission Scanning Electron Microscope

The imaging was performed under secondary electron in-lens (SEI) imaging conditions using an acceleration voltage of 5 kV and a working distance of 10 mm. The particle size distributions and morphologies were analysed using the Image J software (NIH, Bethesda, MD, USA).

2.2.2.7 Transmission Electron Microscopy

A Philips CM10 transmission electron microscope (Philips, Amsterdam, Netherlands), represented in **Figure 21**, was used to record the 2D images for morphology and particle size analysis. One drop of the dispersed sponge (in water) was placed on a copper grid and dried at room temperature for 24 hours before analysis. The particle size distributions and morphologies were analysed using the Image J software (NIH, Bethesda, MD, USA).

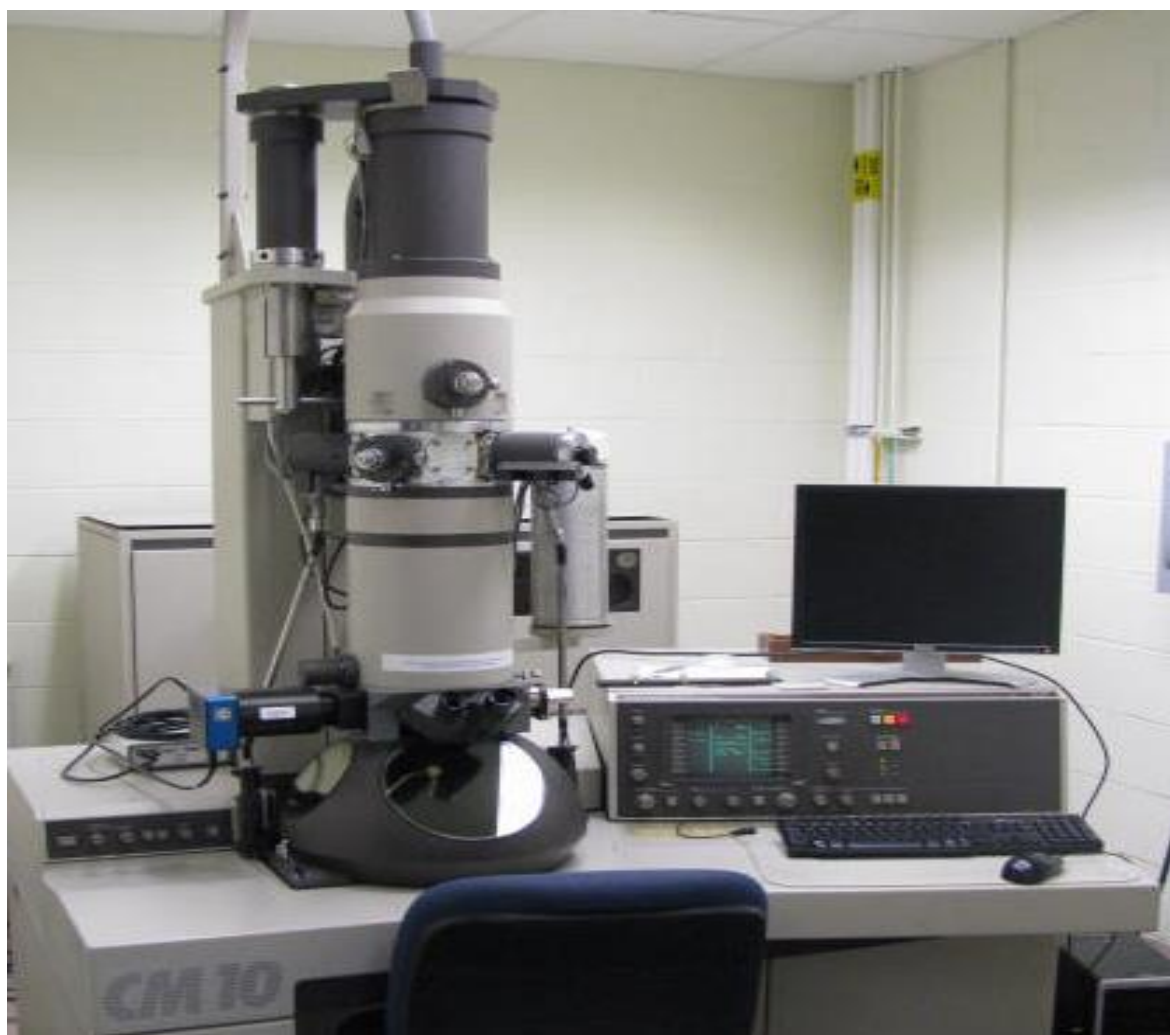


Figure 21: Philips CM10 transmission electron microscope

2.3 Adsorption Studies

2.3.1 Batch Adsorption Studies

Batch adsorption studies were carried out to determine the effectiveness of the prepared nanosponges to remove both organic and inorganic pollutants. Methylene blue (MB), fluoride and nickel were chosen as representative organic, inorganic and heavy metal pollutant respectively. In a 50 mL conical flask, 20 mL of adsorbate (20 ppm methylene blue or 50 ppm fluoride or 50 ppm nitrate) and 0.2 g of adsorbent was added and the solution stirred at 150 rpm for a fixed time and the supernatant solutions suction-filtered. The adsorption kinetics and equilibrium were studied for nickel adsorption by varying the contact time from 0 to 80 minutes and concentration from 0 to 80 ppm, an adsorbent mass of 0.2 g at room temperature.

The percentage removal and the quantity adsorbed were calculated using [Equation 24 and 25](#) respectively.

$$\%R = \frac{C_0 - C_e}{C_0} \times 100 \quad 24$$

$$Q_e = \frac{C_0 - C_e}{m} V \quad 25$$

Where Q_e (mg/g) is the quantity of substance adsorbed, C_0 is the initial adsorbate concentration (mg/L \approx ppm), C_e the equilibrium concentration of adsorbate (mg/L), V is the volume of solution (L), and m is the mass of sorbent in aqueous solution (g).

The equilibrium data was analysed through non-linear regression of the Langmuir, Freundlich, Redlich–Peterson and Sips models. The adsorption kinetics (dynamics) was tested through non-linear regression of the Pseudo-first-order, Pseudo-second-order and Elovich kinetic models (equations given in [Section 1.5.2 and 1.5.3](#)).

2.3.2 Column Adsorption Studies

For the nickel ion column adsorption test, 100 ppm nickel solution was loaded into a 60 ml plastic syringe. A syringe pump (Pump 33, Harvard Apparatus, Holliston, MA) was used to dispense the pre-filtrate solutions (downflow mode) at a flow rate of 10 ml/min via silicone

tubing connected to the syringes into a chromatography column (Sigma-Aldrich) loaded at the bottom with 2 g of CDN with a bed height of 9.4 cm. For methylene blue test, 20 ppm of methylene blue solution and 1 g CDN (bed height of 4.5 cm) was used. The filtrates were collected every 10 minutes and analysed using an ICP-MS for nickel and a UV-Vis spectrophotometer for methylene blue.



Figure 22: Setup for column adsorption

2.3.3 Analysis of Solution

Methylene blue concentrations were measured using a ThermoScientific Evolution 300 UV-Vis spectrophotometer ($\lambda_{\text{max}} = 663 \text{ nm}$). The residual concentrations were automatically calculated to double precision as defined by ANSI/IEEE STD 754-1985 using the Thermo Scientific ~ VISIONpro SOFTWARE V4.50. A ThermoScientific DIONEX 2100 Ion Chromatography System (**Figure 23**) with a Dionex EGC III KOH Eluent Generator Column

(EGC) was used to analyse fluoride and nitrate. A Perkin Elmer NexION 350X Inductively Coupled Plasma Mass Spectrometer (ICP-MS), see [Figure 24](#).

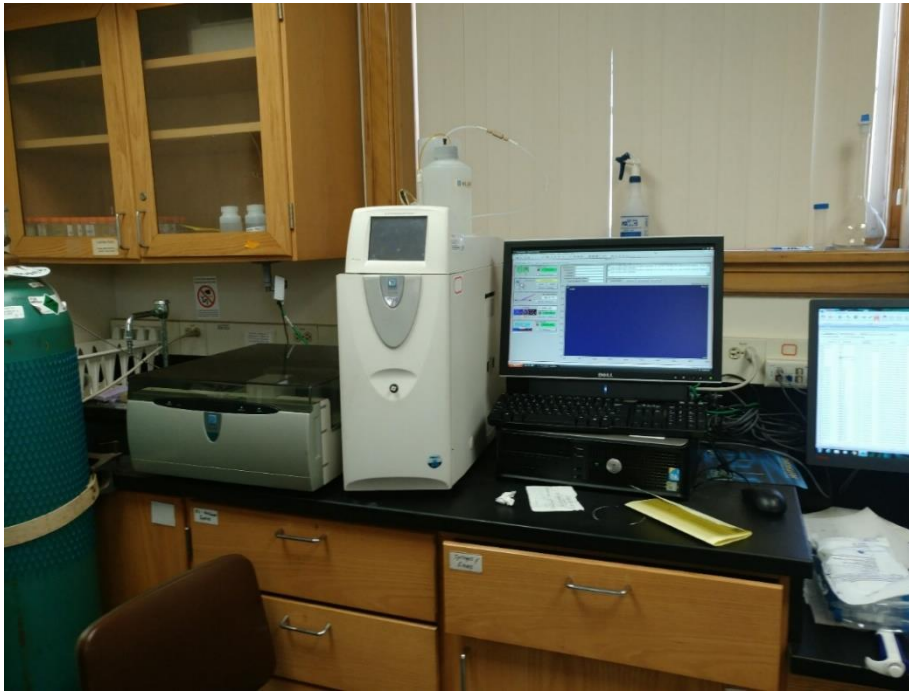


Figure 23: DIONEX 2100 Ion Chromatography System



Figure 24: Perkin Elmer NexION 350X Inductively Coupled Plasma Mass Spectrometer (ICP-MS).

2.4 Bacterial Removal

The efficiency of *E. coli* removal by the cyclodextrin based nanosponge was estimated by determining the concentration of *E. coli* (number of viable cells) in pre-filtrate (C_{PF}) and filtrate (C_F) suspensions and calculating the percent removal and log reduction values (LRV) from [Equations 26 and 27](#).

$$\% \text{Removal} = \frac{C_{PF} - C_F}{C_{PF}} \times 100 \quad 26$$

$$\text{LRV} = -\log_{10} \left(\frac{C_F}{C_{PF}} \right) \quad 27$$

Escherichia coli (C-3000 strain, ATCC 15597) was grown in nutrient broth at 37 °C for 24 hours in a shaker incubator (Model G25, New Brunswick Scientific, Edison, NJ) at 100 rpm to reach stationary growth phase. The stationary phase cultures were subsequently diluted 1:2 in deionised water to prepare 50 ml pre-filtrate suspensions containing approximately 10^6 to 10^7 colony-forming units per ml (cfu/ml). These were loaded into 60 ml plastic syringes and a syringe pump (Pump 33, Harvard Apparatus, Holliston, MA) was used to dispense the pre-filtrate *E. coli* suspensions at a feed rate of 50 ml/h via silicone tubing connected to the syringes into chromatography columns loaded at the bottom with 2 g of CDN and CDG sponges with a bed height of 9.4 cm. The number of viable cells in the pre-filtrate and filtrate suspensions were determined by serial dilution followed by the plating of 1 ml aliquots onto 3M Petrifilm *E. coli*/Coliform Count Plates (3M, St Paul, MN). The plates were counted after incubating them at 37 °C for 24 hours and the number of *E. coli* expressed in cfu/ml.

CHAPTER III
RESULTS AND DISCUSSION

CHAPTER III - RESULTS AND DISCUSSION

Chapter III presents the results obtained from this research: these include results of the synthesis and characterization of the goethite nanopowder and the four different nanosponges. The experimental results on adsorption for the batch and column studies, where the adsorptive removal and interactions of organic pollutant (methylene blue) and inorganic pollutants (nickel, fluoride and nitrates) with the nanosponges are described. The removal of *E. Coli* was also described. The chapter ends with overall conclusions of the work and propositions for future work.

3.1 Formation of CD and CD Functionalised Nanosponges

Anionic cyclodextrin functionalised nanosponges were obtained by ultrasound-assisted polycondensation polymerisation using native beta cyclodextrin as the cyclodextrin source, citric acid as cross linker, disodium phosphate as catalyst and, goethite and hydroxyapatite nanopowder for functionalisation. Four types of nanosponges were synthesised; the non-functionalised cyclodextrin nanosponge denoted CDN, goethite functionalised cyclodextrin nanosponge denoted CDG, hydroxyapatite functionalised cyclodextrin nanosponge denoted CDHA, and goethite/hydroxyapatite functionalised cyclodextrin nanosponge denoted CDGHA. The polymerisation reaction was carried out in two stages. The first stage involved the formation of low molecular weight pre-polymers by heating (at 110 °C) the cyclodextrin-cross linker-catalyst mixture to form a dry gel. In the second stage, the dry gel was mixed with bicarbonate and condensed to high molecular weight polymers by esterification reaction at high temperature (140 °C) and under vacuum; the vacuum is required to shift the reaction equilibrium to products[185], as seen in [Figure 25](#). The bicarbonate played two roles: to enhance the pore structures (as a porogen) and to activate the polymer surface by converting the carboxylic acid groups (-COOH) to carboxylates (-COO⁻Na⁺). Ducuroy et al and Euvrard et al [186, 187] have shown that activating the citric acid crosslinked cyclodextrin with bicarbonate enhances the ability of the nanosponge to react with charged ions through electrostatic interaction and ion exchange (chemisorption). The proposed mechanism for crosslinking of cyclodextrin with citric acid using disodium phosphate as catalyst is given in [Figure 26](#).

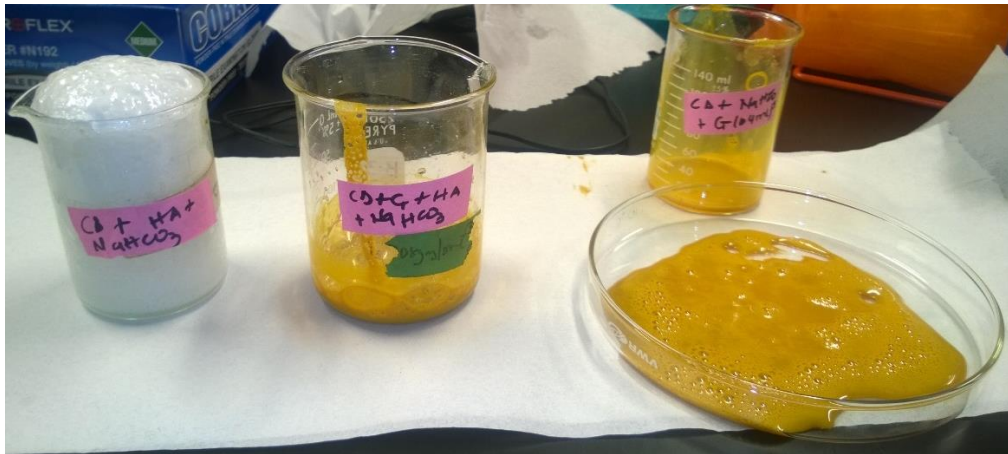


Figure 25: Polymer formation: adding of bicarbonate, goethite and/or hydroxyapatite to the dry gel

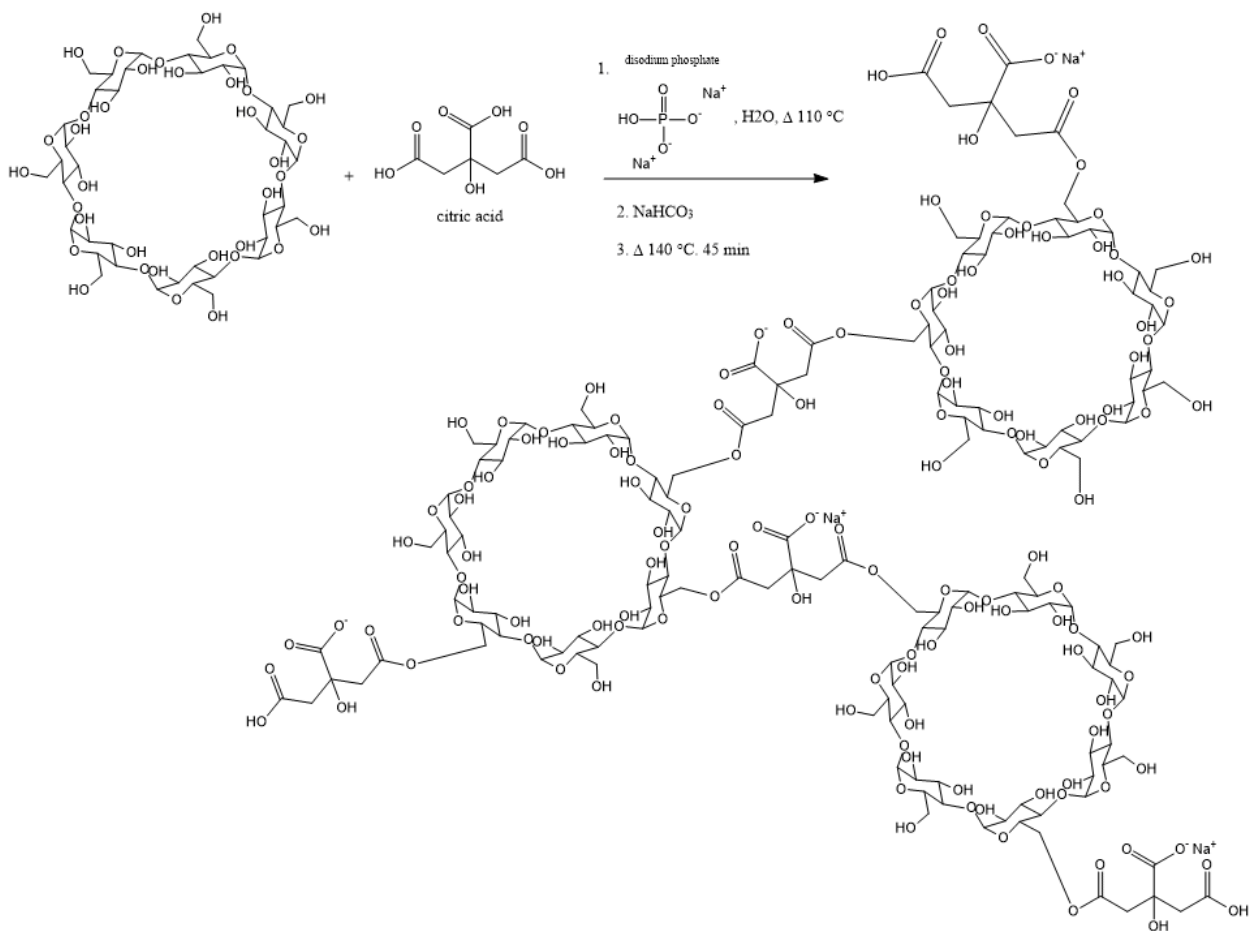


Figure 26: Proposed mechanism for crosslinking of cyclodextrin with citric acid using disodium phosphate as catalyst

The mechanism of crosslinking involves a nucleophilic attack of the carbonyl group of citric acid that converts the citric acid into a five membered cyclic anhydride intermediate which rapidly abstracts a proton from the –OH groups of the CD ring to yield an ester crosslink [85, 188, 189]. The citric acid readily esterifies the primary hydroxyls of β CD due to steric hindrance [190].

For goethite and/or hydroxyapatite grafting interactions, the –COOH of the tertiary carbon of citric acid reacts with –OH [99] of goethite and/or hydroxyapatite to form a hypothetical ester bond. Hence grafting of goethite and/or hydroxyapatite occurs as an additional crosslinking reaction, which may explain its more porous nature. The two-step process describing the proposed mechanism for the synthesis of CDG is given in **Figure 27**.

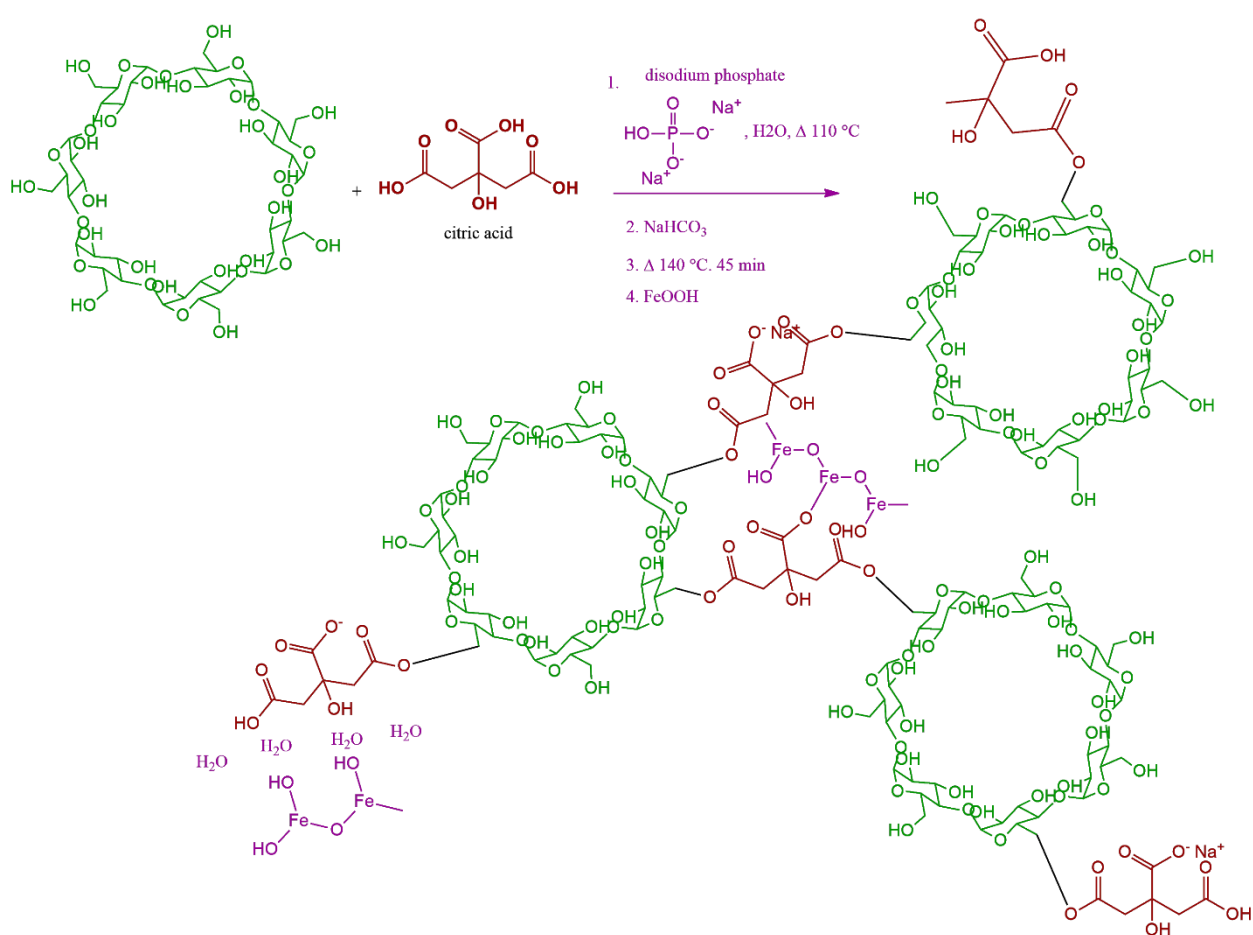


Figure 27: Proposed mechanism for the grafting of goethite onto crosslinked cyclodextrin (CDG)

3.2 Characterisation

3.2.1 Swelling test

The results from the swelling tests show that both adsorbents had high capacity to swell upon addition of water with CDN swelling up to 379.8 % times its weight $((2.399 \text{ g} - 0.5 \text{ g})/0.5 \text{ g})$, and CDG swelling 558.4 % times its initial weight $(3.292 \text{ g} - 0.5 \text{ g})/0.5 \text{ g}$. This is an indication of the hydrophilic nature of the three-dimensional polymer network.

3.2.2 Surface area analysis

The specific surface area of iron oxides is a function of the available sorption sites and influences their reactivity particularly interaction with sorbents. Goethite surface has structural and functional groups (FeO- and FeOH sites) which interact with gaseous and soluble species.

Figure 28 N₂-adsorption isotherm plot.

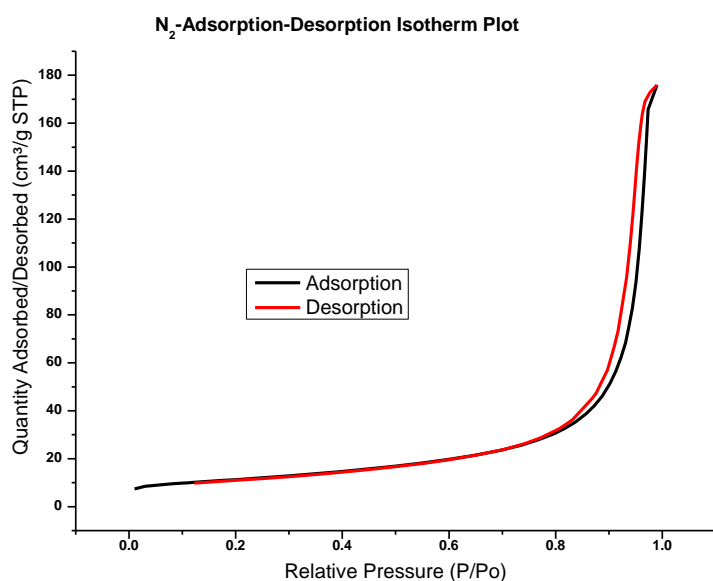


Figure 28: N₂-adsorption-desorption Isotherm plot for goethite nanopowder

The specific surface area of the goethite nanostructured powder was found to be 97.0173 m²/g. The average pore diameter calculated using the Barrett-Joyner-Halenda (BJH) method is approximately 2 nm, hence microporous. The N₂-adsorption isotherm plot is a type III isotherm and indicates weak adsorbent-adsorbate interaction and formation of a multilayer. A specific surface area of 6.291 m²/g, 7.340 m²/g, 7.085 m²/g and 7.500 m²/g were recorded for CDN, CDG, CDHA and CDGHA respectively.

CD polymers generally have low surface areas ($<10 \text{ m}^2/\text{g}$) which can be increased by loading of CD on high surface area carriers [191]. Because they trap pollutants through host-guest interactions or electrostatic interactions (as in the case of anionic CD polymeric nanosponges), the specific surface area is not a significant factor in the adsorption mechanism. Additionally, though goethite nanopowder has a higher surface area, $97.0173 \text{ m}^2/\text{g}$, the low surface area reported for CDG is due to the fact that the goethite is rather grafted on to the polymer chain.

3.2.3 FTIR

CD functionalization and inclusion complexation can be validated by the appearance of new peaks, shift in peak position or change in peak intensity as a result of changes on pure CD molecules. As shown in [Figure 29](#), functionalisation of CDN with goethite was carried out at varying conditions and FTIR analysis was used to monitor changes on the resultant material and also to determine the best synthetic route.

The changes observed in the FTIR spectra involve variations in the intensity of a band, band splitting and/or appearance of a new band. Overall, the CDG air dried sample show the highest intensity bands, indicating strong interactions. Major changes in the IR spectra were observed at 1020 and 1155 cm^{-1} . Both bands split into doublets for CDG air dried and CDG suspension. Hence using goethite as a powder or suspension in the synthesis did not change the properties of the resultant material. Though the band at 1155 cm^{-1} also splits for the freeze-dried sample, there is no corresponding split at 1020 cm^{-1} and the band corresponding to the carboxylate ion disappears. For CDG, CDG2 and CDG stirred samples, the band at 1155 cm^{-1} appears as a shoulder to the band at 1020 cm^{-1} , rather than a fully developed split band as is seen in CDG air dried and CDG suspension samples. Based on these observations, the cyclodextrin nanosponge was functionalised with goethite and/or hydroxyapatite through the CDG air dried route (as outlined in [Section 2.2.1.](#)), as this method presented a material that showed the highest interaction between the goethite nanopowder and the cyclodextrin nanosponge.

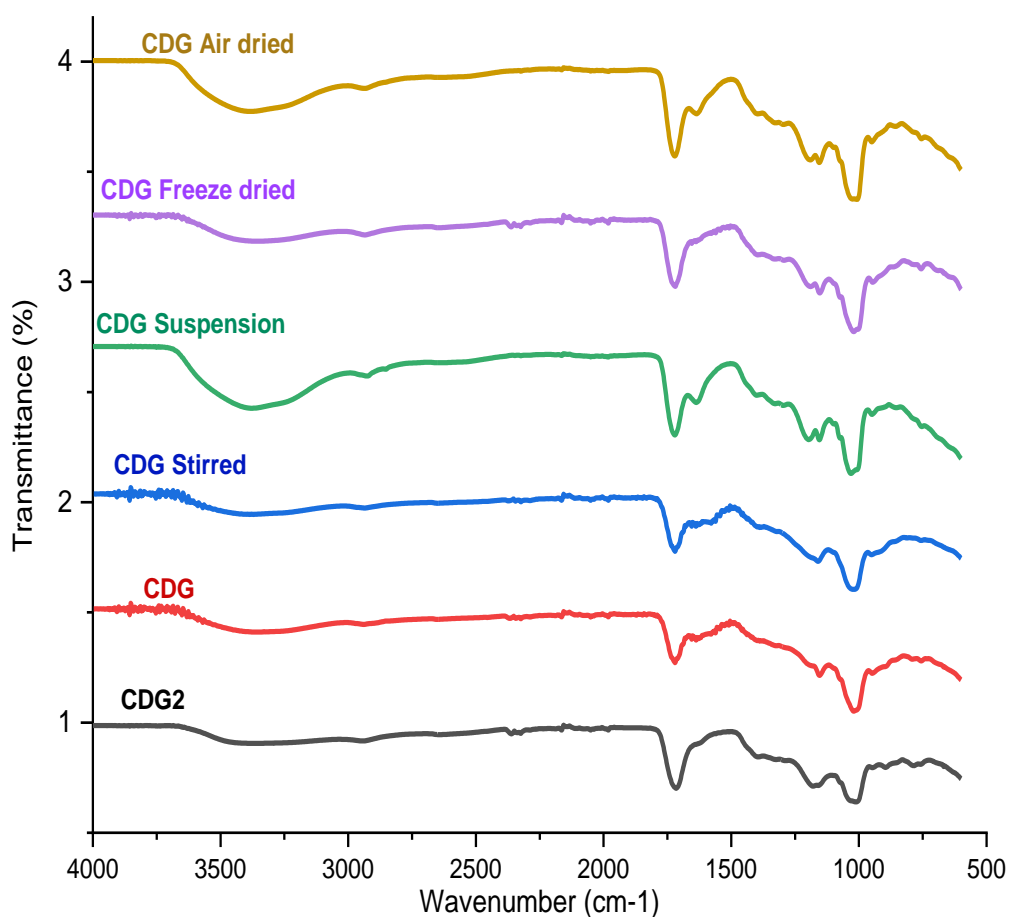


Figure 29: Functionalising CDN with goethite

The stacked plot for cyclodextrin, CDN, CDG and goethite is given in **Figure 29**. From the goethite nanopowder spectrum, the peaks around 3123 cm^{-1} and 1655 cm^{-1} could be attributed respectively to the O-H stretching of adsorbed water and the bending modes of the hydroxyl group on goethite. The sharp band at 1357 cm^{-1} corresponds to the antisymmetric stretching mode of NO_3^- . The bands at 892 cm^{-1} ($\delta\text{-OH}$) and 793 cm^{-1} ($\gamma\text{-OH}$) which are in-plane and out-of plane vibrations respectively can be assigned to the Fe-O-H bending vibrational modes of goethite [192]. The band at 628 cm^{-1} is due to stretching vibrations of the Fe-O bond, characteristic of the metal oxide [193].

The characteristic bands of CDN are: hydrogen bonded O-H stretch (3367.68 cm^{-1}), C-H symmetric stretch (2933.68 cm^{-1}), C=O stretch of ester (1720.47 cm^{-1}), COO- of carboxylate ion (1637 cm^{-1}), C-O-C antisymmetric glycosidic vibration [194] (1155.34 cm^{-1}), coupled C-C stretch/C-OH stretch (1020.33 cm^{-1}) of the cyclodextrin ring [61, 195, 196] and ester moiety, and ring vibration (948.96 cm^{-1}).

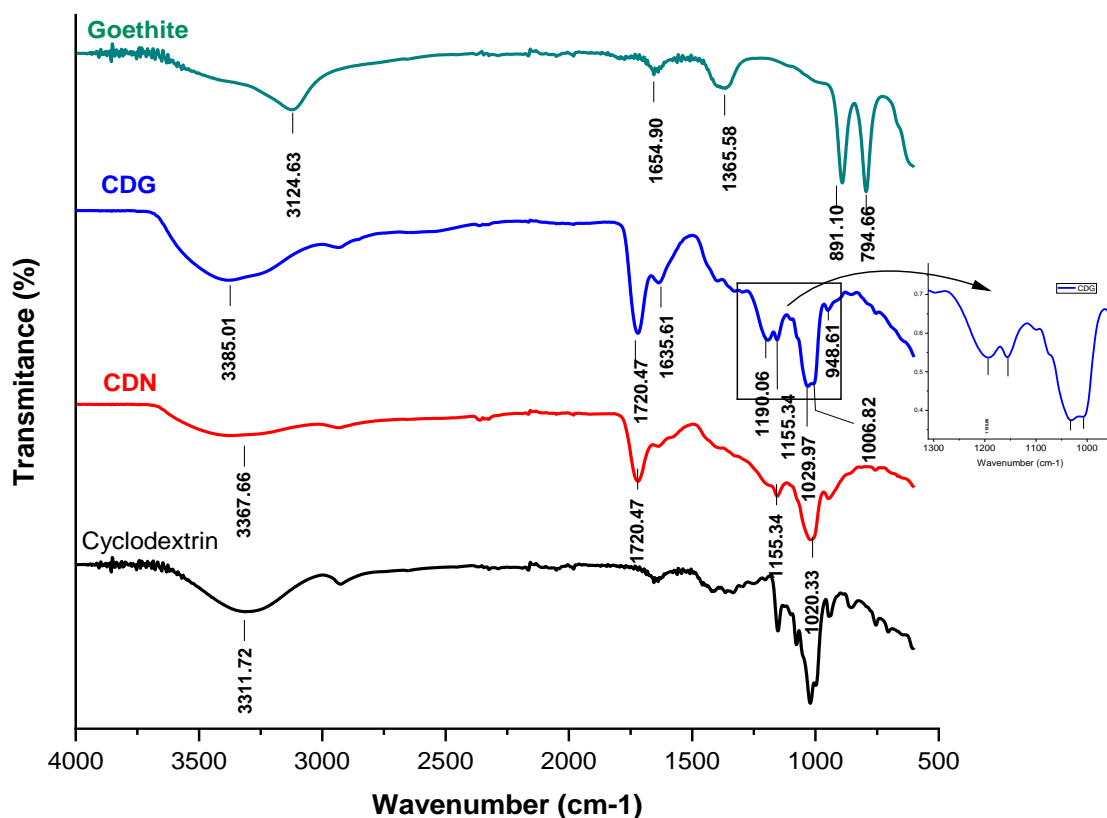


Figure 30: FTIR stacked plot for cyclodextrin, CDN, CDG and goethite

In the spectra of CDG, all the characteristic bands of the CD nanosponge are observed, indicating that the structural characteristics of the CDN polymer are maintained in CDG. The C=O stretch is more intense and shifts to a lower wavenumber (1716.62 cm^{-1}). The band at 1155.34 cm^{-1} splits into a broader more intense doublet with the appearance of a new band at 1190.06 cm^{-1} in CDG corresponding -C-O-Fe- stretch (increase in bond strength). The C-C/C-OH coupled stretch is slightly broader and splits into a doublet in CDG. The band at 1020.33 cm^{-1} is slightly shifted to 1029.97 cm^{-1} in CDG with the new split band appearing at 1006.82 cm^{-1} . This split differentiates the respective contributions of the carbonyl ester and the cyclodextrin ring on the -C-C/C-OH stretch respectively. These band-splitting confirm the grafting of goethite nanopowder onto the surface of the cross-linked cyclodextrin nanosponge by reaction with the free acid group on citrate crosslinks. Hence, goethite functionalisation occurs through a monodentate complex where goethite reacts with the lone carboxylate group to form an -O=C-O-Fe (ester-like) linkage (two new bands in IR), and an outer-sphere complex in the aqueous interface through hydrogen bonding (account for distinct goethite nanoparticles seen in TEM images of CDG). Shift of band to lower frequency/wavelength as a result of an

increase in the number of H-bond forming groups -COOH, -OH leads to a negatively charged or acidic surface at particular pH range attributed to deprotonation in solution.

The stacked plot for the synthesized nanosponges CDN, CDG, CDN and CDGHA is given in **Figure 31**. All the characteristic bands of the CD nanosponge are observed in the spectra of CDHA, indicating that the structural characteristics of the CDN polymer are maintained in CDHA.

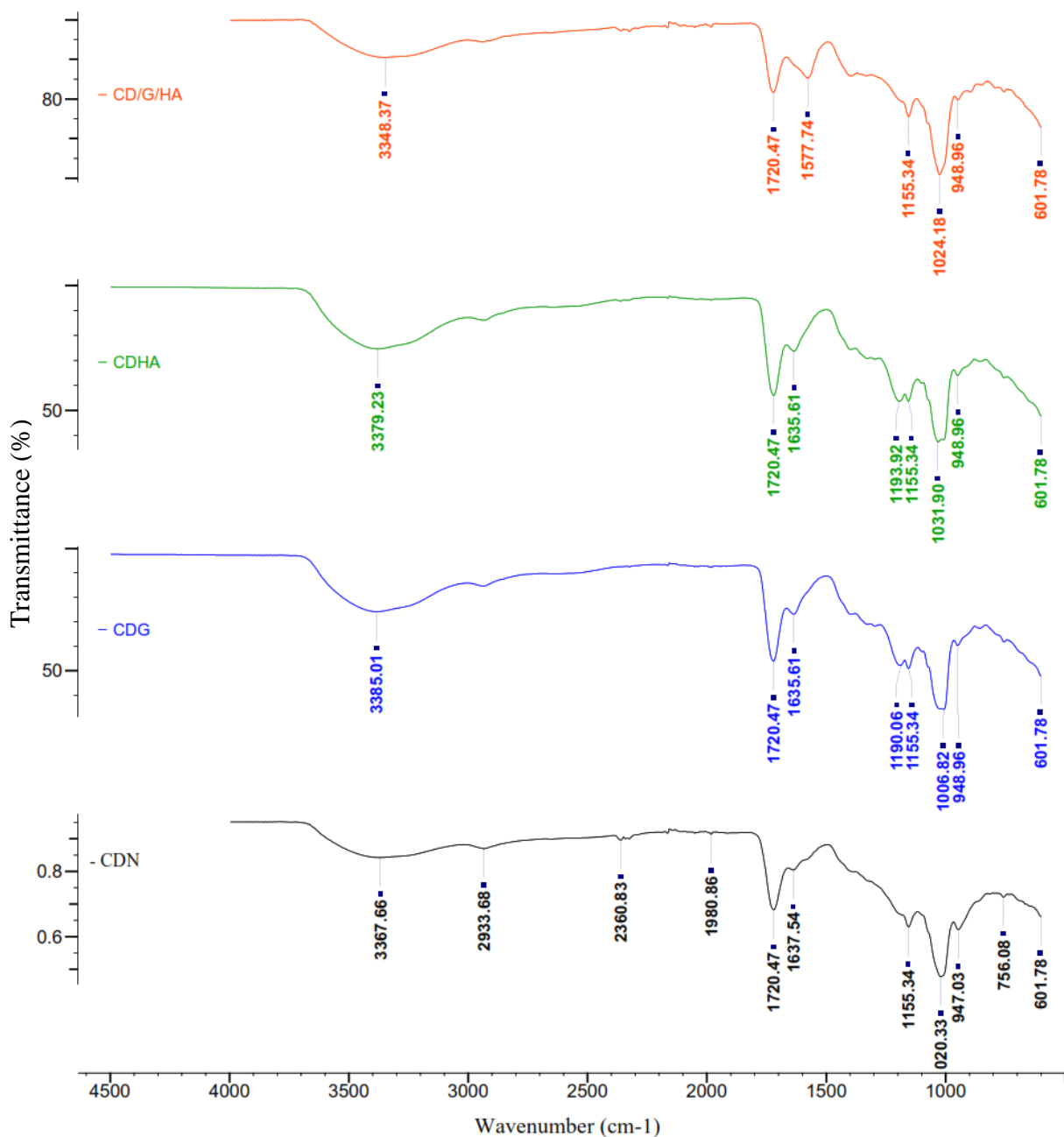


Figure 31: FTIR stacked plot for CDN, CDG, CDN and CDGHA

The band at 1155.34 cm^{-1} splits into a broader more intense doublet with the appearance of a new band at 1193.92 cm^{-1} in CDHA corresponding -C-O-P- aromatic stretch (increase in bond strength). The C-C/C-OH coupled stretch is slightly broader and splits into a doublet in CDHA. The band at 1020.33 cm^{-1} is slightly shifted to 1031.90 cm^{-1} in CDHA with the new split band appearing at 1001.90 cm^{-1} . This could indicate an interaction between the ν_3 P-O stretch and the coupled C-C stretch/C-OH stretch of the cyclodextrin ring. The PO_4^{3-} group generally has a characteristic triple degenerate absorption peak and these can be usually seen in the range $450\text{-}1100\text{ cm}^{-1}$. The band at 601.78 can be attributed to the ν_4 O-P-O bending vibration [119].

These band-splitting confirms the grafting of hydroxyapatite onto the surface of the cross-linked cyclodextrin nanosponge by reaction with the free acid group on citrate crosslinks. Hence, it can also be assumed that hydroxyapatite functionalisation also occurs through a monodentate complex where it reacts with the lone carboxylate group to form an -O=C-O-P- (ester-like) linkage (two new bands in IR), and an outer-sphere complex in the aqueous interface through hydrogen bonding (account for distinct hydroxyapatite nanoparticles seen in TEM images of CDHA). **Figure 32** shows the overlaid spectra of CDG and CDHA.

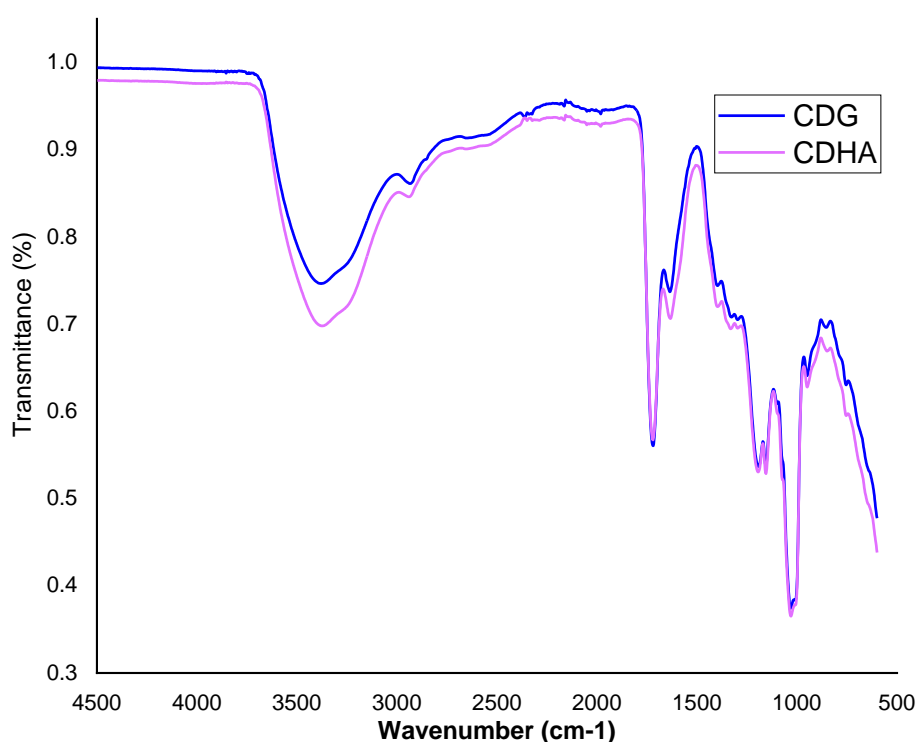


Figure 32: Overlaid spectra of CDG and CDHA

The spectra show more similarities in the major peak position and shapes. The CDHA spectrum has higher intensity vibrations for the hydrogen bonded O-H stretch.

3.2.4 XRD

The powder diffraction pattern of the goethite nanopowder is shown in **Figure 33**. The position of the diffraction peaks matches well with standard FeOOH patterns with characteristic peaks at $2\theta = 20.80^\circ, 24.74^\circ, 30.81^\circ, 38.84^\circ, 40.59^\circ, 42.83^\circ, 46.87^\circ, 48.25^\circ, 59.50^\circ$ and 62.64° corresponding to (020), (110), (120), (130), (120), (111), (121), (140), (151), (171) respectively. The peaks at $2\theta = 34.22^\circ$ and 45.66° correspond to sodium nitrate.

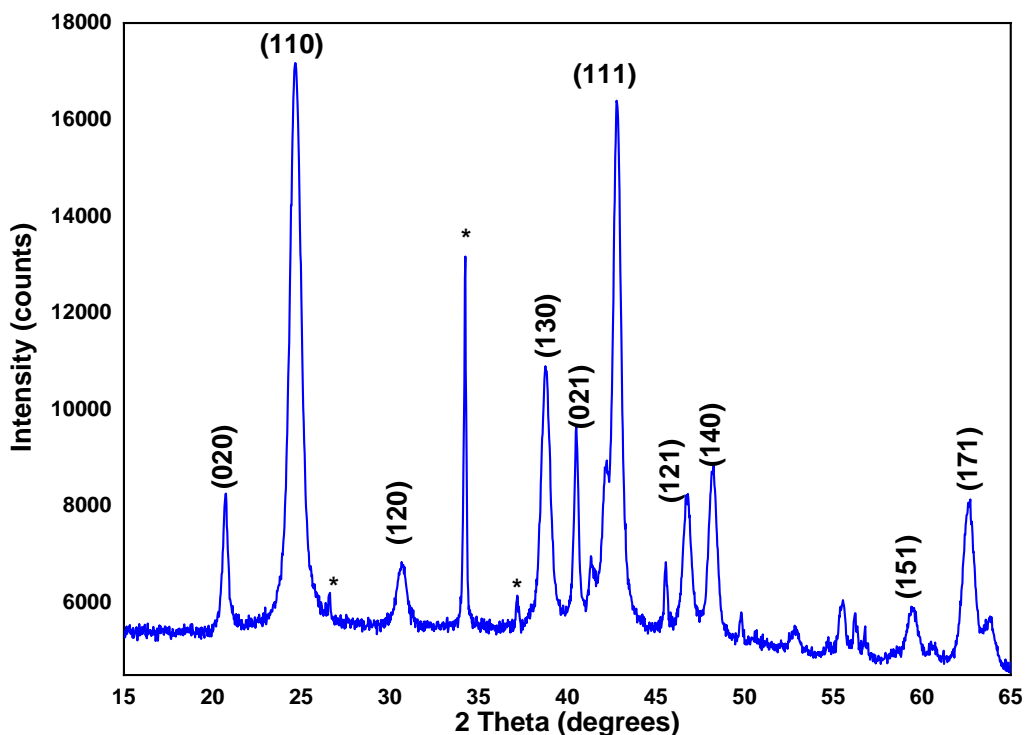


Figure 33: XRD Spectra of Goethite Nanopowder

Since a line broadening corresponds to a decrease of the coherence length in the goethite particles, the observed line broadening in the (111) peak suggests a kinetics effect, which tends to modify the crystallinity and/or the crystal size. Furthermore, the small signal-to-noise ratio of the goethite pattern is also more likely due to the decrease of crystallinity and/or crystal size. The composition and lattice parameters of all the components in goethite nanopowder sample is given in **Table VIII**. Reference file calculated from ICSD using PowD-12++(1997) [197].

Table VIII: Phase Composition and Lattice Parameters

Sample	Lattice	Lattice parameters			Space group	ICSD code
		A	b	c		
Goethite	Orthorhombic	4.60480	9.95950	3.02300	Pbnm	033692
Goethite Sodium nitrate	Rhombohedral	5.07010	5.07010	16.32902	R-3c	078801

Phase identification reveals the presence of two phases, goethite (99.24%) and sodium nitrate (ICSD collecting code: 071809). The presence sodium nitrate implies washing was incomplete (see [Figure 34](#)).

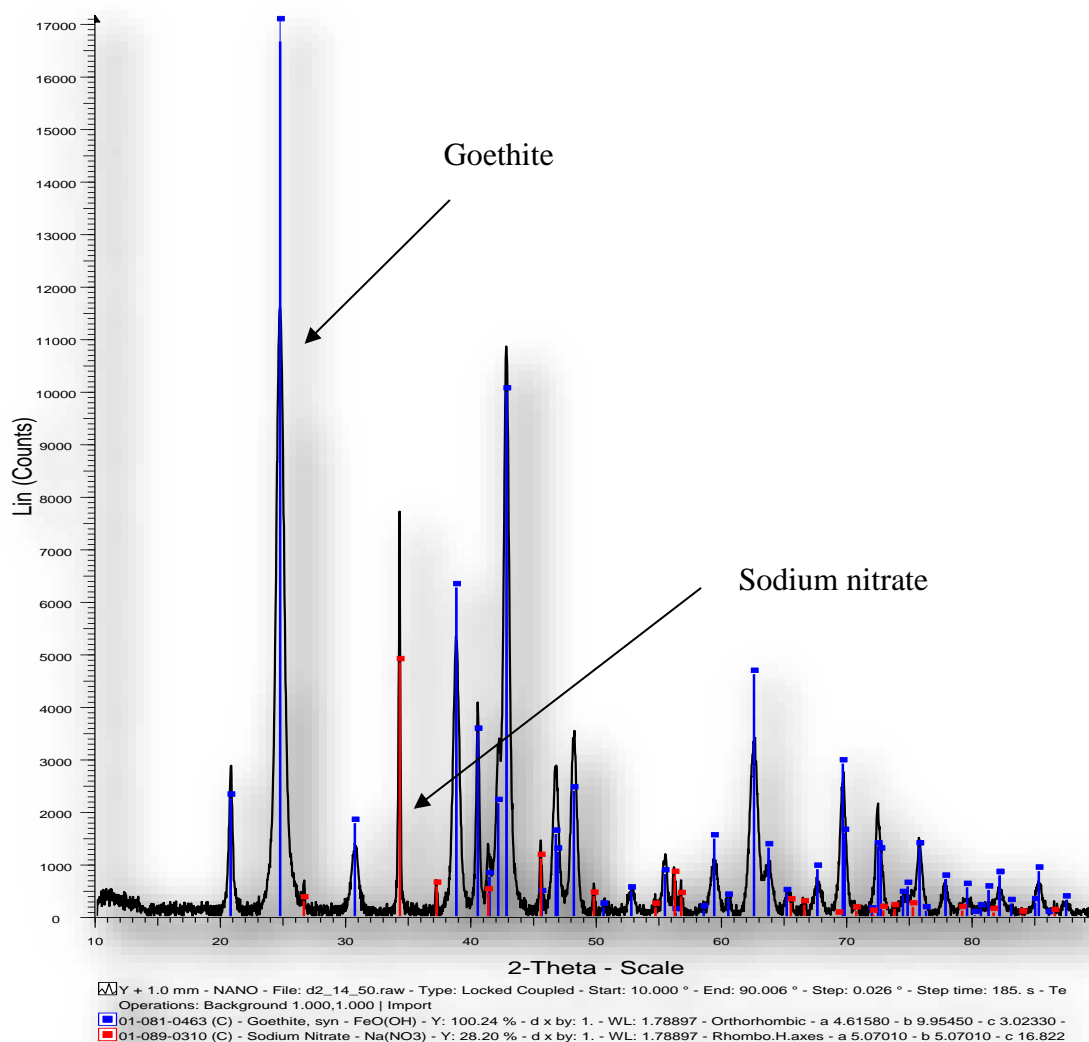


Figure 34: Whole pattern fitted PXRD spectra of goethite nanopowder

The combined powder XRD patterns of the as prepared sponges and goethite nanopowder are shown in [Figure 35](#). Typically, cyclodextrin, goethite and hydroxyapatite are crystalline powders and though the powder patterns of the as-prepared nanosponges show that these materials are not purely crystalline, the patterns however indicate that some of their crystallinity is retained in the sponges. The powder spectrum of CDN shows the material is amorphous (broad peak). During crosslinking of cyclodextrin, citric acid forms strong covalent bonds that links up the CD units. This alters the ordered nature of the cyclodextrin units to a distorted amorphous structure [198]. The CDG spectrum exhibit both the amorphous

nature (halo at $2\theta = 13^\circ - 21^\circ$) and some long-range order with weak and less intense peaks at $2\theta = 22.75^\circ, 36.63^\circ, 39.96^\circ, 47.96^\circ, 59.09^\circ$ whose values respectively correspond to the (110), (130), (120), (140), (151), (171) planes of goethite. This indicate that the goethite nanoparticles retain a discrete phase in the material (as seen in the TEM micrograph) and that CDG is nanocrystalline. A similar trend was observed by Kung and Wilson [199] for cellulose-goethite composites.

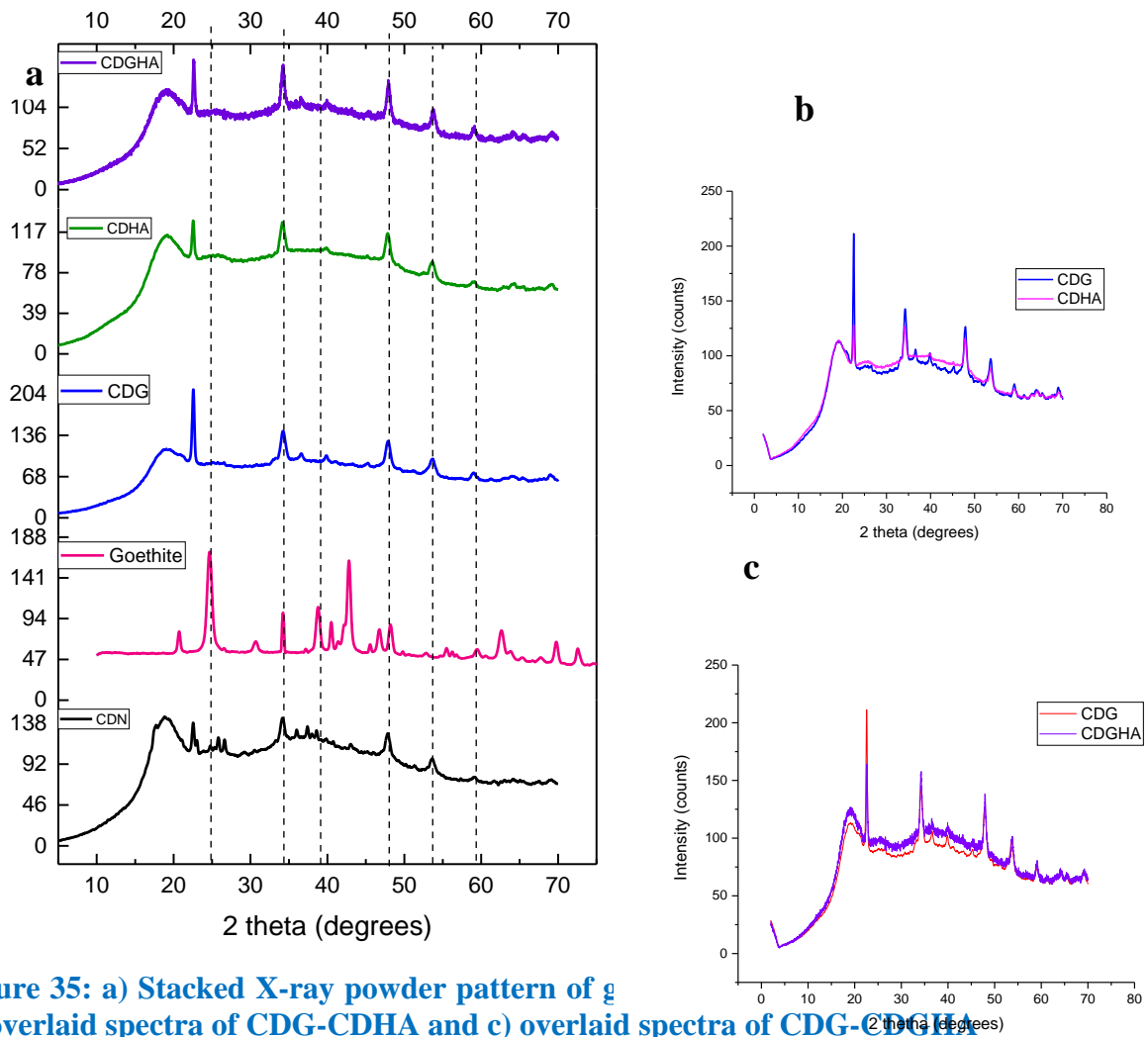


Figure 35: a) Stacked X-ray powder pattern of g b) overlaid spectra of CDG-CDHA and c) overlaid spectra of CDG-CDGHA

A non-systematic peak shift to lower 2θ values (larger d-spacing) is observed in the CDG spectrum. This shift indicates that functionalisation of crosslinked cyclodextrin with goethite increases in unit cell dimensions of the resulting CDG entity [61, 200].

The powder pattern of the CDHA nanosponge show a similar trend of peaks shifting to lower 2θ values. When compared to the standard XRD peaks of hydroxyapatite (based on ICDD 9–432) [200], the peaks appearing at $2\theta = 22.51^\circ, 34.30^\circ, 47.88^\circ, 59.07^\circ$ can be attributed

respectively to the (002), (211), (213), (004) planes of hydroxyapatite. Hence, it can be concluded that CDN functionalisation with either goethite or HA results to a material with two distinct phases, an amorphous CD and a crystalline goethite or HA phase.

3.2.5 Pair Distribution Function Analysis

3.2.5.1 Overall structural information

The overall structural information is extracted by visual inspections of PDFs. Samples are expected to be cyclodextrin network linked by citric acid and thus the PDFs should contain strong peaks in the low- r region generated by the intra-molecule atomic pairs and relatively weak peaks in high- r region coming from inter-molecule atomic pairs and mediate- r region contains both signals. Since glucose molecule is flexible in cyclodextrin, the peaks in high- r region should be broader and much weaker than those in low- r region because the random position and orientation of glucose enlarge the deviation of intermolecule atomic pair distance and thus weaken their positional correlation while has little effect the intra-molecule pair distance. If the molecules randomly distribute in network without periodic structure, there is large uncertainty in distance between the atoms in separated molecules and thus only decaying wave-like signal appears in high- r region PDF, revealing the density modulation of molecules. On the other hand, if the molecules form certain degree of crystalline structure, there should be sharp peaks in mediate and high- r region due to the strong positional correlation from periodicity.

The samples do show the feature of cyclodextrin network linked by citric acid, as shown in **Figure 36**, with strong sharp peaks in low- r region and weak broader peaks in mediate and high- r region. The difference is that the sample CD and CDHA shows the feature of polymer cyclodextrin, since there is only noise and density modulation after the 13 Å in their PDFs, while the CDG and CDGHA show the feature of crystallinity that there is signal even after 13 Å, which is approximately the largest the atomic distance in cyclodextrin.

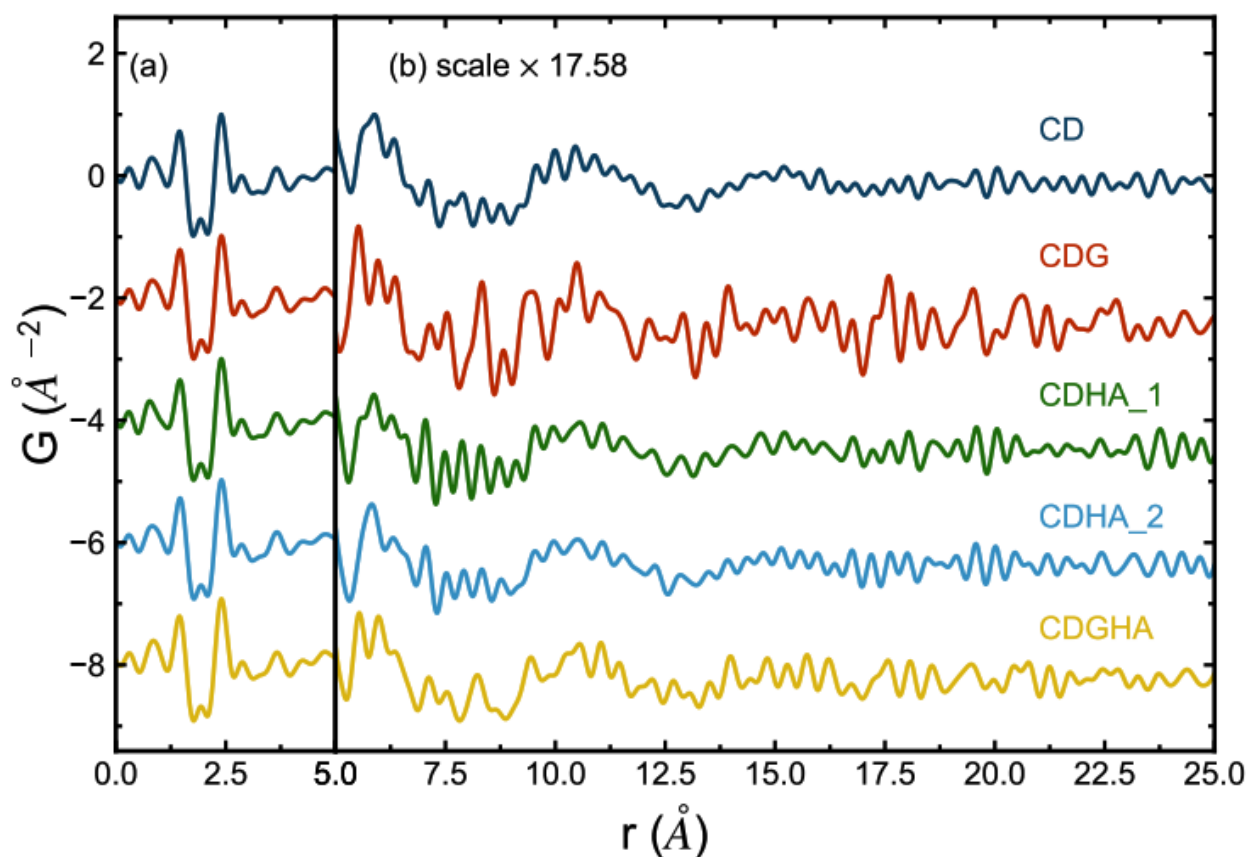


Figure 36: PDFs obtained from synchrotron x-ray powder diffraction: (a) PDFs in low- r region; (b) PDFs in high- r region, they are multiplied by the same scale for better visual inspection. All data is normalized for comparison.

The feature could originate from the crystalline goethite or crystalline cyclodextrin. To test the origin of it, the PDF of CDG is compared with PDFs simulated from goethite and cyclodextrin crystal structure in [Figure 37](#). The PDF of CDG is similar to that of goethite indicating that there is crystalline goethite mixed with the cyclodextrin network in the CDG sample. CDGHA is supposed to be a mixture of the phase of CDHA and the phase of CDG. It is motivated by the fact that the PDF of CDGHA can be well fit by a linear combination of PDFs of CDHA and CDG, as shown in [Figure 38](#). The scales of PDFs of CDHA and CDG are 0.51 and 0.46. Assuming the average atom density of CDHA and CDG is similar, the ratio of PDF scale is approximately equal to the ratio of their molar fraction and thus it is estimated that CDGHA contains 52% CDHA phase and 48% CDG phase.

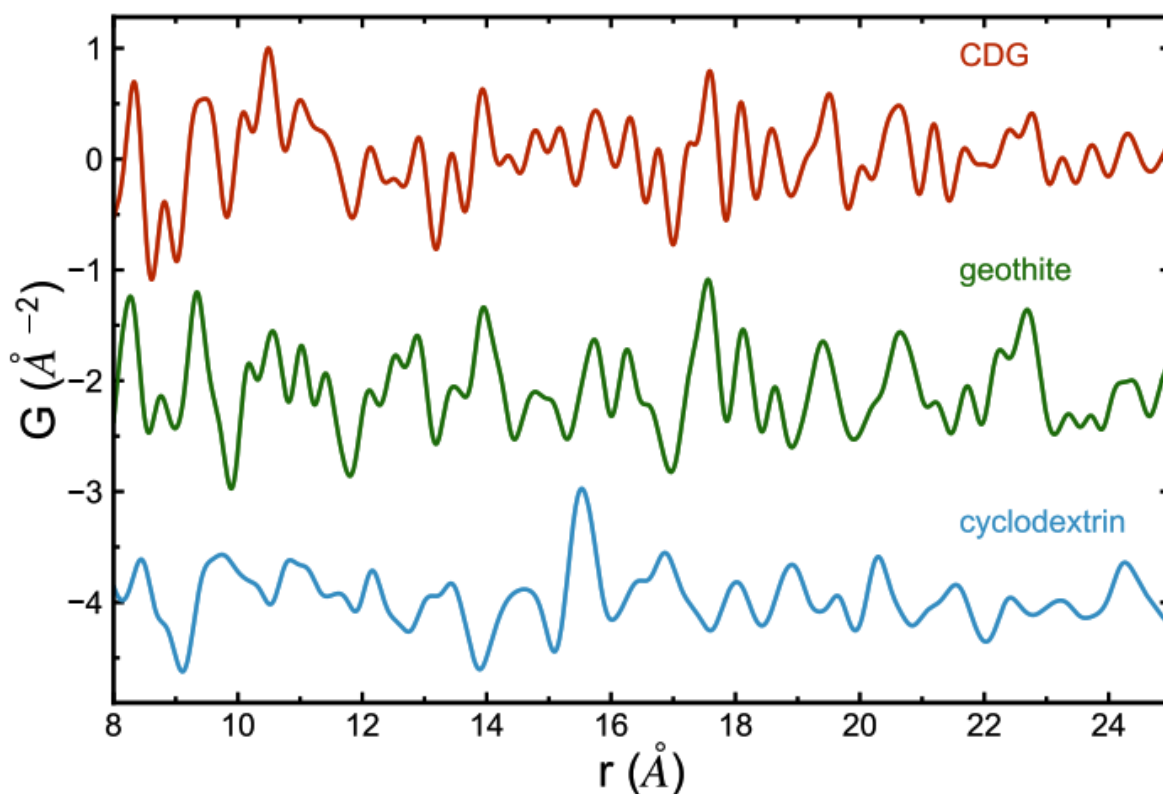


Figure 37: (top) Measured PDF of CDG and simulated PDFs of crystalline (middle) geothite and (bottom) cyclodextrin. The simulation is based on real space calculation of PDF and the parameters used are $U_{\text{iso}} = 0.008 \text{ \AA}^2$, $Q_{\text{max}} = 16.0 \text{ \AA}^{-1}$. PDFs are normalized for comparison

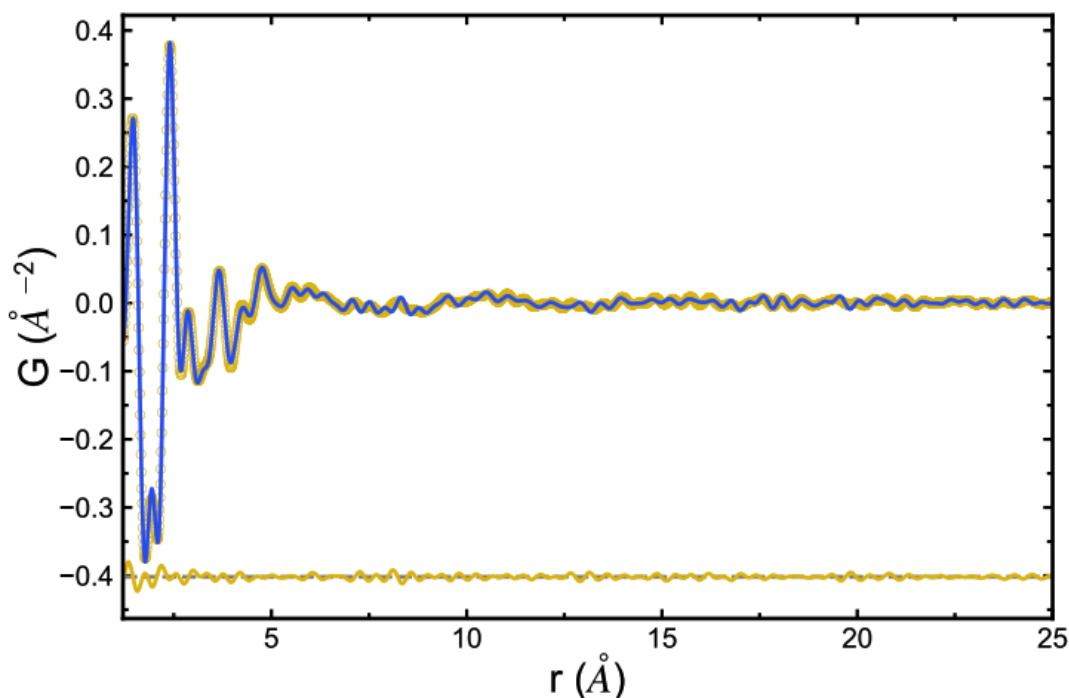


Figure 38: PDF of CDGHA fitted by a linear combination of PDFs of CDG and CDHA. The yellow dots are the PDF data of CDGHA, blue line is the calculated PDF in best fit and yellow line is the residual.

3.2.5.2 Comparison between structures

Difference between structures could be revealed by comparing the PDFs. Since all samples are synthesized mainly by cyclodextrin and citric acid, the local structure is similar for all samples and thus the low- r region should look similar with major peak at 1.4 Å and 2.4 Å, which are the nearest and second nearest distance of carbon-carbon or carbon-oxygen pair in cyclodextrin and citric acid. As evident in **Figure 39**, this is exactly what we see. Also, the short-range order in structure, which is spacing of neighbour glucose and glucose connected by citric acid inside networks, is similar for all samples despite their difference in crystallization. It is shown by the similar wave shape signal of PDF in mediate and high- r region. CD and CDHA have quite similar cyclodextrin network according to their similarity in PDF while CDG and CDGHA also have cyclodextrin network but contains crystalline goethite.

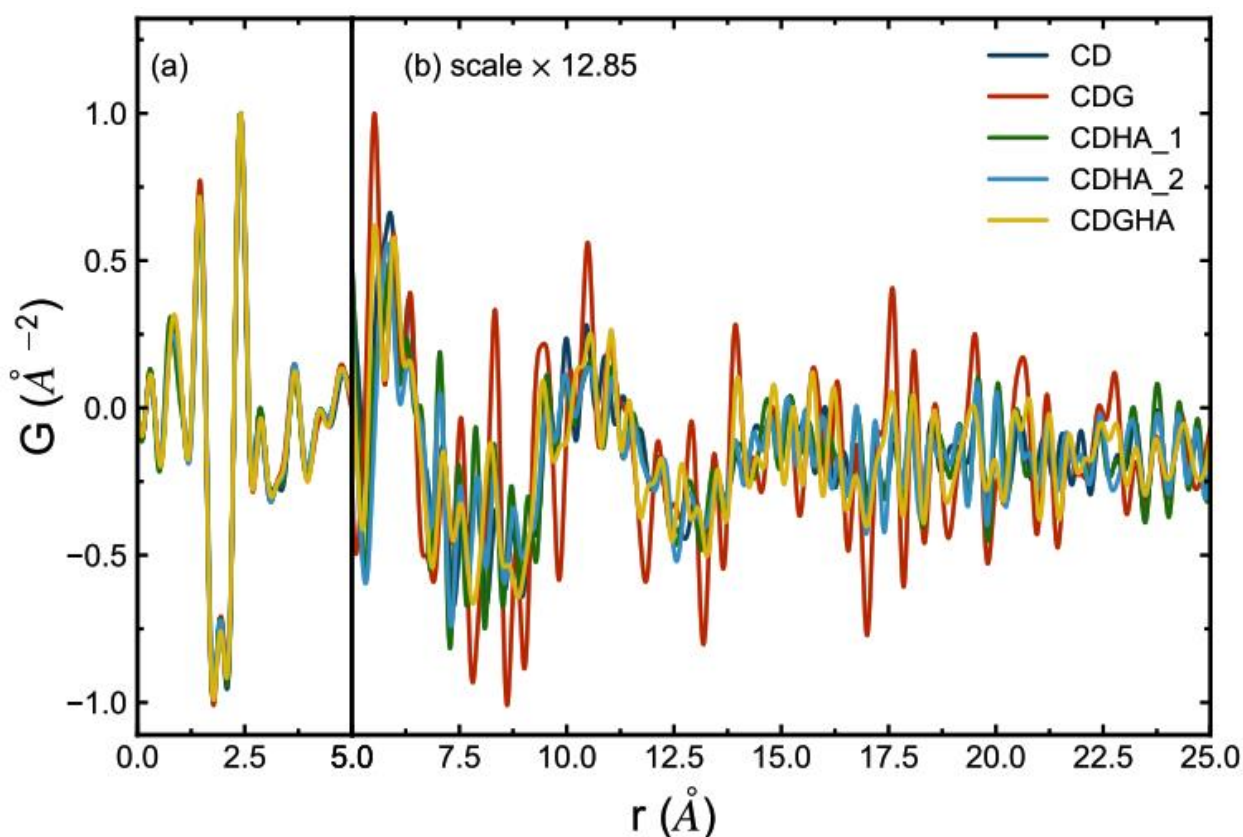


Figure 39: Comparison between PDFs: (a) PDFs in low- r region; (b) PDFs in high- r region, they are multiplied by the same scale for better visual inspection. All data is normalized for comparison.

3.2.5.3 Local structures

Structure model is used to extract average local structure from PDFs. The model is a linear combination of PDFs from isolated cyclodextrin molecule and isolated citric acid molecule (with three ionized hydrogens removed) and an analytic function simulating the density modulation from inter-molecule atomic pairs. An example of the fit is demonstrated in **Figure 40**. This model explains the main features of the average local structure with residual R_w around 0.15 ~ 0.18, as shown in **Figure 41**, probably because the flexibility of specific bonds and deformation of cyclodextrin are excluded in fitting.

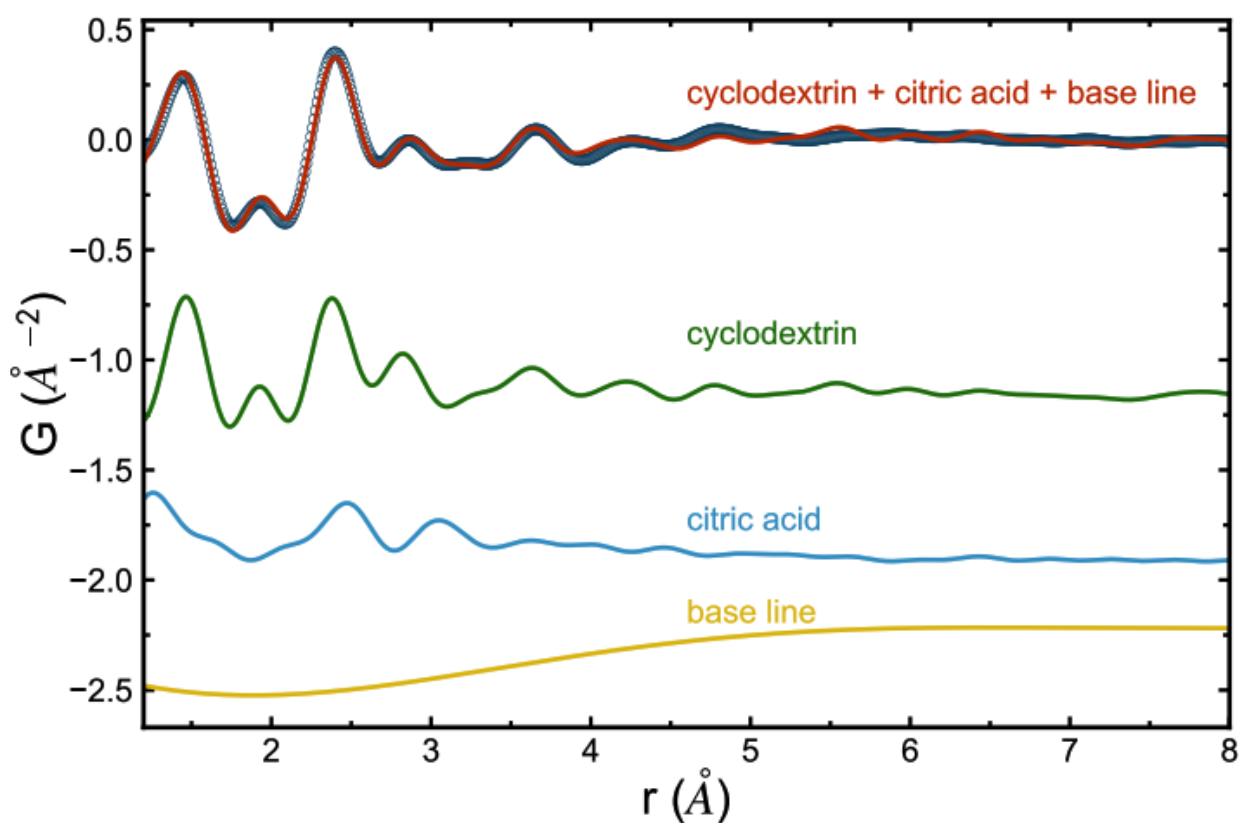


Figure 40: PDF of CD fitted by a linear combination of PDFs from isolated molecule and base line from density modulation. The blue dots are PDF data of CD and the red line is calculated PDF from the best fit to the data. The green line, sky blue line and yellow line show the contribution to the calculated PDF from cyclodextrin, citric acid and base line respectively.

The atoms in molecule are usually more flexible in position than those in crystal, which means larger deviation of atomic pair distance and faster decaying correlation with increasing distance, and thus the fitting should show atomic displacement parameter (ADP) and larger δ value than those in crystal. Indeed, the result confirms this feature of flexible atoms in molecule. This flexibility is especially obvious in cyclodextrin, which is formed by small

glucose linked in a circle. The atomic bonding allows random shift and tilt of glucose, causing deformation of the molecule and thus leading to larger ADP than that in small molecule like citric acid, which is confirmed in [Table IX](#). The value of delta is also larger since the inter-glucose atoms distance is less rigid and thus the correlation decays fast when atomic distance is larger than the size of glucose, as shown in [Table IX](#).

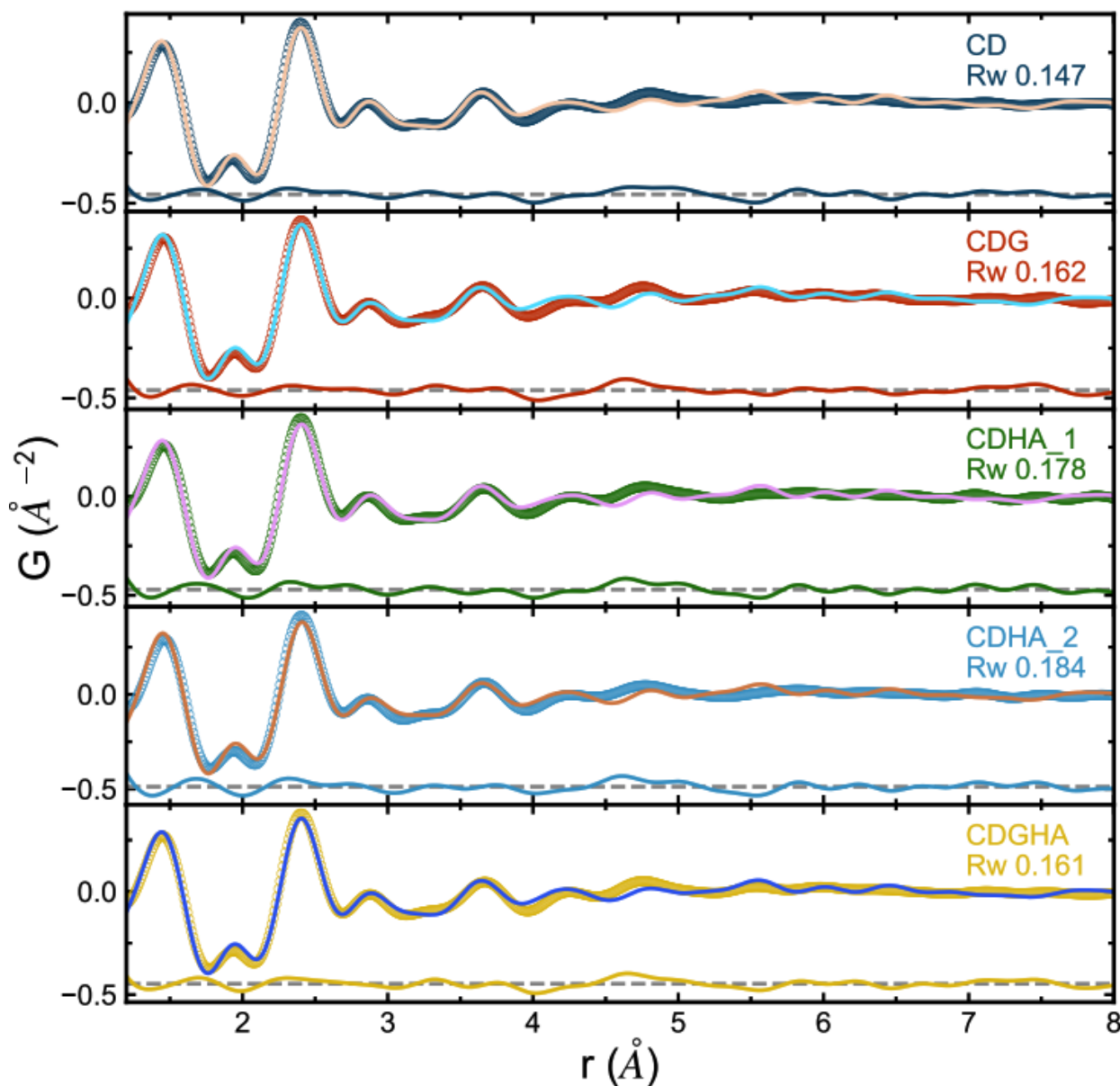


Figure 41: PDFs fitted by the structure model. The dots are data from measurement, the overlapping lines are the calculation of PDF from the best fit and the lines with same colour as the data dots are the residuals. The “Rw” is a metric for the goodness of fit.

How many citric acids are linked to one cyclodextrin on average sense may be indicated by the scale of cyclodextrin and citric acid in [Table II](#). The molar fraction of citric acid is calculated according to [Equation 28](#).

$$\frac{x_{CA}}{x_{CD}} = \frac{X_{CA}/(\sum_i^{n_{CA}} c_i^{CA} b_i^{CA})^2}{X_{CD}/(\sum_i^{n_{CD}} c_i^{CD} b_i^{CD})^2}$$

28

where x is the molar fraction, X is the scale of PDF, n is the number of atom species, c_i is the proportion of atom species i and b_i is the scattering factor of atom species i and index “CA” and “CD” mean citric acid and cyclodextrin. The average number of linked citric acid to cyclodextrin is two times the molar fraction since one citric acid is shared by two cyclodextrins.

Table IX: Fitting result

	CD	CDG	CDHA-1	CDHA-2	CDGHA
CA_Uiso_C(Å ²)	0.075	0.097	0.093	0.094	0.089
CA_Uiso_H(Å ²)	1.052	1.052	1.052	1.052	1.052
CA_Uiso_O(Å ²)	0.087	0.118	0.108	0.114	0.105
CA_delta2(Å ²)	1.537	1.548	1.534	1.559	1.546
CA_scale	0.073	0.063	0.071	0.066	0.070
CA_zoom	0.016	1.014	1.011	1.018	1.014
CA_Uiso_C(Å ²)	5.839	5.836	5.839	5.838	5.840
CA_Uiso_H(Å ²)	14.399	14.400	14.400	14.400	14.400
CA_Uiso_O(Å ²)	5.851	5.850	5.850	5.850	5.846
CA_delta2(Å ²)	7.87.	7.716	7.835	7.752	7.779
CA_scale	0.050	0.053	0.050	0.055	0.049
CA_zoom	1.000	1.002	1.002	1.003	1.000
CA:CD	1.7	1.4	1.6	1.4	1.7

“CA” and “CD” are the abbreviation of “citric acid” and “cyclodextrin” respectively. The “Uiso_C”, “Uiso_O” and “Uiso_H” mean the isotropic atomic displacement parameter of carbon, oxygen and hydrogen respectively with unit Å². “delta2” is the parameter of quadratic broadening of peak width due to correlation motion of atoms with the unit Å². “scale” is the scaling factor of the PDF. “zoom” is the isotropic expansion or compression of molecule size. “CA:CD” is the molar ratio of citric acid and cyclodextrin estimated from the “CA CD”, “CD scale” and their composition.

There is about 1.4 ~1.7 citric acid linked with one cyclodextrin. This is close to, but a little lower than the expected 2 citric acids per cyclodextrin. It could indicate some dextrose in the sample that is not included in the network, or perhaps simply that all citric acid sites are not

saturated on the network. This is also a rather approximate number from the fitting and should be verified by other means.

3.2.5.4 Cyclodextrin network

Since there is a deformation of cyclodextrin molecule, the density modulation could come from the short-range order of cyclodextrin network or just the weak correlation of glucose inside cyclodextrin. To reveal the origin of density modulation and motivate the existence of cyclodextrin network, PDFs of crystal cyclodextrin is calculated using a large ADP and attenuated by a Gaussian envelope to simulate the density modulation in cyclodextrin network. The large ADP simulate the large uncertainty in positions while the attenuation mimics the decaying in correlation in cyclodextrin network. The PDF of single cyclodextrin is also calculated using same ADP for comparison. The results are shown in **Figure 42**. If density modulation wave signal originates from the short-range order of cyclodextrin in network, the PDF of samples should be more alike the PDF of simulated network instead of single cyclodextrin molecule. Comparison shows that there is cyclodextrin network in samples and its short-range order manifests itself in the density modulation wave in PDFs.

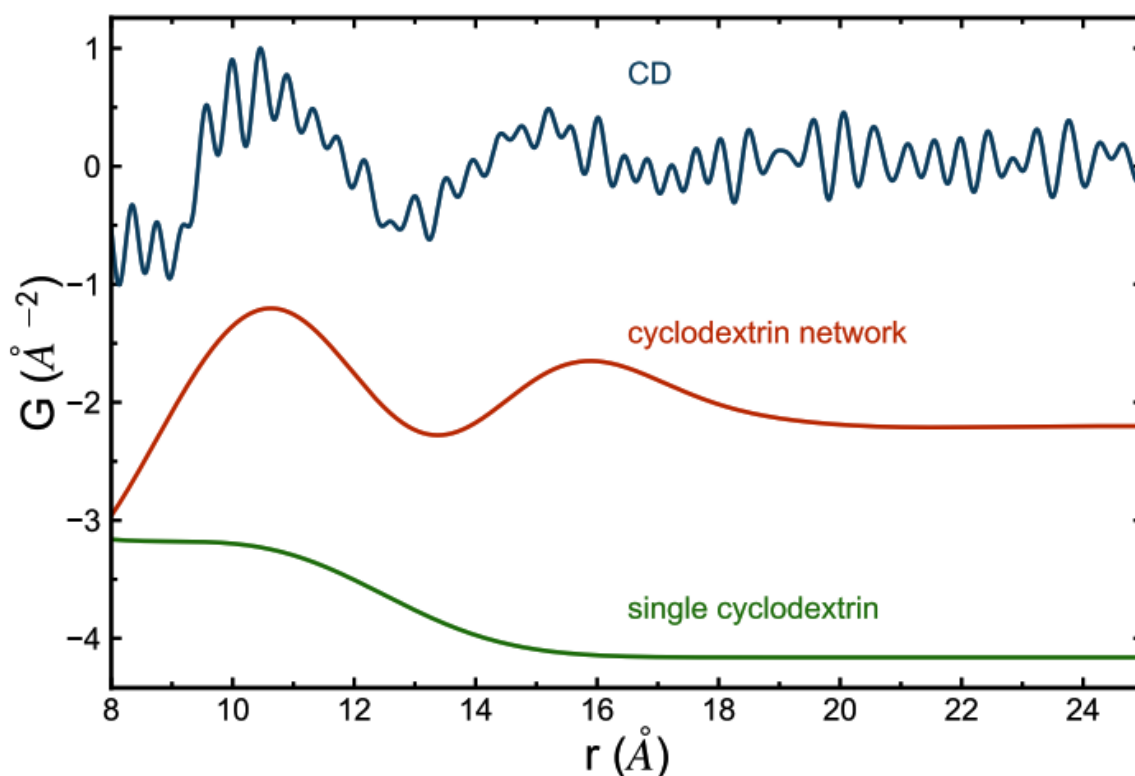


Figure 42: Comparison between measured PDF of CD (blue), calculated PDF of crystal cyclodextrin (red) with $U_{\text{iso}} = 1 \text{ \AA}^2$, and calculated PDF of single cyclodextrin molecule (green) with $U_{\text{iso}} = 1 \text{ \AA}^2$. The calculated PDF of crystal cyclodextrin is attenuated by a Gaussian envelope to simulate the decaying of correlation in polymer network.

Thus, from the PDF analysis, the structure of all samples is mainly formed by network of cyclodextrin linked by citric acid while CDG and CDGHA contains crystalline goethite. Local structure of all samples is similar. The atomic bonding of goethite, hydroxyapatite with other molecules in network is not obvious in PDFs. The density modulation is similar in all samples, which means that the average spacing of molecules inside all samples are almost the same so the spacing of molecules in network is not changed by adding the goethite and hydroxyapatite. The local structure of samples can be approximately described by single molecule structure of cyclodextrin and citric acid with density modulation. The cyclodextrin shows large flexibility in the position of glucose subunit and probably is randomly deformed in network.

3.2.5 Thermal analysis

The thermal behaviour such as weight loss, composition, decomposition and residual car level was studied using TGA/DTG methods. **Figure 43** shows the TGA curves of CDN, CDG, CDHA and CDGHA showing mass loss as a function of temperature.

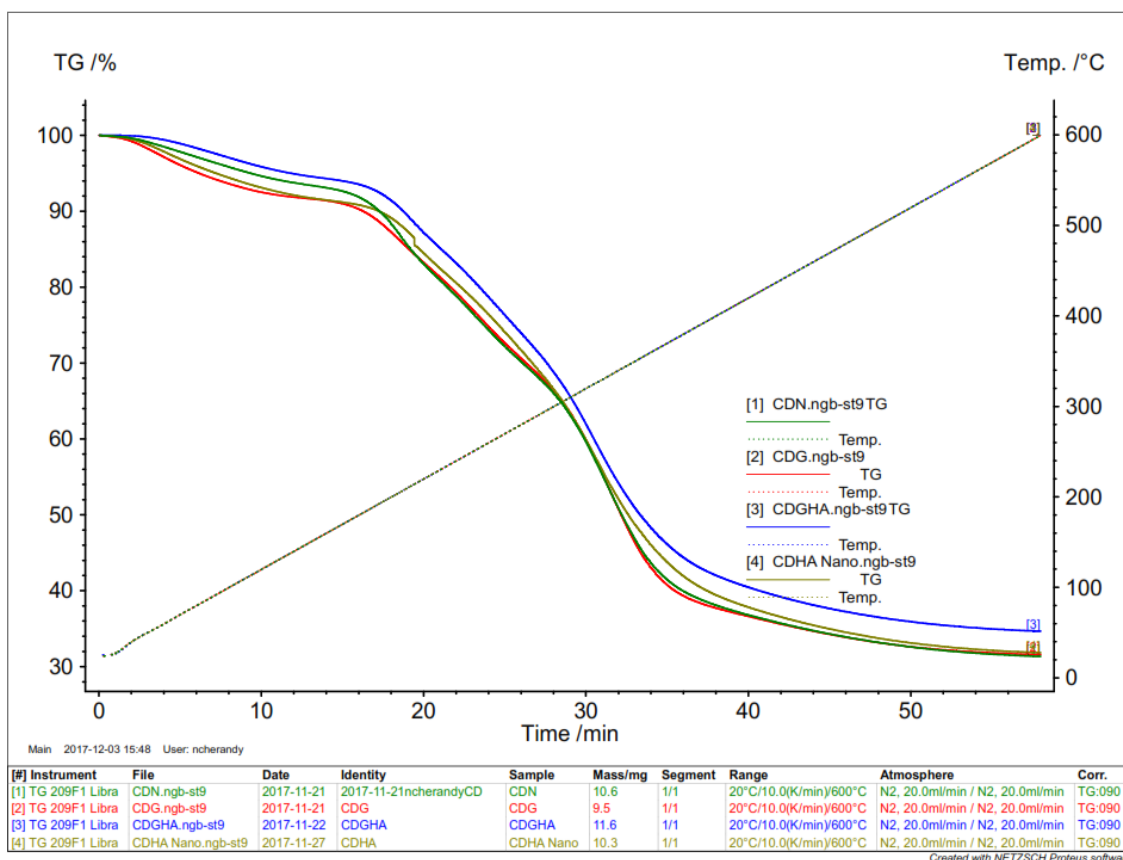


Figure 43: TGA curves of CD, CDG, CDHA and CDGHA showing mass loss as a function of temperature

The shape of the TGA curves for all four samples suggests a two-stage decomposition with one unstable intermediate. Due to the similarities in the peak profile of the four samples, we will limit our discussion of the DTG results to two of the samples (CDN and CDG) and the results inferred for the others (CDHA and CDGHA). **Figure 44** illustrates the TGA/DTG curves of CDN and CDG nanosponge; the insert figure shows the variation in mass loss for the two sponges. The first derivative curve was plotted to accurately evaluate the position of inflection points and hence the mass loss steps. The DTG curves reveal a more complex decomposition pattern with intermediate decomposition products for both polymers. The mass loss steps are iterated in **Table X**, where T_m is the temperature of maximum decomposition.

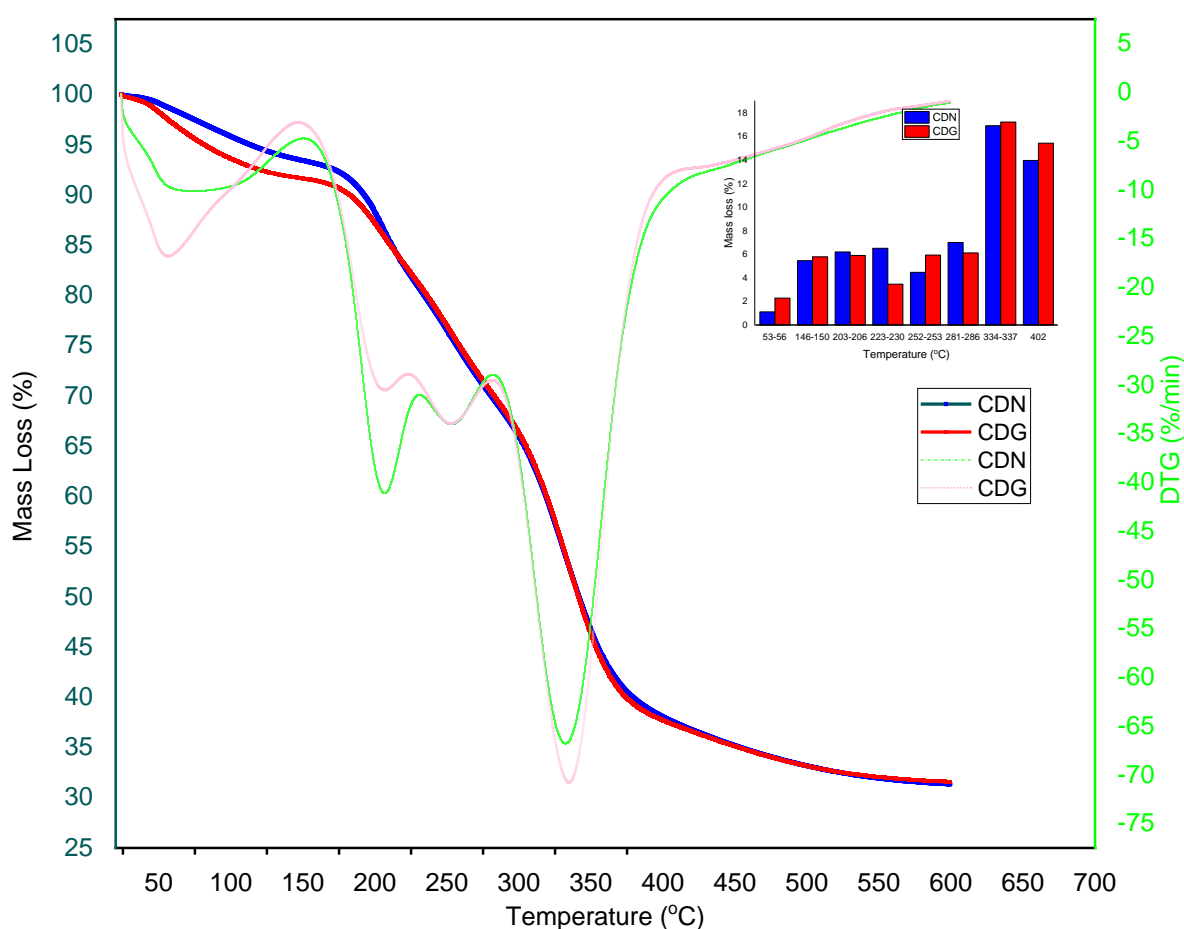


Figure 44: TGA/DTG curves of CDN and CDG showing mass loss as a function of temperature, and the variation in mass loss (insert figure)

The first mass loss below 100 °C (1.12 % at 54 °C for CDN and 2.29 % at 56 °C for CDG), represented by an endothermic peak in the DTG curve results from the elimination of moisture. The next stage, with a mass loss of 5.47 % CDN at 150 °C and 5.80 % CDG at 146 °C is an exothermic process for the loss of physically adsorbed surface water. Water adsorbed in the

CD cavity is lost by an endothermic process at 204 °C (6.20 % CDN), and 207°C (5.91 % CDG). An exothermic thermal reaction is observed at 231 °C, 6.52 % mass loss for CDN and 223 °C, 3.48 % mass loss for CDG corresponding to the decomposition and volatilization of oxygen containing functional groups (–OH and –COOH) to CO₂[52]. The endothermic peak at 253 °C, 4.87 % mass loss for CDN and 253 °C, 5.95% mass loss for CDG, is consistent with the decarboxylation of surface carbonyl groups[176]. At 287 °C (7.01 % CDN) and 281°C (6.12 % CDG), the decomposition of citrate crosslinks is observed [201]. Melting and thermal decomposition of glucose units and ester bonds leading to the formation of a residual char is observed at 402 °C at a mass loss of 13.98 % for CDN and 15.44 % for CDG. This is followed by a slow thermal degradation of the residual char above 402 °C; comparable results were obtained by [202].

A total mass loss of 62.1 % CDN and 62.23 % CDG, with a residual char of 37.90 % CDN (4.02 g from an initial mass of 10.6 g) and 37.56 % CDG (3.57 g from an initial mass of 9.5 g) was recorded. This indicates that approximately 0.13 g of the goethite nanopowder is grafted onto the CDN polymer. CDG has more moisture content and physically adsorbed water and these mass losses occur at slightly higher temperatures than for CDN. A higher mass loss is observed for water adsorption from the cyclodextrin cavities and in the decomposition of oxygen containing functional groups in CDN than CDG.

Table X: DTG mass loss steps for CDN and CDG at the temperature of maximum decomposition

CDN		CDG		Peak characteristic
Temperature (T _m)	% mass loss	Temperature (T _m)	% mass loss	
54	1.12	56	2.29	Endothermic, elimination of moisture
150	5.47	146	5.80	Exothermic, loss of surface physically adsorbed water
204	6.20	207	5.91	Endothermic, loss of water adsorbed in the CD cavity
231	6.52	223	3.48	Exothermic, decomposition and of oxygen containing functional groups (–OH and –COOH)
253	4.87	253	5.95	Endothermic, decarboxylation of surface carbonyl groups
287	7.01	281	6.12	Exothermic, thermal decomposition of citrate crosslinks
337	16.93	334	17.24	Endothermic, dihydroxylation
402	13.98	402	15.44	Exothermic

3.2.6 Scanning Electron Microscopy (SEM)

SEM was used to characterize the surface morphology of the as-synthesized goethite nanopowder and nanosponges. The morphology of the goethite nanoparticles as studied using SEM is presented in **Figure 45**. Goethite nanoparticles exhibit monodispersed acicular (needle-like) - shaped (a) and rod-shaped features, seen at higher magnification (b). The particle diameters calculated using ImageJ range from 12.97 nm to 47.14 nm with mean particle diameter of 30.13 nm.

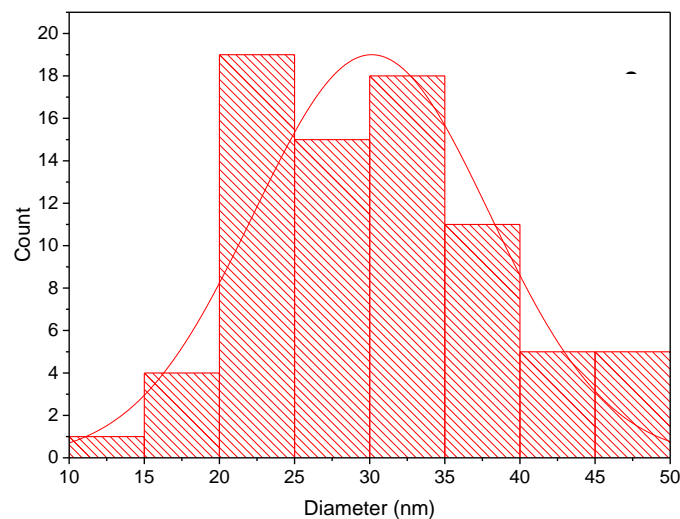
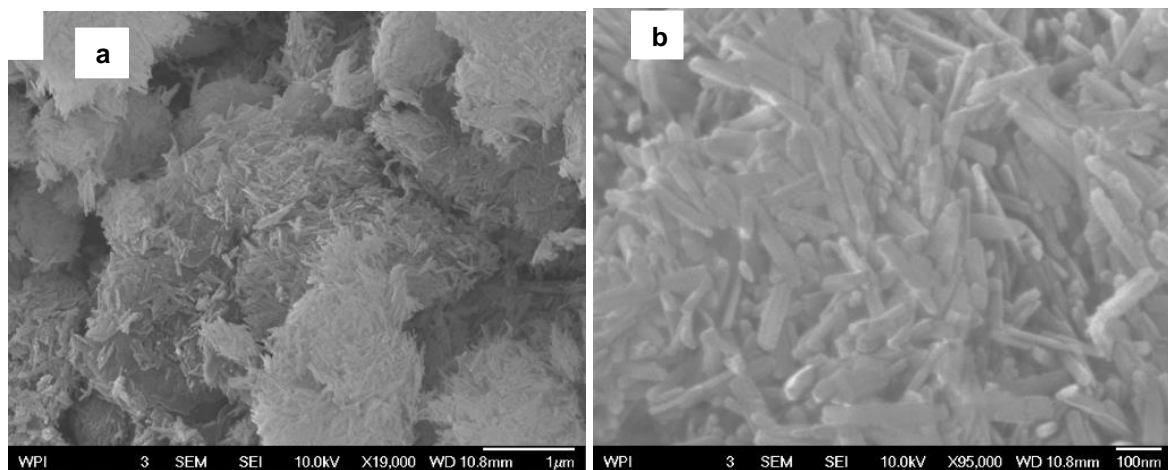


Figure 45: SEM Micrograph of as-synthesized goethite nanoparticles at magnifications: (a) x19000 and (b) x95000; and (c) particle size distribution

Figure 46 and 47 shows the SEM images of the CDN, CDG, CDHA and CDGHA nanosponges. Though both materials are porous, CDG is seen to be considerably more porous, with more defined pores, than the CDN. From the histogram, the CDN pore diameter is in the

range 0.13-21.28 μm , a mean pore size diameter of 2.67 μm with 70 % less than 3 μm (a total of 20 measured points). For CDG, the pore diameter is in the range 0.47-14.79 μm , with a mean pore size diameter of 3.68 μm (for a total of 180 measured points).

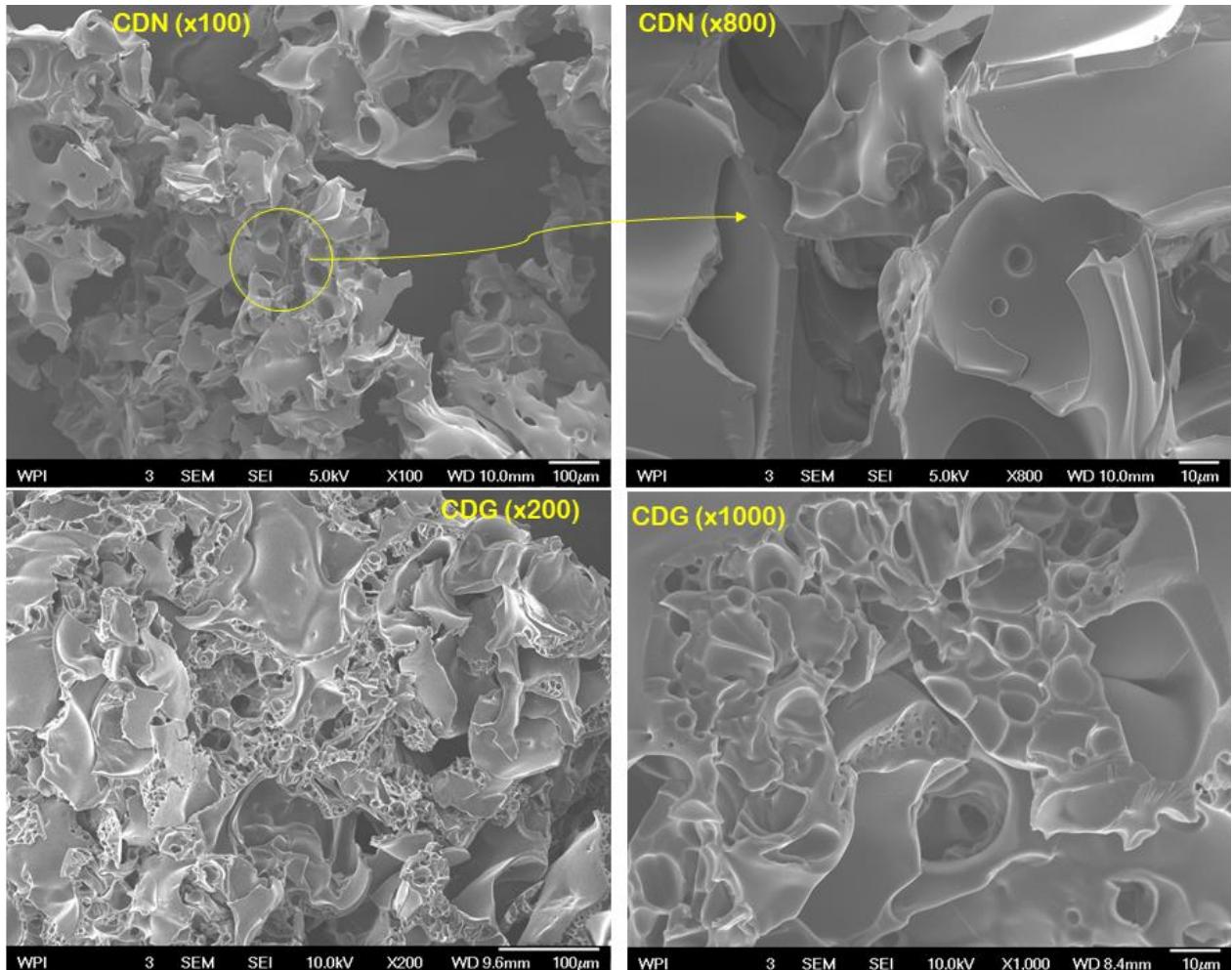


Figure 46: 3D Surface morphology of CDN and CDG at different magnifications using SEM

From **Figure 47**, the CDHA sample also appears porous. CDG is seen to be markedly more porous than CDN. The CDGHA sample shows distinct regions of localised porosity, more porous than CDHGA and less porous than CDG. Hence, it can be inferred that HA has reduces the degree of porosity in the CDGHA sample.

From the histogram and descriptive statistics (**Figure 47**), the CDHA pore diameter is in the range 0.025-15.41 μm , a mean pore size diameter of 4.43 μm for a total of 34 measured points. For CDGHA, the pore diameter is in the range 0.005-13.44 μm , with a mean pore size diameter of 3.51 μm (for a total of 199 measured points).

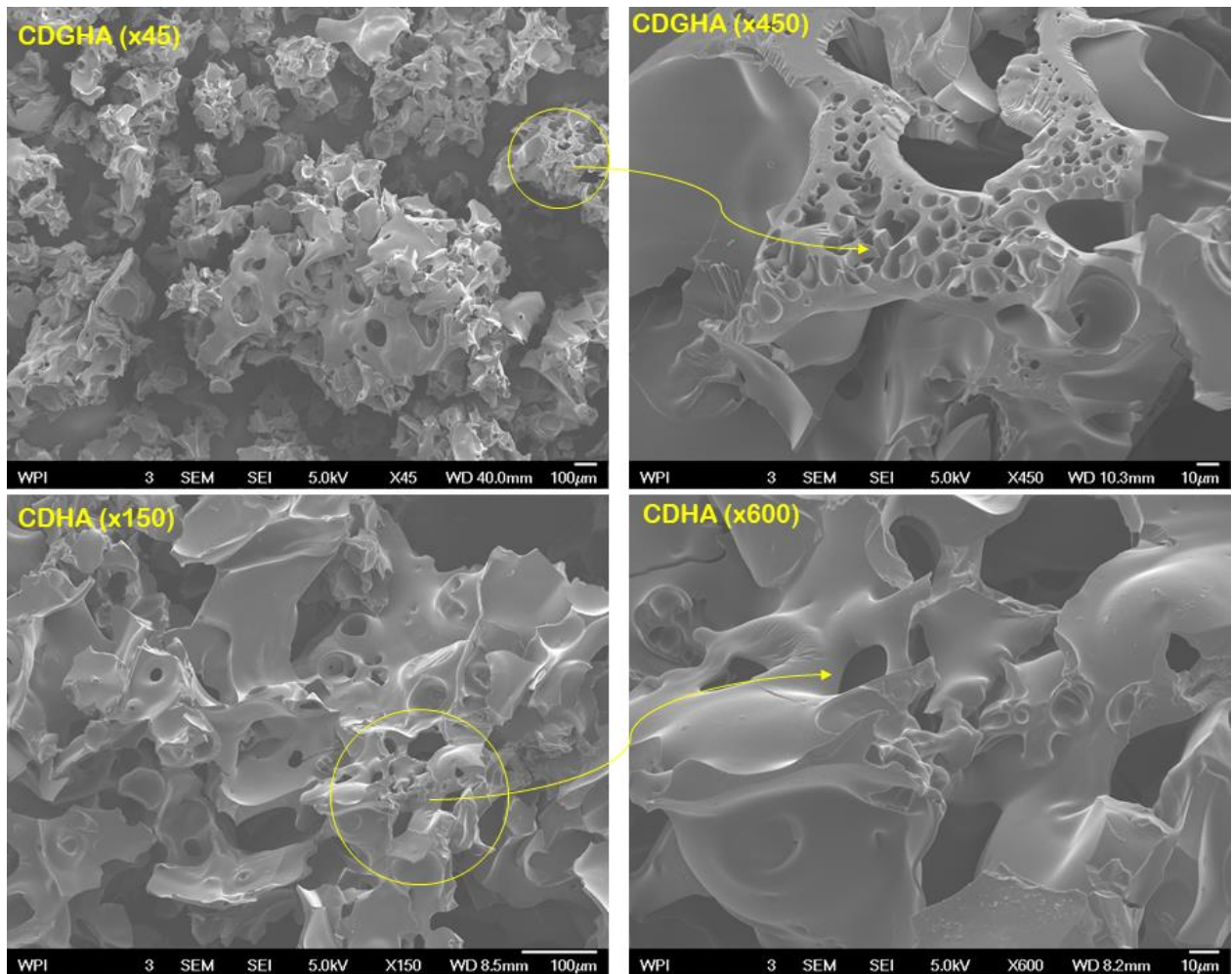


Figure 47: 3D Surface morphology of CDHA and CDGHA at different magnifications using SEM

Hence, functionalisation with goethite greatly increases the porosity of CDG, but not so much for CDHA, while that of CDGHA, though higher than that of CDN and CDHA, is somewhat reduced by the presence of HA in the material. Other than the observed differences in the pore structure of the functionalised materials, no other observable changes on the morphology of the materials are noticed at the magnifications studied.

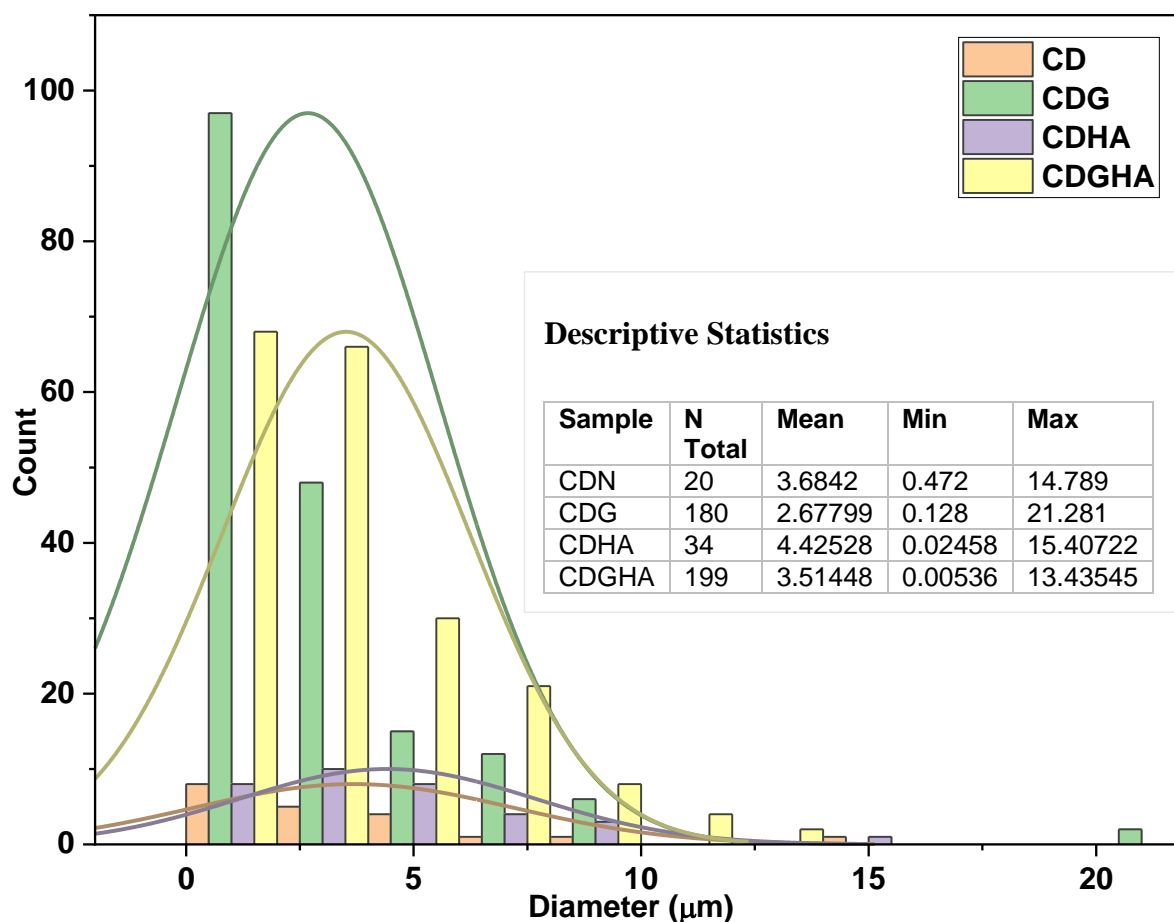


Figure 48: Pore size distribution and descriptive statistics

3.2.7 TEM

Transmission Electron Microscopy provided additional insight on the morphology, crystallinity and particle size (distribution) of the goethite nanoparticles in the nanosponge. The TEM images of CDN (Figure 49.a) reveal spherical particles of nanometre dimensions typical of cyclodextrins. The average pore diameter is 9.93 nm. The CDG TEM images show the heterogeneous nature of the morphology of this sponge with distinct regions of the same sample. These are, a highly porous zone with mean pore diameter of 41.78 nm (Figure 49.b), zones with distinct spherical cyclodextrin and goethite nanoparticles (Figure 49.c), zones where acicular goethite nanoparticles of mean particle diameter 36.45 nm are singularly observed (Figure 49.d), and a composite structure of this sponge (Figure 49.f). The distinct

goethite nanoparticles indicate that Fe-O binds to citric acid through both outer and inner sphere complexation as seen in the FTIR spectra.

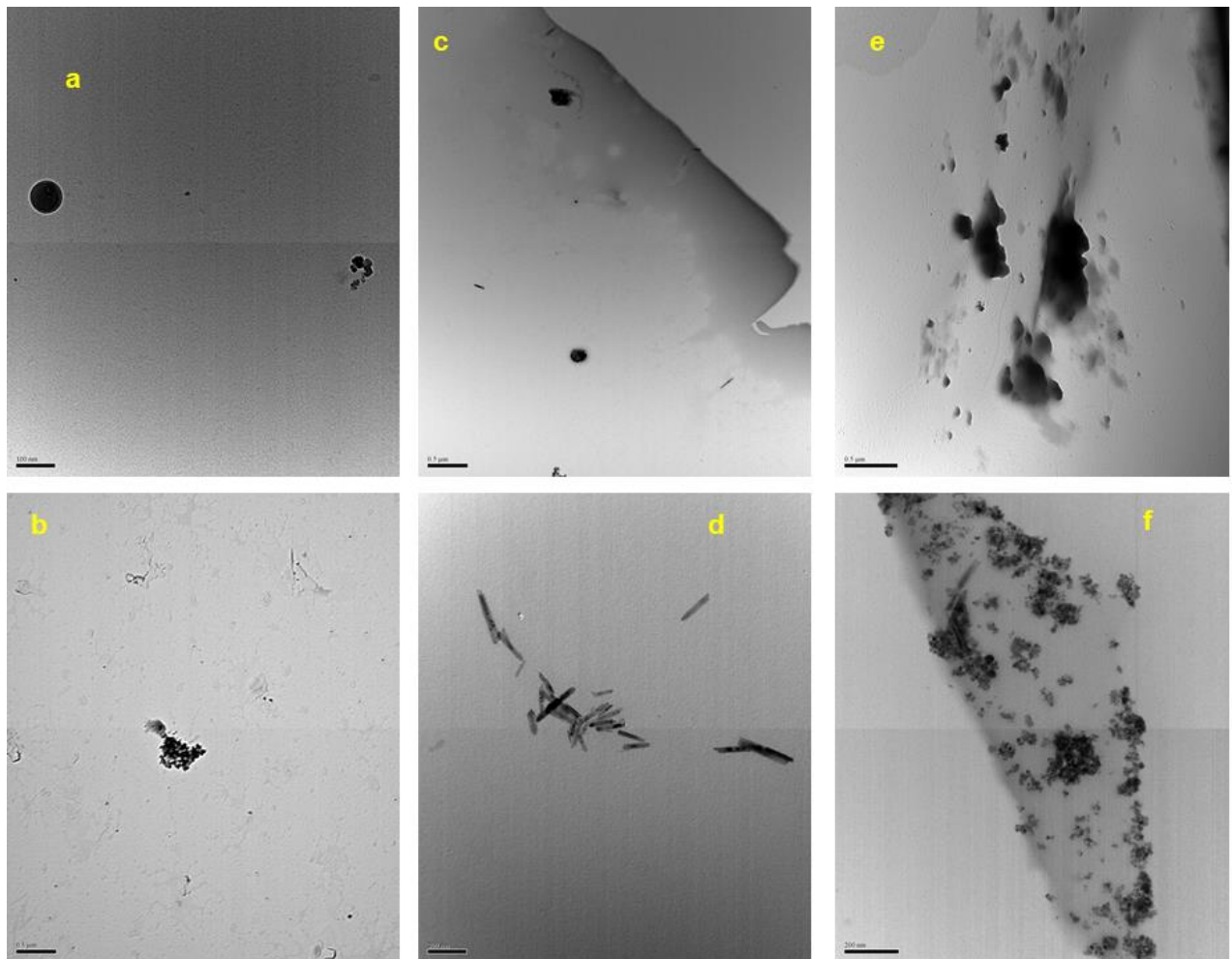


Figure 49: TEM micrograph of CDN (a-b) and CDG (c-f) nanosponge showing different structural domains

In **Figure 50.a**, only one structural domain was observed for the CDHA sample (probably due to experimental error during sampling and analysis). The image reveals a spherical particle of nanometre dimensions, attesting to the presence of cyclodextrin. The CDGHA sample (**Figure 50.b-d**) also present different structural domains almost similar to CDG, i.e. zones with distinct spherical cyclodextrin and zones with acicular or needle-like nanoparticles (resulting from the goethite and hydroxyapatite nanoparticles). In Figure 50.d, the nanoparticles seem to aggregate on the surface of the cyclodextrin nanosponge. The CDGHA sample does not show any porous zones.

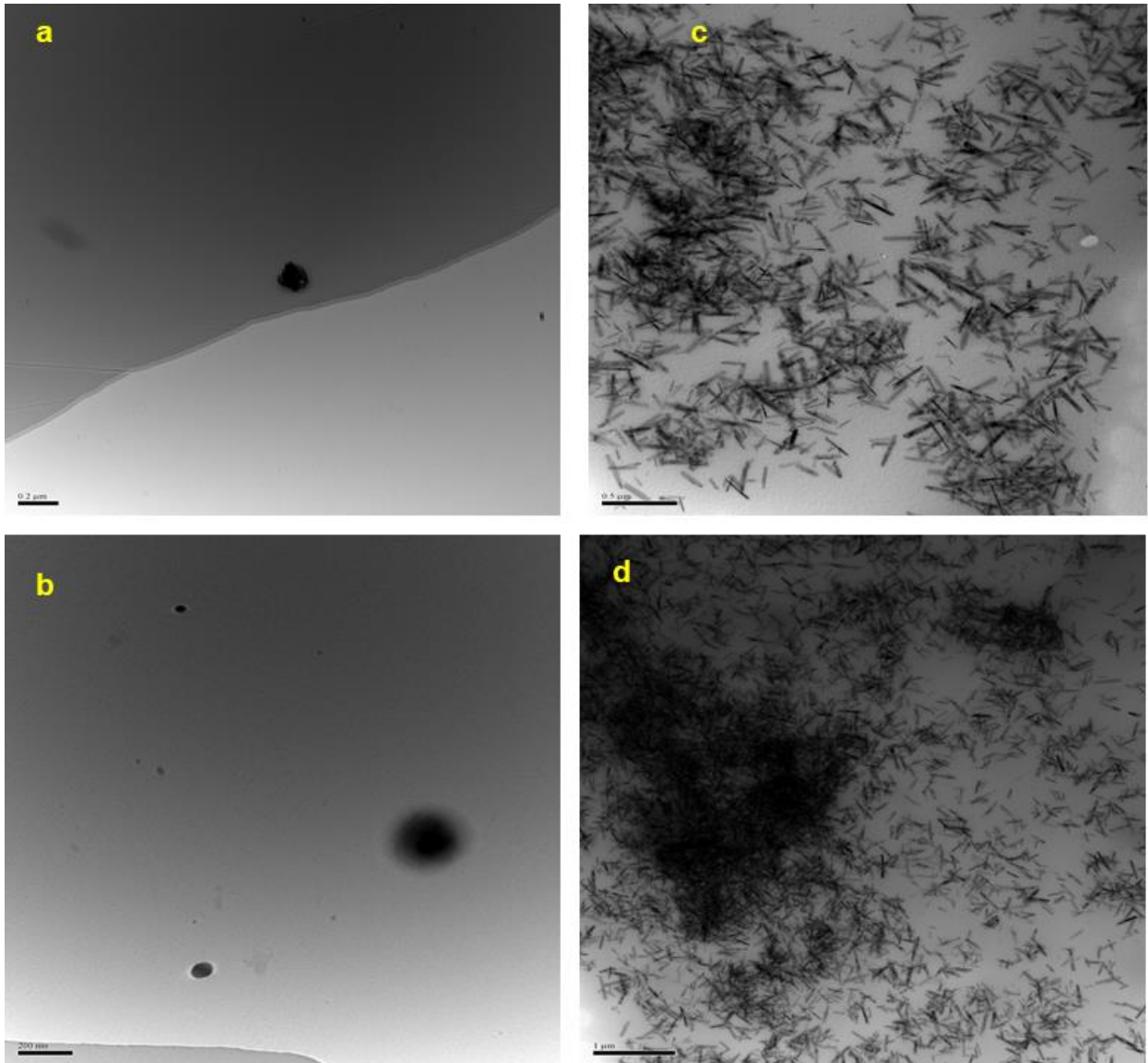


Figure 50: TEM micrograph showing different structural domains of CDHA (a) and CDGHA (b-d) nanosponge

3.3 Batch Adsorption Studies

Batch adsorption studies were carried out on the four adsorbents for the removal of Ni(II) ion, MB and F⁻. The adsorption equilibrium and kinetics were modelled through several non-linear models using the Generalized Reduced Gradient (GRG) nonlinear algorithm of add-in solver function of MS Excel (Microsoft, USA, 2019). Five error functions were used to determine the best fit model from a total of four isotherm and three kinetic models. The coefficient of determination, residual root-mean square error and the chi-square test are used to test the goodness of fit of the equilibrium models; the coefficient of determination, normalized standard

deviation and average relative error are used to test the goodness of fit the kinetic models. The isotherm and kinetic parameters were determined by minimising the respective error functions. The lower the value of the error function, the better the performance of the predictive model.

3.3.1 Nickel Ion Removal

Variation of contact time and adsorbate concentration

Contact time is an effective factor in batch adsorption technique. To study the effect of contact time on the removal of the Ni(II) ions, experiments were conducted at different contact times from 5 to 80 mins using 0.2 g of adsorbent and 20 ml of 50 ppm Ni (II) ions. The quantity of Ni(II) ion adsorbed is shown in **Figure 51**. As observed the extent of removal of the Ni(II) ion increases initially, then stabilizes after the optimum contact time of 5 minutes for all four adsorbents. This variation is due to the available adsorption sites on the adsorbents at the beginning for metal ion adsorption. As the surface adsorption sites diminish, the uptake rate is controlled by the rate at which the adsorbate is transported from the exterior to the interior sites of the adsorbent particles, is depicted by the plateau-shape of the curve at higher contact times. Hence, Ni(II) ion adsorption was rapid, attaining equilibrium within the first five minutes at a percentage removal of 98.89 % (4.95 mg/g) for CDN, 97.41 % 4.87 mg/g) for CDG, 97.91% (4.50 mg/g) for CDHA and 100.01 % (5.00 mg/g) for CDGHA.

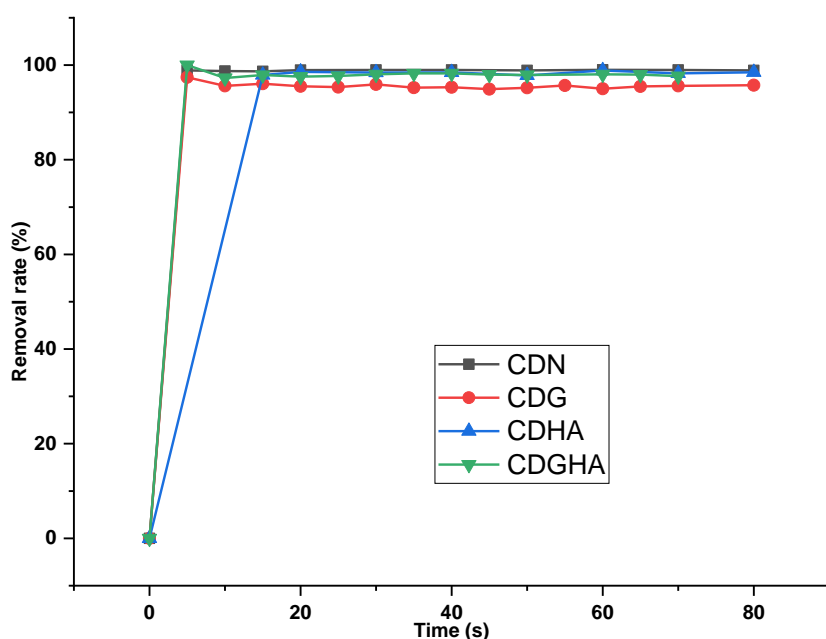


Figure 51: Variation of Contact Time for Ni(II) Ion Adsorption

Figure 52 illustrates the effect of the initial metal ion concentration on its uptake. The graphs indicate that the percentage of Ni(II) ion removal increases initially with concentration and the system attains an equilibrium at 20 ppm for all four adsorbents. The system is seen to maintain this equilibrium between 20 ppm and 80 ppm for CDG and CDGHA and 20 ppm to 60 ppm for CDN and CDHA. These are respectively the concentration ranges in which the system can operate.

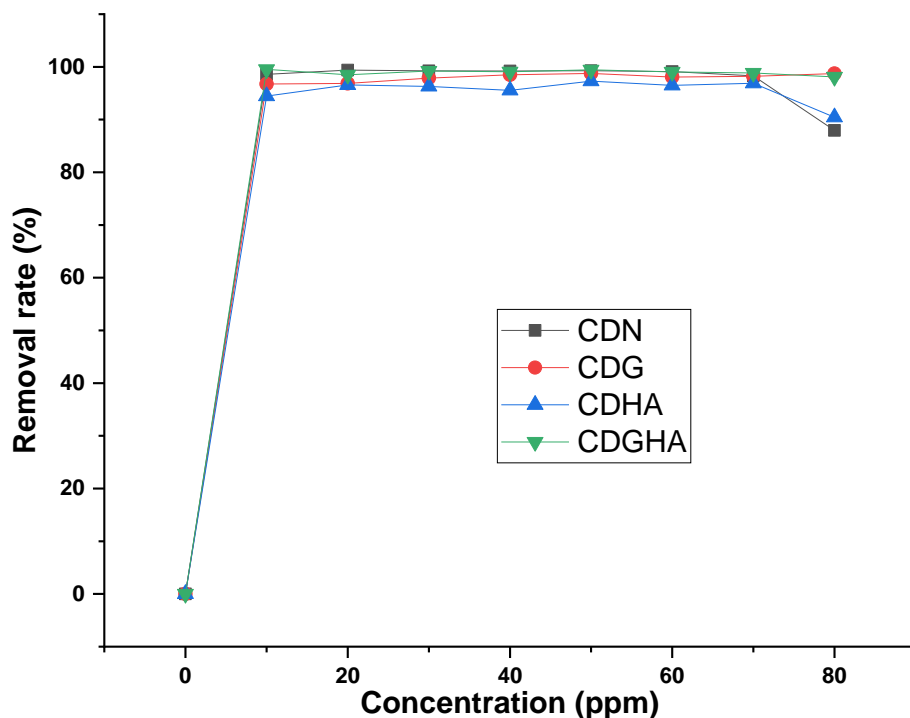


Figure 52 : Variation of Concentration for Ni(II) Ion Adsorption

Equilibrium and modelling

For equilibrium modelling, nickel ion concentration was varied from 10 to 80 ppm using 0.2 g of adsorbent at 10 mins. **Figure 53-56** illustrates the nonlinear Langmuir, Freundlich, Redlich Peterson, Sips equilibrium isotherm models. The nonlinear parameter estimates for the equilibrium and kinetic models are given in **Table XI**.

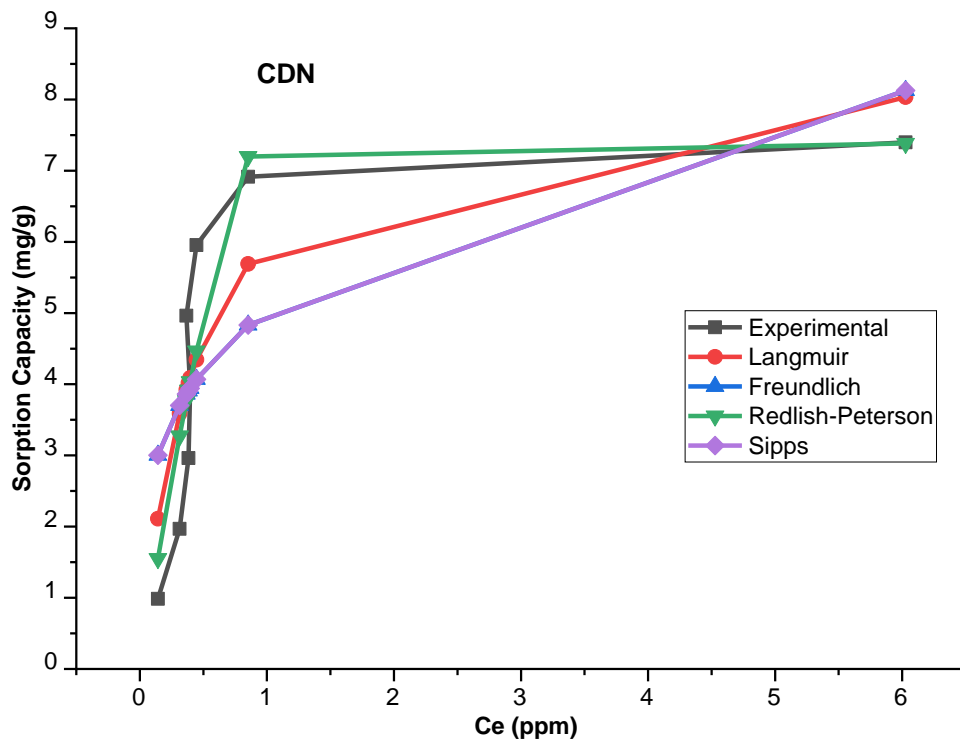


Figure 53: Langmuir, Freundlich, Redlich Peterson, Sips equilibrium isotherm models for Ni(II) ion adsorption on CDN (at constant time, mass and temperature)

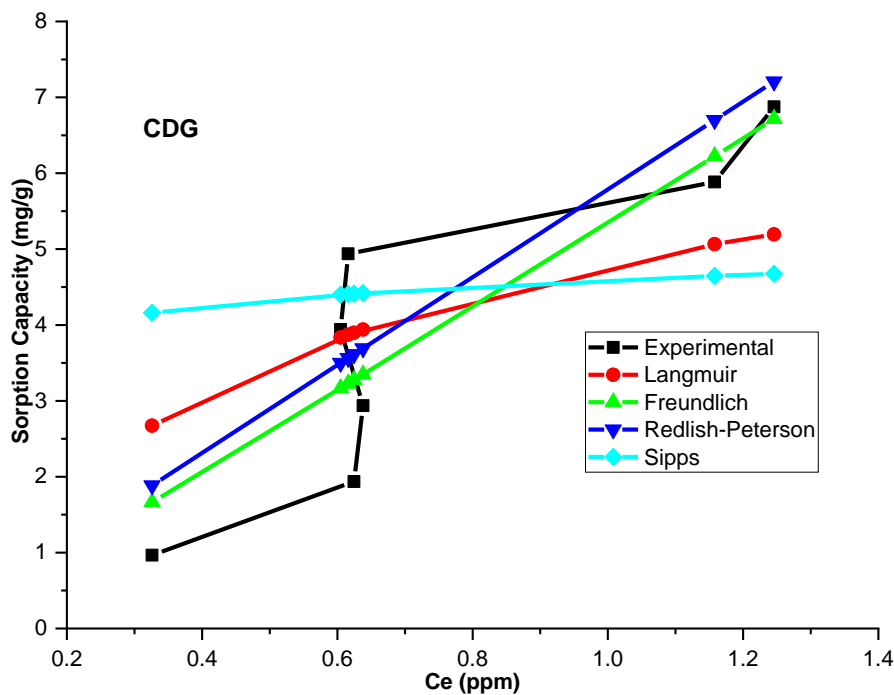


Figure 54: Langmuir, Freundlich, Redlich Peterson, Sips equilibrium isotherm models for Ni(II) ion adsorption on CDG (at constant time, mass and temperature)

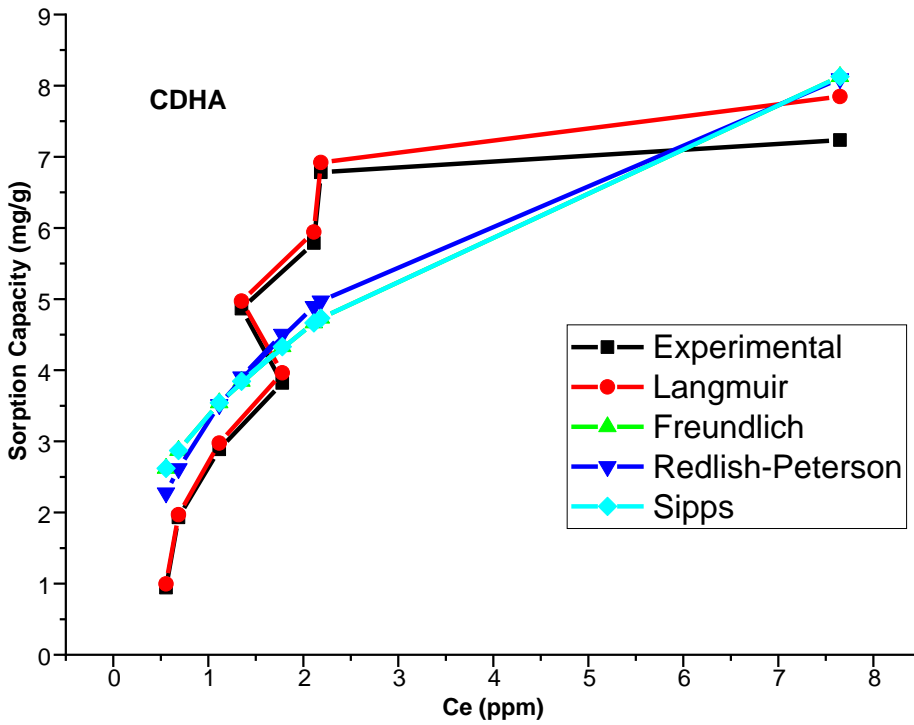


Figure 55: Langmuir, Freundlich, Redlich Peterson, Sips equilibrium isotherm models for Ni(II) ion adsorption on CDHA (at constant time, mass and temperature)

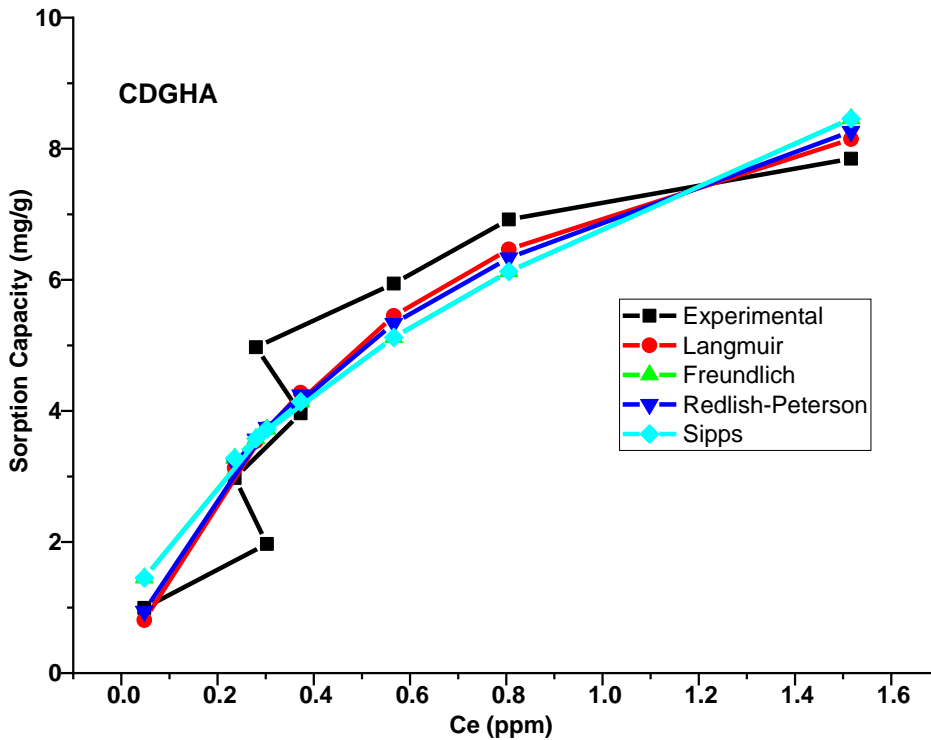


Figure 56: Langmuir, Freundlich, Redlich Peterson, Sips equilibrium isotherm models for Ni(II) ion adsorption on CDGHA (at constant time, mass and temperature)

Based on the values of the coefficient of determination (R^2 values), none of the equilibrium models gave a good fit to the experimental data (all R^2 values < 0.8 [203]) for CDN and CDG. However, in comparing the parameter estimates of the four models tested, the Langmuir model (highest R^2 value at 0.7201) provided the best model fit for Ni(II) ion adsorption on CDN. Also, the value of the parameter $\beta=0.8000$ in the Redlich-Peterson model is close to unity, indicating the model reduces to a Langmuir model.

Table XI: Nonlinear parameter estimates for equilibrium and kinetic adsorption models for Ni(II) ion adsorption

Adsorbent			CDN	CDG	CDHA	CDGHA
Model	Equation	Parameters	Parameters values			
Langmuir	$q_e = \frac{q_m K_L C_e}{1 + K_L C_e}$	q_m K_L r^2 RMSE CHI ²	8.6190 2.2786 0.7201 1.3291 2.7983	7.800 1.600 0.5445 1.5754 2.7600	9.9232 0.4990 0.9873 0.2775 0.0679	11.5532 1.5776 0.8557 0.9888 1.5765
Freundlich	$q_e = K_F C_e^{1/n}$	K_F $1/n$ r^2 RMSE CHI ²	5.0412 0.2658 0.5349 1.7132 4.5486	5.3437 1.0402 0.7757 1.1053 2.0067	3.3785 0.4314 0.6791 1.3953 3.0877	6.8421 0.5093 0.8271 1.0821 1.8275
Redlich Peterson	$q_e = \frac{K_R C_e}{1 + a_R C_e^\beta}$	K_R a_R β r^2 RMSE CHI ²	42.7578 7.0055 0.8000 0.6082 1.5726 3.8123	7.1974 0.3505 0 0.7747 1.1078 2.0021	6.8471 1.0739 0.8000 0.7574 1.2130 2.3205	24.010 2.4411 0.8000 0.8487 1.0123 1.5762
Sips	$q_e = \frac{K_S (C_e)^{\beta_S}}{1 + a_S C_e^{\beta_S}}$	K_S a_S m_S r^2 RMSE CHI ²	3.4554 1.5915 0.2658 0.5349 1.7172 0.2658	7.8000 6.0000 0.2000 0.0678 2.2538 5.8162	2.4142 0.9759 0.4314 0.6791 1.3953 3.0877	4.6071 1.4782 0.5093 0.8271 1.0821 1.8275
Pseudo- first order	$q_t = q_e(1 - e^{-kt})$	q_e K_1 r^2 NSD ARE	4.9447 12 0.9999 0.0048 0.0103	4.7804 4.0279 0.9994 0.1003 -0.0197	4.9174 12.000 0.9999 0.0322 0.0153	4.9026 4.0279 0.9994 0.0537 0.0152
Pseudo- second order	$q_t = \frac{q_e^2 K_2 t}{1 + K_2 q_e t}$	q_e K_2 r^2 NSD ARE	4.9447 3688015 0.9999 0.0048 0.0102	4.7804 471733 0.9994 0.1004 -0.0197	4.9174 3688015 0.9999 0.0318 0.0154	4.9025 471733 0.9994 0.0548 0.0154
Elovich	$Q_t = \frac{1}{\beta} \ln(\alpha\beta) + \frac{1}{\beta} \ln t$	α β r^2 NSD ARE	4.94E+20 10.7964 0.9972 0.3343 -0.1279	4.78E+20 11.2045 0.9944 0.1127 -0.0395	2.53E+18 9.8361 0.9989 0.4297 -0.1594	4.90E+20 10.9017 0.9955 0.0180 -0.0239

Likewise, both the Redlich-Peterson ($R^2=0.7747$) and the Freundlich model ($R^2=0.7757$) best describe Ni(II) ion adsorption on CDG; the parameter $\beta=0$, indicating that the Redlich-Peterson model reduces to a Freundlich model. In addition, the Chi Squared (CHI^2) and Root Mean Square Error (RMSE) values are lowest for Langmuir in CD and lowest for Freundlich and Redlich-Peterson models for CDG. Though these models do not provide a statistically good fit to the data ($R^2<0.8$), the closeness of CDG to the Freundlich and Redlich-Peterson models indicates a higher degree of the heterogeneity of the binding sites in CDG as compared to CDN (Langmuir-like). This is backed by the results from the TEM analysis which clearly show the heterogeneous nature of CDG.

For CDHA, the Langmuir model show a higher correlation ($R^2=0.9873$) with the equilibrium data. The value of the parameter $\beta=0.8000$ in the Redlich-Peterson model is also close to unity, indicating the model reduces to a Langmuir model. The CHI^2 and RMSE values are lowest for Langmuir. For CDGHA, all four models had relatively similar correlations with the data. The values of the coefficient of determination for all these models (Langmuir, $R^2=0.8557$; Freundlich $R^2=0.8271$; Redlich-Peterson $R^2=0.8487$; Sips, $R^2=0.8271$) indicate a high degree of correlation.

Kinetic modelling

For the kinetic test, the contact time was varied from 5 to 80 mins using 0.2 g of adsorbent and 20 ml of 50 ppm nickel (II). **Figure 57-60** shows the Pseudo-first order, Pseudo-second order and Elovich kinetic models for Ni(II) ion adsorption on CDN, CDG, CDHA and CDGHA. From the R^2 values, both the Pseudo-first ($R^2=0.9999$ for CDN, $R^2=0.9994$ for CDG, $R^2=0.9999$ for CDHA and $R^2=0.9994$ for CDGHA) and Pseudo second order ($R^2=0.9999$ for CDN, $R^2=0.9994$ for CDG, $R^2=0.9999$ for CDHA and $R^2=0.9994$ for CDGHA) models provided a good fit to kinetic data. Also, the Normalized Standard Deviation (NSD) and Average Relative Error (ARE) values for both models and adsorbents are very low, indicating a statistically very good fit of the Pseudo-first and Pseudo-second order kinetic models. The first order model signify reversible interactions with an equilibrium being established between liquid and solid phases whereas the second order kinetic model assumes that the rate-limiting step is most likely to involve chemical interactions leading to binding of the ions to the surface by bonding as strong as covalent bonding. Therefore, the sorption of Ni(II) ions on CDN, CDG, CDHA and CDGHA involved both physical and chemical processes.

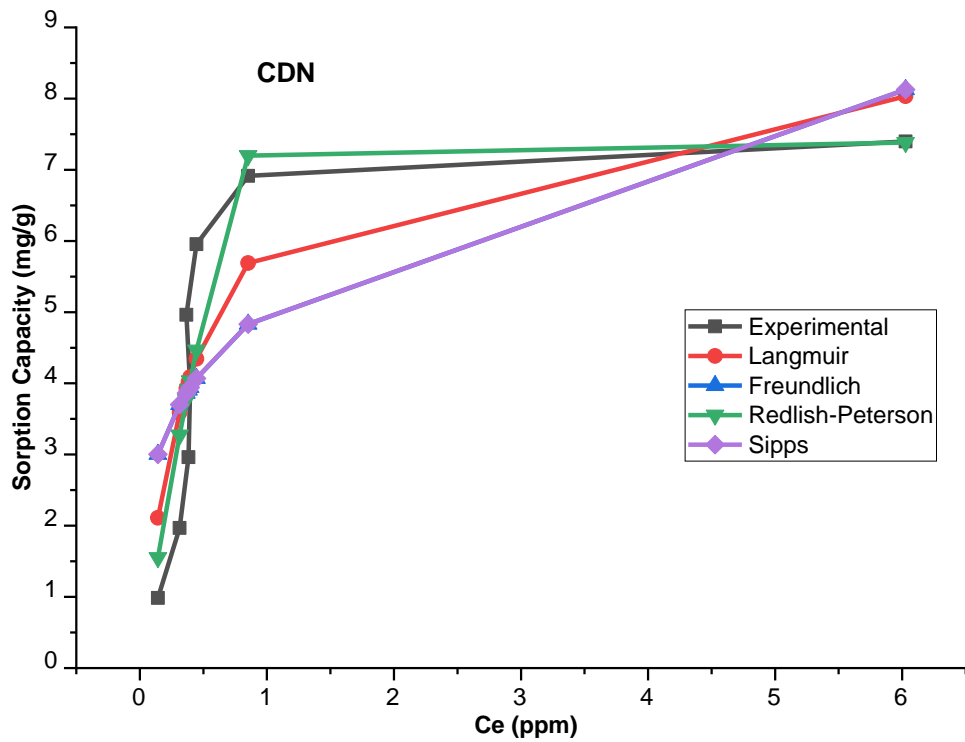


Figure 57: Pseudo-first order, Pseudo-second order and Elovich kinetic models for Ni(II) ion adsorption on CDN (at constant concentration, mass and temperature)

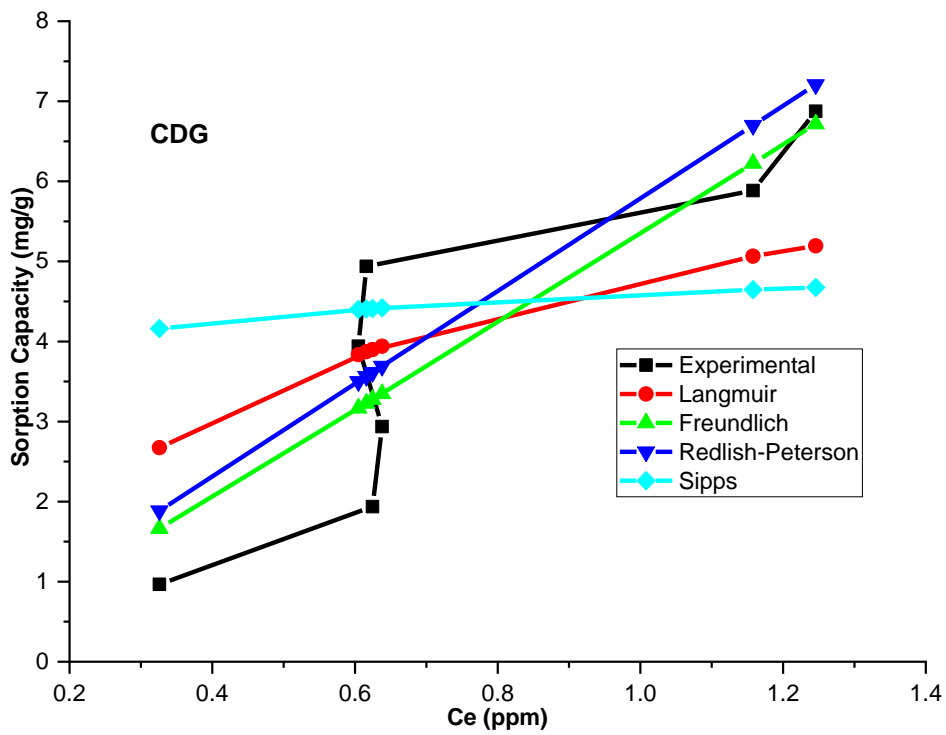


Figure 58: Pseudo-first order, Pseudo-second order and Elovich kinetic models for Ni(II) ion adsorption on CDG (at constant concentration, mass and temperature)

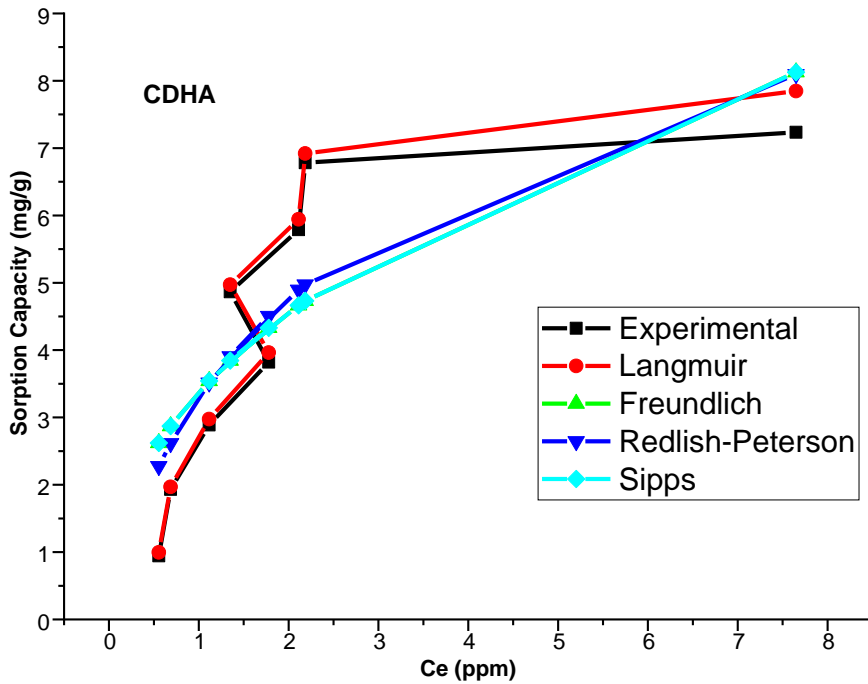


Figure 59: Pseudo-first order, Pseudo-second order and Elovich kinetic models for Ni(II) ion adsorption on CDGHA (at constant concentration, mass and temperature)

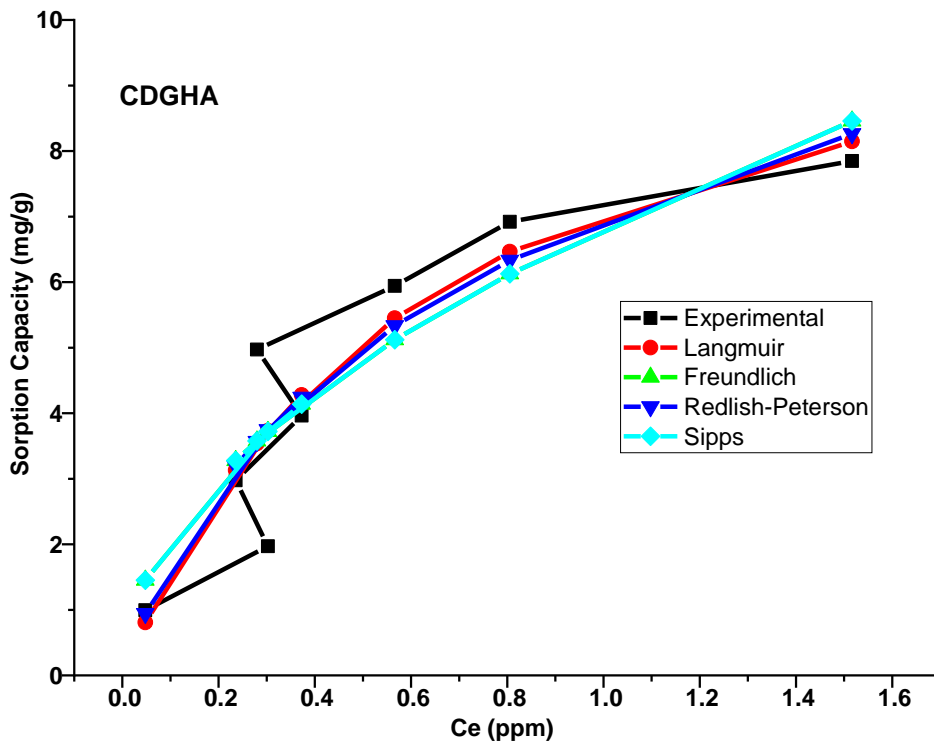


Fig. 60. Pseudo-first order, Pseudo-second order and Elovich kinetic models for Ni(II) ion adsorption on CDGHA (at constant concentration, mass and temperature)

Figure 61 shows the stacked FTIR plot of CDN before and after Ni(II) ion adsorption. There is an increase in the intensity of the OH stretch, a decrease in the intensity of the -COO and the coupled C-C/C-H band. The band corresponding to the -C-O-C antisymmetric glycoside vibrations also splits similarly to that observed for the IR spectra of CDG. The FTIR results after adsorption thus confirms both chemical and physical interactions between Ni(II) ions and the CDN polymer.

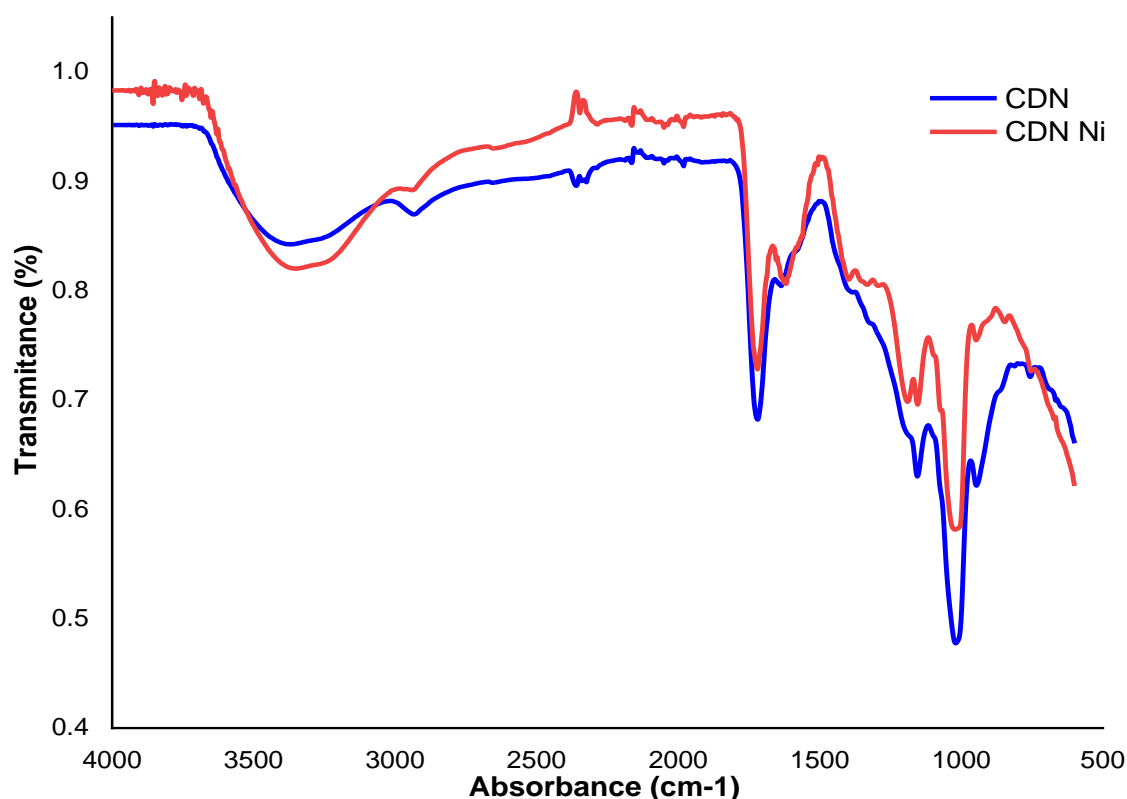


Figure 61: Before and after stacked FTIR plot of Ni(II) ion adsorption on CDN

3.3.2 MB Removal

For methylene blue (MB) adsorption using 0.2 g of adsorbent, 20 ml of 20 ppm of methylene blue, a maximum equilibrium removal of 99.98% (1.93 mg/g), 100% (2.01 mg/g), 93.64% (1.95 mg/g), and 104.73% (2.06 mg/g) was observed for CDN, CDG, CDHA and CDGHA respectively. MB adsorption was studied through kinetic modelling only. The nonlinear parameter estimates for the kinetic models for MB adsorption on CDN, CDG, CDHA and CDGHA are given in **Table XII**. All three kinetic models provided a good fit to kinetic data ($R^2 > 0.9956$). Also, the NSD and ARE values for these models are very low, indicating a

statistically very good fit of both models. This indicates that the sorption of MB on CDN also involves both physical and chemical processes.

Table XII: Nonlinear parameter estimates for kinetic adsorption models for MB adsorption on CDN, CDG, CDHA and CDGHA

Adsorbent			CDN	CDG	CDHA	CDGHA
Model	Equation	Parameters	Parameters values			
Pseudo-first order	$q_t = q_e(1 - e^{-kt})$	q_e	1.9237	2.0092	1.9606	2.0967
		K_1	12.000	12.000	12.000	12.000
		r^2	0.9999	0.999978	0.999996	0.999999
		NSD	0.0941	0.0225	0.0156	0.0051
		ARE	0.0505	-0.0052	-0.0089	-0.0025
Pseudo-second order	$q_t = \frac{q_e^2 K_2 t}{1 + K_2 q_e t}$	q_e	1.9353	2.0092	1.9606	2.9669
		K_2	3.69E+7	3.69E+7	3.69E+7	3.69E+7
		r^2	0.9999	0.999978	0.999997	0.999999
		NSD	0.0658	0.0225	0.0156	0.0051
		ARE	0.0079	-0.0052	-0.0089	-0.0025
Elovich	$Q_t = \frac{1}{\beta} \ln(\alpha\beta) + \frac{1}{\beta} \ln t$	α	1.99+21	1.99E+41	1.99E+41	5.19E+48
		β	28.854	50.961	52.269	57.087
		r^2	0.9959	0.9988	0.9992	0.9994
		NSD	0.1260	0.0248	0.4853	0.0116
		ARE	-0.0252	-0.0294	-0.0270	-0.0142

Figure 62-65 illustrates the Pseudo-first order and Pseudo-second order and Elovich kinetic models for MB adsorption on CDN, CDG, CDHA and CDGHA.

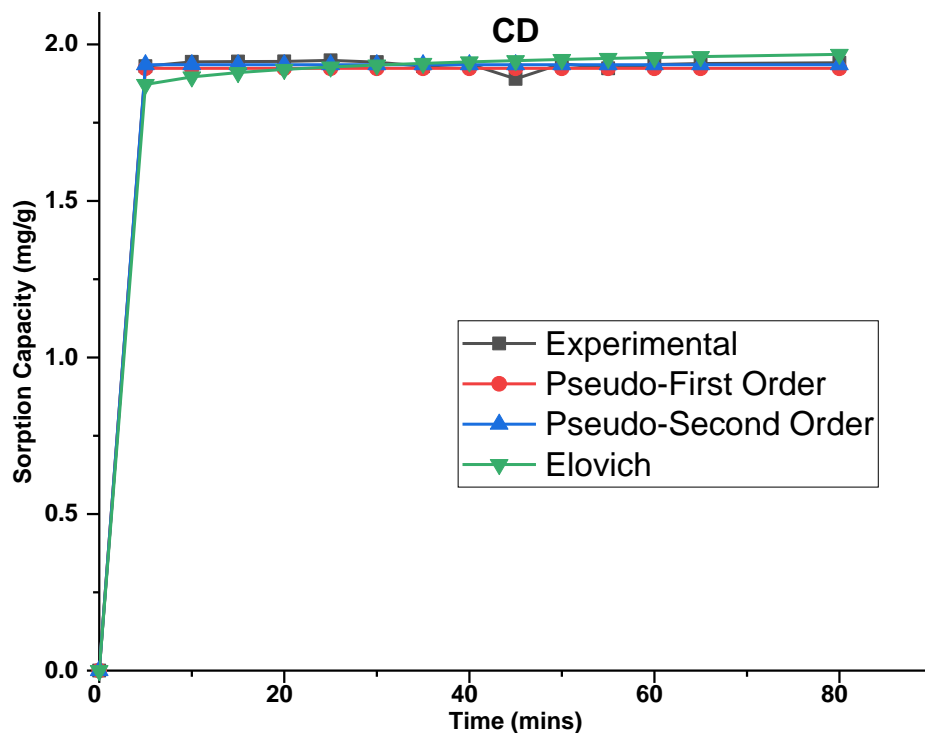


Figure 62: Pseudo-first order, Pseudo-second order and Elovich kinetic models for MB adsorption on CDN (at constant concentration, mass and temperature)

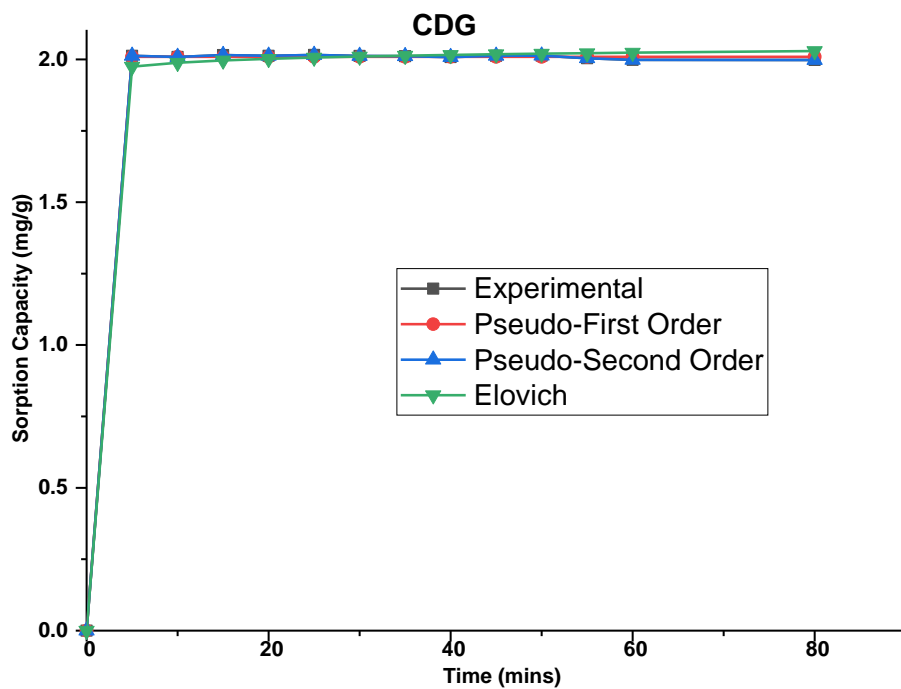


Figure 63: Pseudo-first order, Pseudo-second order and Elovich kinetic models for MB adsorption on CDG (at constant concentration, mass and temperature)

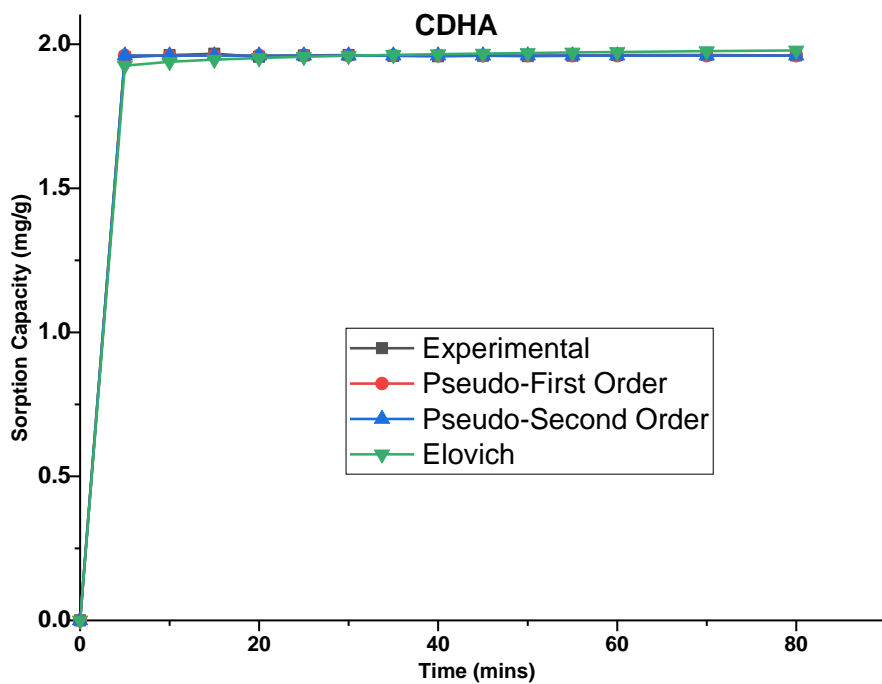


Figure 64: Pseudo-first order, Pseudo-second order and Elovich kinetic models for MB adsorption on CDHA (at constant concentration, mass and temperature)

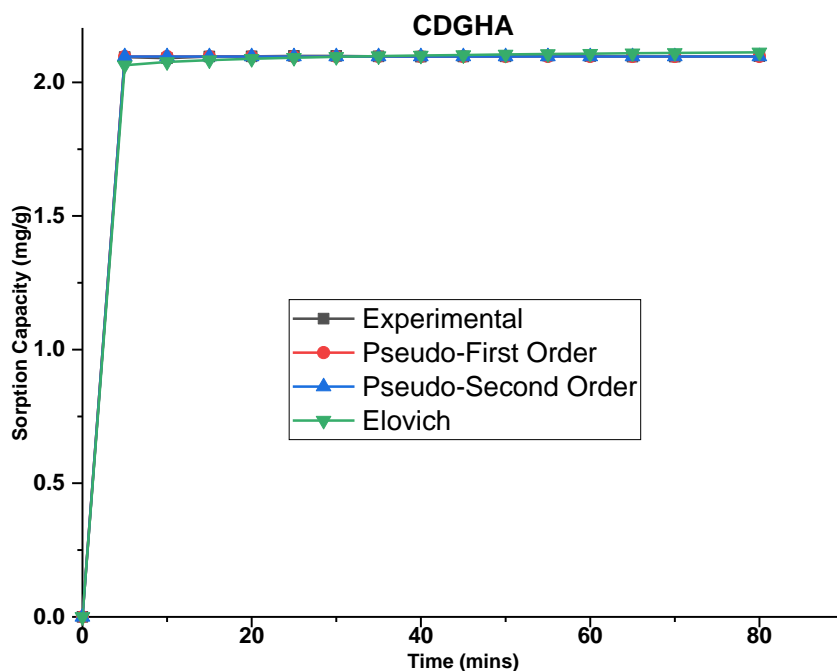


Figure 65: Pseudo-first order, Pseudo-second order and Elovich kinetic models for MB adsorption on CDN, CDG, CDHA and CDGHA (at constant concentration, mass and temperature)

3.3.4 Fluoride Removal

Fluoride ion adsorption was studied on CDHA and CDGHA. For the kinetic test, the contact time was varied from 5 to 80 mins using 0.2 g of adsorbent and 20 ml of 50 ppm fluoride solution. CDN and CDG showed no activity for fluoride ion removal. A maximum equilibrium removal of 69.58% (3.48 mg/g), and 71.33% (3.57 mg/g) was observed for CDHA and CDGHA respectively. The nonlinear parameter estimates for the kinetic models for fluoride adsorption on CDHA and CDGHA are given in **Table XIII**.

Figure 66-67 shows the Pseudo-first order, Pseudo-second order and Elovich kinetic models for fluoride adsorption on CDHA and CDGHA. From the R^2 values, all three models ($R^2 \geq 0.9942$) provided a good fit to kinetic data. Also, the Normalized Standard Deviation (NSD) and Average Relative Error (ARE) values for these models are very low, indicating a statistically very good fit.

Table XIII: Nonlinear parameter estimates for kinetic adsorption models for fluoride ion adsorption on CDHA and CDGHA

Adsorbent		CDHA	CDGHA	
Model	Equation	Parameters values		
Pseudo-first order	$q_t = qe(1 - e^{-kt})$	q_e	3.5170	3.4883
		K_1	4.0279	4.0279
		r^2	0.9989	0.9992
		NSD	0.6322	0.0678
		ARE	-0.0329	-0.0301
Pseudo-second order	$q_t = \frac{q_e^2 K_2 t}{1 + K_2 q_e t}$	q_e	3.5170	3.4883
		K_2	4.0279	4.0279
		r^2	0.9989	0.9992
		NSD	0.6322	0.0678
		ARE	-0.0329	-0.0301
Elovich	$Q_t = \frac{1}{\beta} \ln(\alpha\beta) + \frac{1}{\beta} \ln t$	α	1.29E+21	1.10E+21
		β	15.624	15.6794
		r^2	0.9967	0.9942
		NSD	0.5261	0.0971
		ARE	-0.078	-0.055

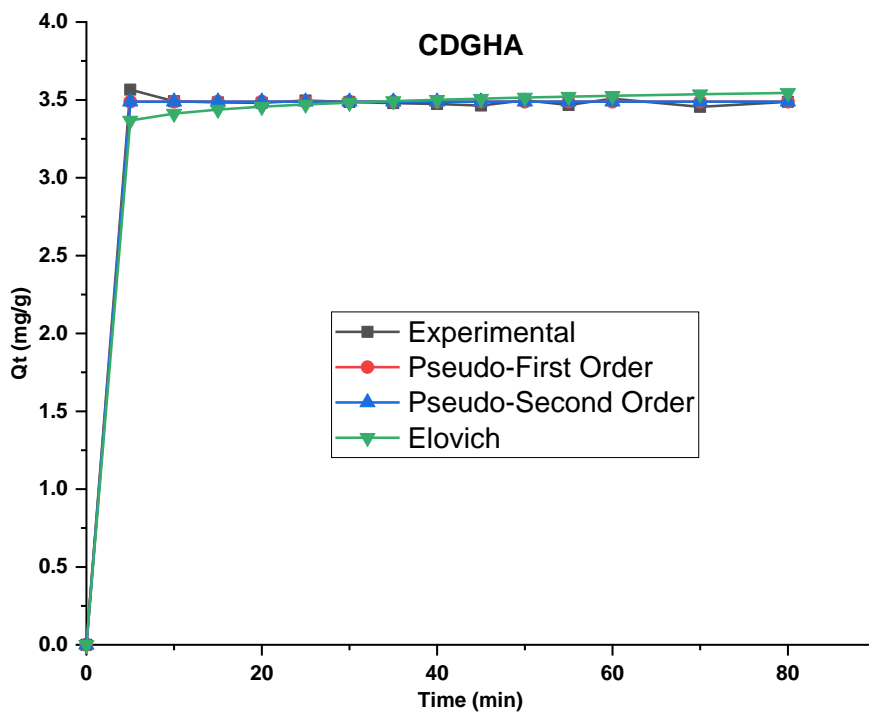


Figure 66: Pseudo-first order, Pseudo-second order and Elovich kinetic models for Fluoride adsorption on CDHA (at constant concentration, mass and temperature)

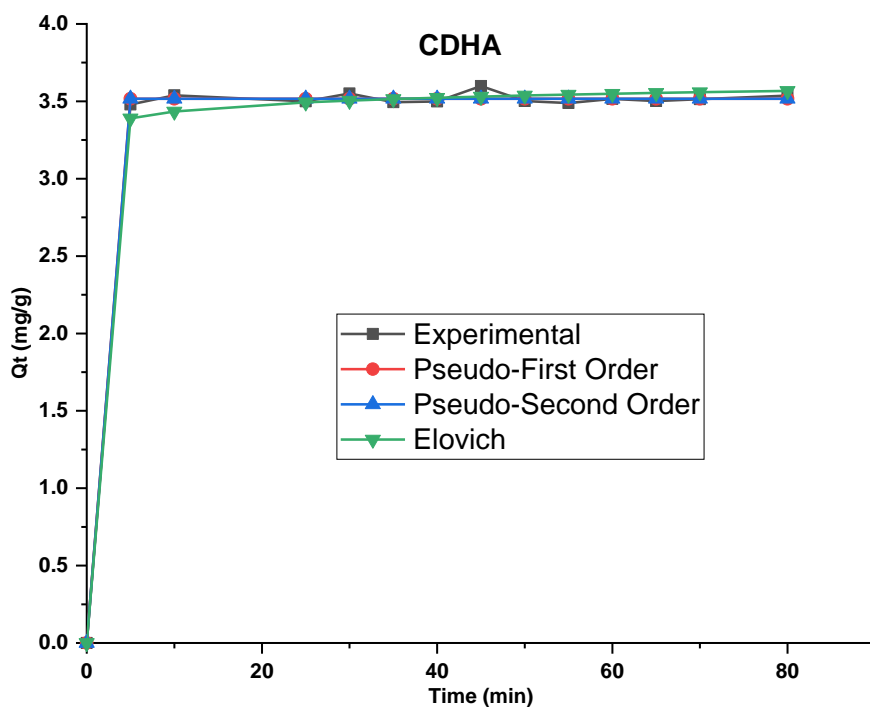


Figure 67: Pseudo-first order, Pseudo-second order and Elovich kinetic models for Fluoride adsorption on CDGHA (at constant concentration, mass and temperature)

3.4 Preliminary Column Adsorption Studies

The preliminary column adsorption test for MB and nickel(II) ions was conducted using CDN. After passing a 20 mg/L MB solution of volume 300 mL at a rate of 10 ml/min for the duration of five hours, MB was not detected in the filtrate (Loss on Detection, following equation of the calibration curve and the absorbance values being less than that of the calibrated region; calibration was carried out from 0.05 ppm to 20 ppm).

For Ni(II) ion, the breakthrough curve of relative effluent concentration (C_t/C_o) against time is plotted in **Figure 68**. The percentage removal ranged from 99.92 % ($t=5$ mins) at the start of the experiment to 95.02% ($t=190$ min) at the end of the experiment. From the curve and recorded percentage removal, the system did not attain the breakthrough point (when the mass transfer zone reaches the bottom of the column).

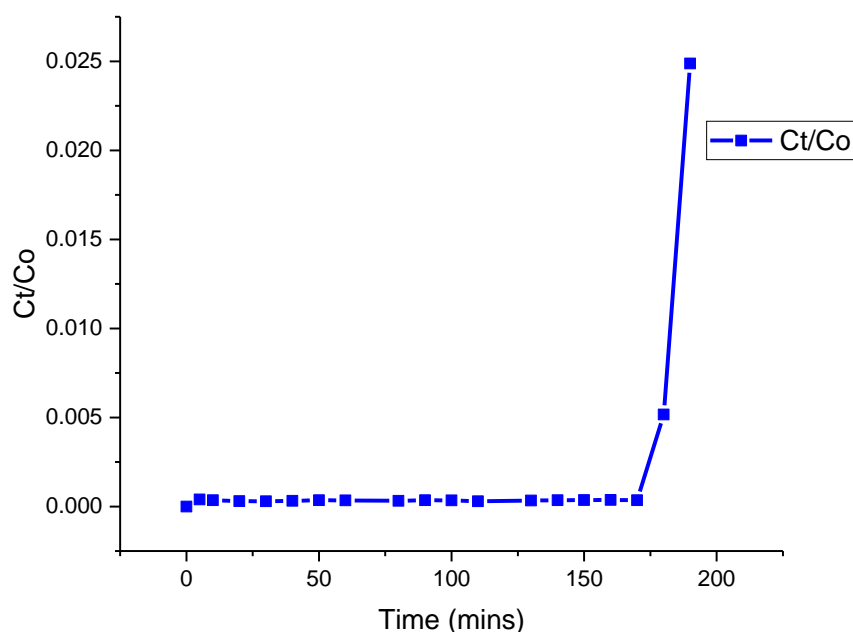


Figure 68: Breakthrough curve of relative effluent concentration (Ct/Co) against time (at constant concentration, mass and temperature)

3.4.3 *E. Coli* Removal

The removal efficiency of *E. coli* by CDN, CDG, CDHA and CDGHA nanosponges are given in **Table XIV**. From the count, at a bacteria concentration of 10^{-7} cfu/mL, the *E. coli* removal rate of CDN is 40 %, CDG 83.75% and CDHA 64.06%. However, CDGHA did not show positive removal rate for *E. coli*. The removal rate for CDG is twice as high as that of CDN indicating that CDG is more effective at removing bacteria contamination. *E. coli* is a gram-negative bacterial and has an outer hydrophobic membrane[204] which imparts a negative charge to the surface of the bacterial. The surface charge, hydrophobicity and surface properties of bacteria and their matrix are the forces responsible for bacterial capture[61] . It is expected that hydrophobic forces will drive the inclusion complex formation between the beta cyclodextrin cavity and the *E. coli*. However, because the CD sponge is negatively charged (due to the presence of carboxylate groups on its surface), there is an antagonistic repulsive effect that prevents efficient binding of *E. coli* to the CDN surface.

Table XIV: Removal efficiency of *E. coli* on CDN, CDG, CDHA and CDGHA

N°	Sample	<i>E. coli</i> count				% Removal
			Stock	Diluted stock (1:2 dilution)	Filtrate	
1	CDN	10 ⁻²	TNTC	TNTC	TNTC	24/61*100= 40%
		10 ⁻⁴	TNTC	TNTC	TNTC	
		10 ⁻⁵	TNTC	TNTC	TNTC	
		10 ⁻⁶	39/4*20	61	37	
		10 ⁻⁷	48	6	4	
2	CDG	10 ⁻⁵		TNTC	TNTC	$\frac{240-39}{240} \times 100 = 83.75\%$
		10 ⁻⁶		TNTC	(65/4)*20	
		10 ⁻⁷		48/4*20 =240	39	
3	CDHA	10 ⁻⁵		TNTC	TNTC	$\frac{64 - 23}{64} \times 100 = 64.06\%$
		10 ⁻⁶		(71/4)*20	(47/4)*20	
		10 ⁻⁷		64	23	
4	CDGHA	10 ⁻⁵		TNTC	TNTC	
		10 ⁻⁶		(64/4)*20	(58/4)*20	
		10 ⁻⁷		33	40	

Goethite is reported to have a high affinity towards high-molecular weight aromatic constituents rich in carboxylic group; its interaction with anions by electrostatic attraction leads to a decrease in surface charge and shift its point zero charge to lower pH [205]. Thus, interaction of goethite with the carboxylate groups on CDN reduces its surface charge. With a lower surface charge, the repulsive effect between the gram-negative *E. coli* and the CDG nanosponge is somewhat reduced leading to a higher removal rate of *E. coli* by CDG. Though not measured, it can also be said that HA has a similar effect on CDN but with a reduced intensity.

The saturated adsorption amount (Q_m) obtained from the Langmuir isotherm model has been extensively used as an index to evaluate the maximum adsorption capacity adsorbents. The basis for this is the assumption that Q_m is independent of the concentration of the adsorbate (C_e). However, from observations and as demonstrated by Li and co-workers [206], the regression Langmuir Q_m is highly dependent on the adsorbate concentration. They showed that the regression Q_m increased from 0.066 to 2.17 mg/g (by ~3-fold) for the selected soil sample, and from 2.12 to 48.4 mg/g by ~23-fold) for the chosen biochar when the highest initial aqueous concentration increased from 2.34 to 887 mg/L. Therefore, it is inaccurate to directly compare adsorption capacity among different adsorbents without considering the Q_m of the saturated isotherm and the differences in experimental conditions. In this case, the efficiency

of the CD functionalised nanosponges were compared to that of other citric acid crosslinked cyclodextrin or cyclodextrin functionalised polymers and some nanosorbents on the basis of percentage removal and adsorption conditions. See [Table XV](#).

Table XV: comparison of some of the results obtained by other authors on citric acid crosslinked cyclodextrin or cyclodextrin functionalised polymers and some nanosorbents with that obtained in this work.

Adsorbent	Method of synthesis or crosslinker	Adsorbate	Adsorption conditions	Percentage removal	Ref.
CDN	Ultrasound assisted polycondensation using citric acid as crosslinker	MB Ni <i>E. coli</i>	0.2 g, 20 mL, 20 mg/L 1 g, 300 mL, 20 mg/L 0.2 g, 20 mL, 50 mg/L 2 g, 100 mg/L 1g,50 mL,10 ⁻⁷ cfu/mL	99.98% 100 % 98.89% 99.92 % 39.3%	This work
CDG	Ultrasound assisted polycondensation using citric acid as crosslinker	MB Ni <i>E. coli</i>	0.2 g, 20 mL, 20 mg/L 0.2 g, 20 mL, 50 mg/L 1g,50 mL,10 ⁻⁷ cfu/mL	100% 97.41% 83.75%	This work
CDHA	Ultrasound assisted polycondensation using citric acid as crosslinker	MB Ni <i>E. coli</i>	0.2 g, 20 mL, 20 mg/L 0.2 g, 20 mL, 50 mg/L 1g,50 mL,10 ⁻⁷ cfu/mL		This work
CDGHA	Ultrasound assisted polycondensation using citric acid as crosslinker	MB Ni <i>E. coli</i>	0.2 g, 20 mL, 20 mg/L 0.2 g, 20 mL, 50 mg/L 1g,50 mL,10 ⁻⁷ cfu/mL		This work
CA-β-CD	Condensation using citric acid as crosslinker	MB BPA Cu ²⁺	0.4 g, 200 mL, 100 mg/L	>99%, pH 4.1 87.2% 58.6%, pH 6.1	[207]

Adsorbent	Method of synthesis or crosslinker	Adsorbate	Adsorption conditions	Percentage removal	Ref.
CT-β-CD	Citric acid	MB	10 mg, 25 mL 38 mg/L MB, 30°C	98.11%	[208]
(PolyCyC	Direct melt copolycondensation using BTCA crosslinker	Progesterone	500 mg, 60 cm ³ , 2h (column)	98 %	[209]
PolyBTCA-CD		Al ³⁺ Co ²⁺ Cr ³⁺ Ni ²⁺ Zn ²⁺ PAH AP	2 g/L, 50 mg/L	69% 92% 78% 92% 92% 65-82% 60-90%	[186]
B-CDs/RCNFs	Citric acid	Toluene	30 mg, 100 ppm, 10 ml	69.9%	[99]
CDPA-MNPS	Phosphorylation polyamidation	<i>E. coli</i>	0.3g, 10 ⁻⁷ cfu/mL	97%	[61]
PBST/CDP-2.0	Electrospinning and in situ polymerization with citric acid	MB	50 mg, 40 mL, 5mg/L	98.8%	[98]

CONCLUSIONS AND FUTURE WORK

CONCLUSIONS AND FUTURE WORK

Conclusions

The main objective of this thesis was to synthesise novel cyclodextrin functionalised nanosponges and investigate the potential of these materials to remove organic, inorganic and microbial contaminants from drinking water. To this effect, cyclodextrin nanosponges were synthesized through ultrasound-assisted polycondensation polymerization. The polymerisation reaction occurs in two stages, including an additional surface activation stage using NaHCO_3 . Crosslinking cyclodextrin with citric acid (tricarboxylic acid) forms a pre-polymer (monomeric unit), the pre-polymers are then condensed to a high molecular weight polymer followed by activation of the free $-\text{COOH}$ groups on the citrate crosslinks with NaHCO_3 . Goethite functionalisation occurs through a monodentate and an outer-sphere complex in the aqueous interface. For goethite and/or hydroxyapatite grafting interactions, the $-\text{COOH}$ of the tertiary carbon of citric acid reacts with $-\text{OH}$ of goethite and/or hydroxyapatite to form a hypothetical ester bond.

Functionalisation of CDN with goethite and/or hydroxyapatite nanopowders was investigated and validated using FTIR analysis. The spectra of CDG, CDHA and CDGHA show all the characteristic bands of CDN spectra, variations in band intensity, band splitting and/or appearance of a new band were also observed in these spectra. Notable changes involve the split of the $-\text{C}-\text{O}-\text{C}$ stretch (1155.34 cm^{-1}) and coupled $\text{C}-\text{C}/\text{C}-\text{OH}$ stretch (1020.33 cm^{-1}), resulting from the formation of a $\text{C}-\text{O}-\text{Fe}$ and $\text{C}-\text{O}-\text{P}$ stretch in CDG and CDHA.

Functionalising CDN with a small quantity goethite nanopowder (0.13 g), hydroxyapatite (0.2 g) and goethite/hydroxyapatite (0.2+0.2)g considerably improve its chemical (porosity, swelling and thermal) and adsorptive properties. For example, CDN swells up to 379.8 % times its weight while CDG swells 558.4 % times its weight in water. This is an indication of the hydrophilic nature of the three-dimensional polymer network. The XRD spectrum of CDG exhibit both the amorphous nature of crosslinked cyclodextrin and some long-range order with weak and less intense peaks characteristic of goethite, indicating that the goethite nanoparticles retain a discrete phase in the material and that CDG is nanocrystalline. Similar trends were observed for CDHA and CDGHA, hence, CDN functionalisation with either goethite or HA

results to a material with two distinct phases, an amorphous CD and a crystalline goethite or HA phase.

From PDF analysis, the structure of all samples is mainly formed by network of cyclodextrin linked by citric acid while CDG and CDGHA contains crystalline goethite. The local structure of all samples is similar. The atomic bonding of goethite, hydroxyapatite with other molecules in network is not obvious in PDFs. The density modulation is similar in all samples, which means that the average spacing of molecules inside all samples are almost the same so the spacing of molecules in network is not changed by adding the goethite and hydroxyapatite. The local structure of samples can be approximately described by single molecule structure of cyclodextrin and citric acid with density modulation. The cyclodextrin shows large flexibility in the position of glucose subunit and probably is randomly deformed in network.

From the morphological studies, functionalisation with goethite greatly increases the nanoporosity of CDG, but not so much for CDHA, while that of CDGHA, though higher than that of CDN and CDHA, is somewhat reduced by the presence of HA in the material. TEM analysis presented a better insight into the heterogeneous nature of the functionalised nanosponges. The pore and particle diameters were all in the nanometre range (a mean diameter of 9.93 nm for CDN, 41.78 nm for the surface pores in CDG and 36.45 nm for the acicular nanoparticles).

The preliminary adsorption studies already demonstrate a rapid adsorption for Ni(II) and MB, with the system attaining equilibrium within the first five minutes. Equilibrium studies on Ni indicates a higher degree of the heterogeneity of the binding sites in CDG as compared to CDN (Langmuir-like). For CDHA, the Langmuir model show a very high correlation ($R^2=0.9873$) with the equilibrium data, and all four models had similar correlations with the data for CDGHA. This is backed by the results from the TEM analysis which clearly show the heterogeneous nature of CDG and CDGHA. The FTIR results after adsorption confirms both chemical and physical interactions between Ni(II) ions and the CDN polymer.

Kinetic modelling indicates a good correlation of the data (Ni(II), MB and F⁻) to all three models tested (Pseudo-first and Pseudo second order and Elovich model). Studies on E Coli removal showed a removal rate of 40 % for CDN, 64.06% for CDHA and 83.75 % for CDG. From this study, we were able to ascertain that these sponges possess the ability to remove effectively different classes of pollutant from water. Overall, the goethite functionalised

cyclodextrin nanosponge showed an all-round better performance to pollutant removal. This modified nanosponge is a biodegradable multi-adsorbent which has potential for use in existing water treatment technologies, tap faucets, water filters and for source water purification in localities without access to tap water.

Suggestions for future work

The following recommendations are suggested for future research work:

- Develop a pollutant removal performance data sheet for this nanosponge;
- Regeneration studies for reusability of the nanosponge;
- Use of silver to improve the microbial activity of the nanosponge;
- Design and develop a prototype tap faucet filter model and test its flow characteristics and filtration mechanisms for source water purification.

REFERENCES

REFERENCES

- [1] Ki-moon B., General U.S. The Human Right to Water and Sanitation. Media Brief at the United Nations General Assembly. (2010). Available from: https://www.un.org/waterforlifedecade/pdf/human_right_to_water_and_sanitation_media_brief.pdf. 12/5/2018.
- [2] WHO U. Progress on Drinking Water, Sanitation and Hygiene: 2017 Update and Sdg Baselines(2017):[1-116 pp.]. Available from: <https://www.un.org/africarenewal/documents/progress-drinking-water-sanitation-and-hygiene-2017-updates-and-sdg-baselines>. 12/01/2018.
- [3] Corcoran E., C. Nellemann, E. Baker, R. Bos, D. Osborn, H. Savelli Sick Water? The Central Role of Wastewater Management in Sustainable Development. A Rapid Response Assessment. United Nations Environment Programme(2010). Available from: <https://www.grida.no>.
- [4] Benner J., Helbling D.E., Kohler H.P., Wittebol J., Kaiser E., Prasse C., Ternes T.A., Albers C.N., Aamand J., Horemans B., Springael D., Walravens E., Boon N., Is Biological Treatment a Viable Alternative for Micropollutant Removal in Drinking Water Treatment Processes?, *Water Res*, **47** (2013) 5955-5976, [10.1016/j.watres.2013.07.015](https://doi.org/10.1016/j.watres.2013.07.015).
- [5] WHO, Global Health Statistics 2016: Deaths by Cause and by Region, 200-2016, (2018).
- [6] Armah F.A., Ekumah B., Yawson D.O., Odoi J.O., Afitiri A.R., Nyieku F.E., Access to Improved Water and Sanitation in Sub-Saharan Africa in a Quarter Century, *Heliyon*, **4** (2018) e00931, [10.1016/j.heliyon.2018.e00931](https://doi.org/10.1016/j.heliyon.2018.e00931).
- [7] Mkwate R.C., Chidya R.C.G., Wanda E.M.M., Assessment of Drinking Water Quality and Rural Household Water Treatment in Balaka District, Malawi, *Phys. Chem. Earth* **100** (2017) 353-362, [10.1016/j.pce.2016.10.006](https://doi.org/10.1016/j.pce.2016.10.006).
- [8] Nhamo G., Nhemachena C., Nhamo S., Is 2030 Too Soon for Africa to Achieve the Water and Sanitation Sustainable Development Goal?, *Sci Total Environ*, **669** (2019) 129-139, [10.1016/j.scitotenv.2019.03.109](https://doi.org/10.1016/j.scitotenv.2019.03.109).
- [9] Nganyanyuka K., Martinez J., Wesselink A., Lungo J.H., Georgiadou Y., Accessing Water Services in Dar Es Salaam: Are We Counting What Counts?, *Habitat Int*, **44** (2014) 358-366, [10.1016/j.habitatint.2014.07.003](https://doi.org/10.1016/j.habitatint.2014.07.003).
- [10] Satterthwaite D., Missing the Millennium Development Goal Targets for Water and Sanitation in Urban Areas, *Environ Urbanization*, **28** (2016) 99-118, [10.1177/0956247816628435](https://doi.org/10.1177/0956247816628435).
- [11] Adams E.A., Thirsty Slums in African Cities: Household Water Insecurity in Urban Informal Settlements of Lilongwe, Malawi, *Int. J. Water Resour. Dev.*, **34** (2017) 869-887, [10.1080/07900627.2017.1322941](https://doi.org/10.1080/07900627.2017.1322941).
- [12] Dos Santos S., Adams E.A., Neville G., Wada Y., de Sherbinin A., Mullin Bernhardt E., Adamo S.B., Urban Growth and Water Access in Sub-Saharan Africa: Progress, Challenges, and Emerging Research Directions, *Sci Total Environ*, **607-608** (2017) 497-508, [10.1016/j.scitotenv.2017.06.157](https://doi.org/10.1016/j.scitotenv.2017.06.157).

- [13] WHO, World Health Statistics 2013. Available from: <https://apps.who.int/iris/rest/bitstreams/289240/retrieve>, 22/04/2016.
- [14] Organisation W.H., World Health Statistics 2016: Monitoring Health for the Sdgs, Sustainable Development Goals. Available from: <https://apps.who.int/iris/rest/bitstreams/1435584/retrieve>, 18/07/2022.
- [15] Yongsi H.B.N., Suffering for Water, Suffering from Water: Accessto Drinking Water and Associated Health Risks in Cameroon, *J Health Population Nutr.*, **28** (2010) 424-435.
- [16] Djomassi L.D., Gessner B.D., Andze G.O., Mballa G.A., National Surveillance Data on the Epidemiology of Cholera in Cameroon, *J Infect Dis*, **208 Suppl 1** (2013) 592-597, [10.1093/infdis/jit197](https://doi.org/10.1093/infdis/jit197).
- [17] Cotruvo J.A., Andrew R., Herman R., Point of Use and Point of Entry Treatment Technologies Applicable in the Home for Controlling Chemical, Microbial, and Aesthetic Contaminants in Drinking Water, in: *Comprehensive Water Quality and Purification*, Elsevier Inc., 2014, pp. 196-211.
- [18] Sharma S., Bhattacharya A., Drinking Water Contamination and Treatment Techniques, *Appl Water Sci*, **7** (2016) 1043-1067, [10.1007/s13201-016-0455-7](https://doi.org/10.1007/s13201-016-0455-7).
- [19] Xagorarakis H.-W.D.K.a.I., Contaminants Associated with Drinking Water, in: *International Encyclopedia of Public Health*, Elsevier Inc., 2017. [10.1016/B978-0-12-803678-5.00489-6](https://doi.org/10.1016/B978-0-12-803678-5.00489-6).
- [20] Hlongwane G.N., Sekoai P.T., Meyyappan M., Moothi K., Simultaneous Removal of Pollutants from Water Using Nanoparticles: A Shift from Single Pollutant Control to Multiple Pollutant Control, *Sci Total Environ*, **656** (2019) 808-833, [10.1016/j.scitotenv.2018.11.257](https://doi.org/10.1016/j.scitotenv.2018.11.257).
- [21] Nguendo-Yongsi H.B., Microbiological Evaluation of Drinking Water in a Sub-Saharan Urban Community (Yaounde), *Am. J. Biochem. Mol. Biol.*, (2010).
- [22] Annan E., Kan-Dapaah K., Azeko S.T., Mustapha K., Asare J., Zebaze Kana M.G., Soboyejo W., Clay Mixtures and the Mechanical Properties of Microporous and Nanoporous Ceramic Water Filters, *J. Mater. Civ. Eng.*, **28** (2016) [10.1061/\(asce\)mt.1943-5533.0001596](https://doi.org/10.1061/(asce)mt.1943-5533.0001596).
- [23] Nigay P.-M., Nzihou A., White C.E., Soboyejo W.O., Removal Mechanisms of Contaminants in Ceramic Water Filters, *J Environ Eng*, **144** (2018) [10.1061/\(asce\)ee.1943-7870.0001471](https://doi.org/10.1061/(asce)ee.1943-7870.0001471).
- [24] Soboyejo P.-M.N.A.A.S.J.D.O.C.E.W.A.N.a.W.O., Ceramic Water Filters for the Removal of Bacterial, Chemical, and Viral Contaminants, *J. Environ. Eng.*, **145** (2019) [10.1061/\(ASCE\)](https://doi.org/10.1061/(ASCE)).
- [25] Al-Ghouti M.A., Da'ana D.A., Guidelines for the Use and Interpretation of Adsorption Isotherm Models: A Review, *J Hazard Mater*, **393** (2020) 122383, [10.1016/j.jhazmat.2020.122383](https://doi.org/10.1016/j.jhazmat.2020.122383).
- [26] Dina D.J.D. N.A.R., Ndi J.N. and Ketcha Mbadcam J., Adsorption of Acetic Acid onto Activated Carbons Obtained from Maize Cobs by Chemical Activation with Zinc Chloride (ZnCl₂), *Res. J. Chem. Sci.*, **2** (2012) 42-49.

- [27] Ahmed M.J., Adsorption of Quinolone, Tetracycline, and Penicillin Antibiotics from Aqueous Solution Using Activated Carbons: Review, *Environ Toxicol Pharmacol*, **50** (2017) 1-10, [10.1016/j.etap.2017.01.004](https://doi.org/10.1016/j.etap.2017.01.004).
- [28] Largitte L., Pasquier R., A Review of the Kinetics Adsorption Models and Their Application to the Adsorption of Lead by an Activated Carbon, *Chem. Eng. Res. Des.*, **109** (2016) 495-504, [10.1016/j.cherd.2016.02.006](https://doi.org/10.1016/j.cherd.2016.02.006).
- [29] Kyzas G.Z., Deliyanni E.A., Bikiaris D.N., Mitropoulos A.C., Graphene Composites as Dye Adsorbents: Review, *Chem. Eng. Res. Des.*, **129** (2018) 75-88, [10.1016/j.cherd.2017.11.006](https://doi.org/10.1016/j.cherd.2017.11.006).
- [30] Kim S., Park C.M., Jang M., Son A., Her N., Yu M., Snyder S., Kim D.H., Yoon Y., Aqueous Removal of Inorganic and Organic Contaminants by Graphene-Based Nano-adsorbents: A Review, *Chemosphere*, **212** (2018) 1104-1124, [10.1016/j.chemosphere.2018.09.033](https://doi.org/10.1016/j.chemosphere.2018.09.033).
- [31] Wan D., Chen F., Geng Q., Lu H., Willcock H., Liu Q., Wang F., Zou K., Jin M., Pu H., Du J., A Multifunctional Azobenzene-Based Polymeric Adsorbent for Effective Water Remediation, *Sci Rep*, **4** (2014) 7296, [10.1038/srep07296](https://doi.org/10.1038/srep07296).
- [32] Hu Y., Liu F., Sun Y., Xu X., Chen X., Pan B., Sun D., Qian J., Bacterial Cellulose Derived Paper-Like Purifier with Multifunctionality for Water Decontamination, *Chem. Eng. J.*, **371** (2019) 730-737, [10.1016/j.cej.2019.04.091](https://doi.org/10.1016/j.cej.2019.04.091).
- [33] Li L., Qi G., Wang B., Yue D., Wang Y., Sato T., Fulvic Acid Anchored Layered Double Hydroxides: A Multifunctional Composite Adsorbent for the Removal of Anionic Dye and Toxic Metal, *J Hazard Mater*, **343** (2018) 19-28, [10.1016/j.jhazmat.2017.09.006](https://doi.org/10.1016/j.jhazmat.2017.09.006).
- [34] Caldera F., Tannous M., Cavalli R., Zanetti M., Trotta F., Evolution of Cyclodextrin Nanosponges, *Int J Pharm*, **531** (2017) 470-479, [10.1016/j.ijpharm.2017.06.072](https://doi.org/10.1016/j.ijpharm.2017.06.072).
- [35] Sherje A.P., Dravyakar B.R., Kadam D., Jadhav M., Cyclodextrin-Based Nanosponges: A Critical Review, *Carbohydr Polym*, **173** (2017) 37-49, [10.1016/j.carbpol.2017.05.086](https://doi.org/10.1016/j.carbpol.2017.05.086).
- [36] Trotta F., Cavalli R., Characterization and Applications of New Hyper-Cross-Linked Cyclodextrins, *Compos. Interfaces*, **16** (2012) 39-48, [10.1163/156855408x379388](https://doi.org/10.1163/156855408x379388).
- [37] Selvamuthukumar Subramanian, Anandam Singireddy, Kannan Krishnamoorthy, Rajappan M., Nanosponges: A Novel Class of Drug Delivery System, *J. Pharm. Sci.*, **15** (2012) 103-111.
- [38] Min Ma, Li D., New Organic Nanoporous Polymers and Their Inclusion Complexes, *Chem. Mater.*, **11** (1999) 872-874.
- [39] Leudjo Taka A., Pillay K., Yangkou Mbianda X., Nanosponge Cyclodextrin Polyurethanes and Their Modification with Nanomaterials for the Removal of Pollutants from Waste Water: A Review, *Carbohydr Polym*, **159** (2017) 94-107, [10.1016/j.carbpol.2016.12.027](https://doi.org/10.1016/j.carbpol.2016.12.027).
- [40] Liu H., Cai X., Wang Y., Chen J., Adsorption Mechanism-Based Screening of Cyclodextrin Polymers for Adsorption and Separation of Pesticides from Water, *Water Res*, **45** (2011) 3499-3511, [10.1016/j.watres.2011.04.004](https://doi.org/10.1016/j.watres.2011.04.004).

- [41] Morin-Crini N., Crini G., Environmental Applications of Water-Insoluble B-Cyclodextrin–Epichlorohydrin Polymers, *Prog. Polym. Sci.*, **38** (2013) 344-368, [10.1016/j.progpolymsci.2012.06.005](https://doi.org/10.1016/j.progpolymsci.2012.06.005).
- [42] Garcia-Fernandez M.J., Tabary N., Chai F., Cazaux F., Blanchemain N., Flament M.P., Martel B., New Multifunctional Pharmaceutical Excipient in Tablet Formulation Based on Citric Acid-Cyclodextrin Polymer, *Int J Pharm*, **511** (2016) 913-920, [10.1016/j.ijpharm.2016.07.059](https://doi.org/10.1016/j.ijpharm.2016.07.059).
- [43] Zhao R., Wang Y., Li X., Sun B., Jiang Z., Wang C., Water-Insoluble Sericin/Beta-Cyclodextrin/Pva Composite Electrospun Nanofibers as Effective Adsorbents Towards Methylene Blue, *Colloids Surf B Biointerfaces*, **136** (2015) 375-382, [10.1016/j.colsurfb.2015.09.038](https://doi.org/10.1016/j.colsurfb.2015.09.038).
- [44] Zou C., Liu Y., Yan X., Qin Y., Wang M., Zhou L., Synthesis of Bridged B-Cyclodextrin–Polyethylene Glycol and Evaluation of Its Inhibition Performance in Oilfield Wastewater, *Mater Chem Phys*, **147** (2014) 521-527, [10.1016/j.matchemphys.2014.05.025](https://doi.org/10.1016/j.matchemphys.2014.05.025).
- [45] Krause R.W.M., Mamba B.B., Dlamini L.N., Durbach S.H., Fe–Ni Nanoparticles Supported on Carbon Nanotube-Co-Cyclodextrin Polyurethanes for the Removal of Trichloroethylene in Water, *J. Nanopart. Res.*, **12** (2009) 449-456, [10.1007/s11051-009-9659-1](https://doi.org/10.1007/s11051-009-9659-1).
- [46] Mphahlele K., Onyango M.S., Mhlanga S.D., Adsorption of Aspirin and Paracetamol from Aqueous Solution Using Fe/N-Cnt/B-Cyclodextrin Nanocomposites Synthesized Via a Benign Microwave Assisted Method, *J Environ Chem Eng*, **3** (2015) 2619-2630, [10.1016/j.jece.2015.02.018](https://doi.org/10.1016/j.jece.2015.02.018).
- [47] Kwon J.H., Wilson L.D., Surface Modified Activated Carbon with Beta-Cyclodextrin-Part I. Synthesis and Characterization, *J Environ Sci Health A Tox Hazard Subst Environ Eng*, **45** (2010) 1775-1792, [10.1080/10934529.2010.513290](https://doi.org/10.1080/10934529.2010.513290).
- [48] Kwon J.H., Wilson L.D., Surface-Modified Activated Carbon with Beta-Cyclodextrin-Part II. Adsorption Properties, *J Environ Sci Health A Tox Hazard Subst Environ Eng*, **45** (2010) 1793-1803, [10.1080/10934529.2010.513292](https://doi.org/10.1080/10934529.2010.513292).
- [49] Majumdar D., Sonochemically Synthesized Beta-Cyclodextrin Functionalized Graphene Oxide and Its Efficient Role in Adsorption of Water Soluble Brilliant Green Dye, *J. Environ. Anal. Toxicol.*, **6** (2016) [10.4172/2161-0525.1000402](https://doi.org/10.4172/2161-0525.1000402).
- [50] Yan J., Zhu Y., Qiu F., Zhao H., Yang D., Wang J., Wen W., Kinetic, Isotherm and Thermodynamic Studies for Removal of Methyl Orange Using a Novel B-Cyclodextrin Functionalized Graphene Oxide-Isophorone Diisocyanate Composites, *Chem. Eng. Res. Des.*, **106** (2016) 168-177, [10.1016/j.cherd.2015.12.023](https://doi.org/10.1016/j.cherd.2015.12.023).
- [51] Jiang L., Liu Y., Liu S., Hu X., Zeng G., Hu X., Liu S., Liu S., Huang B., Li M., Fabrication of B-Cyclodextrin/Poly (L -Glutamic Acid) Supported Magnetic Graphene Oxide and Its Adsorption Behavior for 17 β -Estradiol, *Chem. Eng. J.*, **308** (2017) 597-605, [10.1016/j.cej.2016.09.067](https://doi.org/10.1016/j.cej.2016.09.067).
- [52] Ragavan K.V., Rastogi N.K., Beta-Cyclodextrin Capped Graphene-Magnetite Nanocomposite for Selective Adsorption of Bisphenol-A, *Carbohydr Polym*, **168** (2017) 129-137, [10.1016/j.carbpol.2017.03.045](https://doi.org/10.1016/j.carbpol.2017.03.045).

- [53] Arslan M., Sayin S., Yilmaz M., Removal of Carcinogenic Azo Dyes from Water by New Cyclodextrin-Immobilized Iron Oxide Magnetic Nanoparticles, *Water Air Soil Pollut.* , **224** (2013) [10.1007/s11270-013-1527-z](https://doi.org/10.1007/s11270-013-1527-z).
- [54] Li R.X., Liu S.M., Zhao J.Q., Otsuka H., Takahara A., Preparation and Characterization of Cross-Linked B-Cyclodextrin Polymer/Fe₃O₄ Composite Nanoparticles with Core-Shell Structures, *Chin. Chem. Lett.* , **22** (2011) 217-220, [10.1016/j.ccllet.2010.09.014](https://doi.org/10.1016/j.ccllet.2010.09.014).
- [55] Badruddoza A.Z., Shawon Z.B., Tay W.J., Hidajat K., Uddin M.S., Fe₃O₄/Cyclodextrin Polymer Nanocomposites for Selective Heavy Metals Removal from Industrial Wastewater, *Carbohydr Polym*, **91** (2013) 322-332, [10.1016/j.carbpol.2012.08.030](https://doi.org/10.1016/j.carbpol.2012.08.030).
- [56] Ghorbani Z., Baharvand H., Nezhati M.N., Panahi H.A., Magnetic Polymer Particles Modified with B-Cyclodextrin, *J. Polym. Res.*, **20** (2013) [10.1007/s10965-013-0199-0](https://doi.org/10.1007/s10965-013-0199-0).
- [57] Gaber Ahmed G.H., Badía Laíño R., García Calzón J.A., Díaz García M.E., Magnetic Nanoparticles Grafted with B-Cyclodextrin for Solid-Phase Extraction of 5-Hydroxy-3-Indole Acetic Acid, *Microchimica Acta*, **181** (2014) 941-948, [10.1007/s00604-014-1192-y](https://doi.org/10.1007/s00604-014-1192-y).
- [58] Zhou Y., Sun L., Wang H., Liang W., Yang J., Wang L., Shuang S., Investigation on the Uptake and Release Ability of B-Cyclodextrin Functionalized Fe₃O₄ Magnetic Nanoparticles by Methylene Blue, *Mater. Chem. Phys.* , **170** (2016) 83-89, [10.1016/j.matchemphys.2015.12.022](https://doi.org/10.1016/j.matchemphys.2015.12.022).
- [59] Huang J., Su P., Zhao B., Yang Y., Facile One-Pot Synthesis of B-Cyclodextrin-Polymer-Modified Fe₃O₄ Microspheres for Stereoselective Absorption of Amino Acid Compounds, *Anal. Methods*, **7** (2015) 2754-2761, [10.1039/c5ay00013k](https://doi.org/10.1039/c5ay00013k).
- [60] Kiasat A.R., Nazari S., B-Cyclodextrin Conjugated Magnetic Nanoparticles as a Novel Magnetic Microvessel and Phase Transfer Catalyst: Synthesis and Applications in Nucleophilic Substitution Reaction of Benzyl Halides, *J. Inclusion Phenom. Macrocyclic Chem.* , **76** (2012) 363-368, [10.1007/s10847-012-0207-8](https://doi.org/10.1007/s10847-012-0207-8).
- [61] Abdolmaleki A., Mallakpour S., Mahmoudian M., Sabzalian M.R., A New Polyamide Adjusted Triazinyl-B-Cyclodextrin Side Group Embedded Magnetic Nanoparticles for Bacterial Capture, *Chem Eng J*, **309** (2017) 321-329, [10.1016/j.cej.2016.10.063](https://doi.org/10.1016/j.cej.2016.10.063).
- [62] Gong T., Zhou Y., Sun L., Liang W., Yang J., Shuang S., Dong C.J., Effective Adsorption of Phenolic Pollutants from Water Using B-Cyclodextrin Polymer Functionalized Fe₃O₄ Magnetic Nanoparticles, *RSC Adv.*, **6** (2016) 80955-80963.
- [63] Celebioglu A., Demirci S., Uyar T., Cyclodextrin-Grafted Electrospun Cellulose Acetate Nanofibers Via “Click” Reaction for Removal of Phenanthrene, *Appl. Surf. Sci.*, **305** (2014) 581-588, [10.1016/j.apsusc.2014.03.138](https://doi.org/10.1016/j.apsusc.2014.03.138).
- [64] Rima J., Assaker K., B-Cyclodextrin Polyurethanes Copolymerised with Beetroot Fibers (Bio-Polymer), for the Removal of Organic and Inorganic Contaminants from Water, *J Food Res*, **2** (2013) [10.5539/jfr.v2n1p150](https://doi.org/10.5539/jfr.v2n1p150).
- [65] Hu Q., Gao D.-W., Pan H., Hao L., Wang P., Equilibrium and Kinetics of Aniline Adsorption onto Crosslinked Sawdust-Cyclodextrin Polymers, *RSC Adv.*, **4** (2014) 40071-40077, [10.1039/c4ra05653a](https://doi.org/10.1039/c4ra05653a).
- [66] Campos E.V.R., Proenca P.L.F., Oliveira J.L., Melville C.C., Della Vechia J.F., de Andrade D.J., Fraceto L.F., Chitosan Nanoparticles Functionalized with Beta-

- Cyclodextrin: A Promising Carrier for Botanical Pesticides, *Sci Rep*, **8** (2018) 2067, [10.1038/s41598-018-20602-y](https://doi.org/10.1038/s41598-018-20602-y).
- [67] Kyzas G.Z., Lazaridis N.K., Bikiaris D.N., Optimization of Chitosan and Beta-Cyclodextrin Molecularly Imprinted Polymer Synthesis for Dye Adsorption, *Carbohydr Polym*, **91** (2013) 198-208, [10.1016/j.carbpol.2012.08.016](https://doi.org/10.1016/j.carbpol.2012.08.016).
- [68] Cornell R.M., Schwertmann U., The Iron Oxides Structure, Properties, Reactions, Occurrences and Uses.Pdf>, WILEY-VCH Verlag GmbH & Co, 2003,
- [69] Kugbe J., Matsue N., Henmi T., Synthesis of Linde Type a Zeolite-Goethite Nanocomposite as an Adsorbent for Cationic and Anionic Pollutants, *J Hazard Mater*, **164** (2009) 929-935, [10.1016/j.jhazmat.2008.08.080](https://doi.org/10.1016/j.jhazmat.2008.08.080).
- [70] Feynman R., Plenty of Room at the Bottom, *American Physical Society annual meeting, CalTech*, (1959).
- [71] Gakkai S., Proceedings of the International Conference on Production Engineering, Tokyo, 1974, in: Japan Society of Precision Engineering, Tokyo.
- [72] Mulvaney P., Nanoscience Vs Nanotechnology--Defining the Field, *ACS Nano*, **9** (2015) 2215-2217, [10.1021/acsnano.5b01418](https://doi.org/10.1021/acsnano.5b01418).
- [73] Trotta S.S.a.F., Nanosponges-Synthesis and Applications, WILEY-VCH, 2019, pp. 27-49
- [74] Ninithi, Nanomaterials. Available from: <https://ninithi.wordpress.com/nanomaterials/.Date> Accessed
- [75] Habiba K M.V., Weiner BR, Morell G. , Fabrication of Nanomaterials by Pulsed Laser Synthesis, in: A.N. Waqar A (Ed.) Manufacturing Nanostructures, UK, 2014.
- [76] Gubbels E., Melt Copolymerisation and Solid-State Modification as Methods to Prepare Novel Bio-Based Nanocomposites. Technische Universiteit Eindhoven,(2014)
- [77] Khanna P., Kaur A., Goyal D., Algae-Based Metallic Nanoparticles: Synthesis, Characterization and Applications, *J Microbiol Methods*, **163** (2019) 105656, [10.1016/j.mimet.2019.105656](https://doi.org/10.1016/j.mimet.2019.105656).
- [78] Aytac Z., Kusku S.I., Durgun E., Uyar T., Quercetin/Beta-Cyclodextrin Inclusion Complex Embedded Nanofibres: Slow Release and High Solubility, *Food Chem*, **197** (2016) 864-871, [10.1016/j.foodchem.2015.11.051](https://doi.org/10.1016/j.foodchem.2015.11.051).
- [79] Song W., Yu X., Wang S., Blasier R., Markel D.C., Mao G., Shi T., Ren W., Cyclodextrin-Erythromycin Complexes as a Drug Delivery Device for Orthopedic Application, *Int J Nanomedicine*, **6** (2011) 3173-3186, [10.2147/IJN.S23530](https://doi.org/10.2147/IJN.S23530).
- [80] Tang W., Zou C., Da C., Cao Y., Peng H., A Review on the Recent Development of Cyclodextrin-Based Materials Used in Oilfield Applications, *Carbohydr Polym*, **240** (2020) 116321, [10.1016/j.carbpol.2020.116321](https://doi.org/10.1016/j.carbpol.2020.116321).
- [81] Kayaci F., Uyar T., Solid Inclusion Complexes of Vanillin with Cyclodextrins: Their Formation, Characterization, and High-Temperature Stability, *J Agric Food Chem*, **59** (2011) 11772-11778, [10.1021/jf202915c](https://doi.org/10.1021/jf202915c).
- [82] Song L.X., Teng C.F., Xu P., Wang H.M., Zhang Z.Q., Liu Q.Q., Thermal Decomposition Behaviors of B-Cyclodextrin, Its Inclusion Complexes of Alkyl

- Amines, and Complexed B-Cyclodextrin at Different Heating Rates, *J. Inclusion Phenom. Macrocyclic Chem.*, **60** (2007) 223-233, [10.1007/s10847-007-9369-1](https://doi.org/10.1007/s10847-007-9369-1).
- [83] Erdoğar N., Varan G., Varan C., Bilensoy E., Cyclodextrin-Based Polymeric Nanosystems, in: Drug Targeting and Stimuli Sensitive Drug Delivery Systems, Elsevier Inc., 2018, pp. 715-748.
- [84] Cheirsilp B., Kittha S., Maneerat S., Kinetic Characteristics of B-Cyclodextrin Production by Cyclodextrin Glycosyltransferase from Newly Isolated Bacillus Sp. C26, *Electron. J. Biotechnol.*, **13** (2010) [10.2225/vol13-issue4-fulltext-6](https://doi.org/10.2225/vol13-issue4-fulltext-6).
- [85] Ahmed R.Z., Patil G., Zaheer Z., Nanosponges - a Completely New Nano-Horizon: Pharmaceutical Applications and Recent Advances, *Drug Dev Ind Pharm*, **39** (2013) 1263-1272, [10.3109/03639045.2012.694610](https://doi.org/10.3109/03639045.2012.694610).
- [86] Sharma N., Baldi A., Exploring Versatile Applications of Cyclodextrins: An Overview, *Drug Deliv*, **23** (2016) 739-757, [10.3109/10717544.2014.938839](https://doi.org/10.3109/10717544.2014.938839).
- [87] Zhao H.T., Ma S., Zheng S.Y., Han S.W., Yao F.X., Wang X.Z., Wang S.S., Feng K., Beta-Cyclodextrin Functionalized Biochars as Novel Sorbents for High-Performance of Pb(2+) Removal, *J Hazard Mater*, **362** (2019) 206-213, [10.1016/j.jhazmat.2018.09.027](https://doi.org/10.1016/j.jhazmat.2018.09.027).
- [88] Sikder M.T., Rahman M.M., Jakariya M., Hosokawa T., Kurasaki M., Saito T., Remediation of Water Pollution with Native Cyclodextrins and Modified Cyclodextrins: A Comparative Overview and Perspectives, *Chem. Eng. J.*, **355** (2019) 920-941, [10.1016/j.cej.2018.08.218](https://doi.org/10.1016/j.cej.2018.08.218).
- [89] Dora C.P., Trotta F., Kushwah V., Devasari N., Singh C., Suresh S., Jain S., Potential of Erlotinib Cyclodextrin Nanosponge Complex to Enhance Solubility, Dissolution Rate, in Vitro Cytotoxicity and Oral Bioavailability, *Carbohydr Polym*, **137** (2016) 339-349, [10.1016/j.carbpol.2015.10.080](https://doi.org/10.1016/j.carbpol.2015.10.080).
- [90] Ma D.L.a.M., Nanosponges for Water Purification, *Clean Prod. Processes* **2**(2000) 112-116.
- [91] <New Organic Nanoporous Polymers Nd Their Inclusion Complexes.Pdf>.
- [92] Krabicova I., Appleton S.L., Tannous M., Hoti G., Caldera F., Rubin Pedrazzo A., Cecone C., Cavalli R., Trotta F., History of Cyclodextrin Nanosponges, *Polymers (Basel)*, **12** (2020) [10.3390/polym12051122](https://doi.org/10.3390/polym12051122).
- [93] Agocs T.Z., Puskas I., Varga E., Molnar M., Fenyvesi E., Stabilization of Nanosized Titanium Dioxide by Cyclodextrin Polymers and Its Photocatalytic Effect on the Degradation of Wastewater Pollutants, *Beilstein J Org Chem*, **12** (2016) 2873-2882, [10.3762/bjoc.12.286](https://doi.org/10.3762/bjoc.12.286).
- [94] Badruddoza A.Z., Tay A.S., Tan P.Y., Hidajat K., Uddin M.S., Carboxymethyl-Beta-Cyclodextrin Conjugated Magnetic Nanoparticles as Nano-Adsorbents for Removal of Copper Ions: Synthesis and Adsorption Studies, *J Hazard Mater*, **185** (2011) 1177-1186, [10.1016/j.jhazmat.2010.10.029](https://doi.org/10.1016/j.jhazmat.2010.10.029).
- [95] G. Crini S.F., É. Fenyvesi, G. Torri, M. Fourmentin, and N. Morin-Crini, Fundamentals And applications Of cyclodextrins, in: G.C. Sophie Fourmentin, Eric Lichtfouse (Ed.) Cyclodextrin Fundamentals, Reactivity and Analysis, Springer International Publishing, 2018, pp. 1-56.

- [96] Menezes P.D.P., Andrade T.A., Frank L.A., de Souza E., Trindade G., Trindade I.A.S., Serafini M.R., Guterres S.S., Araujo A.A.S., Advances of Nanosystems Containing Cyclodextrins and Their Applications in Pharmaceuticals, *Int J Pharm*, **559** (2019) 312-328, [10.1016/j.ijpharm.2019.01.041](https://doi.org/10.1016/j.ijpharm.2019.01.041).
- [97] Loftsson T., Brewster M.E., Pharmaceutical Applications of Cyclodextrins: Basic Science and Product Development, *J Pharm Pharmacol*, **62** (2010) 1607-1621, [10.1111/j.2042-7158.2010.01030.x](https://doi.org/10.1111/j.2042-7158.2010.01030.x).
- [98] Zhenzhen W., Yinli L., Hongmei H., Jianyong Y., Faxue L., Biodegradable Poly (Butylene Succinate-Co-Terephthalate) Nanofibrous Membranes Functionalized with Cyclodextrin Polymer for Effective Methylene Blue Adsorption *R. Soc. Chem*, (2016) [10.1039/C6RA22941G](https://doi.org/10.1039/C6RA22941G)
[10.1039/x0xx00000x](https://doi.org/10.1039/x0xx00000x).
- [99] Yuan G., Prabakaran M., Qilong S., Lee J.S., Chung I.-M., Gopiraman M., Song K.-H., Kim I.S., Cyclodextrin Functionalized Cellulose Nanofiber Composites for the Faster Adsorption of Toluene from Aqueous Solution, *J. Taiwan Inst. Chem. Eng.*, **70** (2017) 352-358, [10.1016/j.jtice.2016.10.028](https://doi.org/10.1016/j.jtice.2016.10.028).
- [100] Astray G., Mejuto J.C., Simal-Gandara J., Latest Developments in the Application of Cyclodextrin Host-Guest Complexes in Beverage Technology Processes, *Food Hydrocolloids*, **106** (2020) [10.1016/j.foodhyd.2020.105882](https://doi.org/10.1016/j.foodhyd.2020.105882).
- [101] Alvarez M., Sileo E.E., Rueda E.H., Structure and Reactivity of Synthetic Co-Substituted Goethites, *American Mineralogist*, **93** (2008) 584-590, [10.2138/am.2008.2608](https://doi.org/10.2138/am.2008.2608).
- [102] Gilbert F., Refait P., Lévêque F., Remazeilles C., Conforto E., Synthesis of Goethite from Fe(OH)₂ Precipitates: Influence of Fe(II) Concentration and Stirring Speed, *J. Phys. Chem. Solids* **69** (2008) 2124-2130, [10.1016/j.jpcs.2008.03.010](https://doi.org/10.1016/j.jpcs.2008.03.010).
- [103] Yang H., Lu R., Downs R.T., Costin G., Goethite, A-Feo(OH), from Single-Crystal Data, *Acta Crystallogr. Sect. E: Struct. Rep. Online*, **62** (2006) i250-i252, [10.1107/s1600536806047258](https://doi.org/10.1107/s1600536806047258).
- [104] Guo H., Barnard A.S., Naturally Occurring Iron Oxide Nanoparticles: Morphology, Surface Chemistry and Environmental Stability, *J. Mater. Chem. A*, **1** (2013) 27-42, [10.1039/c2ta00523a](https://doi.org/10.1039/c2ta00523a).
- [105] R. M. Cornell U.S., The Iron Oxides: Structure, Properties, Reactions, Occurrences and Uses, WILEY-VCH Verlag GmbH & Co, 2003,
- [106] Mohapatra M., Rout K., Gupta S.K., Singh P., Anand S., Mishra B.K., Facile Synthesis of Additive-Assisted Nano Goethite Powder and Its Application for Fluoride Remediation, *J. Nanopart. Res.*, **12** (2009) 681-686, [10.1007/s11051-009-9779-7](https://doi.org/10.1007/s11051-009-9779-7).
- [107] Kosmulski M., Durand-Vidal S., Maczka E., Rosenholm J.B., Morphology of Synthetic Goethite Particles, *J Colloid Interface Sci*, **271** (2004) 261-269, [10.1016/j.jcis.2003.10.032](https://doi.org/10.1016/j.jcis.2003.10.032).
- [108] Kimberly M. C., Yunfeng L., Gary M., Tonghua Z., Jingjing Z., Vijay J., Nanotechnology for Clean Water Applications, in: J. ramsden (Ed.), William Andrew inc., 2009, pp. 347-364.

- [109] Samira Bagheri C.K.G.a.S.B.A.H., Generation of Hematite Nanoparticles Via Sol-Gel Method, *Research Journal of Chemical Sciences*, **3** (2013) 62-68.
- [110] Liu H., Chen T., Frost R.L., An Overview of the Role of Goethite Surfaces in the Environment, *Chemosphere*, **103** (2014) 1-11, [10.1016/j.chemosphere.2013.11.065](https://doi.org/10.1016/j.chemosphere.2013.11.065).
- [111] Yousef H.H.a.H., A Study on the Use of Nano/Micro Structured Goethite and Hematite as Adsorbents for the Removal of Cr(II), Co(II), Cu(II), Ni(II), and Zn(II) Metal Ions from Aqueous Solutions, *Int. J. Eng. Sci. Technol.*, **4** (2012).
- [112] Chen Y.H., Li F.A., Kinetic Study on Removal of Copper(II) Using Goethite and Hematite Nano-Photocatalysts, *J Colloid Interface Sci*, **347** (2010) 277-281, [10.1016/j.jcis.2010.03.050](https://doi.org/10.1016/j.jcis.2010.03.050).
- [113] Nguyen V.D., Kynicky J., Ambrozova P., Adam V., Microwave-Assisted Synthesis of Goethite Nanoparticles Used for Removal of Cr(VI) from Aqueous Solution, *Mater (Basel)*, **10** (2017) [10.3390/ma10070783](https://doi.org/10.3390/ma10070783).
- [114] M. Mohapatra L.M., P. Singh, S. Anand and B.K. Mishra, A Comparative Study on Pb(II), Cd(II), Cu(II), Co(II) Adsorption from Single and Binary Aqueous Solutions on Additive Assisted Nano-Structured Goethite, *Int J Eng, Sci Technol*, **2** (2010) 89-103.
- [115] Dan Nicolae U., Nicolae A., Rodica Mariana I., Elena Valentina S., Cristiana Zizi R., Synthesis and Characterization of Hydroxyapatite Nanopowders by Chemical Precipitation, *Recent Res. Commun. Autom Sign. Proces. Nanotechnol Astron. Nucl. Phys.*, 296-301.
- [116] Nayak B., Samant A., Misra P.K., Saxena M., Nanocrystalline Hydroxyapatite: A Potent Material for Adsorption, Biological and Catalytic Studies, *Mater Today: Proc*, **9** (2019) 689-698, [10.1016/j.matpr.2018.11.015](https://doi.org/10.1016/j.matpr.2018.11.015).
- [117] Fan S., Huang Z., Zhang Y., Hu H., Liang X., Gong S., Zhou J., Tu R., Magnetic Chitosan-Hydroxyapatite Composite Microspheres: Preparation, Characterization, and Application for the Adsorption of Phenolic Substances, *Bioresour Technol*, **274** (2019) 48-55, [10.1016/j.biortech.2018.11.078](https://doi.org/10.1016/j.biortech.2018.11.078).
- [118] Rivera-Muñoz E.M., Hydroxyapatite-Based Materials: Synthesis and Characterization, in: R. Fazel (Ed.) *Biomed Eng – Front Challenges*, InTech, 2011.
- [119] Jung K.-W., Lee S.Y., Choi J.-W., Lee Y.J., A Facile One-Pot Hydrothermal Synthesis of Hydroxyapatite/Biochar Nanocomposites: Adsorption Behavior and Mechanisms for the Removal of Copper(II) from Aqueous Media, *Chem. Eng. J.*, **369** (2019) 529-541, [10.1016/j.cej.2019.03.102](https://doi.org/10.1016/j.cej.2019.03.102).
- [120] Xia X., Shen J., Cao F., Wang C., Tang M., Zhang Q., Wei S., A Facile Synthesis of Hydroxyapatite for Effective Removal Strontium Ion, *J Hazard Mater*, **368** (2019) 326-335, [10.1016/j.jhazmat.2019.01.040](https://doi.org/10.1016/j.jhazmat.2019.01.040).
- [121] Guo H., Jiang C., Xu Z., Luo P., Fu Z., Zhang J., Synthesis of Bitter Gourd-Shaped Nanoscaled Hydroxyapatite and Its Adsorption Property for Heavy Metal Ions, *Materials Letters*, **241** (2019) 176-179, [10.1016/j.matlet.2019.01.028](https://doi.org/10.1016/j.matlet.2019.01.028).
- [122] Du J., Gan S., Bian Q., Fu D., Wei Y., Wang K., Lin Q., Chen W., Huang D., Preparation and Characterization of Porous Hydroxyapatite/Beta-Cyclodextrin-Based Polyurethane Composite Scaffolds for Bone Tissue Engineering, *J Biomater Appl*, **33** (2018) 402-409, [10.1177/0885328218797545](https://doi.org/10.1177/0885328218797545).

- [123] Attia M.A., Moussa S.I., Sheha R.R., Someda H.H., Saad E.A., Hydroxyapatite/NiFe₂O₄ Superparamagnetic Composite: Facile Synthesis and Adsorption of Rare Elements, *Appl Radiat Isot*, **145** (2019) 85-94, [10.1016/j.apradiso.2018.12.003](https://doi.org/10.1016/j.apradiso.2018.12.003).
- [124] Oulguidoum A., Bouyarmene H., Laghzizil A., Nunzi J.-M., Saoiabi A., Development of Sulfonate-Functionalized Hydroxyapatite Nanoparticles for Cadmium Removal from Aqueous Solutions, *Colloid Interface Sci. Commun.*, **30** (2019) [10.1016/j.colcom.2019.100178](https://doi.org/10.1016/j.colcom.2019.100178).
- [125] W. Yi L.L., H. He, Z. Hao, B. Liu, Y. Shen and Z. Chao, Synthesis of Poly(L-Lactide)/B-Cyclodextrin/Citrate Networks Modified Hydroxyapatite and Its Biomedical Properties *New J. Chem.*, (2018) [10.1039/C8NJ01194J](https://doi.org/10.1039/C8NJ01194J)
[10.1039/x0xx00000x](https://doi.org/10.1039/x0xx00000x).
- [126] S J., S S., V S.R., M S., Facile Green Synthesis of Silver Doped Fluor-Hydroxyapatite/B-Cyclodextrin Nanocomposite in the Dual Acting Fluorine-Containing Ionic Liquid Medium for Bone Substitute Applications, *Appl. Surf. Sci.*, **371** (2016) 468-478, [10.1016/j.apsusc.2016.03.007](https://doi.org/10.1016/j.apsusc.2016.03.007).
- [127] Dai Y., Sun Q., Wang W., Lu L., Liu M., Li J., Yang S., Sun Y., Zhang K., Xu J., Zheng W., Hu Z., Yang Y., Gao Y., Chen Y., Zhang X., Gao F., Zhang Y., Utilizations of Agricultural Waste as Adsorbent for the Removal of Contaminants: A Review, *Chemosphere*, **211** (2018) 235-253, [10.1016/j.chemosphere.2018.06.179](https://doi.org/10.1016/j.chemosphere.2018.06.179).
- [128] Harmanescu M., Alda L.M., Bordean D.M., Gogoasa I., Gergen I., Heavy Metals Health Risk Assessment for Population Via Consumption of Vegetables Grown in Old Mining Area; a Case Study: Banat County, Romania, *Chem Cent J*, **5** (2011) 64, [10.1186/1752-153X-5-64](https://doi.org/10.1186/1752-153X-5-64).
- [129] Repo E., Kurniawan T.A., Warchol J.K., Sillanpaa M.E., Removal of Co(II) and Ni(II) Ions from Contaminated Water Using Silica Gel Functionalized with Edta and/or Dtpa as Chelating Agents, *J Hazard Mater*, **171** (2009) 1071-1080, [10.1016/j.jhazmat.2009.06.111](https://doi.org/10.1016/j.jhazmat.2009.06.111).
- [130] Zan F., Huo S., Xi B., Su J., Li X., Zhang J., Yeager K.M., A 100 Year Sedimentary Record of Heavy Metal Pollution in a Shallow Eutrophic Lake, Lake Chaohu, China, *J Environ Monit*, **13** (2011) 2788-2797, [10.1039/c1em10385g](https://doi.org/10.1039/c1em10385g).
- [131] WHO, Guidelines for Drinking Water Quality, (2011).
- [132] H. Aregawi B., A. Mengistie A., Removal of Ni(II) from Aqueous Solution Using Leaf, Bark and Seed of *Moringa Stenopetala* Adsorbents, *Bull. Chem. Soc. Ethiop.*, **27** (2012) [10.4314/bcse.v27i1.4](https://doi.org/10.4314/bcse.v27i1.4).
- [133] Curtis D. Klaassen M.O.A., John Doull, Casarett & Doull's Toxicology-the Basic Science of Poisons, McGraw-Hill Education, 2019,
- [134] O. Olayinka Kehinde T.A.O., and O. Oyeyiola Aderonke, Comparative Analysis of the Efficiencies of Two Low Cost Adsorbents in the Removal of Cr(VI) and Ni(II) from Aqueous Solution, *Afr J Eng, Sci Technol*, **3** (2009) 360-369.
- [135] P. Apostoli B.R.C.J.D., Edinburgh; P. Hoet, D. Lison and Professor D. Templeton. Elemental Speciation in Human Health Risk Assessment(2006).

- [136] Chuah C.J., Lye H.R., Ziegler A.D., Wood S.H., Kongpun C., Rajchagool S., Fluoride: A Naturally-Occurring Health Hazard in Drinking-Water Resources of Northern Thailand, *Sci Total Environ*, **545-546** (2016) 266-279, [10.1016/j.scitotenv.2015.12.069](https://doi.org/10.1016/j.scitotenv.2015.12.069).
- [137] Craig L., Lutz A., Berry K.A., Yang W., Recommendations for Fluoride Limits in Drinking Water Based on Estimated Daily Fluoride Intake in the Upper East Region, Ghana, *Sci Total Environ*, **532** (2015) 127-137, [10.1016/j.scitotenv.2015.05.126](https://doi.org/10.1016/j.scitotenv.2015.05.126).
- [138] Hiew B.Y.Z., Lee L.Y., Lee X.J., Thangalazhy-Gopakumar S., Gan S., Lim S.S., Pan G.-T., Yang T.C.-K., Chiu W.S., Khiew P.S., Review on Synthesis of 3d Graphene-Based Configurations and Their Adsorption Performance for Hazardous Water Pollutants, *Process Saf. Environ. Prot.* , **116** (2018) 262-286, [10.1016/j.psep.2018.02.010](https://doi.org/10.1016/j.psep.2018.02.010).
- [139] Jia P., Tan H., Liu K., Gao W., Removal of Methylene Blue from Aqueous Solution by Bone Char, *Appl. Sci.*, **8** (2018) [10.3390/app8101903](https://doi.org/10.3390/app8101903).
- [140] Hooshyari G., Evaluating Filter Materials for E. Coli Removal from Stormwater. South Dakota State University, (2017)
- [141] Ihsanullah, Abbas A., Al-Amer A.M., Laoui T., Al-Marri M.J., Nasser M.S., Khraisheh M., Atieh M.A., Heavy Metal Removal from Aqueous Solution by Advanced Carbon Nanotubes: Critical Review of Adsorption Applications, *Sep. Purif. Technol.* , **157** (2016) 141-161, [10.1016/j.seppur.2015.11.039](https://doi.org/10.1016/j.seppur.2015.11.039).
- [142] Roque-Malherbe R.M.A., Adsorption and Diffusion in Nanoporous Materials Taylor & Francis Group, LLC, 2007,
- [143] Sophia A.C., Lima E.C., Removal of Emerging Contaminants from the Environment by Adsorption, *Ecotoxicol Environ Saf*, **150** (2018) 1-17, [10.1016/j.ecoenv.2017.12.026](https://doi.org/10.1016/j.ecoenv.2017.12.026).
- [144] Mouni L., Belkhiri L., Bollinger J.-C., Bouzaza A., Assadi A., Tirri A., Dahmoune F., Madani K., Remini H., Removal of Methylene Blue from Aqueous Solutions by Adsorption on Kaolin: Kinetic and Equilibrium Studies, *Appl. Clay Sci.* , **153** (2018) 38-45, [10.1016/j.clay.2017.11.034](https://doi.org/10.1016/j.clay.2017.11.034).
- [145] P. Atkins J.D.P., Atkins' Physical Chemistry, Oxford University Press, Great Britain, 2006,
- [146] Zhao L., Deng J., Sun P., Liu J., Ji Y., Nakada N., Qiao Z., Tanaka H., Yang Y., Nanomaterials for Treating Emerging Contaminants in Water by Adsorption and Photocatalysis: Systematic Review and Bibliometric Analysis, *Sci Total Environ*, **627** (2018) 1253-1263, [10.1016/j.scitotenv.2018.02.006](https://doi.org/10.1016/j.scitotenv.2018.02.006).
- [147] Suyamboo B.K., Equilibrium, Thermodynamic and Kinetic Studies on Adsorption of a Basic Dye by Citrullus Lanatus Rind, *Iranica J Eng Environ*, **3** (2012) 23-34, [10.5829/idosi.ijee.2012.03.01.0130](https://doi.org/10.5829/idosi.ijee.2012.03.01.0130).
- [148] Ngomo H.M., Anagho G.S., Ngakou C.S., Non-Linear Regression Analysis for the Adsorption Kinetics and Equilibrium Isotherm of Phenacetin onto Activated Carbons, *Curr J Appl Sci Technol*, (2019) 1-18, [10.9734/cjast/2019/v36i430246](https://doi.org/10.9734/cjast/2019/v36i430246).
- [149] Chen X., Modeling of Experimental Adsorption Isotherm Data, *Inf*, **6** (2015) 14-22, [10.3390/info6010014](https://doi.org/10.3390/info6010014).

- [150] Wang C., Boithias L., Ning Z., Han Y., Sauvage S., Sánchez-Pérez J.-M., Kuramochi K., Hatano R., Comparison of Langmuir and Freundlich Adsorption Equations within the Swat-K Model for Assessing Potassium Environmental Losses at Basin Scale, *Agric Water Manage*, **180** (2017) 205-211, [10.1016/j.agwat.2016.08.001](https://doi.org/10.1016/j.agwat.2016.08.001).
- [151] Wu F.-C., Liu B.-L., Wu K.-T., Tseng R.-L., A New Linear Form Analysis of Redlich–Peterson Isotherm Equation for the Adsorptions of Dyes, *Chem. Eng. J.*, **162** (2010) 21-27, [10.1016/j.cej.2010.03.006](https://doi.org/10.1016/j.cej.2010.03.006).
- [152] Ayawei N., Ebelegi A.N., Wankasi D., Modelling and Interpretation of Adsorption Isotherms, *J Chem*, **2017** (2017) 1-11, [10.1155/2017/3039817](https://doi.org/10.1155/2017/3039817).
- [153] Wu F.-C., Tseng R.-L., Juang R.-S., Characteristics of Elovich Equation Used for the Analysis of Adsorption Kinetics in Dye-Chitosan Systems, *Chem Eng J*, **150** (2009) 366-373, [10.1016/j.cej.2009.01.014](https://doi.org/10.1016/j.cej.2009.01.014).
- [154] Foo K.Y., Hameed B.H., Insights into the Modeling of Adsorption Isotherm Systems, *Chem. Eng. J.*, **156** (2010) 2-10, [10.1016/j.cej.2009.09.013](https://doi.org/10.1016/j.cej.2009.09.013).
- [155] Miraboutalebi S.M., Nikouzad S.K., Peydayesh M., Allahgholi N., Vafajoo L., McKay G., Methylene Blue Adsorption Via Maize Silk Powder: Kinetic, Equilibrium, Thermodynamic Studies and Residual Error Analysis, *Process Saf. Environ. Prot.*, **106** (2017) 191-202, [10.1016/j.psep.2017.01.010](https://doi.org/10.1016/j.psep.2017.01.010).
- [156] Md Anwar Hossain H.H.N., Wenshan Guo, Introductory of Microsoft Excel Solver Function - Spreadsheet Method for Isotherm and Kinetics Modelling of Metals Biosorption in Water and Wastewater, *J Water Sustainability*, **3** (2013) 223-237.
- [157] Berger J.A.C.a.R.D., Factors That Influence the Value of the Coefficient of Determination in Simple Linear and Nonlinear Regression Models, *Phytopathology* **77** (1986) 63-70.
- [158] Ahmed M.J., Hameed B.H., Removal of Emerging Pharmaceutical Contaminants by Adsorption in a Fixed-Bed Column: A Review, *Ecotoxicol Environ Saf*, **149** (2018) 257-266, [10.1016/j.ecoenv.2017.12.012](https://doi.org/10.1016/j.ecoenv.2017.12.012).
- [159] López-Cervantes J., Sánchez-Machado D.I., Sánchez-Duarte R.G., Correa-Murrieta M.A., Study of a Fixed-Bed Column in the Adsorption of an Azo Dye from an Aqueous Medium Using a Chitosan–Glutaraldehyde Biosorbent, *Adsorpt. Sci. Technol.*, **36** (2017) 215-232, [10.1177/0263617416688021](https://doi.org/10.1177/0263617416688021).
- [160] Scherdel C., Reichenauer G., Wiener M., Relationship between Pore Volumes and Surface Areas Derived from the Evaluation of N₂-Sorption Data by Dr-, Bet- and T-Plot, *Microporous Mesoporous Mater.*, **132** (2010) 572-575, [10.1016/j.micromeso.2010.03.034](https://doi.org/10.1016/j.micromeso.2010.03.034).
- [161] Neil Gibson P.K., Kirsten Rasmussen, Vasile-Dan Hodoroaba, Hubert Rauscher, Volume-Specific Surface Area by Gas Adsorption Analysis with the Bet Method, Elsevier Inc., 2020, pp. 265-294. [10.1016/B978-0-12-814182-3.00017-1](https://doi.org/10.1016/B978-0-12-814182-3.00017-1)
- [162] Singh P.S.N.a.B.K., Instrumental Characterization of Clay by Xrf, Xrd and Ftir, *Bull. Mater. Sci.*, **30** (2007) 235-238.
- [163] Davies P.L., Gather U., Meise M., Mergel D., Mildenberger T., Residual-Based Localization and Quantification of Peaks in X-Ray Diffractograms, *Annals Appl. Stat.*, **2** (2008) 861-886, [10.1214/08-aos181](https://doi.org/10.1214/08-aos181).

- [164] Jan Masta E.V., Vasile-Dan Hodoroaba, Ralf Kaegi, Characterization of Nanomaterials by Transmission Electron Microscopy: Measurement Procedures, Elsevier Inc., 2019.[10.1016/B978-0-12-814182-3.00004-3](https://doi.org/10.1016/B978-0-12-814182-3.00004-3)
- [165] Marturi N., Vision and Visual Servoing for Nanomanipulation and Nanocharacterization in Scanning Electron Microscope. Universite de Franche-Comte, (2013)
- [166] Egami T., Billinge S.J., Underneath the Bragg Peaks: Structural Analysis of Complex Materials, Newnes, 2012,
- [167] Bell J.L., Sarin P., Provis J.L., Haggerty R.P., Driemeyer P.E., Chupas P.J., van Deventer J.S.J., Kriven W.M., Atomic Structure of a Cesium Aluminosilicate Geopolymer: A Pair Distribution Function Study, *Chem. Mater.* , **20** (2008) 4768-4776, [10.1021/cm703369s](https://doi.org/10.1021/cm703369s).
- [168] Young C.A., Goodwin A.L., Applications of Pair Distribution Function Methods to Contemporary Problems in Materials Chemistry, *J. Mater. Chem.* , **21** (2011) [10.1039/c0jm04415f](https://doi.org/10.1039/c0jm04415f).
- [169] Billinge S.J., Nanoscale Structural Order from the Atomic Pair Distribution Function (Pdf): There's Plenty of Room in the Middle, *J. Solid State Chem.* , **181** (2008) 1695-1700.
- [170] Billinge S.J., Kanatzidis M.G., Beyond Crystallography: The Study of Disorder, Nanocrystallinity and Crystallographically Challenged Materials with Pair Distribution Functions, *Chem Commun (Camb)*, (2004) 749-760, [10.1039/b309577k](https://doi.org/10.1039/b309577k).
- [171] Farrow C.L., Billinge S.J., Relationship between the Atomic Pair Distribution Function and Small-Angle Scattering: Implications for Modeling of Nanoparticles, *Acta Crystallogr., Sect. A: Found. Crystallogr.* , **65** (2009) 232-239.
- [172] Billinge S.J., Dykhne T., Juhás P., Božin E., Taylor R., Florence A.J., Shankland K., Characterisation of Amorphous and Nanocrystalline Molecular Materials by Total Scattering, *J Cryst Eng Comm*, **12** (2010) 1366-1368.
- [173] Dykhne T., Taylor R., Florence A., Billinge S.J., Data Requirements for the Reliable Use of Atomic Pair Distribution Functions in Amorphous Pharmaceutical Fingerprinting, *Pharm. Res.*, **28** (2011) 1041-1048.
- [174] Farrow C.L., Juhas P., Liu J.W., Bryndin D., Bozin E.S., Bloch J., Proffen T., Billinge S.J., PdfFit2 and Pdfgui: Computer Programs for Studying Nanostructure in Crystals, *J Phys Condens Matter*, **19** (2007) 335219, [10.1088/0953-8984/19/33/335219](https://doi.org/10.1088/0953-8984/19/33/335219).
- [175] Juhas P., Farrow C.L., Yang X., Knox K.R., Billinge S.J., Complex Modeling: A Strategy and Software Program for Combining Multiple Information Sources to Solve Ill Posed Structure and Nanostructure Inverse Problems, *Acta Crystallogr A Found Adv*, **71** (2015) 562-568, [10.1107/S2053273315014473](https://doi.org/10.1107/S2053273315014473).
- [176] Plante A.F., Fernández J.M., Leifeld J., Application of Thermal Analysis Techniques in Soil Science, *Geoderma*, **153** (2009) 1-10, [10.1016/j.geoderma.2009.08.016](https://doi.org/10.1016/j.geoderma.2009.08.016).
- [177] N. G. Hădărugă G.N.B., and D. I. Hădărugă, Thermal Analyses Of cyclodextrin Complexes, in: G.C. Sophie Fourmentin, Eric Lichtfouse (Ed.) Cyclodextrin Fundamentals, Reactivity and Analysis, Springer International Publishing, 2048, pp. 155-221.

- [178] Toraldo F., New Frontiers of Cyclodextrin-Based Nanosponges: From Synthesis to Physical Investigation. Politecnico Di Milano, (2014)
- [179] Szejtli J., Introduction and General Overview of Cyclodextrin Chemistry, *Chem Rev*, **98** (1998) 1743-1754, [10.1021/cr970022c](https://doi.org/10.1021/cr970022c).
- [180] G. H. Lee S.H.K., B. J. Choi, S. H. Huh, Y. Chang, B. Kim, J. Park and S. J. Oh, Magnetic Properties of Needle-Like α -Fe₃O₄ and γ -Fe₃O₄ Nanoparticles, *J. Korean Phy. Soc.*, **45** (2004) 1019-1024.
- [181] Chupas P.J., Qiu X., Hanson J.C., Lee P.L., Grey C.P., Billinge S.J., Rapid-Acquisition Pair Distribution Function (Ra-Pdf) Analysis, *J. Appl. Crystallogr.*, **36** (2003) 1342-1347.
- [182] Ashiotis G., Deschildre A., Nawaz Z., Wright J.P., Karkoulis D., Picca F.E., Kieffer J., The Fast Azimuthal Integration Python Library: Pyfai, *J Appl Crystallogr*, **48** (2015) 510-519, [10.1107/S1600576715004306](https://doi.org/10.1107/S1600576715004306).
- [183] Juhás P., Davis T., Farrow C.L., Billinge S.J., Pdfgetx3: A Rapid and Highly Automatable Program for Processing Powder Diffraction Data into Total Scattering Pair Distribution Functions, *J. Appl. Crystallogr.*, **46** (2013) 560-566.
- [184] Yang X., Juhás P., Farrow C., Billinge S., Xpdfsuite: An End-to-End Software Solution for High Throughput Pair Distribution Function Transformation, Visualization and Analysis. Arxiv.(2015); 1402.3163, *arXiv.*, (2015) [1402.3163](https://arxiv.org/abs/1402.3163).
- [185] Yong-Chan Chung B.C.C., Mi-Hwa Chung, Yong-Sik Shim and Jae Whan Cho, Development of Polyester Types Shape Memory Polymer and Its Applications to Composite Material, © 2008 Nova Science Publishers, Inc., 2008,
- [186] Euvrard E., Morin-Crini N., Druart C., Bugnet J., Martel B., Cosentino C., Moutarlier V., Crini G., Cross-Linked Cyclodextrin-Based Material for Treatment of Metals and Organic Substances Present in Industrial Discharge Waters, *Beilstein J Org Chem*, **12** (2016) 1826-1838, [10.3762/bjoc.12.172](https://doi.org/10.3762/bjoc.12.172).
- [187] Ducoroy L., Bacquet M., Martel B., Morcellet M., Removal of Heavy Metals from Aqueous Media by Cation Exchange Nonwoven Pet Coated with B-Cyclodextrin-Polycarboxylic Moieties, *React. Funct. Polym.*, **68** (2008) 594-600, [10.1016/j.reactfunctpolym.2007.10.033](https://doi.org/10.1016/j.reactfunctpolym.2007.10.033).
- [188] Gawish S.M., Ramadan A.M., Abo El-Ola S.M., Abou El-Kheir A.A., Citric Acid Used as a Cross-Linking Agent for Grafting B-Cyclodextrin onto Wool Fabric, *Polym-Plast Technol Eng*, **48** (2009) 701-710, [10.1080/03602550902824572](https://doi.org/10.1080/03602550902824572).
- [189] Ghorpade V.S., Yadav A.V., Dias R.J., Mali K.K., Pargaonkar S.S., Shinde P.V., Dhane N.S., Citric Acid Crosslinked Carboxymethylcellulose-Poly(Ethylene Glycol) Hydrogel Films for Delivery of Poorly Soluble Drugs, *Int J Biol Macromol*, **118** (2018) 783-791, [10.1016/j.ijbiomac.2018.06.142](https://doi.org/10.1016/j.ijbiomac.2018.06.142).
- [190] Ghorpade V.S., Yadav A.V., Dias R.J., Citric Acid Crosslinked Cyclodextrin/Hydroxypropylmethylcellulose Hydrogel Films for Hydrophobic Drug Delivery, *Int J Biol Macromol*, **93** (2016) 75-86, [10.1016/j.ijbiomac.2016.08.072](https://doi.org/10.1016/j.ijbiomac.2016.08.072).
- [191] Duan Z., Zhang M., Bian H., Wang Y., Zhu L., Xiang Y., Xia D., Copper(II)-Beta-Cyclodextrin and CuO Functionalized Graphene Oxide Composite for Fast Removal of Thiophenic Sulfides with High Efficiency, *Carbohydr Polym*, **228** (2020) 115385, [10.1016/j.carbpol.2019.115385](https://doi.org/10.1016/j.carbpol.2019.115385).

- [192] S M.M.a.A., Synthesis and Applications of Nano-Structured Iron Oxides/Hydroxides—a Review, *Int. J. Eng. Sci. Technol.*, **2** (2010).
- [193] Zhao Y., Liu F., Qin X., Adsorption of Diclofenac onto Goethite: Adsorption Kinetics and Effects of Ph, *Chemosphere*, **180** (2017) 373-378, [10.1016/j.chemosphere.2017.04.007](https://doi.org/10.1016/j.chemosphere.2017.04.007).
- [194] T. Gong Y.Z., L. Sun, W. Liang, J. Yang, S. Shuang and C. Dong, Effective Adsorption of Phenolic Pollutants from Water Using B-Cyclodextrin Polymer Assembled Fe₃O₄ Magnetic Nanocomposites *RSC Adv.*, (2016) [10.1039/C6RA16383A10.1039/x0xx00000x](https://doi.org/10.1039/C6RA16383A10.1039/x0xx00000x).
- [195] Zhao D., Zhao L., Zhu C.-S., Huang W.-Q., Hu J.-L., Water-Insoluble B-Cyclodextrin Polymer Crosslinked by Citric Acid: Synthesis and Adsorption Properties toward Phenol and Methylene Blue, *J. Inclusion Phenom. Macrocyclic Chem.*, **63** (2008) 195-201, [10.1007/s10847-008-9507-4](https://doi.org/10.1007/s10847-008-9507-4).
- [196] Zhao D., Zhao L., Zhu C., Tian Z., Shen X., Synthesis and Properties of Water-Insoluble B-Cyclodextrin Polymer Crosslinked by Citric Acid with Peg-400 as Modifier, *Carbohydr. Polym.*, **78** (2009) 125-130, [10.1016/j.carbpol.2009.04.022](https://doi.org/10.1016/j.carbpol.2009.04.022).
- [197] Hazemann J.L., Bézar J.F., Manceau A., Rietveld Studies of the Aluminium-Iron Substitution in Synthetic Goethite, *Mater. Sci. Forum* **79-82** (1991) 821-826, [10.4028/www.scientific.net/MSF.79-82.821](https://doi.org/10.4028/www.scientific.net/MSF.79-82.821).
- [198] Wang Z., Zhang P., Hu F., Zhao Y., Zhu L., A Crosslinked Beta-Cyclodextrin Polymer Used for Rapid Removal of a Broad-Spectrum of Organic Micropollutants from Water, *Carbohydr Polym*, **177** (2017) 224-231, [10.1016/j.carbpol.2017.08.059](https://doi.org/10.1016/j.carbpol.2017.08.059).
- [199] Kong D., Wilson L.D., Synthesis and Characterization of Cellulose-Goethite Composites and Their Adsorption Properties with Roxarsone, *Carbohydr Polym*, **169** (2017) 282-294, [10.1016/j.carbpol.2017.04.019](https://doi.org/10.1016/j.carbpol.2017.04.019).
- [200] Shahabi S., Najafi F., Majdabadi A., Hooshmand T., Haghbin Nazarpak M., Karimi B., Fatemi S.M., Effect of Gamma Irradiation on Structural and Biological Properties of a Plga-Peg-Hydroxyapatite Composite, *Sci World J*, **2014** (2014) 420616, [10.1155/2014/420616](https://doi.org/10.1155/2014/420616).
- [201] Tabary N., Garcia-Fernandez M.J., Danede F., Descamps M., Martel B., Willart J.F., Determination of the Glass Transition Temperature of Cyclodextrin Polymers, *Carbohydr Polym*, **148** (2016) 172-180, [10.1016/j.carbpol.2016.04.032](https://doi.org/10.1016/j.carbpol.2016.04.032).
- [202] Skiba M., Lahiani-Skiba M., Novel Method for Preparation of Cyclodextrin Polymers: Physico-Chemical Characterization and Cytotoxicity, *J. Inclusion Phenom. Mol. Recognit. Chem.*, **75** (2012) 341-349, [10.1007/s10847-012-0246-1](https://doi.org/10.1007/s10847-012-0246-1).
- [203] Taylor R., Interpretation of the Correlation Coefficient: A Basic Review, *J Diagn Med Sonography*, **6** (1990) 35-39.
- [204] Kell A.J., Stewart G., Ryan S., Peytavi R., Boissinot M., Huletsky A., Bergeron M.G., Simard B., Vancomycin-Modified Nanoparticles for Efficient Targeting and Preconcentration of Gram-Positive and Gram-Negative Bacteria, *ACS Nano*, **2** (2008) 1777-1788, [10.1021/nn700183g](https://doi.org/10.1021/nn700183g).
- [205] Dultz S., Steinke H., Mikutta R., Woche S.K., Guggenberger G., Impact of Organic Matter Types on Surface Charge and Aggregation of Goethite, *Colloids Surf., A* **554** (2018) 156-168, [10.1016/j.colsurfa.2018.06.040](https://doi.org/10.1016/j.colsurfa.2018.06.040).

- [206] Li Y., Li Q., Wu C., Luo X., Yu X., Chen M., The Inappropriate Application of the Regression Langmuir Qm for Adsorption Capacity Comparison, *Sci Total Environ*, **699** (2020) 134222, [10.1016/j.scitotenv.2019.134222](https://doi.org/10.1016/j.scitotenv.2019.134222).
- [207] Huang W., Hu Y., Li Y., Zhou Y., Niu D., Lei Z., Zhang Z., Citric Acid-Crosslinked B-Cyclodextrin for Simultaneous Removal of Bisphenol a, Methylene Blue and Copper: The Roles of Cavity and Surface Functional Groups, *J Taiwan Inst. Chem. Eng*, **82** (2018) 189-197, [10.1016/j.jtice.2017.11.021](https://doi.org/10.1016/j.jtice.2017.11.021).
- [208] Jiang H.-L., Lin J.-C., Hai W., Tan H.-W., Luo Y.-W., Xie X.-L., Cao Y., He F.-A., A Novel Crosslinked B-Cyclodextrin-Based Polymer for Removing Methylene Blue from Water with High Efficiency, *Colloids Surf., A* **560** (2019) 59-68, [10.1016/j.colsurfa.2018.10.004](https://doi.org/10.1016/j.colsurfa.2018.10.004).
- [209] Moulahcene L., Skiba M., Senhadji O., Milon N., Benamor M., Lahiani-Skiba M., Inclusion and Removal of Pharmaceutical Residues from Aqueous Solution Using Water-Insoluble Cyclodextrin Polymers, *Chem. Eng. Res. Des.*, **97** (2015) 145-158, [10.1016/j.cherd.2014.08.023](https://doi.org/10.1016/j.cherd.2014.08.023).

APPENDICES

APPENDIX A - PREPARATION OF SOLUTIONS

The standard solutions of nickel nitrate hexahydrate, $\text{Ni}(\text{NO}_3)_2 \cdot 6\text{H}_2\text{O}$, methylene blue, $\text{C}_{16}\text{H}_{18}\text{N}_3\text{S}$ were prepared by dissolving appropriate amounts of the as-purchased compounds in 18 M Ω double-deionised water.

A-1 Preparation of stock solutions of $\text{Ni}(\text{NO}_3)_2 \cdot 6\text{H}_2\text{O}$

A 1000 ppm (1 M) $\text{Ni}(\text{NO}_3)_2 \cdot 6\text{H}_2\text{O}$ stock solution was prepared by dissolving 4.9530 g of nickel(II) nitrate hexahydrate in double-deionised water in a 1000 mL volumetric flask and made up to the mark. A 1000 ppm MB stock solution was prepared by dissolving 1 g of MB in double-deionised water in 1000 mL volumetric flask and made up to the mark. The solutions were agitated for one hour using a magnetic agitator and stirrer to obtain homogeneity.

Dilute solutions of known concentrations were prepared from the standard solutions by pipetting a known volume of the standard solution in a 200 mL volumetric flask and completing with double deionised water up to the mark. We have,

$$C_i V_i = C_f V_f \quad \leftrightarrow \quad V_i = \frac{C_f V_f}{C_i}$$

Where V_i = volume of stock solution needed to make the new solution

V_f = final volume of new (dilute) solution

C_i = concentration of stock solution

C_f = final concentration of new (dilute) solution

APPENDIX B - DATA

B-1 Data for Batch and Column Adsorption Studies, Ni(II) ion

Table B-1 Data for Ni(II) ion Removal, Variation of Time

	Sample Id	Acquisition Time	Raw Intensities Be 9 (cps)	Raw Intensities RSDs Be 9	Net Intensities Be 9 (cps)	Net Intensities RSDs Be 9	Concentration Be 9 (ug/L)	Concentration RSDs Be 9	Unfactored Conc Be 9 (ug/L)
1	Blk	12/7/2017 3:18:54 PM	59.5	9.4%	59.467	9.4%			
2	10	12/7/2017 3:21:26 PM	5908.2	2.6%	5848.771	2.7%	10.000	2.7%	10.000
3	50	12/7/2017 3:23:58 PM	16594.8	1.8%	16535.319	1.8%	48.564	1.8%	48.564
4	100	12/7/2017 3:26:31 PM	31238.0	2.8%	31178.540	2.8%	98.136	2.8%	98.136
5	500	12/7/2017 3:29:04 PM	145746.3	3.1%	145686.796	3.1%	497.841	3.1%	497.841
6	Calibration Curves	12/7/2017 3:29:04 PM							
7	100	12/7/2017 3:31:37 PM	31514.0	0.9%	31454.496	0.9%	107.486	0.9%	107.486
8	CDG_5	12/7/2017 3:34:09 PM	3839.9	2.1%	3780.397	2.1%	1291.838	2.1%	12.918
9	CDG_10	12/7/2017 3:36:39 PM	6502.2	3.2%	6442.703	3.3%	2201.602	3.3%	22.016
10	CDG_15	12/7/2017 3:39:10 PM	5802.3	1.5%	5742.848	1.5%	1962.447	1.5%	19.624
11	CDG_20	12/7/2017 3:41:40 PM	6625.2	0.9%	6565.708	0.9%	2243.635	0.9%	22.436
12	CDG_25	12/7/2017 3:44:11 PM	6861.1	0.5%	6801.584	0.5%	2324.238	0.5%	23.242
13	CDG_30	12/7/2017 3:46:42 PM	6006.2	2.0%	5946.690	2.0%	2032.104	2.0%	20.321
14	CDG_35	12/7/2017 3:49:13 PM	7027.0	1.2%	6967.555	1.2%	2380.954	1.2%	23.810
15	CDG_40	12/7/2017 3:51:45 PM	6896.0	0.7%	6836.539	0.7%	2336.183	0.7%	23.362
16	CDG_45	12/7/2017 3:54:17 PM	7511.3	3.0%	7451.873	3.0%	2546.455	3.0%	25.465
17	CDG_50	12/7/2017 3:56:49 PM	7080.7	2.5%	7021.189	2.5%	2399.282	2.5%	23.993
18	CDG_55	12/7/2017 3:59:22 PM	6370.4	1.3%	6310.892	1.3%	2156.559	1.3%	21.566
19	CDG_60	12/7/2017 4:01:55 PM	7382.7	2.3%	7323.253	2.4%	2502.503	2.4%	25.025
20	CDG_65	12/7/2017 4:04:27 PM	6648.9	1.6%	6589.456	1.6%	2251.750	1.6%	22.517
21	CDG_70	12/7/2017 4:06:58 PM	6478.2	1.8%	6418.688	1.8%	2193.395	1.8%	21.934
22	CDG_80	12/7/2017 4:09:28 PM	6254.6	1.9%	6195.093	1.9%	2116.988	1.9%	21.170
23	CDGHA_5	12/7/2017 4:11:59 PM	42.9	15.2%	-16.533	39.4%	-5.650	39.4%	-0.056
24	CDGHA_10	12/7/2017 4:14:30 PM	4037.8	4.7%	3978.334	4.8%	1359.477	4.8%	13.595
25	CDGHA_15	12/7/2017 4:17:01 PM	3130.6	1.4%	3071.108	1.5%	1049.459	1.5%	10.495
26	CDGHA_20	12/7/2017 4:19:32 PM	3629.4	2.1%	3569.926	2.1%	1219.916	2.1%	12.199
27	CDGHA_25	12/7/2017 4:22:04 PM	3408.5	3.8%	3349.056	3.9%	1144.440	3.9%	11.444

28	CDGHA_30	12/7/2017 4:24:36 PM	2897.7	0.5%	2838.244	0.5%	969.885	0.5%	9.699
29	CDGHA_35	12/7/2017 4:27:08 PM	2629.4	1.9%	2569.911	2.0%	878.190	2.0%	8.782
30	CDGHA_40	12/7/2017 4:29:41 PM	2624.3	2.0%	2564.843	2.0%	876.459	2.0%	8.765
31	CDGHA_45	12/7/2017 4:32:14 PM	2977.2	2.6%	2917.732	2.7%	997.048	2.7%	9.970
32	CDGHA_50	12/7/2017 4:34:46 PM	3141.2	1.3%	3081.777	1.3%	1053.105	1.3%	10.531
33	CDGHA_55	12/7/2017 4:37:18 PM	37.1	2.5%	-22.400	4.1%	-7.655	4.1%	-0.077
34	CDGHA_60	12/7/2017 4:39:49 PM	2891.6	1.4%	2832.109	1.4%	967.789	1.4%	9.678
35	CDGHA_65	12/7/2017 4:42:21 PM	3008.9	4.8%	2949.475	4.9%	1007.895	4.9%	10.079
36	CDGHA_70	12/7/2017 4:44:52 PM	3456.0	2.3%	3396.537	2.4%	1160.665	2.4%	11.607

Table B-2 Data for Ni(II) ion Removal, Variation of Time/Concentration

	Sample Id	Acquisition Time	Raw Intensities Be 9 (cps)	Raw Intensities RSDs Be 9	Net Intensities Be 9 (cps)	Net Intensities RSDs Be 9	Concentration Be 9 (ug/L)	Concentration RSDs Be 9	Unfactored Conc Be 9 (ug/L)
1	Blk	12/15/2017 12:03:06 PM	107.7	14.6%	107.734	14.6%			
2	5	12/15/2017 12:05:38 PM	1904.2	1.6%	1796.429	1.7%	5.000	1.7%	5.000
3	20	12/15/2017 12:08:10 PM	7139.6	0.9%	7031.893	1.0%	19.974	1.0%	19.974
4	50	12/15/2017 12:10:43 PM	17952.9	3.9%	17845.173	3.9%	50.099	3.9%	50.099
5	Calibration Curves	12/15/2017 12:10:43 PM							
6	20	12/15/2017 12:13:16 PM	6414.7	2.3%	6306.918	2.4%	17.706	2.4%	17.706
7	CD 5min	12/15/2017 12:15:47 PM	2083.7	3.6%	1975.928	3.8%	554.728	3.8%	5.547
8	CD 10 min	12/15/2017 12:18:18 PM	2346.4	0.9%	2238.647	0.9%	628.484	0.9%	6.285
9	CD 15 min	12/15/2017 12:20:48 PM	2438.7	2.9%	2330.934	3.1%	654.393	3.1%	6.544
10	CD 20min	12/15/2017 12:23:19 PM	1979.1	4.9%	1871.376	5.2%	525.375	5.2%	5.254
11	CD 30 min	12/15/2017 12:25:50 PM	1953.5	5.4%	1845.772	5.7%	518.187	5.7%	5.182
12	CD 40 min	12/15/2017 12:28:20 PM	1934.6	3.3%	1826.835	3.5%	512.871	3.5%	5.129
13	CD 50 min	12/15/2017 12:30:52 PM	2103.9	4.0%	1996.199	4.3%	560.419	4.3%	5.604
14	CD 60 min	12/15/2017 12:33:23 PM	1895.9	2.3%	1788.161	2.4%	502.014	2.4%	5.020
15	CD 70 min	12/15/2017 12:35:55 PM	1951.4	2.4%	1843.638	2.5%	517.588	2.5%	5.176
16	CD 80 min	12/15/2017 12:38:28 PM	2081.8	0.9%	1974.061	1.0%	554.204	1.0%	5.542
17	CDHA 15 min	12/15/2017 12:41:00 PM	3829.5	1.1%	3721.726	1.1%	1044.848	1.1%	10.448
18	CDHA 20 min	12/15/2017 12:43:33 PM	2648.8	1.3%	2541.115	1.3%	713.400	1.3%	7.134
19	CDDHA 30 min	12/15/2017 12:46:06 PM	2920.4	2.2%	2812.650	2.3%	789.631	2.3%	7.896
20	CDHA 40 min	12/15/2017 12:48:36 PM	2879.3	2.8%	2771.573	2.9%	778.099	2.9%	7.781
21	CDHA 50 min	12/15/2017 12:51:07 PM	3963.6	1.2%	3855.906	1.3%	1082.518	1.3%	10.825

22	CDHA 60 min	12/15/2017 12:53:38 PM	2126.3	0.2%	2018.603	0.3%	566.708	0.3%	5.667
23	CDHA 70 min	12/15/2017 12:56:09 PM	3209.0	2.3%	3101.263	2.4%	870.657	2.4%	8.707
24	CDHA 80 min	12/15/2017 12:58:40 PM	2834.8	1.8%	2727.028	1.8%	765.594	1.8%	7.656
25	CD 10 ppm	12/15/2017 1:01:11 PM	614.4	1.8%	506.683	2.2%	142.248	2.2%	1.422
26	CD 20 ppm	12/15/2017 1:03:43 PM	1222.7	3.8%	1115.000	4.2%	313.028	4.2%	3.130
27	CD 30 ppm	12/15/2017 1:06:15 PM	1471.6	2.7%	1363.830	2.9%	382.886	2.9%	3.829
28	CD 40 ppm	12/15/2017 1:08:47 PM	1518.0	1.7%	1410.237	1.8%	395.914	1.8%	3.959
29	CD 50 ppm	12/15/2017 1:11:20 PM	1412.9	3.5%	1305.156	3.8%	366.413	3.8%	3.664
30	CD 60 ppm	12/15/2017 1:13:53 PM	1696.9	3.2%	1589.196	3.4%	446.155	3.4%	4.462
31	CD 70 ppm	12/15/2017 1:16:25 PM	3143.6	0.9%	3035.911	0.9%	852.310	0.9%	8.523
32	CD 80 ppm	12/15/2017 1:18:57 PM	21574.5	1.4%	21466.794	1.4%	6026.649	1.4%	60.266
33	CDG 10 ppm	12/15/2017 1:21:28 PM	1268.6	0.7%	1160.872	0.7%	325.907	0.7%	3.259
34	CDg 20 ppm	12/15/2017 1:24:00 PM	2332.5	2.6%	2224.778	2.8%	624.590	2.8%	6.246
35	CDG 30 ppm	12/15/2017 1:26:32 PM	2380.3	3.3%	2272.521	3.4%	637.994	3.4%	6.380
36	CDG 40 ppm	12/15/2017 1:29:03 PM	2261.8	2.2%	2154.096	2.3%	604.747	2.3%	6.047
37	CDG 50 ppm	12/15/2017 1:31:35 PM	2301.6	1.8%	2193.838	1.9%	615.904	1.9%	6.159
38	CDG 60 ppm	12/15/2017 1:34:06 PM	4232.3	1.4%	4124.539	1.4%	1157.935	1.4%	11.579
39	CDG 70 ppm	12/15/2017 1:36:38 PM	4545.2	1.3%	4437.462	1.3%	1245.786	1.3%	12.458
40	CDG 80 ppm	12/15/2017 1:39:11 PM	3703.0	2.4%	3595.283	2.4%	1009.350	2.4%	10.094
41	CDHA 10 ppm	12/15/2017 1:41:43 PM	2085.8	4.6%	1978.062	4.9%	555.327	4.9%	5.553
42	CDHA 20 ppm	12/15/2017 1:44:16 PM	2550.4	1.2%	2442.692	1.2%	685.768	1.2%	6.858
43	CDHA 30 ppm	12/15/2017 1:46:49 PM	4082.6	1.4%	3974.883	1.4%	1115.920	1.4%	11.159
44	CDHA 40 ppm	12/15/2017 1:49:21 PM	6443.5	1.0%	6335.734	1.0%	1778.712	1.0%	17.787
45	CDHA 50 ppm	12/15/2017 1:51:53 PM	4913.9	1.0%	4806.153	1.0%	1349.293	1.0%	13.493
46	CDHA 60 ppm	12/15/2017 1:54:25 PM	7629.3	2.9%	7521.553	2.9%	2111.622	2.9%	21.116
47	CDHA 70 ppm	12/15/2017 1:56:57 PM	27354.4	2.6%	27246.712	2.6%	7649.320	2.6%	76.493
48	CDHA 80 ppm	12/15/2017 1:59:28 PM	7888.1	2.5%	7780.400	2.5%	2184.292	2.5%	21.843
49	CDGHA 10 ppm	12/15/2017 2:02:00 PM	277.6	11.7%	169.870	19.1%	47.690	19.1%	0.477
50	CDGHA 20 ppm	12/15/2017 2:04:32 PM	1185.7	4.0%	1077.929	4.4%	302.621	4.4%	3.026
51	CDGHA 30 ppm	12/15/2017 2:07:04 PM	947.0	1.5%	839.240	1.7%	235.611	1.7%	2.356
52	CDGHA 40 ppm	12/15/2017 2:09:36 PM	1435.0	1.9%	1327.292	2.0%	372.628	2.0%	3.726
53	CDGHA 50 ppm	12/15/2017 2:12:09 PM	1104.1	4.0%	996.321	4.4%	279.710	4.4%	2.797
54	CDGHA 60 ppm	12/15/2017 2:14:42 PM	2124.5	2.9%	2016.736	3.0%	566.184	3.0%	5.662
55	CDGAH 70 ppm	12/15/2017 2:17:15 PM	2975.9	4.9%	2868.132	5.1%	805.208	5.1%	8.052

56	CDGHA 80 ppm	12/15/2017 2:19:47 PM	5509.4	3.2%	5401.633	3.3%	1516.470	3.3%	15.165
57	CD 5	12/15/2017 2:22:19 PM	248.3	2.3%	140.536	4.1%	39.454	4.1%	0.395
58	CD 10	12/15/2017 2:24:51 PM	233.6	8.2%	125.869	15.2%	35.337	15.2%	0.353
59	CD 20	12/15/2017 2:27:24 PM	214.4	6.8%	106.668	13.8%	29.946	13.8%	0.299
60	CD 30	12/15/2017 2:29:56 PM	212.5	5.1%	104.802	10.4%	29.422	10.4%	0.294
61	CD 40	12/15/2017 2:32:28 PM	220.5	3.7%	112.802	7.2%	31.668	7.2%	0.317
62	CD 50	12/15/2017 2:35:00 PM	234.4	7.6%	126.669	14.1%	35.561	14.1%	0.356
63	CD 60	12/15/2017 2:37:32 PM	230.4	7.8%	122.669	14.7%	34.438	14.7%	0.344
64	CD 80	12/15/2017 2:40:05 PM	222.4	2.8%	114.668	5.4%	32.192	5.4%	0.322
65	CD 90	12/15/2017 2:42:37 PM	234.1	10.7%	126.402	19.8%	35.486	19.8%	0.355
66	CD 100	12/15/2017 2:45:10 PM	230.7	1.4%	122.935	2.6%	34.513	2.6%	0.345
67	CD 110	12/15/2017 2:47:43 PM	211.5	3.8%	103.735	7.8%	29.123	7.8%	0.291
68	CD 120	12/15/2017 2:50:16 PM	850.4	4.9%	742.699	5.7%	208.507	5.7%	2.085
69	CD 130	12/15/2017 2:52:48 PM	228.5	6.5%	120.802	12.3%	33.914	12.3%	0.339
70	CD 140	12/15/2017 2:55:21 PM	232.5	4.0%	124.802	7.5%	35.037	7.5%	0.350
71	CD 150	12/15/2017 2:57:53 PM	236.8	4.2%	129.069	7.6%	36.235	7.6%	0.362
72	CD 160	12/15/2017 3:00:26 PM	239.2	6.1%	131.469	11.2%	36.909	11.2%	0.369
73	CD 170	12/15/2017 3:02:58 PM	232.3	8.7%	124.535	16.2%	34.962	16.2%	0.350
74	CD 180	12/15/2017 3:05:31 PM	1946.6	2.9%	1838.837	3.1%	516.240	3.1%	5.162
75	CD 190	12/15/2017 3:08:03 PM	8969.5	6.9%	8861.763	7.0%	2487.877	7.0%	24.879

Table B-3 Data for Removal Rate, Variation of Contact Time

Time	CDN		Time	CDG		Time	CDHA		Time	CDGHA	
	Conc (ppm)	% Removal		Conc (ppm)	% Removal		Conc (ppm)	% Removal		Conc (ppm)	% Removal
0	0	0	0	0	0	0	0	0	0	0	0
5	0.55472779	98.8905444	5	1.291838	97.416324	15	1.04484803	97.9103039	5	100.0113	5.000565
10	0.62848424	98.7430315	10	2.201602	95.596796	20	0.71339997	98.5732001	10	97.281046	4.8640523
15	0.65439306	98.6912139	15	1.962447	96.075106	30	0.78963143	98.4207371	15	97.901082	4.8950541
20	0.52537547	98.9492491	20	2.243635	95.51273	40	0.77809927	98.4438015	20	97.560168	4.8780084
30	0.51818719	98.9636256	25	2.324238	95.351524	50	1.08251822	97.8349636	25	97.71112	4.885556
40	0.5128708	98.9742584	30	2.032104	95.935792	60	0.56670837	98.8665833	30	98.06023	4.9030115
50	0.5604186	98.8791628	35	2.380954	95.238092	70	0.87065746	98.2586851	35	98.24362	4.912181
60	0.50201352	98.995973	40	2.336183	95.327634	80	0.7655936	98.4688128	40	98.247082	4.9123541
70	0.51758809	98.9648238	45	2.546455	94.90709				45	98.005904	4.9002952
80	0.55420359	98.8915928	50	2.399282	95.201436				50	97.89379	4.8946895
			55	2.156559	95.686882				60	98.064422	4.9032211
			60	2.502503	94.994994				65	97.98421	4.8992105
			65	2.25175	95.4965				70	97.67867	4.8839335
			70	2.193395	95.61321						
			80	2.116988	95.766024						

Variation of Contact Time

Table B-4 Data for Removal Rate, Variation of Concentration

Time	CDN		CDG		CDHA		CDGHA	
	Conc (ppm)	% Removal	Conc (ppm)	% Removal	Conc (ppm)	% Removal	Conc (ppm)	% Removal
0	0	0	0	0	0	0	0	0
10	0.14224768	98.5775232	0.3259065	96.740935	0.55532685	94.4467315	0.04768969	99.5231031
20	0.31302834	99.3739433	0.62459048	96.8770476	0.68576841	96.571158	0.30262101	98.486895
30	0.38288563	99.2342287	0.63799413	97.8733529	1.11592	96.2802667	0.2356106	99.2146313
40	0.39591384	99.2081723	0.6047472	98.488132	1.77871215	95.5532196	0.37262781	99.0684305
50	0.36641325	99.2671735	0.61590434	98.7681913	1.34929306	97.3014139	0.27971003	99.4405799
60	0.44615539	99.1076892	1.15793486	98.0701086	2.11162227	96.4806296	0.56618425	99.0563596
70	0.85231031	98.2953794	1.24578592	98.2203058	2.18429172	96.8795833	0.80520758	98.8497035
80	6.02664941	87.9467012	1.00935015	98.7383123	7.64932015	90.4383498	1.51646984	98.1044127

B-2 Data for Isotherm Models and Kinetic Models, Ni(II) ion

Table B-5 Data for Non-linear Equilibrium and Kinetic Model, Ni(II) Adsorption

CDN	Equilibrium sorption models							Kinetic Sorption Models						
	Conc	Ce	Sorption Capacity	Qe Cal	Qe Cal	Qe Cal	Qe Cal	Time	Ct	Sorption Capacity				
	ppm	Ppm	mg/g	mg/g	mg/g	mg/g	mg/g	mins	ppm	mg/g	mg/g	mg/g	mg/g	
	CDN		Experimental	Langmuir	Freundlich	Redlich-Peterson	Sipps	CDN		Experimental	Pseudo-First Order	Pseudo-Second Order	Elovich	
	10	0.142248	0.985775	2.109829	3.001818	1.551003	3.001817	0	0	0	0	0	0	
	20	0.313028	1.968697	3.588296	3.70204	3.274406	3.702039	5	0.554727787	4.944527221	4.944717376	4.944717376	4.782951337	
	30	0.382886	2.961711	4.015967	3.905686	3.918437	3.905684	10	0.628484239	4.937151576	4.944717376	4.944717376	4.847153011	
	40	0.395914	3.960409	4.087806	3.940581	4.034213	3.940579	15	0.654393065	4.934560694	4.944717376	4.944717376	4.884708583	
	50	0.366413	4.963359	3.921805	3.860295	3.770077	3.860293	20	0.525375466	4.947462453	4.944717376	4.944717376	4.911354685	
	60	0.446155	5.955384	4.345037	4.067737	4.467561	4.067735	30	0.518187192	4.948181281	4.944717376	4.944717376	4.948910257	
	70	0.85231	6.914769	5.689484	4.831485	7.19907	4.831481	40	0.512870803	4.94871292	4.944717376	4.944717377	4.975556359	
	80	6.026649	7.397335	8.034011	8.126375	7.383828	8.126363	50	0.560418596	4.94395814	4.944717376	4.944717377	4.996224682	
								60	0.502013523	4.949798648	4.944717376	4.944717377	5.013111931	
								70	0.517588093	4.948241191	4.944717376	4.944717377	5.027389897	
								80	0.554203592	4.944579641	4.944717376	4.944717377	5.039758033	
CDG	CDG		Experimental	Langmuir	Freundlich	Redlich-Peterson	Sipps	CDG		Experimental	Pseudo-First Order	Pseudo-Second Order	Elovich	
	10	0.325907	0.967409	2.673313	1.66466	1.885946	4.161148	0	0	0	0	0	0	
	20	0.62459	1.937541	3.898722	3.27497	3.614362	4.412252	5	1.291838	4.870816	4.7804	4.780431	4.60902	
	30	0.637994	2.936201	3.940125	3.348113	3.691926	4.420388	10	2.201602	4.77984	4.7804	4.780431	4.670883	
	40	0.604747	3.939525	3.835771	3.166803	3.499533	4.399873	15	1.962447	4.803755	4.7804	4.780431	4.707071	
	50	0.615904	4.93841	3.871414	3.227604	3.564097	4.406884	20	2.243635	4.775637	4.7804	4.780431	4.732746	
	60	1.157935	5.884207	5.065744	6.224365	6.700703	4.646647	25	2.324238	4.767576	4.7804	4.780431	4.752661	

	70	1.245786	6.875421	5.194143	6.716355	7.209077	4.674083	30	2.032104	4.79679	4.7804	4.780431	4.768934
								35	2.380954	4.761905	4.7804	4.780431	4.782691
								40	2.336183	4.766382	4.7804	4.780431	4.794609
								45	2.546455	4.745355	4.7804	4.780431	4.805121
								50	2.399282	4.760072	4.7804	4.780431	4.814524
								55	2.156559	4.784344	4.7804	4.780431	4.823031
								60	2.502503	4.74975	4.7804	4.780431	4.830797
								65	2.25175	4.774825	4.7804	4.780431	4.83794
								70	2.193395	4.780661	4.7804	4.780431	4.844554
								80	2.116988	4.788301	4.7804	4.780431	4.856472
CDHA	CDHA		Experimental	Langmuir	Freundlich	Redlish-Peterson	Sipps	CDHA		Experimental	Pseudo-First Order	Pseudo-Second Order	Elovich
	10	0.555327	0.944467	0.995231	2.621322	2.275765	2.621326	0	0	0	0	0	0
	20	0.685768	1.931423	1.969738	2.871115	2.617124	2.871119	15	1.044848	4.895515	4.917408	4.917357	4.81603
	30	1.11592	2.888408	2.976439	3.542227	3.517249	3.542231	20	0.7134	4.92866	4.917408	4.917357	4.845278
	40	1.778712	3.822129	3.962737	4.331385	4.50683	4.331389	30	0.789631	4.921037	4.917408	4.917357	4.8865
	50	1.349293	4.865071	4.972029	3.844651	3.906883	3.844655	40	0.778099	4.92219	4.917408	4.917357	4.915747
	60	2.111622	5.788838	5.943382	4.664145	4.896544	4.664149	50	1.082518	4.891748	4.917408	4.917357	4.938433
	70	2.184292	6.781571	6.919479	4.732727	4.974783	4.732731	60	0.566708	4.943329	4.917408	4.917357	4.956969
	80	7.64932	7.235068	7.848353	8.127137	8.097128	8.12714	70	0.870657	4.912934	4.917408	4.917357	4.972641
								80	0.765594	4.923441	4.917408	4.917357	4.986217
CDGHA	CDGHA		Experimental	Langmuir	Freundlich	Redlish-Peterson	Sipps	CDGHA		Experiment	Pseudo-First Order	Pseudo-Second Order	Elovich
	10	0.04769	0.995231	0.808413	1.452359	0.943254	1.452359	0	0	0	0	`	0
	20	0.302621	1.969738	3.733414	3.722167	3.748918	3.722167	5	-0.00565	5.000565	4.90267	4.902471	4.736875
	30	0.235611	2.976439	3.130733	3.276648	3.199858	3.276648	10	1.359477	4.864052	4.90267	4.902472	4.800457
	40	0.372628	3.962737	4.27733	4.138347	4.244048	4.138347	15	1.049459	4.895054	4.90267	4.902472	4.83765

	50	0.27971	4.972029	3.537303	3.575868	3.570593	3.575867	20	1.219916	4.878008	4.90267	4.902472	4.864039
	60	0.566184	5.943382	5.450879	5.121093	5.33408	5.121093	25	1.14444	4.885556	4.90267	4.902472	4.884508
	70	0.805208	6.919479	6.464465	6.127231	6.333511	6.127231	30	0.969885	4.903012	4.90267	4.902472	4.901232
								35	0.87819	4.912181	4.90267	4.902472	4.915372
								40	0.876459	4.912354	4.90267	4.902472	4.927621
								45	0.997048	4.900295	4.90267	4.902472	4.938425
								50	1.053105	4.89469	4.90267	4.902472	4.948089
								60	0.967789	4.903221	4.90267	4.902472	4.964814
								65	1.007895	4.899211	4.90267	4.902472	4.972156
								70	1.160665	4.883934	4.90267	4.902472	4.978954

B-3 Data for Batch Adsorption Studies, MB

All calculations for MB residual concentration have been performed to double precision as defined by ANSI/IEEE STD 754-1985 but have been rounded for display purposes.

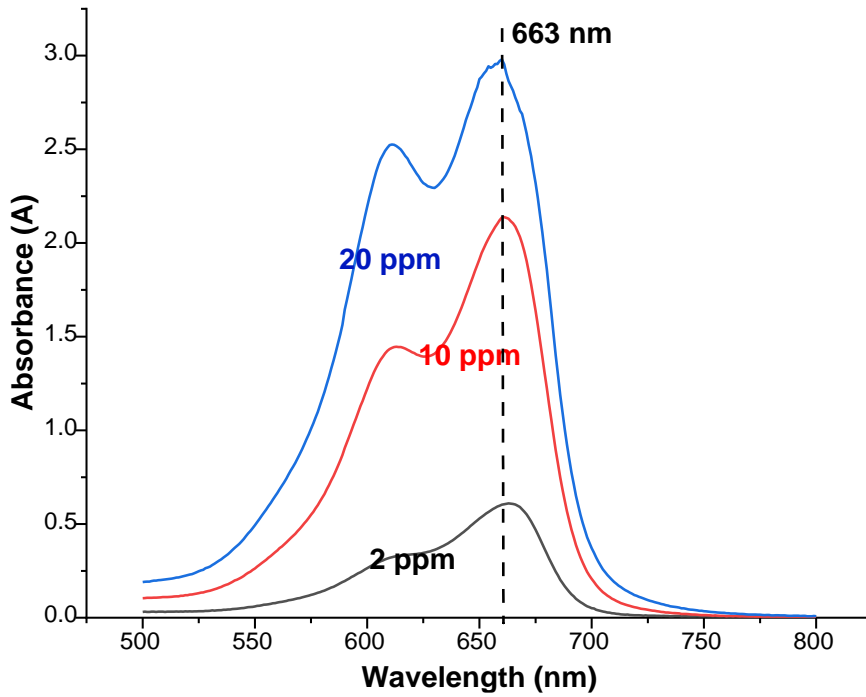


Figure 69: Determination of maximum wavelength of absorption for MB

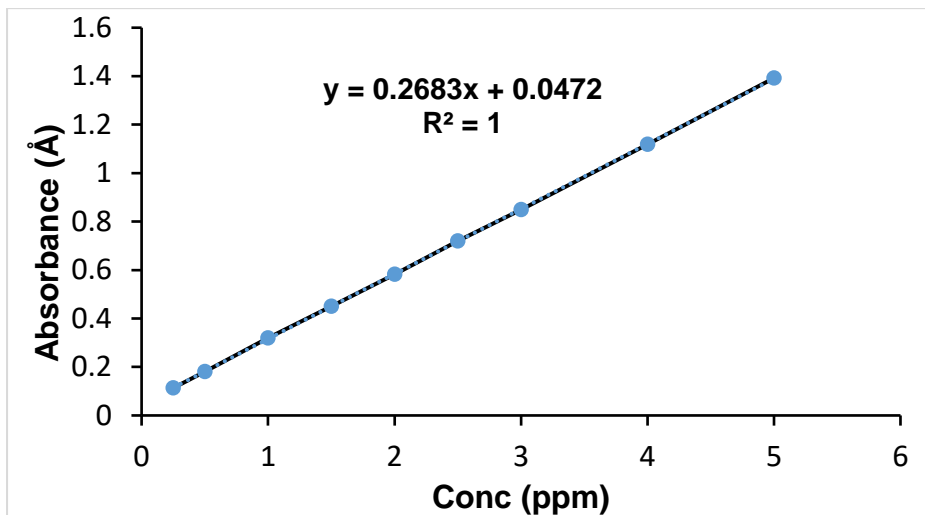


Figure 70: Calibration curve

B-4 Data for Removal Rate, Methylene Blue Adsorption

Table B-6 Data for Contact Time, MB Adsorption

CDN			CDG			CDHA			CDGHA		
Time	Conc (ppm)	% Removal	Time	Conc (ppm)	% Removal	Time	Conc (ppm)	% Removal	Time	Conc (ppm)	% Removal
0	0	0	0	0	0	0	0	0	0	0	0
5	0.699	96.505	5	-0.12747	100.6373	5	1.272	93.64	5	-0.945	104.725
10	0.556	97.22	10	-0.08647	100.4324	10	0.919	95.405	10	-0.903	104.515
15	0.547	97.265	15	-0.14983	100.7492	15	0.655	96.725	15	-0.967	104.835
20	0.545	97.275	20	-0.12374	100.6187	20	1.215	93.925	20	-0.971	104.855
25	0.509	97.455	25	-0.15356	100.7678	25	0.969	95.155	25	-0.987	104.935
30	0.569	97.155	30	-0.12001	100.6001	35	0.905	95.475	30	-0.991	104.955
35	0.695	96.525	35	-0.10883	100.5442	40	1.059	94.705	35	-0.971	104.855
40	0.626	96.87	40	-0.07902	100.3951	45	1.125	94.375	40	-0.959	104.795
45	1.099	94.505	45	-0.12374	100.6187	50	1.029	94.855	45	-0.965	104.825
50	0.614	96.93	50	-0.1312	100.656	55	1.09	94.55	50	-0.969	104.845
55	0.763	96.185	55	-0.03802	100.1901	60	1.025	94.875	55	-0.997	104.985
60	0.644	96.78	60	0.01789	99.91055	65	0.89	95.55	60	-0.985	104.925
65	0.611	96.945	80	0.021618	99.89191	70	0.891	95.545	65	-0.959	104.795
80	0.588	97.06				80	0.965	95.175	70	-0.959	104.795
									80	-0.975	104.875

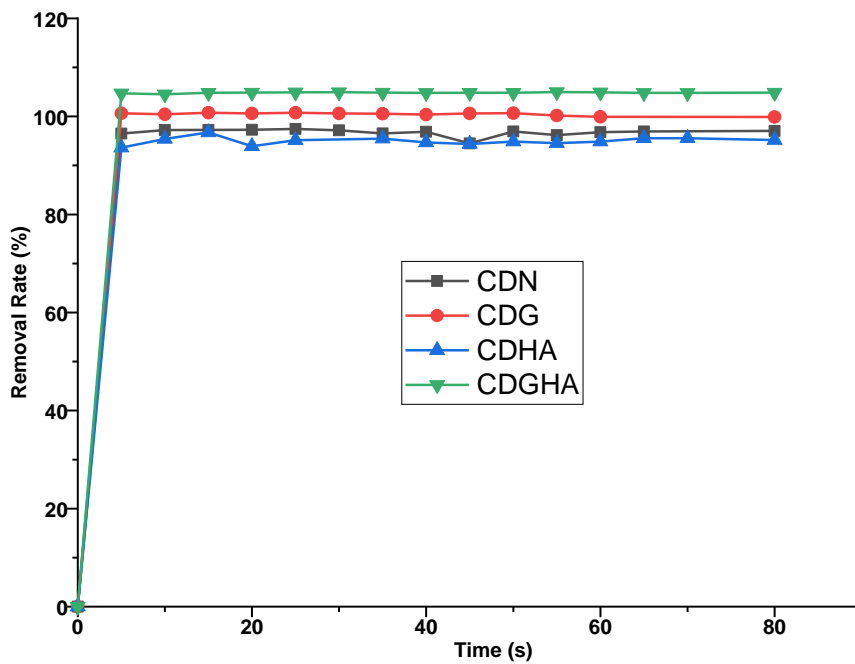


Figure 71: Variation of Contact Time for MB Adsorption

B-5 Data for Kinetic Models, MB Adsorption

Table B-7 Non-linear kinetic models

Time	Qt	Sorption Capacity			Time	Qt	Sorption Capacity		
mins	mg/g	mg/g	mg/g	mg/g	mins	mg/mg	mg/g	mg/g	mg/g
CDN	Experimental	Pseudo-First Order	Pseudo-Second Order	Elovich	CDG	Experimental	Pseudo-First Order	Pseudo-Second Order	Elovich
0	0	0	0	0	0	0	0	0	0
5	1.9301	1.9237	1.93525	1.87216	5	2.01275	2.00925	2.01275	1.97476
10	1.9444	1.9237	1.93525	1.89619	10	2.00865	2.00925	2.00865	1.98836
15	1.9453	1.9237	1.93525	1.91024	15	2.01498	2.00925	2.01498	1.99632
20	1.9455	1.9237	1.93525	1.92021	20	2.01237	2.00925	2.01237	2.00196
25	1.9491	1.9237	1.93525	1.92794	25	2.01536	2.00925	2.01536	2.00634
30	1.9431	1.9237	1.93525	1.93426	30	2.012	2.00925	2.012	2.00992
35	1.9305	1.9237	1.93525	1.9396	35	2.01088	2.00925	2.01088	2.01295
40	1.9374	1.9237	1.93525	1.94423	40	2.0079	2.00925	2.0079	2.01557
45	1.8901	1.9237	1.93525	1.94831	45	2.01237	2.00925	2.01237	2.01788
50	1.9386	1.9237	1.93525	1.95196	50	2.01312	2.00925	2.01312	2.01994
55	1.9237	1.9237	1.93525	1.95527	55	2.0038	2.00925	2.0038	2.02181
60	1.9356	1.9237	1.93525	1.95828	60	1.99821	2.00925	1.99821	2.02352
65	1.9389	1.9237	1.93525	1.96106	80	1.99784	2.00925	1.99784	2.02917
80	1.9412	1.9237	1.93525	1.96825					
Time	Qt	Sorption Capacity			Time	Sorption Capacity			
mins	mg/g	mg/g	mg/g	mg/g	Mins	mg/g	mg/g	mg/g	mg/g
CDN	Experimental	Pseudo-First Order	Pseudo-Second Order	Elovich	CDGH A	Experimental	Pseudo-First Order	Pseudo-Second Order	Elovich
0	0	0	0	0	0	0	0	0	0
5	2.01275	2.00925	2.01275	1.97476	5	2.0945	2.09669	2.09669	2.06395
10	2.00865	2.00925	2.00865	1.98836	10	2.0903	2.09669	2.09669	2.07609
15	2.01498	2.00925	2.01498	1.99632	15	2.0967	2.09669	2.09669	2.0832
20	2.01237	2.00925	2.01237	2.00196	20	2.0971	2.09669	2.09669	2.08824
25	2.01536	2.00925	2.01536	2.00634	25	2.0987	2.09669	2.09669	2.09215
30	2.012	2.00925	2.012	2.00992	30	2.0991	2.09669	2.09669	2.09534
35	2.01088	2.00925	2.01088	2.01295	35	2.0971	2.09669	2.09669	2.09804
40	2.0079	2.00925	2.0079	2.01557	40	2.0959	2.09669	2.09669	2.10038

45	2.01237	2.00925	2.01237	2.01788	45	2.0965	2.09669	2.09669	2.10244
50	2.01312	2.00925	2.01312	2.01994	50	2.0969	2.09669	2.09669	2.10429
55	2.0038	2.00925	2.0038	2.02181	55	2.0997	2.09669	2.09669	2.10596
60	1.99821	2.00925	1.99821	2.02352	60	2.0985	2.09669	2.09669	2.10748
70	1.99784	2.00925	1.99784	2.02917	65	2.0959	2.09669	2.09669	2.10888
80	2.01275	2.00925	2.01275	1.97476	70	2.0959	2.09669	2.09669	2.11018
					80	2.0975	2.09669	2.09669	2.11252

B-5 Data for Removal Rate, Fluoride adsorption

Table B-7 Data for Contact Time, Fluoride Adsorption

Time	Conc	Conc	Removal Rate	Qt	Sorption Capacity		
(min)	ppb	ppm	%	mg/g	mg/g	mg/g	mg/g
CDHA				Experimental	Pseudo-First Order	Pseudo-Second Order	Elovich
0	0	0	0	0	0	0	0
5	15209	15.209	69.582	3.4791	3.51696153	3.5169612	3.36803986
10	14614	14.614	70.772	3.5386	3.51696154	3.51696142	3.41224714
25	14997	14.997	70.006	3.5003	3.51696154	3.51696154	3.43810673
30	14493	14.493	71.014	3.5507	3.51696154	3.51696156	3.45645441
35	15059	15.059	69.882	3.4941	3.51696154	3.51696157	3.47068597
40	15010	15.01	69.98	3.499	3.51696154	3.51696157	3.48231401
45	14010	14.01	71.98	3.599	3.51696154	3.51696158	3.49214537
50	14980	14.98	70.04	3.502	3.51696154	3.51696159	3.50066169
55	15108	15.108	69.784	3.4892	3.51696154	3.51696159	3.50817361
60	14841	14.841	70.318	3.5159	3.51696154	3.51696159	3.51489325
65	14987	14.987	70.026	3.5013	3.51696154	3.51696159	3.52097191
70	14859	14.859	70.282	3.5141	3.51696154	3.5169616	3.52652128
80	14628	14.628	70.744	3.5372	3.51696154	3.5169616	3.53635265
Time	Conc	Conc	Removal Rate	Qt	Sorption Capacity		
(min)	ppb	ppm	%	mg/g	mg/g	mg/g	mg/g
CDGHA				Experimental	Pseudo-First Order	Pseudo-Second Order	Elovich
0	0	0	0	0	0	0	0
5	14337	14.337	71.326	3.5663	3.48832857	3.48832825	3.36803986
10	15092	15.092	69.816	3.4908	3.48832857	3.48832846	3.41224714
15	15163	15.163	69.674	3.4837	3.48832857	3.48832853	3.43810673
20	15185	15.185	69.63	3.4815	3.48832857	3.48832856	3.45645441
25	15042	15.042	69.916	3.4958	3.48832857	3.48832858	3.47068597
30	15132	15.132	69.736	3.4868	3.48832857	3.4883286	3.48231401
35	15205	15.205	69.59	3.4795	3.48832857	3.48832861	3.49214537
40	15263	15.263	69.474	3.4737	3.48832857	3.48832862	3.50066169
45	15362	15.362	69.276	3.4638	3.48832857	3.48832862	3.50817361
50	15026	15.026	69.948	3.4974	3.48832857	3.48832863	3.51489325
55	15328	15.328	69.344	3.4672	3.48832857	3.48832863	3.52097191
60	14923	14.923	70.154	3.5077	3.48832857	3.48832863	3.52652128
70	15447	15.447	69.106	3.4553	3.48832857	3.48832864	3.53635265
80	15129	15.129	69.742	3.4871	3.48832857	3.48832864	3.54486896



PUBLICATION



Synthesis and Characterization of Goethite Nanostructured powder: Application in the Simultaneous Removal of Co(II) and Ni(II) Ions from Aqueous Solution

C.R. Nangah^{1,2}, T.G. Merlain², N.J. Nsami², C.P. Tubwoh¹, K.J. Mbadcam², D. Dodoo-Arhin³

¹Department of Chemistry, University of Buea, Buea; Cameroon

²Physical and Theoretical Chemistry Laboratory, Department of Inorganic Chemistry, University of Yaounde I, Yaounde, Cameroon

³Department of Materials Science and Engineering, University of Ghana, Accra-Ghana

Abstract:

This study investigates the adsorption efficiency of goethite nanostructured powder for the simultaneous removal of cobalt and nickel ions. The nanostructured powder sample was synthesized via a chemical precipitation technique and characterized using SEM, FTIR-ATR and XRD techniques. From batch adsorption studies, maximum adsorption for Co(II) and Ni(II) ions occurred at an equilibrium contact time of 80 min, with an adsorbent mass of 0.1 g, and at pH=7. Co(II) ions showed greater affinity to the nanoparticles as compared to Ni(II). The maximum quantities adsorbed were recorded as 148.5 mg/g for Co(II) and 110.6 mg/g for Ni(II) ions. The best isotherm model fit for both metal ions was the Freundlich model indicating heterogeneity of the surface binding sites. The pseudo-second order kinetic model was the best-fit model: an indication of a strong chemical adsorption between the adsorbent surface and metal ions. The findings show that the goethite nanostructured powder is a very effective adsorbent material and prominent candidate for the simultaneous removal of cobalt and nickel ions from water.

Corresponding Author: Nangah Che Randy, c4nangah@gmail.com

1. INTRODUCTION

Nanotechnology has great potential for providing efficient, cost-effective, and environmentally acceptable solutions for improving water quality [1]. Nanoparticles have much larger surface areas than bulk particles and are ideal building blocks for developing high-capacity sorbents with the ability to be functionalized to enhance their affinity and selectivity [2, 3, 4, 5]. Hydrated iron oxide nanoparticles are nontoxic, inexpensive, readily available and chemically stable over a wide pH range [6]. They can be synthesized by all known wet chemical methods, e.g. chemical

precipitation [7], micro-emulsion precipitation [8] sol gel [9]. Goethite (α -FeOOH) is the most common iron oxyhydroxide in soils [10, 11], sediments and ore deposits, as well as a common weathering product in rocks of all types [12]. Given its affinity to adsorb various contaminants: anions, organic acids, and cations including heavy metal ions, goethite represents an important component of environmental remediation process [13, 14]. This is highlighted in a review on the role of goethite in the environment by Liu *et al.*, [15] which illustrates the extensive research on goethites, for their capacity to remove anions (over a 100 papers), organic/organic acids (over 50 papers) and cations (over 80 papers) from aqueous solutions.

A number of studies have been carried on the use of nanostructured goethite for heavy metal removal. Hala and Hiba compared the removal of five metal cations (Cr(III), Co(II), Cu(II), Ni(II), Zn(II) ions) on nano/micro structured goethite and hematite [16]. Yen-Hua and Fu-An studied the removal of Cu(II) ions using goethite and hematite nano-photocatalysts [17], and Vinh *et al.*, investigated the removal of Cr(III) by goethite nanoparticles [18]. One study by Mohapatra *et al.*, compared Pb(II), Cd(II), Cu(II), Co(II) adsorption from single and binary aqueous solutions on additive assisted nano-structured goethite [19]. However, to the best of our knowledge no study has been carried out to investigate the simultaneous removal of Co(II) and Ni(II) ions on nanostructured goethite.

Mining of nickel ferrous laterite deposits by GEOVIC Cameroon will inadvertently release a considerable amount of cobalt, nickel and manganese into the environment, if effluents are not properly pre-treated. Cobalt and nickel are possible carcinogens [20] if not checked; their presence in local streams will be devastating to health and the aquatic environment. In this study, we tested the ability of goethite nanopowder to simultaneously remove cobalt and nickel ions from aqueous solutions, for its potential as an adsorbent for treating mine water effluent. The goethite nanopowder was synthesised by chemical precipitation and characterised. The adsorption behaviour of cobalt and nickel ions onto the nanopowder was studied through batch adsorption studies and the effects of variation of contact time, dose of adsorbent, and pH on the adsorption of cobalt and nickel ions was examined. The mechanism and kinetics of adsorption was investigated with the help of several isotherm and kinetic models. This work contributes to nanostructured goethite research and adsorption phenomena by elucidating a simple synthetic method to obtain monodisperse goethite nanoparticles and a report on the simultaneous removal of Co(II) and Ni(II) ions by this powder.

2. MATERIALS AND METHOD

All the reagents and chemicals used were of analytical grade and were used without further purification. Distilled water was used for all the synthesis procedures.

2.1 Synthesis

Goethite nanopowder was synthesized by fast hydrolysis of ferrihydrite according to a method described by Lee *et al.*, [21] with slight modifications on the temperature and ageing time and the use of NaHCO₃ as dispersant. Thus, 60.71 g of hydrated ferric nitrate was dissolved in 300 mL distilled water in a 1000 mL beaker and agitated for 1 hour. To this solution (pH 2.0), 250 mL of 1 M NaHCO₃ solution was added while stirring to disperse the particles. This solution was then titrated with 1

M NaOH to a pH of 12.06 to precipitate ferrihydrite (red brown suspension). The suspension was stirred continuously for 24 hours, and aged in an electric furnace at 90 °C for 4 hours then at 57 °C for 20 hours to convert the unstable ferrihydrite to goethite. The resulting brown precipitate was washed twice with distilled water to remove associated impurities (NO_3^- , CO_3^{2-} , OH^- , Na^+) and dried at 57 °C for 16 hours. The dried powder sample was then activated by heating at 110 °C for 20 hours, ground, sieved and stored for characterisation and use.

2.2 Characterization

Nitrogen adsorption–desorption experiments were performed on the sample using a Micromeritics TriStar 3000 V6.05A BET surface area analyzer at -196.15 °C. The specific surface area was estimated by applying the Brunauer-Emmet-Teller (BET) equation [22] in the $0.010 \leq P/P_0 \leq 0.299$ interval of relative pressure, using 0.1620 nm² for the cross-sectional area of molecular nitrogen and a sample mass of 0.2110 g. Prior to analyses, the sample was degassed in vacuum at 105 °C for 12 h.

To determine the phases present and the microstructure of the goethite nanoparticles, X-ray powder diffraction (XRD) patterns were collected on a Bruker D2 Phaser diffractometer with theta/theta geometry, operating a Cu K α radiation tube ($\lambda = 1.5418$ Å) at 30 kV and 10 mA. The XRD pattern of all the randomly oriented powder specimen were recorded in the 10° - 70° 2θ range with a step size of 0.026° and a counting time of 18 s per step. The diffraction pattern was matched against the ICSD's PDF database and qualitative phase analysis conducted using the DIFFRAC Plus EVA software (Bruker AXS GmbH). Attenuated Total Reflection Fourier Transform Infrared Spectroscopy (FTIR- ATR) was performed using a Perkin Elmer Spectrum One FTIR spectrometer in the wavelength region of 4000 cm⁻¹ - 500 cm⁻¹. A high resolution Carl Zeiss EVOHD15 scanning electron microscope operated at 20 KV and 400pA with a chamber pressure of 40 Pa was used in the surface morphological investigations of the as-produced particles. Prior to the SEM analysis, the samples were metallized with carbon coating to render them conductive.

2.3 Batch Adsorption Studies

For batch adsorption studies, 20 mL of 700 ppm Co (NO_3)₃·6H₂O and 20 mL of 700 ppm Ni (NO_3)₃·6H₂O were pipetted into a 250 mL conical flask. These were prepared in sets of eight. 0.1 g of the goethite nanostructured powder was added to these eight bottles. A control experiment was set up by pipetting 20 mL each of the cobalt and nickel nitrate solution in separate conical flasks. The nine bottles were sealed with a stopper and equilibrated for predetermined periods on a magnetic agitator. The solutions were filtered thrice-using Whatman filter paper, and the resulting supernatant was analysed for cobalt and nickel using a 210VPG Flame Atomic Absorption Spectrophotometer (BuckScientific). The quantity of metal ion adsorbed was calculated by the mass balance relationship given in **Eq. 1** [23].

$$Q_e = \left(\frac{C_o - C_e}{m} \right) x V \quad (1)$$

Where: Q_e is the quantity of substance adsorbed (mg/g), C_o is the initial adsorbate concentration (mg/L), C_e the equilibrium concentration of adsorbate (mg/L), V is the volume of solution (L), and m is the mass of sorbent in aqueous solution (g).

To determine the conditions at which maximum adsorption occurs at room

temperature, the contact time was varied from 10 to 120 min at constant concentration of 700 ppm, and 0.1 g of adsorbent. The dose rate was then varied in the range 0.03, 0.05, 0.1, 0.2, 0.3, 0.5g at a concentration of 700 ppm and fixed contact time of 80 min. Finally, the maximum adsorption condition was determined after varying the pH at various values (3 to 8) at 700 ppm, 0.1 g adsorbent, and contact time of 80 min.

3. RESULTS AND DISCUSSION

3.1 Surface Area and Pore Size Distribution

The specific surface area of iron oxides is a function of the available sites per unit mass and influences their reactivity particularly interaction with sorbents. Goethite surface has structural and functional groups (FeO^- and FeOH sites) which interact with gaseous and soluble species [13]. Fig.1 shows the BET surface area and N_2 -adsorption isotherm plot.

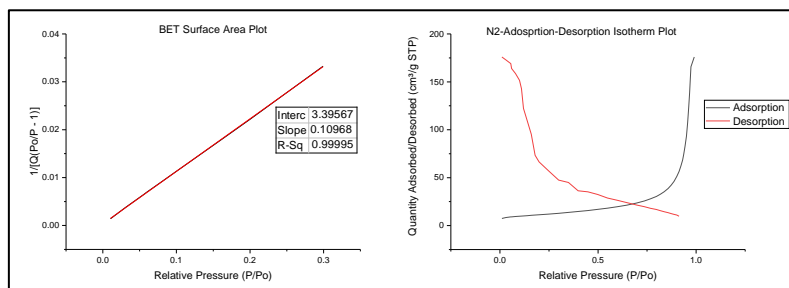


Fig. 1 BET Surface Area (a) and N_2 -adsorption-desorption Isotherm plot (b)

The specific surface area of the goethite nanostructured powder was found to be $97.0173 \text{ m}^2/\text{g}$. The average pore diameter calculated using the Barrett-Joyner-Halenda (BJH) method [24] is approximately 2 nm, hence microporous. The N_2 -adsorption isotherm plot (**Fig. 1b**) is a type III isotherm and indicates weak adsorbent-adsorbate interaction and formation of a multilayer [13].

3.3 Powder X-ray Diffraction (PXRD) Analysis and Scanning Electron Microscopy

The powder diffraction pattern of the goethite nanopowder is shown in **Fig.2**. Phase identification reveals the presence of two phases, goethite (99.24%) and sodium nitrate (ICSD collecting code: 071809). The presence sodium nitrate implies washing was incomplete. Since a line broadening corresponds to a decrease of the coherence length in the goethite particles, the observed line broadening in the (111) peak suggests a kinetics effect, which tends to modify the crystallinity and/or the crystal size. Furthermore, the small signal-to-noise ratio of the goethite pattern is also more likely due to the decrease of crystallinity and/or crystal size.

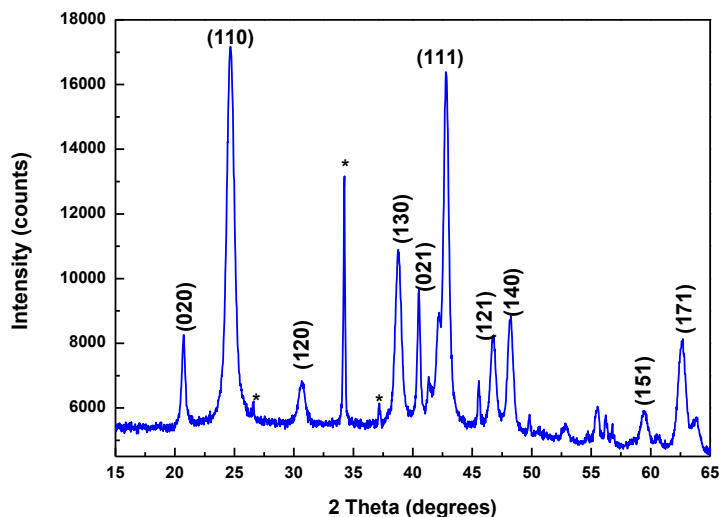


Fig. 2 XRD Spectra of Goethite Nanopowder

The morphology of the goethite nanoparticles as studied using SEM is presented in **Fig. 3**. The goethite nanoparticles exhibit monodispersed acicular (needle-like) - shaped (a) and rod-shaped features at higher magnification (b). The particle diameters range from 12.97 nm to 47.14 nm with mean particle diameter of 30.13 nm (Fig. 3c).

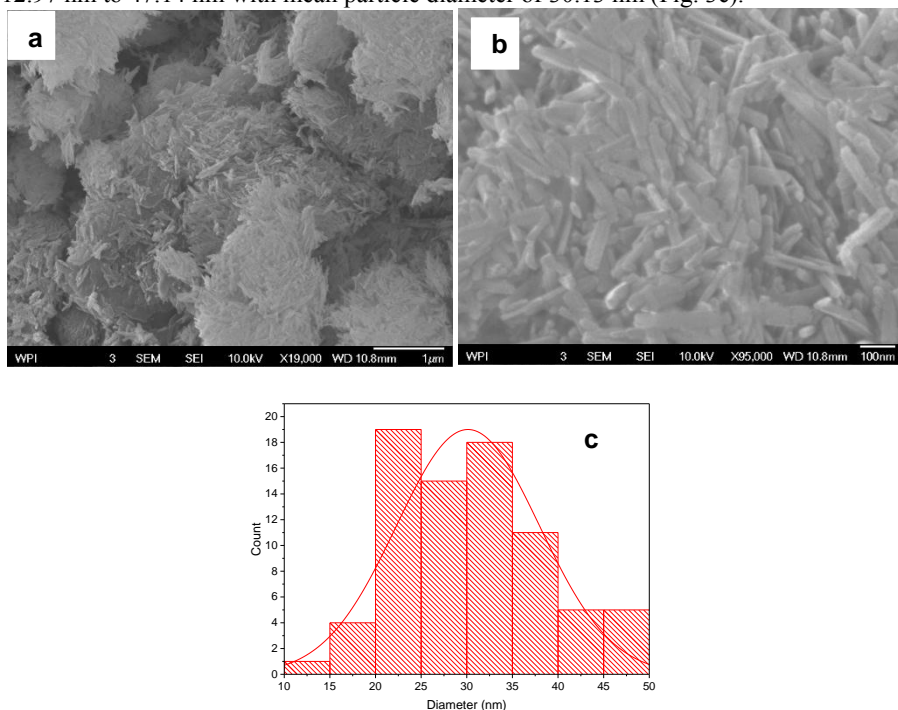


Fig. 3 SEM Micrograph of as-synthesized goethite nanoparticles at magnifications: (a) x19000 and (b) x95000; and (c) particle size distribution

3.3 Identification of Surface Functional Groups by FTIR

The FTIR spectra of the goethite nanostructured powder is shown in **Fig. 4**. The peaks around 3116 cm^{-1} , 3123 cm^{-1} and 1655 cm^{-1} , 1629 cm^{-1} could be attributed to the O-H stretching and bending modes of adsorbed water in the sample and the hydroxyl group on goethite. The sharp band at 1357 cm^{-1} corresponds to the antisymmetric stretching mode of NO_3^- . The bands at 892 cm^{-1} ($\delta\text{-OH}$) and 793 cm^{-1} ($\gamma\text{-OH}$) which are in-plane and out-of plane vibrations respectively can be assigned to the Fe-O-H bending vibrational modes of goethite [25]. The band at 628 cm^{-1} is due to stretching vibrations of the Fe-O bond, characteristic of the metal oxide [26]

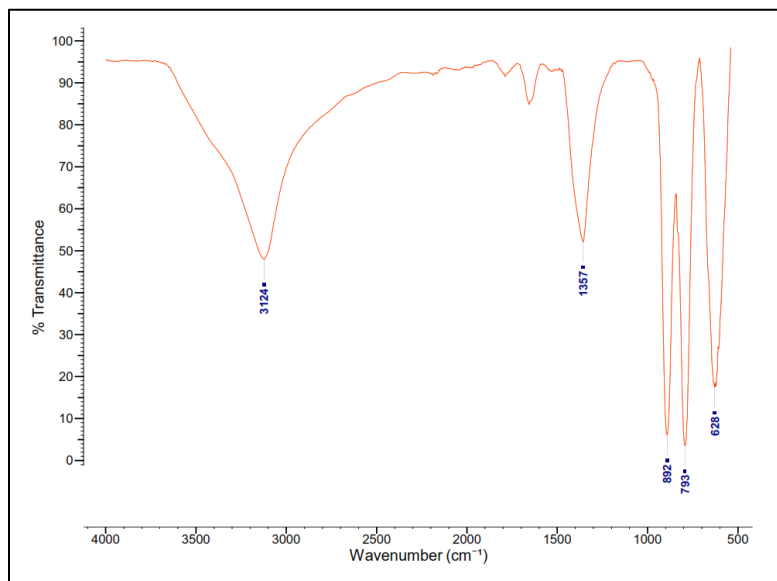


Fig. 4. FTIR Spectra of Goethite Nanostructured powder

3.5 Batch Adsorption Studies

3.5.1 Effect of contact time

The quantity of Co(II) and Ni(II) ions adsorbed as a function of time is shown in **Fig. 5**. From the graph, the quantity of metal ion adsorbed increases initially and then stabilizes after 80 minutes. This observed variation is due to availability of adsorption sites on the adsorbents at the beginning for metal ion adsorption. As the system attains equilibrium, the rate of adsorption becomes equal to the rate of desorption.

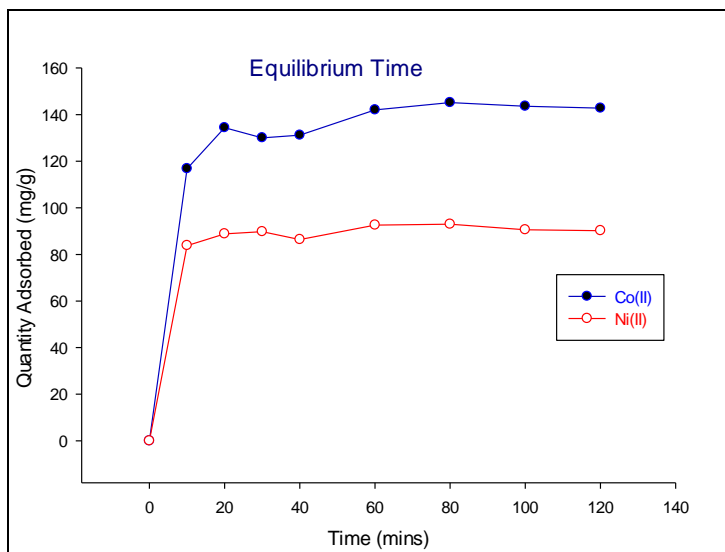


Fig. 5. Effect of Variation of Contact Time

3.5.2 Effect of dose of adsorbent

The variation of the adsorbent dose is illustrated **Fig. 6**. The quantity of Co(II) and Ni(II) ion adsorbed increases as the adsorbent concentration increases up to 0.1 g. Hence, increasing the mass of the adsorbent increases the number of active sites for adsorption. However, any further addition of the adsorbent beyond 0.1 g did not cause any significant change in the adsorption [27]. This may be due to saturation of surface sites and aggregation of adsorbent particles.

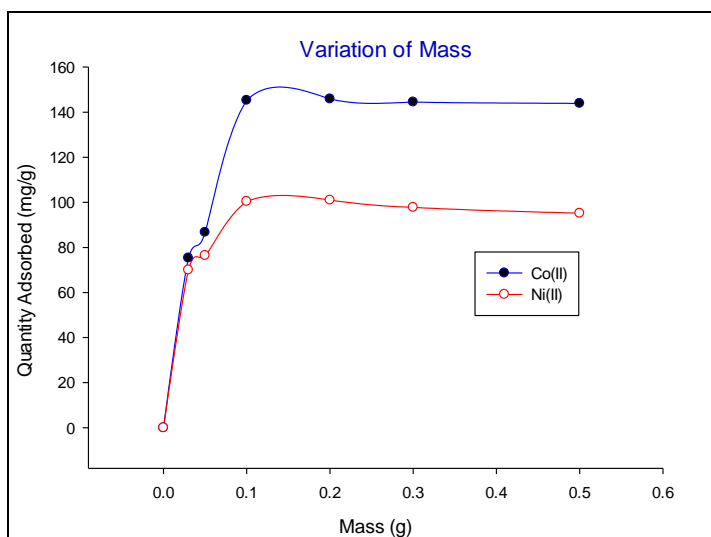


Fig. 6 Effect of Variation of Mass

3.5.3 Effect of pH

The plots for the variation of pH are shown in **Fig. 7**. The quantity of metal ions is low at low pH and increases with the increase in pH. At low pH, a positive charge develops on the surface of the adsorbents and due to repulsion between adsorbent and metal ions, hence poor sorption. As pH increases, the surface of the adsorbents become increasingly negatively charged, enhancing attraction between the metal ion and the adsorbent surface resulting in increased removal of the metal ions. An optimum pH of 7 is recorded, after which no significant change is observed. This indicates the applicability of adsorbents developed for water systems at neutral or slightly basic pH. Adsorption of metal ions onto goethite is a surface complexation reaction between the aqueous metal ions and hydroxyl-specific surface sites.

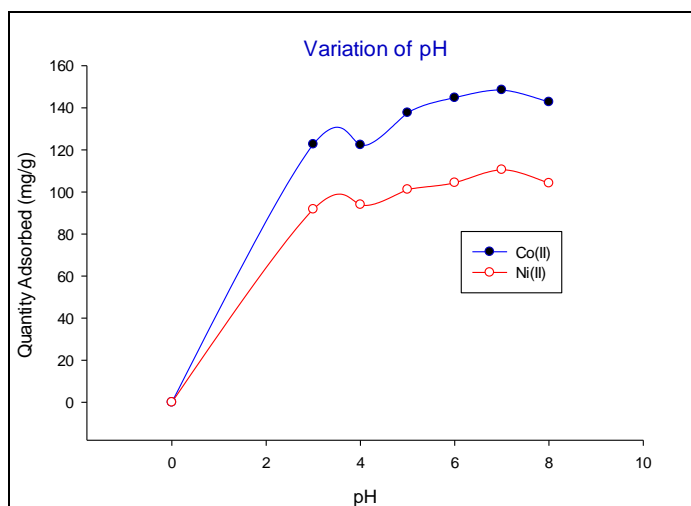


Fig. 7 Effect of Variation of pH

The results from batch adsorption studies gave an indication of the effectiveness of the goethite nanostructured powder to simultaneously remove Co(II) and Ni(II) ions. The conditions at which maximum absorption occurred for both Co(II) and Ni(II) ions (148.5 mg/g of Co(II) and 110.6 mg/g of Ni(II) ions) is; an equilibrium contact time of 80 min, an adsorbent mass of 0.1 g and pH of 7. Co(II) ions showed greater affinity to the nanoparticles as compared to Ni(II). We observe that the quantity of Co(II) ions adsorbed from solution was higher than that of Ni(II) ions.

3.6 Adsorption Isotherms

A good fit to the Langmuir isotherm to imply there is adsorption on a homogeneous surface, and a good fit to the Freundlich isotherm implies adsorption on heterogeneous surfaces. The linear forms of the Langmuir and Freundlich isotherms are given in equation 2 and 3 respectively [28].

$$\frac{1}{Q_e} = \frac{1}{Q_m K C_e} + \frac{1}{Q_m} \dots\dots\dots (2)$$

$$\ln Q_e = \ln K_f + \frac{1}{n} \ln C_e \dots\dots\dots (3)$$

The linear plots of the Langmuir and Freundlich isotherm model for Co(II) and Ni(II) ions are given in **Fig. 8**.

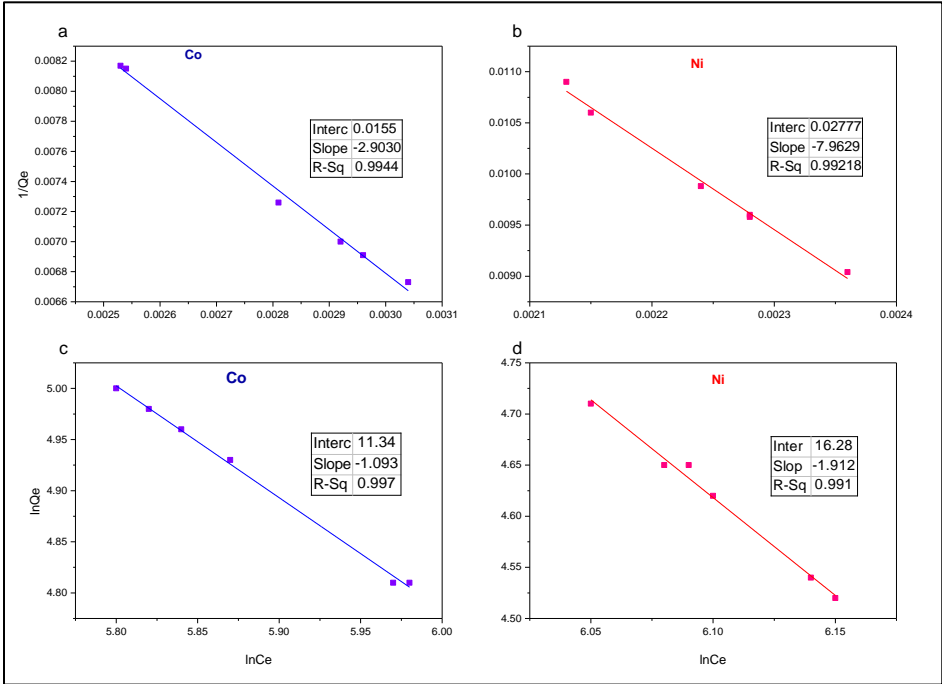


Fig. 8 The Linear Plots of the Langmuir Adsorption Model for Co(II) and Ni(ii) ions (a,b) and Freundlich Isotherm Model for Co(II) and Ni(ii) ions (c,d)

The essential parameters from these models such as the adsorption capacities Q_m and K , the separation factor R and the adsorption intensity $1/n$ are given in Table 1. The R^2 values for the Freundlich model are the highest (in the range 0.976 to 0.9965), thus the Freundlich isotherm model more accurately describes the adsorption for all three adsorbents and for both adsorbates.

Table 1: Langmuir and Freundlich Equilibrium Constants

Parameter		Langmuir Isotherm			Freundlich Isotherm		
		k_L (L/mg)	Q_m (mg/g)	r^2	K_f (L/g) $\times 10^7$	$1/n$	r^2
Goethite nanoparticles	Co(II)	-0.05	64.52	0.995	0.008	-1.094	0.976
	Ni (II)	-0.22	35.84	0.994	11.8	-1.913	0.991

3.7 Kinetics of Adsorption

The kinetics of Co(II) and Ni(II) ion adsorption was studied, with respect to several kinetic models as a function of pH at a constant initial concentration of 700 mg/L, adsorbate dose of 1 g/L at a contact time of 80 mins. Equations 4, 5, 6 are linear transforms of the Lagergren's pseudo-first order, pseudo-second order and Elovich kinetic models respectively [29].

$$\ln(Q_e - Q_t) = \ln Q_e - K_1 t \quad (4)$$

$$\frac{t}{Q_t} = \frac{1}{h_o} + \frac{t}{Q_e} \quad (5)$$

$$Q_t = \frac{1}{\beta} \ln(\alpha\beta) + \frac{1}{\beta} \ln t \quad (6)$$

Where, Q_e and Q_t are the adsorption capacity at equilibrium and at time t respectively (mg/g). K_1 is the rate constant of pseudo-first order adsorption (min^{-1}), K_2 is the rate constant of pseudo second order adsorption ($\text{mg}^{-1} \text{min}^{-1}$), $h_o = K_2 Q_e^2$ is the initial adsorption rate ($\text{mg} \cdot \text{g}^{-1} \text{min}^{-1}$), α is the initial sorption rate ($\text{mg} \cdot \text{g}^{-1} \text{min}$) and β is the rate constant for desorption ($\text{g} \cdot \text{mg}^{-1}$) during any one experiment.

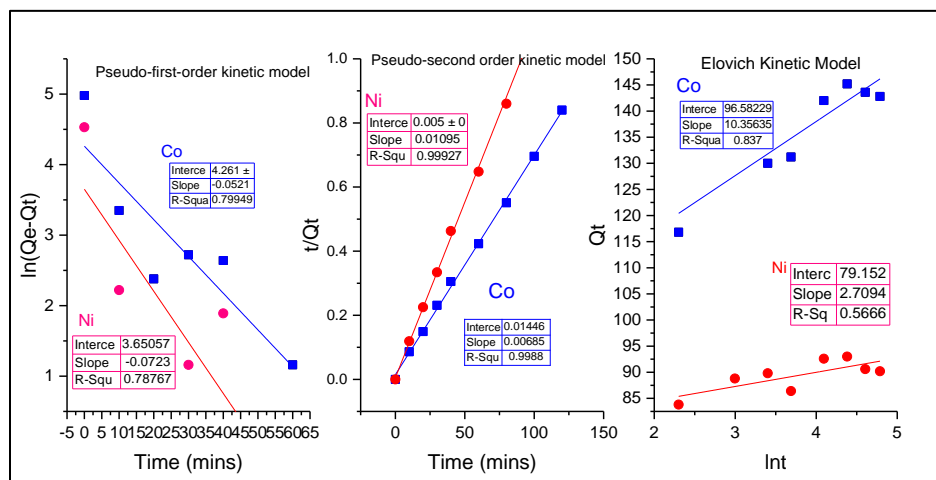


Fig 9. Kinetic models

Table 2 lists the kinetic parameters for the three kinetic models and correlation coefficients of the metal ions. From the table, the pseudo-second order kinetic model best fit (in the range 0.9887 to 0.9993) the kinetic data for all three adsorbents and

two adsorbates. This indicates chemisorption and the formation of covalent bonds between the metal and adsorbents. Thus, the adsorption of cobalt and nickel ion onto iron oxide, goethite and goethite nanopowder is a surface complexation reaction by inner sphere bonding between the adsorbent and adsorbate.

Table 2: Rate Constants and Correlation Coefficients of Kinetic Models

Models	Parameter	Goethite Nanopowder	
Pseudo-first order	R^2	Co(II)	0.7995
		Ni(II)	0.7877
	K_1	Co(II)	0.0521
		Ni(II)	0.0724
	R^2	Co(II)	0.9988
Pseudo-second order	h_0 (mg/g min)	Ni(II)	0.9993
		Co(II)	68.97
	K_2 (g/mg min)	Ni(II)	200
		Co(II)	0.003
		Ni(II)	0.024
	Q_e	Co(II)	147.06
		Ni(II)	90.91
	R^2	Co(II)	0.837
		Ni(II)	0.5666
		Co(II)	0.0965
Elovich	β (g/mg)	Ni(II)	0.3691
		Co(II)	115655
	α (mg/g min)	Co(II)	115655
		Ni(II)	13×10^{12}

4. CONCLUSION

Nanostructured goethite powder has been synthesized via chemical precipitation technique and characterized its structure, microstructure, surface area, porosity and morphological properties. From the batch studies, equilibrium was attained after a contact time of 80 min for all three adsorbents, an adsorbent dose of 0.1 g and pH=7. These were the optimum conditions obtained from varying these parameters at metal ion concentration of 700 ppm. The maximal adsorbed quantities were 148.5 mg/g of Co(II) and 110.6 mg/g of Ni(II) ions. The best isotherm model fit for both metal ions was the Freundlich model (monolayer adsorptions) with least square (R^2) values in the range 0.976 to 0.9965. Analysis of kinetic data presented the pseudo-second order kinetic model as the best-fit model (in the range 0.9887 to 0.9993). This indicates chemisorption and the formation of covalent bonds between the metal and adsorbents, hence a good correlation between equilibrium and kinetics. The study demonstrated the potential (high adsorption capacity) for this the nanostructured powder to simultaneously remove Co(II) and Ni(II) from aqueous solution. We therefore propose this adsorbent as a cheap and effective route for the removal of these dissolved heavy metals in the water purification process. Further studies into its ability for simultaneous adsorption of other heavy metals seem plausible.

Acknowledgements

We are grateful to Dr. Chi Georges of De Montfort University, Leicester, UK for recording the FTIR and SEM spectra and to Prof. Dave Billing of University of the Witwatersrand, SA, for PXRD analysis. Special thanks to Prof. Claude Lecomte, for the travel bursary to SA, under the IUCr Crystallography in Africa Initiative.

REFERENCES

- [1] H. Parham, B. Zargar and R. Shiralipour., (2012) *J. Hazard. Mater* **205-206**, 94-100.
- [2] F. Sandra, B. Meredith, C. Bin, F. B. Jillian and Z. Hengzhong, (2012) *RSC Adv.* **2**, 6768–6772.
- [3] R. G. Pushpa, A.G. Anaselvi and P. Subramaniam, (2013) *Int. J. Nanomater. Biostruct.* **3**, 26-30.
- [4] S. D. Mamadou, S. D. Jeremiah, S. Nora, S. Anita and S. Richard, Nanotechnology applications for clean water, eds. Nora S., Mamadou D., Jeremiah D., Anita S. and Richard S., (William Andrew Inc, USA, 2009), pp 585-587.
- [5] K. T. Dhermendra, J. Behari and S. Prasenjit, (2008) *World Appl. Sci. J.* **3**, 417-433
- [6] M. C. Kimberly, L.U. Yunfeng, Z. Tonghua, Z. Jingjing, M. Gary and J. Vijay: Nanotechnology applications for clean water, eds. Savage N., Mamadou D., Jeremiah D., Anita S. and Richard S., (William Andrew Inc., USA, 2009), pp. 350.
- [7] J. Lodhia, G. Mandarano, J. Feris, S. F. Cowell, P. MacCallum (2009). *Biomed. Imag. Intervention J.*, **6**.
- [8] M. G. Sajuna and S. Mohanty (2010). *Int. J. of Eng. Sci. Tech.*, **2**, 1-12.
- [9] I. Kazuharu and Y. Tsutomu (2002). *Trans.*, **43**, 2097-2103
- [10] G. Françoise, R. Philippe, L. François, R. Céline and C. Egle (2008). *J. Phys. Chem. Solids*, **10**, 1016-1043.
- [11] A. Mariana, E. S. Elsa, and H. R. Elsa (2008). *Am. Mineral.*, **93**, 584–590.
- [12] Y. Hexiong, L. Ren, T. D. Robert and C. Gelu (2006). *Acta Cryst.* **62**, 250–252
- [13] R. M. Cornell and U. Schwertmann (2003). *The Iron Oxides: Structure, Properties, Reactions, Occurrences and Uses*. WILEY-VCH Verlag GmbH & Co., KGaA, Weinheim, pp. 141-143, 253-296.

- [14] M. Mamata, K. Rout, S. K. Gupta, P. Singh, S. Anand, and B. K. Mishra (2010). *J Nanopart Res*, **12**, 681-686.
- [15] H. Liu, T. Chen, L. Ray, and H. Frost (2013). *Chemosphere* **xxx** xxx-xxx.
- [16] H. Hala and H. Yousef (2012). *Intl J. Eng. Sci. Technol.*, **4**, 3018-3028
- [17] Yen-Hua Chen, Fu-An Li, (2010). *J. Colloid Interface Sci.*, **347**, 277-281
- [18] V. D. Nguyen, J. Kynicky, P. Ambrozova and V. Adam (2017). *Mater.*, **10**, 783
- [19] M. Mohapatra, L. Mohapatra, P. Singh, S. Anand and B.K. Mishra (2010). *Intl. J. Eng. Sci. Technol.*, **8**, 89-103
- [20] P. Apostoli, R. Cornelis, J. Duffus and D. Lison D: (2006) *WHO* **234**, 70-158.
- [21] G. H. Lee, S. H. Kim, B. J. Choi and S. H. Huh. (2004) *J. Korean Phys. Soc.* **45**, 1019-1024.
- [22] S. Brunauer, P. H. Emmett, E. Teller, (1938). *J. Am. Chem. Soc.* **60** (2), 309-319. *Ceram. Soc.* **83**, 1649-1657.
- [23] G. Vijayakumar, R. Tamilarasan, and M. Dharmendirakumar (2012). *J. Mater. Environ. Sci.*, **3**, 157-170.
- [24] E. Yagmur, M. Ozmak, Z. Aktas, (2008) *Fuel* **87** 3278-3285.
- [25] M. Mohapatra and S. Anand, (2010) *Int. J. Eng. Sci. Tech.* **2** 127-146.
- [26] Y. Zhao, F. Liu, X. Qin, (2017) *Chemosphere* **180** 373-378
- [27] H. A. Beyene and A.M. Alemayehu, (2013) *Bull. Chem. Soc. Ethiop.* **27** 35-47
- [28] K. Maguie, N. Nsami, K. Daouda, C. Randy, K. Mbadcam, (2017). *IRA Int. J. Appl. Sci.* **8**(1), 18-30.
- [29] S. E. Agarry and M. O. Aremu (2012). *Br. Biotechnol J.* **2**(1): 26-4